UNIVERSITY OF CALIFORNIA
RIVERSIDE

Deep Cavitands for Molecular Recognition in Biomimetic Membrane Environments

A Dissertation submitted in partial satisfaction
of the requirements for the degree of

Doctor of Philosophy

in

Chemistry

by

Lizeth Pérez

September 2018

Dissertation Committee:
Dr. Richard J. Hooley, Chairperson
Dr. Dave Martin
Dr. Jingsong Zhang

The Dissertation of Lizeth Pérez is approved:

_____

_____

_____

Committee Chairperson

University of California, Riverside

Dedication

This thesis is dedicated first and foremost to my parents, Arnulfo and Agustina Ramírez. With this achievement I complete our American Dream while making your tremendous sacrifices in bringing me to this country and working back breaking jobs worthwhile. To my husband, Jorge Pérez for his unconditional love and support from the beginning. To my brothers, Alexis and Arnulfo Ramírez, for believing in me and helping fund my education in times of need. And to Alejandro, Josue, and my future children, nieces and nephews: I hope I can be an example for you to follow and give you the strength to follow your dreams. Sí se pudo!

Esta tesis es dedicada a mis padres, Arnulfo y Agustina Ramírez. Con este logro complete nuestro Sueño Americano y hago valer la pena todo su trabajo y sacrificio de traernos a este pais. Para mi esposo, Jorge Pérez por el apoyo y amor incondicional que me ha brindado. Para mis hermanos, Alexis y Arnulfo Ramírez por creer en mi y por ayudar a financiar mi educacion en tiempos difíciles. Y para Alejandro, Josue, hijos y sobrinos futuros: espero ser un ejemplo a seguir y poder darles la fortaleza para seguir y cumplir sus sueños. ¡Si se pudo!

ABSTRACT OF THE DISSERTATION

Deep Cavitands for Molecular Recognition in Biomimetic Membrane Environments

by

Lizeth Pérez

Doctor of Philosophy, Graduate Program in Chemistry
University of California, Riverside, September 2018
Dr. Richard J. Hooley, Chairperson

The cell's surface is complex and multicomponent in nature. It is the setting where a variety of crucial life processes take place, mediated by the interaction of cell surface receptors with specific molecules outside of the cell. Studying how particular interactions take place in this convoluted environment can be difficult in actual cell membranes. Modeling components of the cell's surface can be beneficial in studying cellular processes, although mimicking these systems poses a substantial challenge. Synthetic receptors such as calix[n]arenes, cyclophanes, and cyclodextrins are capable of performing molecular recognition of ionic and hydrophobic guests in aqueous environments, however, these synthetic receptors are not useful for molecular recognition studies in membrane environments.

This work studies the molecular recognition abilities of water-soluble deep cavitands in membrane environments. The binding behavior of cavitands in membrane-like envrionments was studied using NMR analysis. The differences in binding behavior were elucidated in lipid environments compared to free solution. Supported lipid bilayers

have been previously employed to mimic membrane environments, and the binding of trimethylammonium-tagged compounds and cationic native proteins were monitored via surface plasmon resonance (SPR) spectroscopy. By varying the functionality at the cavitand's rim, a broader range of interactions were explored. The binding of anionic native proteins was possible by positioning a positive charge at the rim of the cavitand and more complex interactions between host and guest were possible by tailoring guests that utilize dual mode binding. In order to imitate larger structures on cell surfaces such as glycopolymers, cavitand-mediated atom transfer radical polymerization (ATRP) was performed in order to create a functional polymer on the SLB surface. Utilizing aminoethyl methacrylate, an amine polymer was formed that can be further derivatized by reacting fluorescent compounds for visualization, or epitopes for the adhesion of larger biomolecules such as avidin. The versatility of the amine-functionalized polymer was demonstrated with its ability to bind large structures such as cells at the interface of SLBs. The diverse interactions of the variably functionalized cavitands also led to their use in indicator displacement assays (IDA) for sensing a variety of analytes ranging from post translational modifications to metals and steroids.

Table of Contents

Chapter Three: Selective Protein Recognition in Supported Lipid Bilayer Arrays by Tailored, Dual-Mode Deep Cavitand Hosts

Chapter Four: Cell and Protein Recognition at a Supported Lipid Bilayer Interface via *In Situ* Cavitand-Mediated Functional Polymer Growth

Chapter Five: Cavitands in Indicator Displacement Assays and Inside Cells

Chapter Six: Steroid Sensing

Chapter Seven: Experimental

List of Figures

List of Tables

Chapter One: Introduction to Molecular Recognition in Membrane Systems

1.1 Molecular Recognition in Biological Systems

Molecular interactions are a common occurrence in biological systems. Recognition events happen constantly between enzymes and small molecules in order to keep the machinery of life going. These interactions include protein-protein and protein-ligand binding. One important setting for such events is the cell's surface. The cell's membrane is extensively decorated with a plethora of molecules ranging in size from small molecular epitopes to large proteins and glycopolymers.[1,2,3] These molecules are crucial to a variety of the cell's functions including cell transport and communication. The roles of these cell surface receptors makes them an important target of study.

Molecular recognition by proteins and enzymes is facilitated by the physical and chemical properties exhibited by their binding cavities. The binding events are mostly due to noncovalent interactions such as hydrogen bonding, electrostatic, cation-π, as well as hydrophobic interactions. Proteins anchored in the cell's membrane with molecular recognition abilities play key roles in transporting molecules in and out of the cell. An example of such proteins are the nicotinic acetylcholine receptors (nAchR). These proteins are multi-subunit ionophores and mediate the effects of acetylcholine.[4] The structure of these receptors is pentameric, with the subunits arranged around a central pore. Ligand binding induces channel opening of the protein, allowing for the flow of ions such as Ca^{2+}, Na^{+} and K^{+} through the pore. The ligand binding site for nAchR is a hydrophobic region composed of aromatic and hydrophobic residues from two different subunits linked by a

disulfide bridge (**Figure 1.1**). Acetylcholine is recognized by the binding site due to cation-π interactions with the aromatic residues lining it, causing a change in conformation of the protein, allowing the channel to open and communication to happen between the inside and outside of the cell.[5,6]

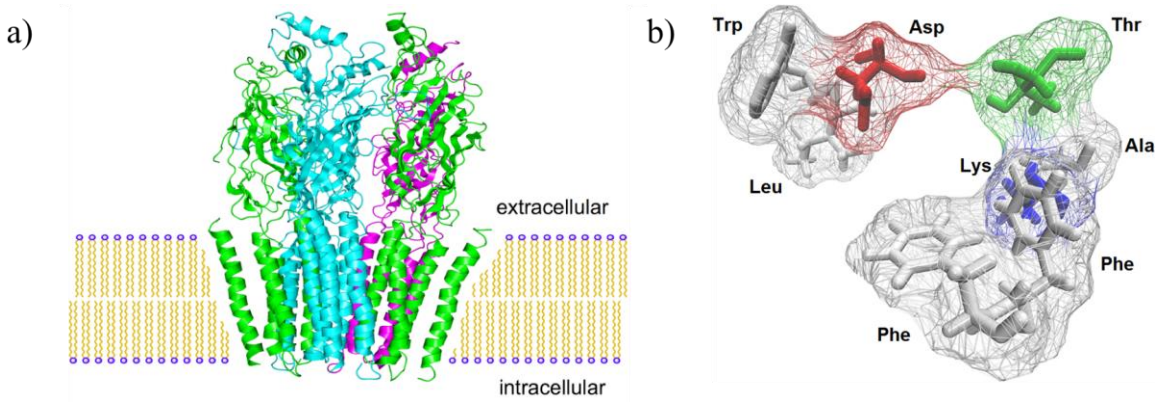

Figure 1.1: a) A transmembrane nicotinic acethylcholine receptor and b) the active site amino acid residues.[7]

1.2 Molecular Recognition by Synthetic Receptors

There are a variety of synthetic receptors capable of performing molecular recognition in aqueous environments. Mimicking cell surface receptors using synthetic structures is challenging due to the complex environment. Performing recognition studies in aqueous environments helps to drive hydrophobic guests into the cavity of the receptor due to the hydrophobic effect; the tendency of nonpolar molecules to exclude water and aggregate in an aqueous solution. Hydrophobic molecules disrupt the hydrogen bonding network between water particles and are not able to participate in these interactions with water. The hydrogen bonds between water molecules orient themselves around the

hydrophobic molecule to minimize hydrogen bond disruption and therefore form a hydrophobic "cage" around the hydrophobic structure. The hydrophobic effect is believed to constitute the principal thermodynamic driving force for the binding of small molecule ligands and their protein receptor.[8,9,10]

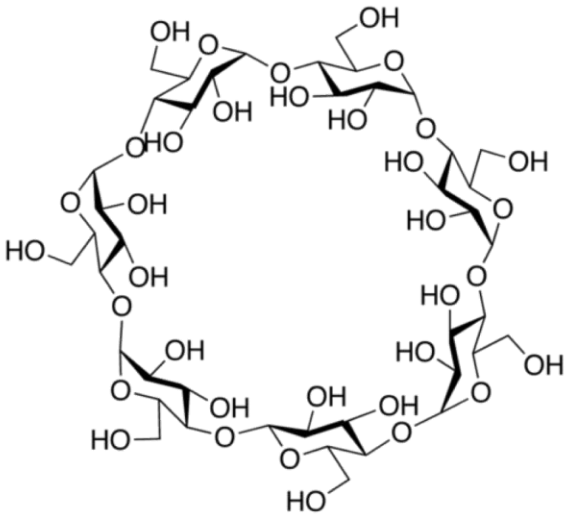

1.1

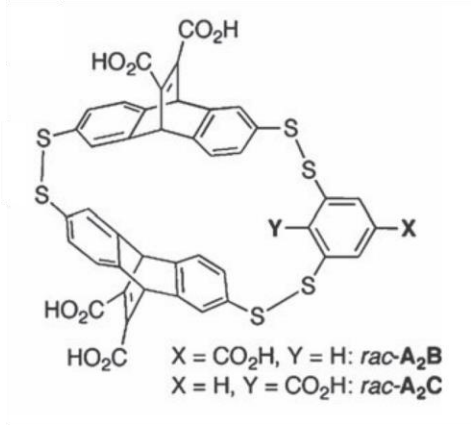

1.2

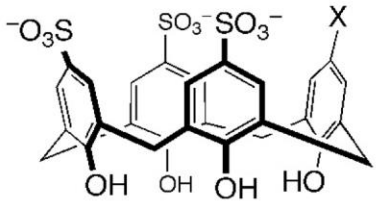

1.3

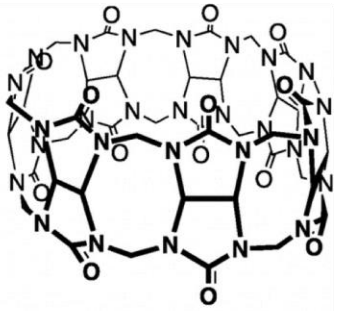

1.4

Figure 1.2: Structure of synthetic receptors capable of molecular recognition in aqueous environments: ß-cyclodextrin **1.1**, cyclophane **1.2**, and calixarene **1.3** and cucurbituril **1.4**.

When performing molecular recognition using synthetic receptors, there are many factors to be considered: the multiple interactions between the host and guest, as well as interactions with the solvent and any other surrounding components. When designing synthetic receptors, water solubility is also desired, as well as a hydrophobic cavity. It is also desirable for the host to bind its targets selectively and with high affinity in order to overcome any competing interactions. A few examples of synthetic receptors with the ability for recognition in water are cyclodextrins, cyclophanes, calix[n]arenes and cucurbit[n]turils (Figure 1.2). Cyclodextrins **1.1** are glycosidic macrocycles with a hydrophobic cavity and hydrophilic exterior surface, allowing for water solubility. Cyclodextrins are known to bind small hydrophobic molecules in aqueous environments, but they lack selectivity.[11] Cyclophanes **1.2** contain a hydrophobic cavity formed by its bridged aromatic rings. Water solubility can be manipulated by functionalizing the linkers with hydrophilic groups or by incorporating heterocyclic aromatic compounds. Cyclophanes can bind hydrophobic compounds and show a good affinity for ammonium ions via cation-π interactions.[12,13] Calix[n]arenes **1.3** are aromatic macrocycles composed of phenol rings bridged by methylene groups. The alcohol groups can be further functionalized, conferring water solubility, while the aromatic cavity allows for hydrophobic guest incorporation. Functionalization of the rims of these receptors can alter their molecular recognition abilities.[14,15,16] Cucurbit[n]urils **1.4** are comprised of glycouril units bridged by methylene groups and possess a hydrophobic pocket that is capable of attracting cationic guest molecules.[17] These varying synthetic receptors have been used to recognize large biomacromolecules and even analyze peptide post-translational

modifications (PTM).[18,19] Sulfonated calixarenes, for example, have been shown to bind effectively to ammonium ions, in particular lysine residues.[20]

These water-soluble synthetic receptors are capable of performing molecular recognition in water, but applying their recognition abilities to a membrane environment would prove rather challenging. In membrane environments, there is extensive competition from its hydrophobic components, forcing the hydrophobic guest into the membrane instead of into the hydrophobic pocket of the guest. This extensive competition would make it almost impossible for these receptors to effectively bind their target molecule. The water solubility of these receptors also prevents them from efficiently incorporating into membranes. Some receptors, such as cyclodextrins, are also incompatible to such environments due to their tendency to disrupt the membrane and remove cholesterol.[21]

Small molecules have been developed to induce endocytosis or transport target molecules through membranes. These artificial membrane receptors work by covalently attaching the desired recognition motif to a lipid or steroid derivative which can then be incorporated into a membrane environment while displaying the recognition element above the surface. The recognition element can attract a variety of targets including drugs, which can then be taken into cells.[22,23,24] Molecular umbrellas[25,26,27] mimic membrane-penetrating proteins[28] and transmembrane pore-forming peptides[29] in order to transport molecules across membranes. These proteins incorporate into the membrane while displaying a cavity that shields polar guests from the lipophilic membrane.[30] A synthetic host that is capable of embedding itself into a membrane while retaining its selectivity would be a simpler approach compared to the covalent derivatization of steroids and lipids for membrane incorporation.

1.3 Water-Soluble Deep Cavitands as Synthetic Receptors

Resorcin[n]arene based cavitands are well established protein mimics.[31,32] These synthetic receptors possess a concave aromatic cavity and are able to bind guests in aqueous environments. Synthetic hosts such as these, with greater curvature (deeper pocket) would provide more control and guest coverage. Bowl-shaped scaffolds such as molecular clips and tweezers provided a linear, all-carbon backbone for guest recognition, but their synthesis is challenging.[33,34] A simpler approach was to form an oxygen-containing carbon skeleton through the condensation of resorcinol with an alkyl aldehyde via electrophilic aromatic substitution to give resorcin[4]arene **1.5** (Figure 1.3).[35]

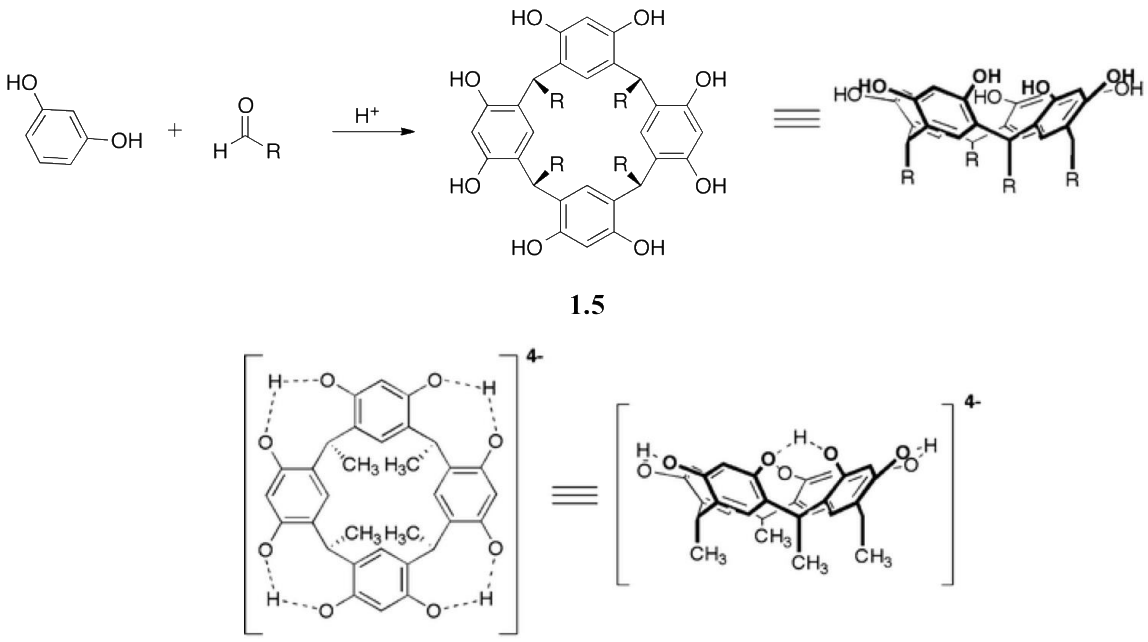

Figure 1.3: Synthesis of resorcin[4]arene **1.5** and it's conformation after deprotonation and formation of tetraanionic resorcin[4]arene.[36]

By varying the alkyl aldehyde used, the "feet" of resorcin[4]arene **1.5** can be varied in order to impart varying solubility properties without affecting the upper rim's binding abilities. The eight hydroxyl groups on the rim of **1.5** allow for further derivatization and water solubility. In the presence of excess sodium hydroxide, only one proton is removed from each resorcinol unit, allowing for the formation of tetraanionic resorcin[4]arene. Tetraanionic resorcin[4]arene is able to fold into a shallow bowl-like structure(C_{4v}) with the aid of four intramolecular hydrogen bonds. The delocalization of the negative charge prevents the full deprotonation of anionic resorcin[4]arene even in the presence stronger bases. The delocalized negative charge at its rim allows for the binding of guests such as

tetramethylammonium (K_a = 3 x 10^5 M^{-1}) and other alkylammonium salts due to electrostatic interactions with the rim in water.[36]

To make the shallow cavity of resorcin[4]arene **1.5** rigid, Cram bridged the phenols with methylene units to form **1.6**.[37] This bridged receptor contains a cavity with a depth varying from 3.3-4.2 Å and allows limited binding to small organic molecules such as CH_2Cl_2, CS_2, and $C_6H_5CH_3$. A deeper cavity can be built onto resorcin[4]arene **1.5** through nucleophilic aromatic substitution with four equivalents of either 2,3-dichloropyrazine or 1,2-difluoro,4,5-dinitrobenzene.[38] A deeper cavity would allow for the encapsulation of larger guests, however, the deeper quinoxaline cavitand **1.7** contained flexible walls that readily converted between two conformations: the "kite" and "vase" (Figure 1.5). These two conformations can be monitored via ^{1}H NMR by observing the bridging methine proton. In the "vase" conformation, where all the walls are oriented up and form a deep cavity, the methine peak is observed above 5 ppm. In the C_{2v} "kite" conformation the walls of the cavitand flexed outward, forming a large flat surface and the methine peak is present at almost 3 ppm due to shielding. In order to reduce the aromatic surface's exposure to water, the kite conformation can form a D_{2d} dimer called a velcrand, as seen in Figure 1.5.[39] If an appropriate guest is added to the system, the velcrand can disassemble and form the C_{4v} vase conformation while accommodating the guest in its aromatic cavity (Figure 1.6).[40] Because the "vase" conformation is desired due to its ability to bind guests, cavitand **1.7** was not ideal due to its flexibility and propensity towards the velcrand conformation, which limited its host properties.[39]

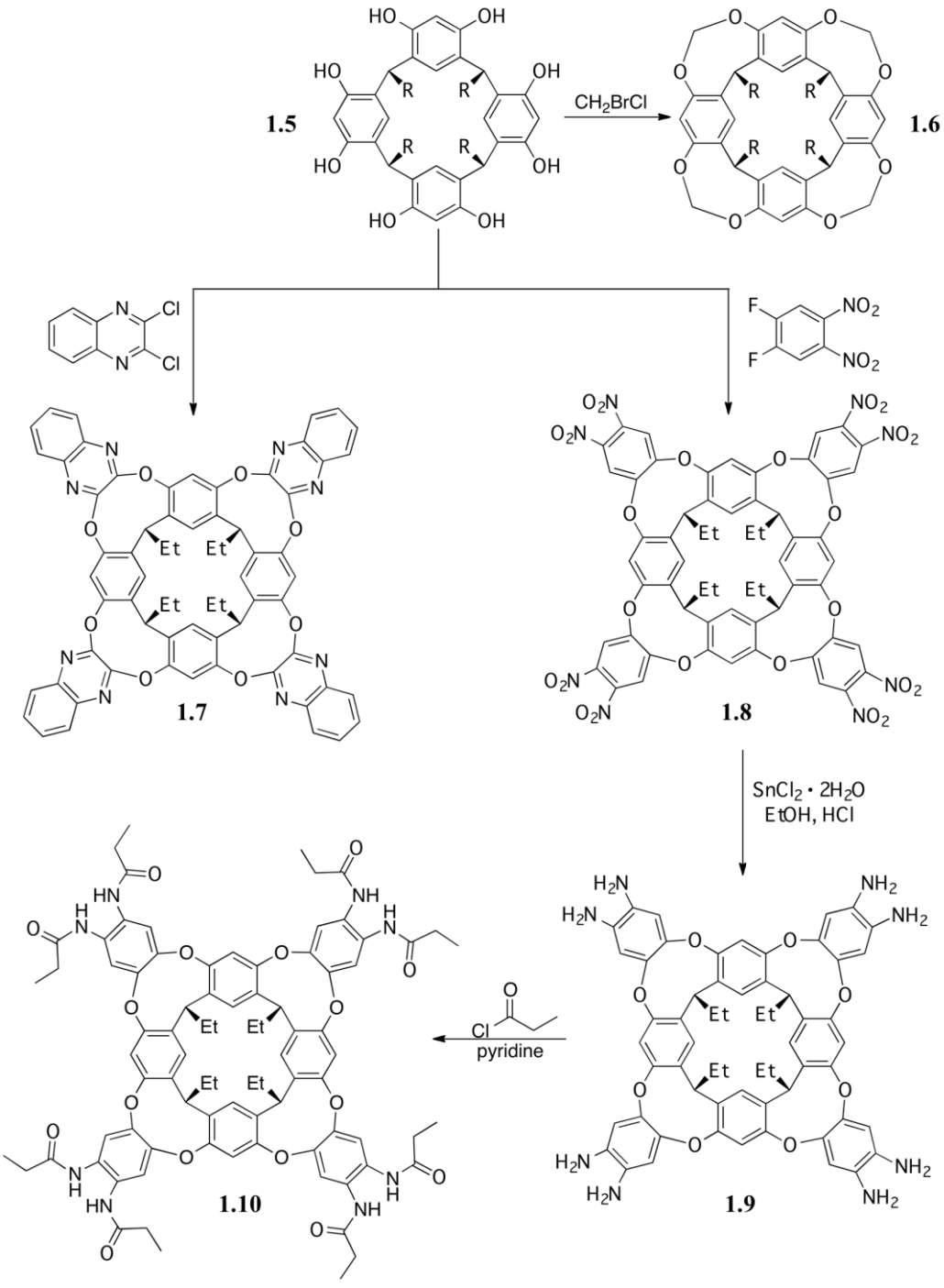

Figure 1.4: Synthesis of quinoxaline **1.7** and octaamide **1.10**cavitands.

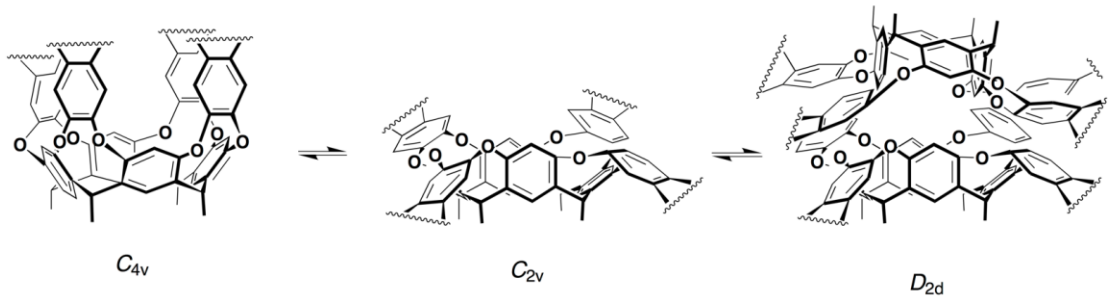

Figure 1.5: Schematic representation of the cavitand walls flexing and changing conformations between vase, kite and velcrand.

Gibb took another approach to deepening the cavitand by bridging the phenols of resorcin[4]arene **1.5** with α,α-dibromobenzyl groups. The aromatic rings are placed above the cavity, deepening it to 380 Å (Figure 1.6). To impart water solubility on the cavitand, eight carboxylate groups were added to both the rim and feet of the cavitand to obtain **1.11**.[41] Neutral and cationic derivatives of Gibb's cavitand are also known and are capable of binding small molecules with binding constants ranging from 10^3-10^6 M^{-1}.[42,43,44] In particular, host **1.11** binds hydrophilic groups such as hexanoate and adamantanecarboxylate ions (highest affinity).[45] The binding affinity of guests in **1.11** dramatically differed depending on the solvent present.

R = CO_2H

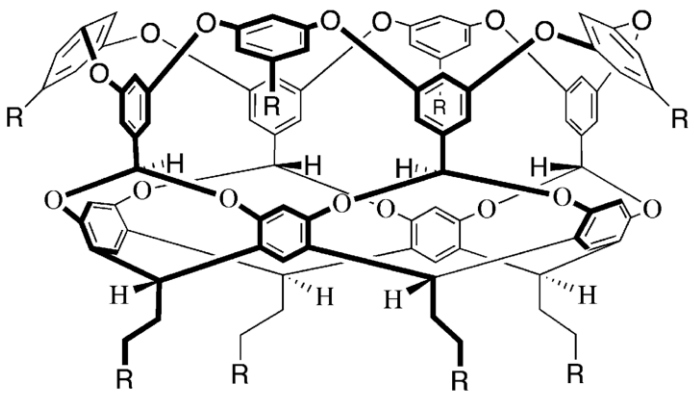

1.11

Figure 1.6: Gibb's water-soluble deep cavitand.[44]

The octanitro cavitand can be reduced into the labile octaamine cavitand **1.9** through treatment with tin(II) chloride in the presence of hydrochloric acid.[36] There are numerous functionalities that can be placed on the cavitand's rim by reacting the octaamine cavitand **1.9**. If reacted with propionyl chloride, an octaamide functionalized cavitand is produced **1.10** (Figure 1.4).[46] The octaamide cavitand **1.10** experiences directional hydrogen bonding at the upper rim, with both the oxygens and nitrogens from the amides at the rim participating. This cavitand binds suitably sized guests with soft charges such as trimethylammonium ions that can exploit the cation-π interactions with the aromatic walls. The three different conformations (vase, kite, velcrand) can be monitored via ^{1}H NMR by monitoring the chemical shift of the methine proton located on the resorcin[4]arene base. In the absence of a suitable guest, **1.10** forms the kite conformation which dimerizes into a velcrand. Upon addition of guest, it forms a 1:1 complex and folds into the vase

conformation that is stabilized by intramolecular hydrogen bonding between the carbonyl oxygen and amine on the amide functionality of the rim.[47]

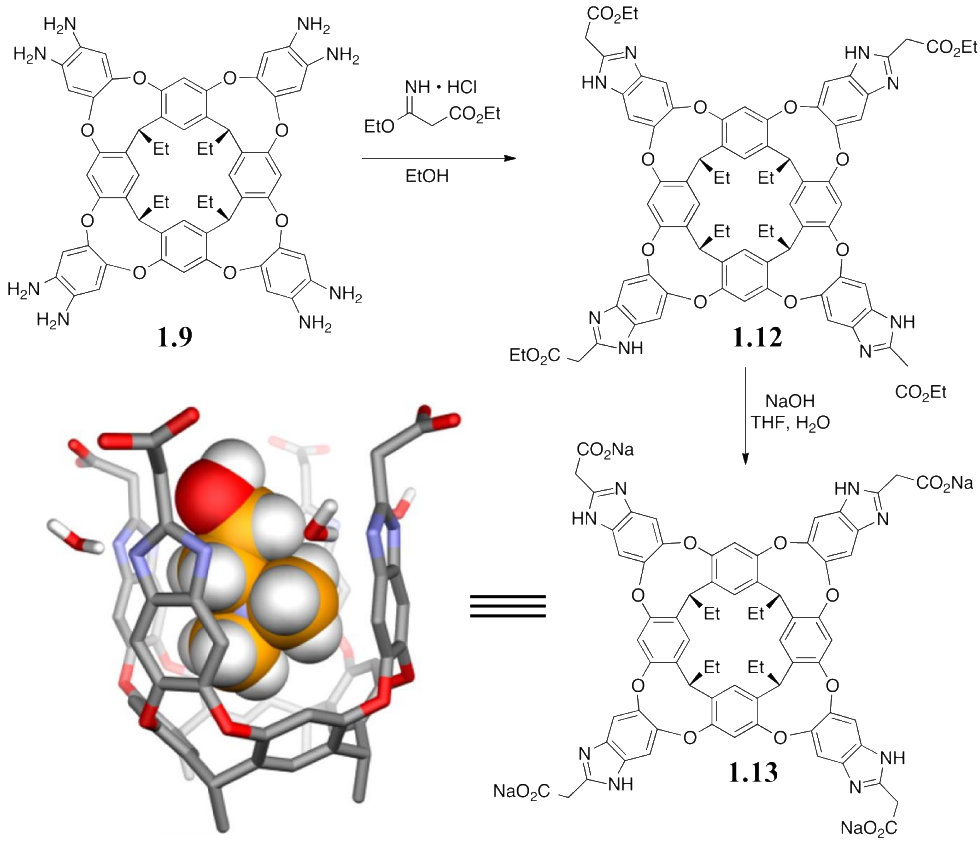

Figure 1.7: Synthesis of the tetraester cavitand **1.12** and consequent saponification to form the tetracarboxylate cavitand **1.13**. Space filling model of **1.13** with THF in the aromatic pocket and 4 water molecules hydrogen bonding to the benzimidazole rim.

In order to confer kinetic stability on the host in water, the octaamine cavitand **1.9** can be reacted with ethyl 3-ethoxy-3-iminopropionate to form a benzimidazole ring at the rim with a protruding ester moiety. This tetraester cavitand **1.12** can undergo hydrolysis to form the tetracarboxylate cavitand **1.13**.[36] The extended benzimidazole ring allows the

cavitand to participate in intermolecular hydrogen binding between four water molecules and an amine on the benzimidazole rings, allowing it to stabilize in the vase conformation even in the absence of proper guest. Though the general binding properties of the benzimidazole cavitands were similar to those of octaamide **1.13**, the benzimidazole displayed a deeper cavity, stronger binding constant and slower guest exchange. The favorability towards the benzimidazole scaffold has to do with the lack of H-bonding of the amide anime with the guest.[48]

One THF molecule is also present in the cavity of the tetracarboxylate cavitand **1.13** which was incorporated during the saponification step. This THF molecule remains in the cavity until it is displaced by a better guest.[36] The tetracarboxylate cavitand **1.13** is water soluble due to its negatively charged rim and short ethyl feet. Using its hydrophobic, aromatic pocket, it can rapidly extract hydrocarbons from water through the hydrophobic effect.[49] N-alkanes coil into a helical conformation within the cavity of **1.13** and rapidly tumble on NMR timescale.[50] Cycloalkanes such as cyclohexane and even adamantane can also bind in the cavitand's pocket[49] as well as alkyl halides.[51]

Deep cavitand **1.13** is able to selectively recognize molecules of the correct shape and size if they also possess a positive charge at their surface. Cavitand **1.13** shows especially good binding affinity for trimethylammonium salts (-R-NMe_3^+).[52] The preferential binding due to cation-π interactions between the guest and the aromatic pocket gives guests like choline binding constants on the order of 10^5 M^{-1}.[36] The cavitand's pocket also discriminates based on size. Although triethylammonium (-R-NEt_3^+) salts possess a cationic charge capable of participating in cation-π interactions with the cavitand's

aromatic pocket, their binding affinities are weaker than those of (-R-NMe_3^+) salts.[53] This is due to the size of the pocket, the (-R-NEt_3^+) salts are bulkier and do not fit as efficiently in the cavity, even larger ammonium moieties will be rejected form the pocket due to size restriction. Although the pocket binds stronger to (-R-NMe_3^+) moieties than hydrocarbons, in the presence long alkyl chains linked to a (-R-NMe_3^+) group, the carbon chain will be found inside the cavity instead of the cationic group. The hydrophobic group is pushed inside the cavity due to the hydrophobic effect while the positively charged $RNMe_3^+$ group interacts positively with the negatively charged rim of cavitand **1.10**.[36]

The cavitand can also recognize longer alkyl chains of surfactants like sodium dodecyl sulfate (SDS). Just like with *n*-alkyl halides, the long hydrocarbon tail of SDS will coil inside the cavity in order to efficiently fill the cavity while maximizing CH-π interactions within the aromatic pocket. When critical micellar concentration is reached, the roles of host and guest are switched between cavitand **1.13** and the surfactant and the cavitand gets incorporated into the SDS micelles. The cavitand's carboxylate rim and aromatic pocket impart it with amphiphilic characteristics, just like SDS. This allows it to incorporate its hydrophobic pocket into the micellar core while it's negatively charged rim is facing out towards the aqueous environment (Figure 1.8).[54] Other studies have shown that cavitand **1.10** can also incorporate itself into micelles composed of other lipids such as dodecylphosphocholine (DPC).[55] In this instance, the cavity was also oriented out into the aqueous environment while the aromatic pocket is oriented into the micellar core. This shows the cavitand's ability to be incorporated into membrane-like environments, but leaves the open question of whether it can retain its recognition abilities.

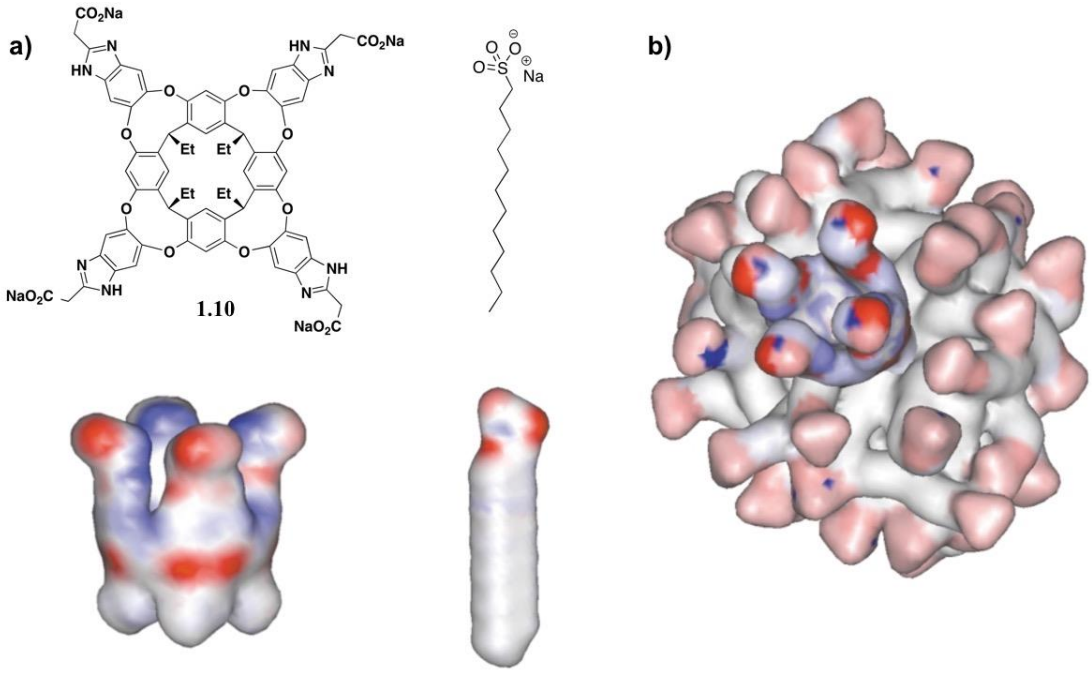

Figure 1.8: a) Structure and electrostatic surface representation of tetracarboxylate **1.13** and SDS; b) Micelle composed of SDS and incorporated cavitand **1.13**.[53]

The conformation of molecules changes depending on their environment. Free molecules in solution are in a dynamic environment, constantly interacting and colliding with other solvent molecules. When placed in confined spaces, these same molecules can experience reduced mobility and resemble substrates inside biological structures such as enzymes.[56] It is of interest to study these interactions not only to get new perspectives on biochemical interactions of more complicated structures such as ligand-enzyme complexes, but to observe and understand phenomena that are barely observed in free solution.

The motion and conformation of molecules confined in small spaces can be studied using proton nuclear magnetic resonance (^{1}H NMR) spectroscopy.[55,57] When small hydrocarbons are surrounded by aromatic π clouds, large changes in proton chemical shifts can be observed. These signals are easily detected at negative ppm and are uninterrupted by ^{1}H signals corresponding to the host or unbound guest. The orientation, motion, conformation and unusual isomerism of small bound guests can be elucidated using ^{1}H NMR as well as the detection of reactive intermediates and unstable species with restricted mobility. Kinetic and thermodynamic quantitation of guest binding is also possible using this powerful analytical tool.[58] To maximize detection, substrate binding interactions are generally measured in controlled environments: in deuterated solvents and in the absence of any NMR-visible impurities or additives.

The guest binding interactions of tetracarboxylate cavitand **1.13** have been extensively studied in D_2O using NMR.[49,59] Cavitand **1.13** is soluble in water up to 20 mM and can bind guests of the proper shape and size ranging from hydrocarbons to trimethylammonium ($RNMe_3^+$) salts. The association constants of guests such as choline (K_a = 2.6 X 10^4 M^{-1}), acetylcholine (K_a = 1.2 X 10^5 M^{-1}), 1-adamantanemethanol (K_a = 2.9 X 10^5 M^{-1}) and cyclohexanone (K_a = 1.6 X 10^5 M^{-1}) are relatively consistent in pure D_2O with an "upper limit" for guest association of 2 X 10^5 M^{-1}.[49,60] Through the application of 2D NMR techniques, the in/out exchange kinetics and motion of bound guests in **1.13** have been demystified.[49,51] The in/out exchange mechanism of **1.10** is independent of guest concentration and was proven to be an "S_N1-like" dissociative process. The rate-determining step of this mechanism is the release of guest from the cavity via flexing of

the cavitand's walls followed by rapid guest exchange. The energy barrier for this process in water is contributed by the rotation of the C-O bonds in the base of the cavitand (~11 kcal mol^{-1}) in addition to the unfavorable interactions of water with the walls of the unfolded cavitand and bound guest. Observed energy barriers for variably sized guests range from 16.0-17.2 kcal $mol^{-1}$and rates of exchange for guests like adamantanol and cyclohexane have been recorded at 1.8 s^{-1} and 14.6 s^{-1} respectively.[49,40,59]

There are extensive NMR studies of biomolecular structure and dynamics in membrane bilayers.[61,62,63] These studies employ the use of isotropically tumbling[64,65] and magnetically-oriented lipid bicelles, as well as unaligned and mechanically oriented phospholipid bilayers; all biomimetic membrane environments.[61,66,67] In order to effectively detect guest signals in these studies, isotopically enriched species such as ^{13}C, ^{15}P and ^{31}P are required. Fast isotropic reorientation restricts the dimensions of isotropic bicelles while magic angle spinning is used for unaligned bilayers. These are not required for aligned systems, which are able to retain high resolution in their absence. Due to the presence of excessive hydrocarbon peaks from the lipids, ^{1}H NMR is not a viable tool for observing individual proton signals for binding studies in these environments. Dynamic NMR experiments aiming to expose the motion and binding kinetics of guests confined in the cavity of synthetic hosts is problematic due to line broadening. The effects on the cavitand's recognition properties while embedded in a lipid bilayer are unknown, as are the effects of the guest's in/out kinetic and conformations in these environments.

1.4 Molecular Recognition in Biomimetic Membrane Environments

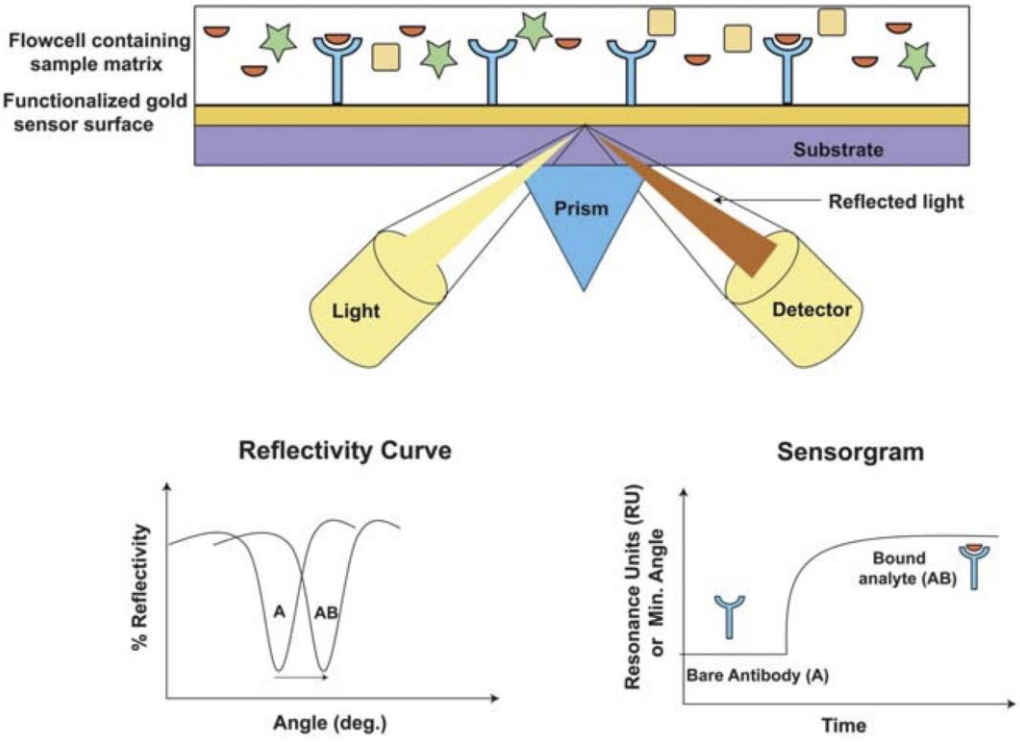

Figure 1.9: SPR sensor setup: light is shined at the gold-glass interface and the change in reflected angle is measured to create corresponding reflectivity curve and sensorgram.[68]

In order to study cavitand recognition in membrane-like environments, an analytical tool is needed that can visualize or measure the discrete binding events in the presence of all the molecules comprising the system (lipids, cavitand, guest, etc.). Although NMR can detect distinct nuclei's environments, the presence of the numerous lipids in the system would make it difficult to properly analyze any interactions between the cavitand and guest, especially if the target guest's signals overlap with the lipid peaks.

Surface Plasmon Resonance (SPR) is an analytical technique that allows the user to measure binding events on a surface in real time. It is a label-free optical assay that utilizes a flow cell, so studies can be made in aqueous environment.[69] The common SPR configuration (Kretschmann configuration) can be observed in Figure 1.9 where a light source is shined at the gold-glass interface. When the light hits the glass-gold interface, it generates an evanescent wave that propagates into the gold surface on the analyte side of the sensor.[68] Any binding events or changes in refractive index of the liquid on the analyte side will cause a change in the angle of the reflected light, which is recorded by a detector on the instrument. These changes in reflected angle are measured to give an SPR sensorgram, an example of which can be seen in Figure 1.9. Cavitand binding events have been successfully monitored using SPR. By immobilizing a cavitand on the gold surface and injecting trimethylammonium-containing guests into the flow cell a signal change was observed on the SPR sensorgram.[32] This study established the use of SPR as an analytical tool for measuring cavitand interactions.

The cavitand's ability to incorporate itself into lipid micelles allowed for the possibility of performing molecular recognition studies in membrane environments and analyzing them using SPR. Because natural membrane environments are so convoluted, supported lipid bilayers (SLB) are a good tool for controlled studies in membrane environments. Supported lipid bilayers are formed by fusing lipid vesicles onto a glass surface.[70] Since SPR employs a gold surface for analysis, a nanolayer of glass needs to be deposited onto the gold through layer-by-layer deposition and calcination.[71] 1-palmitoyl-2-oleoyl-*sn*-glycero-3-phosphocholine (POPC) vesicles were used to form a SLB in the

SPR flow cell before introducing cavitand **1.13** into the system. A change in resonance angle on the SPR sensorgram confirmed the incorporation of the cavitand into the bilayer (with minimal disruption to the bilayer). SPR cavitand binding studies give evidence that cavitand orients itself as seen in Figure 1.11, with the cavity facing out toward the membrane-water interface. The SLB is a fluid membrane and the cavitand within it is also fluid. The cavitand has good selectivity for $RNMe_3^+$ groups and so a variety of compounds were derivatized to contain this binding handle, including proteins. SPR showed the efficient immobilization of these compounds by cavitand **1.13** at the SLB surface with binding constants in the 10^5 M^{-1} range.[32,72] The cavitand is able to effectively display molecules at the membrane's surface and behave as a synthetic receptor by binding specific molecules while incorporated in a membrane.[32,72,73]

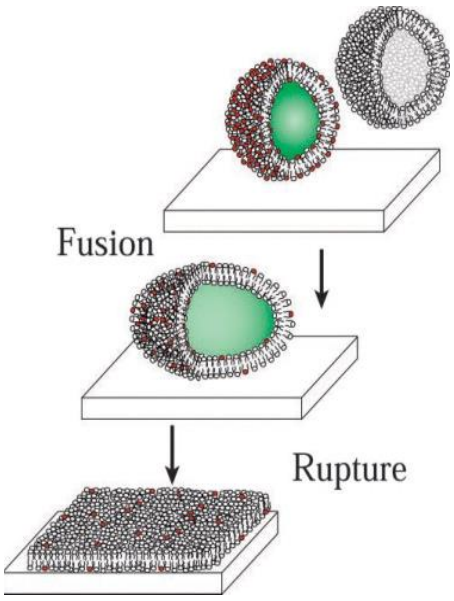

Figure 1.10: Formation of a supported lipid bilayer by a lipid vesicle fusing then rupturing onto a glass surface.[70]

1.5 Binding Capabilities of Water-Soluble Deep Cavitands

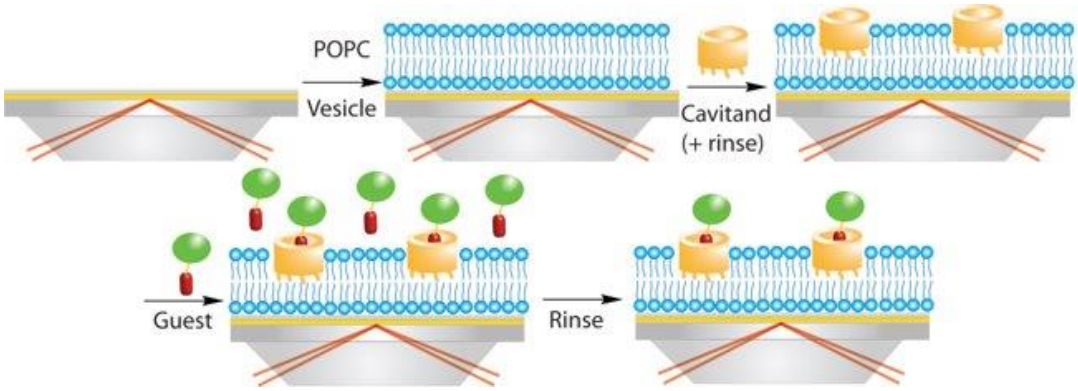

Figure 1.11: The formation of the SLB on a nanoglassified SPR substrate followed by cavitand **1.13** incorporation and guest binding.

In order to test the scope of binding of the cavitand in SLB environments, larger species were introduced into the system. There are many receptors on the cell's surface with the ability to immobilize large structures such as proteins. Because proteins do not naturally contain the cavitand's preferred $RNMe_3^+$ binding moiety, a molecular tag was synthesized in order to modify proteins with the binding handle. Isothiocyanate groups readily react with amines and so **1.14** was synthesized and used to modify amine residues on protein surfaces. Modified protein cytochrome *c* (12.4 kDa) was successfully immobilized on the SLB surface via cavitand **1.13**. When it came to larger modified proteins such as bovine serum albumin (BSA) (66.4 kDa) however, the cavitand was not able to adhere the protein. BSA's large size does not allow the derivatized handle to reach into the cavitand, it is too short. **1.15** was synthesized which contains the cavitand binding

handle and amine-reactive isothiocyanate, but is extended by a oligoethylene glycol spacer. Proteins were derivatized using both handles and were successfully immobilized on the membrane:cavitand surface. (Figure 1.12).[72]

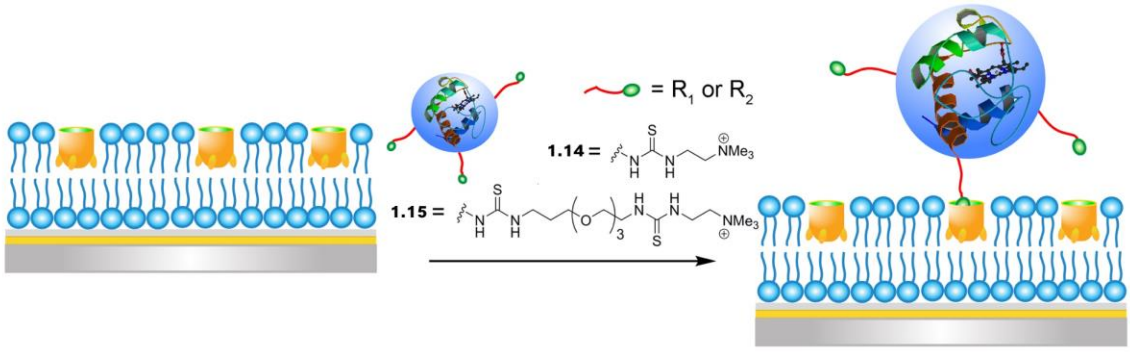

Figure 1.12: Modified protein binding onto SLB:Cavitand surface.[72]

Control experiments were also performed in order to rule out any nonspecific interactions causing the SPR signal change. The labeled proteins did not show any affinity in the absence of cavitand, and so they do not interact with the SLB. Neutral cavitand **1.16**[74] was also utilized as a control in order to rule out any interactions occurring between the positive $RNMe_3^+$ and the negative rim of cavitand **1.13**. Cavitand **1.16** is hydrophobic and has to be incorporated into lipid vesicles before forming the SLB as shown in Figure 1.13.[75] Although the labeled proteins bound to the surface in the presence of **1.16**, some had slightly lower resonance angle changes, indicating some interactions between the proteins and the negatively charged cavitand rim of **1.13**.

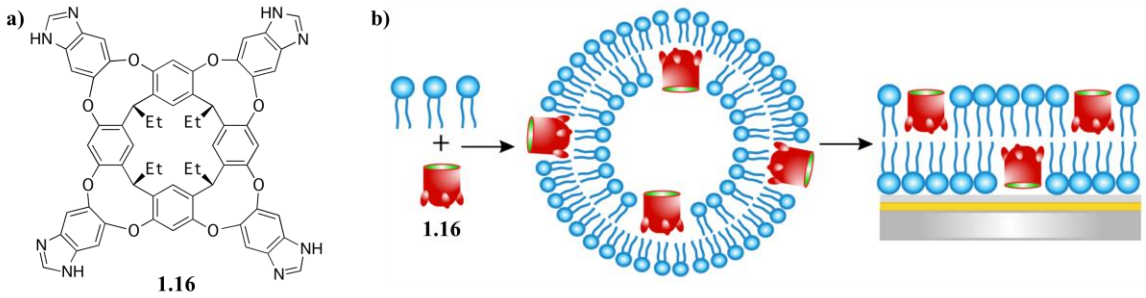

Figure 1.13: a) Hydrophobic deep cavitand **1.16** containing a neutral rim and ethyl feet and b) The neutral cavitand's incorporation into lipid vesicles and formation of a cavitand **1.16**-impregnated supported lipid bilayer.

The recognition properties of the negative rim of **1.13** were further investigated in the presence of native proteins. Various proteins were introduced into the SLB:**1.13** and various interactions were observed. Anionic proteins did not adhere onto the surface while cationic proteins did. The electrostatic interactions between the positive charge on the surface of cationic proteins and the negative charge on the rim of the cavitand exposed at the SLB surface allowed for protein adhesion. Due to charge repulsions, anionic proteins were not adhered onto the membrane surface (Figure 1.13a). In order to discard pocket-based interactions playing a role in the adhesion events, choline was inserted into the pocket of the cavitand before the protein was introduced into the system. The same results were observed as in the open cavity experiments, eliminating any speculation as to whether the cavitand's pocket played any roles in immobilizing native proteins. The active, cationic enzyme trypsin was also immobilized on the SLB surface and was able to function properly by cleaving a peptide.[75]

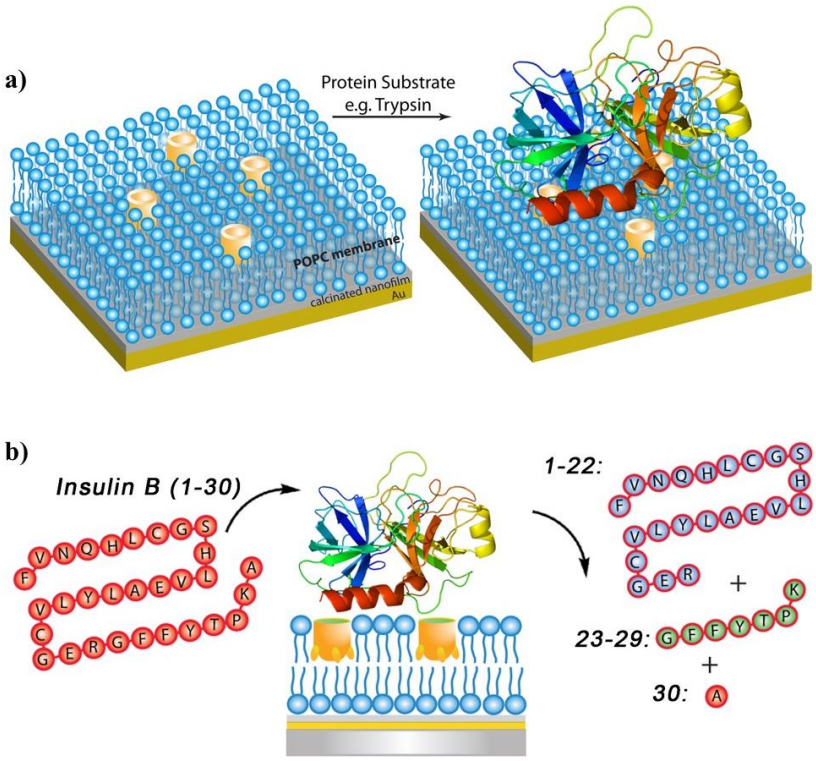

Figure 1.14: a) Immobilization of an unmodified protein by the negatively charged rim of cavitand **1.13**; b) Immobilization of the unmodified protein trypsin and its reactive activity on the SLB surface.[75]

Since cavitand **1.13** can incorporate itself into membranes, its ability and potential to transport its bound cargo into the cell were investigated. In order to probe the location of the cavitand inside the cell, it was incubated with HeLa cells and a fluorescein guest. Through confocal microscopy it is evident that the cavitand gets transported into the cell more efficiently than in the absence of the synthetic receptor.[76] It was not evident, however, where in the cell the cavitand resides, since the guest is visualized in the studies and there is no way of knowing if the guest is still bound in the cavitand. The fluorescein guest was thought to end up in the endosome due to the punctate appearance of fluorescence within

the cells (Figure 1.14b/d). These experiments established the cavitand's prominence as a mimic for membrane receptors.

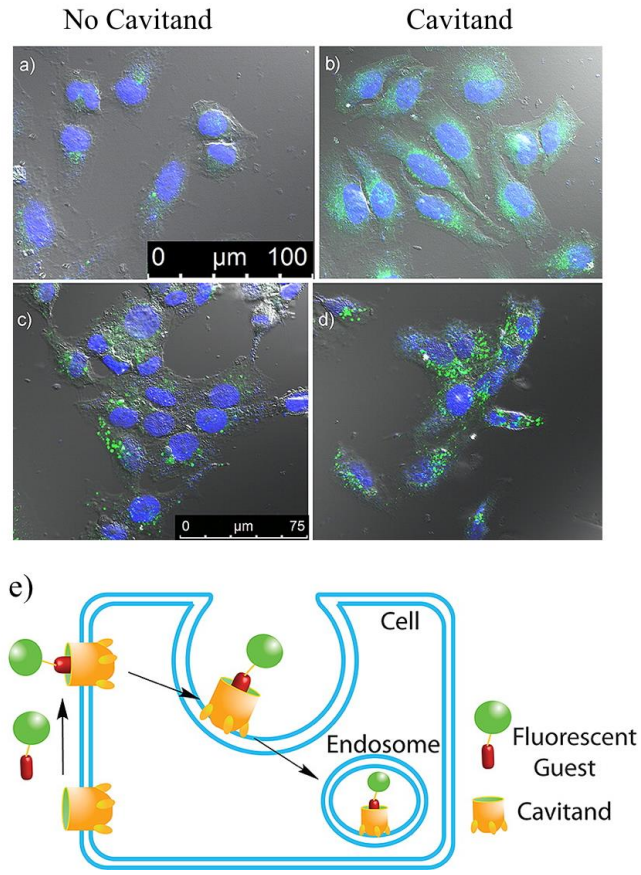

Figure 1.15: Cavitand-mediated endocytosis. DIC/CFM images of the addition of fluorescent guest to live cells (nuclei stained with DAPI): (a) HeLa cells, 50 µM guest only, 1 h incubation; (b) HeLa cells, 50 µM guest, 50 µM cavitand **1.13**, 1 h incubation; (c) GM00637 cells, 50 µM guest only, 1 h incubation; (d) GM00637 cells, 50 µM guest, 50 µM cavitand **1.13**, 1 h incubation; e) Cartoon of the cavitand-mediated endocytosis process.[76]

1.6 Reactions of Cavitand Embedded Guests at the Water-Membrane Interface

Cavitand **1.13** can bind and expose a variety of molecules on the surface of a supported lipid bilayer as long as they possess the $RNMe_3^+$ binding handle. Reactive species such as the atom transfer radical polymerization (ATRP) initiator **1.17** can be exposed at the membrane-water interface and perform a polymerization reaction upon exposure to ATRP catalyst and monomer. The methylmethacrylate (MMA) monomer was used to form hydrophobic poly(MMA) while hydroxyl ethylmethacrylate was used to construct hydrophilic poly(HEMA). The biotinylated monomer, biotin-amino ethylmethacrylate was also synthesized and introduced into the bilayer to form the functional polymer poly(biotin-AEMA). Forming a functional polymer allowed the corresponding polymer to perform further recognition events.[44] Biotin binds strongly to the protein avidin, upon introduction of avidin, the polymer efficiently adheres the protein (Figure 1.13).[73]

Deep, water-soluble cavitand **1.13** is a good mimic for cell surface receptors. The amphiphilic properties of **1.13** allow it to insert itself into both synthetic and actual cell membranes while retaining its selectivity. The pocket of cavitand **1.13** is selective for $RNMe_3^+$ groups and is able to perform recognition of these groups even in membrane environments. This cavitand is capable of performing molecular recognition through electrostatic interactions with its charged rim and bind both derivatized and native proteins. **1.13** can also anchor reactive molecules on a SLB surface and perform reactions at the membrane:water interface. By incorporating itself into HeLa cell membranes, **1.13** can also be transported inside cells and be visualized by binding derivatized fluorescein. This

dissertation will further investigate the abilities of deep cavitands to perform more complex binding and form more complex biomimetic membrane surfaces, as well as their capabilities in biosensing.

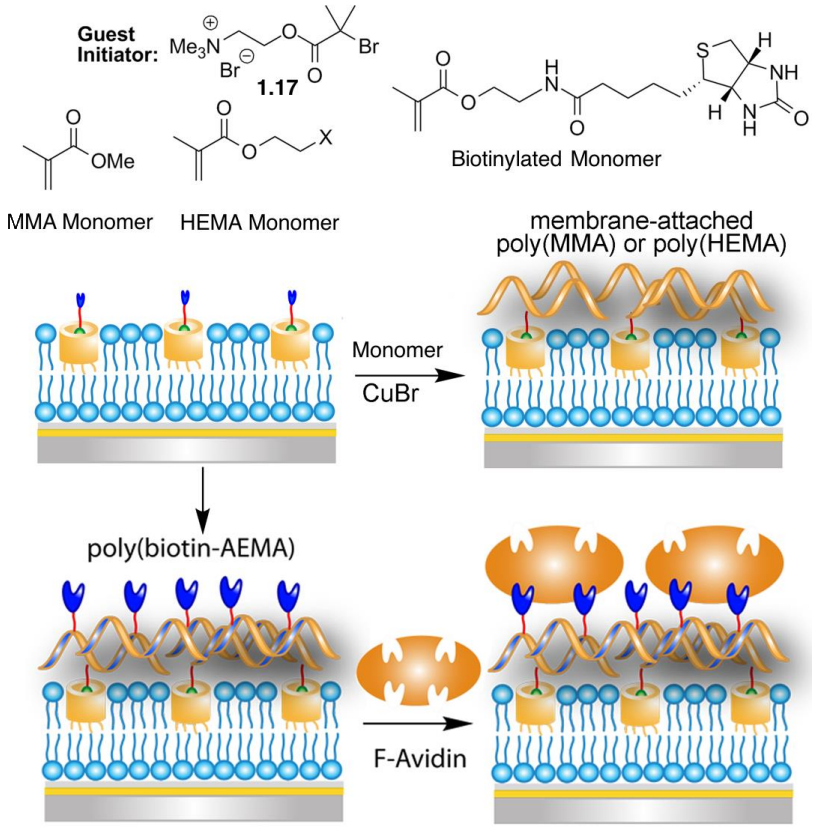

Figure 1.16: The structure of ATRP initiator **1.17** and the methacrylate monomers for polymerization. Also, the exposure of reactive **1.17** and polymerization upon introduction of catalyst and monomer. The binding of avidin by functional polymer.[73]

1.7 References

1. Connor, S. D.; Schmid, S. L. "Regulated Portals of Entry Into The Cell" *Nature* **2003**, *422*, 37-44.

2. Deller, M. C.; Jones, E. Y. "Cell Surface Receptors" *Curr. Opin. Struct. Biol.* **2000**, *10*, 213-219.

3. Jacobson, K.; Derzko, Z.; Wu, E-S.; Hou, Y.; Poste, G. "Measurement of the Lateral Mobility of Cell Surface Components in Single Living Cells by Fluorescence Recovery After Photobleaching" *J. Supramol. Struct.* **1976**, *5*, 565-576.

4. Imoto, K.; Methfessel, C.; Sakmann, B.; Mishina, M.; Mori, Y.; Konno, T.; Fukuda, K.; Kurasaki, M.; Bujo, H.; Fujita, Y.; Numa, S. "Location of a –Subunit Region Determining Ion Transport Through the Acetylcholine Receptor Channel" *Nature* **1986**, *324*, 670-674.

5. Wu, Z-S.; Cheng, H.; Jiang, Y.; Meclcher, K.; Xu, H. E. "Ion Channels Gated by Acetylcholine and Serotonin: Structures, Biology and Drug Discovery" *Acta. Pharmacol. Sin.* **2015**, *36*, 895-907.

6. Imoto, K.; Busch, C.; Sakmann, B.; Mishina, M.; Konno, T.; Nakai, J.; Bujo, H.; Mori, Y.; Fukuda, K.; Numa, S. "Rings of Negatively Charged Amino Acids Determine the Acetylcholine Receptor Channel Conductance" *Nature*, **1988**, 645-648.

7. Möller-Acuña, P.; Contreras-Riquelme, J. S.; Rojas-Fuentes, C.; Nuñez-Vivanco, G.; Alzate-Morales, J.; Iturriaga-Vásquez, P.; Arias, H. R.; Reyes-Parada, M. "Similarities Between the Binding Sites of SB-206553 at Serotonin Type 2 and Alpha 7Acetylcholine Nicotinic Receptors: Rationale for its Polypharmacological Profile" *PloS One*, **2015**, *1*, 1-17.

8. Silverstein, T. P. "The Real Reason Why Oil and Water Don't Mix" *J. Chem. Educ.* **1998**, *75*, 116-118.

9. Pratt, L. R.; Chandler, D. "Theory of the Hydrophobic Effect" *J. Chem. Phys.* **1977**, *67*, 3683-3704.

10. Young, T.; Abel, R.; Kim, B.; Berne, B. J.; Friesner, R. A. "Motifs for Molecular Recognition Exploiting Hydrophobic Enclosure in Protein-Ligand Binding" *Proc. Natl. Acad. Sci.* **2007**, *104*, 808-813.

11. Breslow, R.; Yang, Z.; Ching, R.; Trojandt, G.; Odobel, F., "Sequence selective

binding of peptides by artificial receptors in aqueous solution." *J. Am. Chem. Soc.* **1998,** *120*, 3536-3537.

12. Ingerman, L. A.; Cuellar, M. E.; Waters, M. L., "A small molecule receptor that selectively recognizes trimethyl lysine in a histone peptide with native protein-like affinity." *Chem. Commun.* **2010**, 1839-1841.

13. Pinkin, N. K.; Waters, M. L., "Development and mechanistic studies of an optimized receptor for trimethyllysine using iterative redesign by dynamic combinatorial chemistry." *Org. Biomol. Chem.* **2014,** *12*, 7059-7067.

14. Norouzy, A.; Azizi, Z.; Nau, W.M. "Indicator Displacement Assays Inside Live Cells" *Angew. Chem. Int. Ed.* **2015**, *54*, 792–795.

15. Minaker, S.A.; Daze, K.D.; Ma, M.C.F.; Hof, F. "Antibody-Free Reading of the Histone Code Using a Simple Chemical Sensor Array" *J. Am. Chem. Soc.* **2012**, *134*, 11674−11680.

16. Garnett, G.A.E.; Starke, M.J.; Shaurya, A.; Li, J.; Hof, F. "Supramolecular Affinity Chromatography for Methylation-Targeted Proteomics" *Anal. Chem.* **2016**, *88*, 3697−3703.

17. Gamal-Eldin, M.A.; Macartney, D.H. "Cucurbit[7]uril host–guest complexes and [2]pseudorotaxanes with N-methylpiperidinium, N-methylpyrrolidinium, and N-methylmorpholinium cations in aqueous solution" *Org. Biomol. Chem.* **2013**, *11*, 1234–1241.

18. Daze, K.D.; Hof, F. "The Cation-π Interaction at Protein-Protein Interaction Interfaces: Developing and Learning from Synthetic Mimics of Proteins That Bind Methylated Lysines" *Acc. Chem. Res.* **2013**, *46*, 937–945.

19. Daze, K.D.; Pinter, T.; Beshara, C.S.; Ibraheem, A.; Minaker, S.A.; Ma, M.C.; Courtemanche, R.J.; Campbell, R.E.; Hof, F. "Supramolecular hosts that recognize methyllysines and disrupt the interaction between a modified histone tail and its epigenetic reader protein" *Chem. Sci.* **2012**, *3*, 2695–2699.

20. Daze, K.D.; Ma, M.C.; Pineux, F.; Hof, F. "Synthesis of New Trisulfonated Calix[4]arenes Functionalized at the Upper Rim, and Their Complexation with the Trimethyllysine Epigenetic Mark" *Org. Lett.* **2012**, *14*, 1512–1515.

21. Mahammad, S.; Parmryd, I. "Cholesterol Depletion Using Methyl-ß-Cyclodextrin" *Methods Mol. Biol.* **2015**, *1232*, 91-102.

22. Boonyarattanakalin, S.; Martin, S. E.; Dykstra, S. A.; Peterson, B. R. "Synthetic Mimics of Small Mammalian Cell Surface Receptors" *J. Am. Chem. Soc.* **2004**, *126*, 16379-16386.

23. Boonyarattanakalin, S.; Hu, J.; Dykstra-Rummel, S. A.; August, A.; Peterson, B. R. "Endocytotic Delivery of Vancomycin Mediated by a Synthetic Cell Surface Receptor: Rescue of Bacterially Infected Mammalian Cells and Tissue Targeting *In Vivo*" *J. Am. Chem. Soc.* **2007**, *129*, 268-269.

24. Boonyarattanakalin, S.; Martin, S. E.; Sun, Q.; Peterson, B. R. "A Synthetic Mimic of Human Fc Receptors: Defined Chemical Modification of Cell Surfaces Enables Efficient Endocytotic Uptake of Human Immunoglobulin-G" *J. Am. Chem. Soc.* **2006**, *128*, 11463-11470.

25. Janout, V.; Lanier, M.; Regen, S. L. "Molecular Umbrellas" *J. Am. Chem. Soc.* **1996**, *118*, 1573-1574.

26. Janout, V.; Lanier, M.; Regen, S. L. "Design and Synthesis of Molecular Umbrellas" *J. Am. Chem. Soc.* **1997**, *119*, 640-647.

27. Janout, V.; Di Giorgio, C.; Regen, S. L. "Molecular Umbrella-Assisted Transport of a Hydrophilic Peptice Across a Phospholipid Membrane" *J. Am. Chem. Soc.* **2000**, *122*, 2671-2672.

28. Mackenzie, K. R. "Folding and Stability of α-Helical Integral Membrane Proteins" *Chem. Rev.* **2006**, *106*, 1931-1977.

29. Ghadiri, M. R.; Granja, J. R.; Buehler, L. K. "Artificial Transmembrane Ion Channels from Self-Assembling Peptide Nanotubes" *Nature* **1994**, *369*, 301-304.

30. Cho, W.; Stahelin, R. V. "Membrane-Protein Interactions in Cell Signaling and Membrane Trafficking" *Annu. Rev. Biophys. Biomol. Struct.* **2005**, *34*, 119-151.

31. Hooley, R. J.; Rebek J., Jr. "Chemistry and Catalysis in Functional Cavitands" *Chem. Biol.* **2009**, *16*, 255-264.

32. Liu, Y.; Liao P.; Cheng, Q.; Hooley, R. J. "Protein and Small Molecule Recognition Properties of Deep Cavitands in a Supported Lipid Membrane Determined by Calcination-Enhanced SPR Spectroscopy" *J. Am. Chem. Soc.* **2010**, *132*, 10383.

33. Hardouin-Lerouge, M.; Hudhomme, P.; Salle, M. "Molecular Clips and Tweezers Hosting Neutral Guests" *Chem. Soc. Rev.* **2011**, *40*, 30-43.

34. Klarner, F. G.; Kahlert, B.; Nellesen, A.; Zienau, J.; Ochsenfeld, C.; Schrader, T.

"Molecular Tweezer and Clips in Aqueous Solution: Unexpected Self-Assembly, Powerful Host-Guest Complex Formation, Quantum Chemical 1H NMR Shift Calculation" *J. Am. Chem. Soc.* **2006**, *128*, 4831-4841.

35. Hoegberg, A. G. S. "Two Stereoisomeric Macrocyclic Resorcinol-Acetaldehyde Condensation Products" *J. Org. Chem.* **1980**, *45*, 4498- 4500.

36. Biros, S. M.; Rebek, J., Jr. "Structure and Binding Properties of Water-Soluble Cavitands and Capsules" *Chem. Soc. Rev.* **2007**, *36*, 93-104.

37. Cram, D. J.; Cram, J. M. "Container Molecules and their Guests" *R. Soc. Chem.*, Cambridge, **1994**.

38. Moran, J. R.; Karbach, S.; Cram, D. J. "Cavitands - Synthetic Molecular Vessels" *J. Am. Chem. Soc.* **1982**, *104*, 5826-5828.

39. Moran, J. R.; Ericson, J. L.; Dalcanale, E.; Bryant, J. A.; Knobler, C. B.; Cram, D. J. "Vases and Kites as Cavitands" *J. Am. Chem. Soc.* **1991**, *113*, 5707-5714.

40. Cram, D. J.; Choi, H. J.; Bryant, J. A.; Knobler, C. B. "Host-Guest Complexation. 62. Solvophobic and Entropic Driving Forces for Forming Velcraplexes, Which Are 4-Fold, Lock-Key Dimers in Organic Media" *J. Am. Chem. Soc.* **1992**, *114*, 7748-7765.

41. Gibb, C. L.; Gibb, B. C. "Well-defined, Organic Nanoenvironments in Water: The Hydrophobic Effect Drives a Capsular Assembly" *J. Am. Chem. Soc.* **2004**, *126*, 11408-11409.

42. Jordan, J. H.; Gibb, B. C. "Molecular Containers Assembled Through the Hydrophobic Effect" *Chem. Soc. Rev.* **2015**, *44*, 547-585.

43. Laughrey, Z. R.; Gibb, B. C. "Macrocycle Synthesis Through Templation" *Templates in Chemistry* **2005**, *249*, 67-125.

44. Laughrey, Z.; Gibb, B. C. "Water-Soluble, Self-Assembling Container Molecules: An Update" *Chem. Soc. Rev.* **2011**, *40*, 363-386.

45. Gibb, D. L.; Gibb, B. C. "Binding of Cyclic Carboxylates to Octa-Acid Deep-Cavity Cavitand" *J. Comput. Aided. Mol. Des.* **2014**, *28*, 319-325.

46. Ampurdanes, J.; Crespo, G. A.; Maroto, A.; Sarmentero, M. A.; Ballester, P.; Rius, F. X. "Determination of Choline and Derivatives with a Solid-Contact Ion-Selective Electrode Based on Octaamide Cavitand and Carbon Nanotubes" *Biosens. Bioelectron.* **2009**, *25*, 344-349.

47. Korom, S.; Martin, E.; Serapian, S. A.; Bo, C.; Ballester, P. "Molecular Motion and Conformational Interconversion of Ir(I).COD Included in Rebek's Self- Folding Octaamide Cavitand" *J. Am. Chem. Soc.* **2016**, *138*, 2273-2279.

48. Menozzi, E.; Onagi, H.; Rheingold, A. L.; Rebek, J. "Extended Cavitands of Nanoscale Dimensions" *Eur. J. Org. Chem.* **2005**, 3633-3636.

49. Hooley, R. J.; Van Anda, H. J.; Rebek, J., Jr. "Extraction of Hydrophobic Species into a Water-Soluble Synthetic Receptor" *J. Am. Chem. Soc.* **2007**, *129*, 13464-13473.

50. Trembleau, L.; Rebek, J., Jr. "Helical Conformation of Alkanes in a Hydrophobic Cavitand" *Science* **2003**, *301*, 1219-1220.

51. Hooley, R. J.; Gavette, J.; Mettry, M.; Ajami, D.; Rebek, J., Jr. "Unusual Orientation and Reactivity of Alkyl Halides in Water-Soluble Cavitands" *Chem. Sci.* **2014**, *5*, 4382-4387.

52. Hof, F.; Trembleau, L.; Ullrich, E. C.; Rebek, J., Jr. "Acetylcholine Recognition by a Deep, Biomimetic Pocket." *Angew. Chem. In. Ed.*, **2003**, *42*, 3150-3153.

53. Purse, B. W.; Rebek, J., Jr. "Functional Cavitands: Chemical Reactivity in Structured Environments" *Proc. Natl. Acad. Sci.* **2005**, *102*, 10777-10782.

54. Trembleau, L.; Rebek, J., Jr. "Interactions Between a Surfactant and Cavitand in Water Blur Distinctions Between Host and Guest" *Chem. Commun.* **2004**, 58-59.

55. Schramm, M. P.; Hooley, R. J.; Rebek, J., Jr. "Guest Recognition with Micelle-Bound Cavitands" *J. Am. Chem. Soc.* **2007**, *129*, 9773-9779.

56. Rebek, J. R. "Molecular Behavior in Small Spaces." *Acc. Chem. Res.*, **2009**, *42*, 1660-1668.

57. Scarso, A.; Trembleau, L.; Rebek, J., Jr. "Helical Folding of Alkanes in a Self-Assembled, Cylindrical Capsule" *J. Am. Chem. Soc.* **2004**, *126*, 13512-13518.

58. Perez, L.; Caulkins, B. G.; Mettry, M.; Mueller, L. J.; Hooley, R. J. "Lipid Bilayer Environments Control Exchange Kinetics of Deep Cavitand Hosts and Enhance Disfavored Guest Conformations" *Chem. Sci.* **2018**, *9*, 1836-1845.

59. Craig, S. L.; Lin, S.; Chen, J.; Rebek, J., Jr. "An NMR Study of the Rates of Single-Molecule Exchange in a Cylindrical Host Capsule" *J. Am. Chem. Soc.* **2002**, *124*,

8780-8781.

60. Biros, S. M.; Ullrich E. C.; Hof, F.; Trembleau, L.; Rebek, J. Jr. "Kinetically Stable Complexes in Water: The Role of Hydration and Hydrophobicity" *J. Am. Chem. Soc.* **2004**, *126*, 2870–2876.

61. Park, S. H.; Das, B. B.; Casagrande, F.; Tian, Y.; Nothnagel, H. J.; Chu, M.; Kiefer, H.; Maier, K.; De Angelis, A. A.; Marassi, F. M.; Opella, S. J. "Structure of the Kemokine Receptor CXCR1 in Phospholipid Bilayers" *Nature*, **2012**, *491*, 779-783.

62. Gustavsson, M.; Verardi, R.; Mullen, D. G.; Mote, K. R.; Traaseth, N. J.; Gopinath, T.; Veglia, G. "Allosteric Regulation of SERCA by Phosphorylation-Mediated Conformational Shift of Phospholamban" *Proc. Natl. Acad. Sci. U. S. A.* **2013**, *110*, 17338–17343

63. Wright, A. K.; Batsomboon, P.; Dai, J.; Hung, I.; Zhou, H.-X.; Dudley, G. B.; Cross, T. A. "Differential Binding of Rimantadine Enantiomers to Influenza A M2 Proton Channel" *J. Am. Chem. Soc.* **2016**, *138*, 1506-1509.

64. Dürr, U. H. N.; Gildenberg, M.; Ramamoorthy, A. "The Magic of Bicelles Lights Up Membrane Protein Structure" *Chem. Rev.* **2012**, *112*, 6054–6074.

65. Dürr, U. H. N.; Soong, R.; Ramamoorthy, A. "When Detergent Meets Bilayer: Birth and Coming of Age of Lipid Bicelles" *Prog. Nucl. Magn. Reson. Spectrosc.* **2013**, *69*, 1-22.

66. Opella, S. J. "Structure Determination of Membrane Proteins in their Native Phospholipid Bilayer Environment by Rotationally Aligned Solid-State NMR Spectroscopy" *Acc. Chem. Res.* **2013**, *46*, 2145–2153.

67. Murray, D. T.; Das, N.; Cross, T. A. "Solid State NMR Strategy for Characterizing Native Membrane Protein Structures" *Acc. Chem. Res.* **2013**, *46*, 2172–2181.

68. Linman, M. J.; Abbas, A.; Cheng, Q. "Interface Design and Multiplexed Analysis with Surface Plasmon Resonance (SPR) Spectroscopy and SPR Imaging" *Analyst* **2010**, *135*, 2759-2767.

69. Bakhtiar, R. "Surface Plasmon Resonance Spectroscopy: A Versatile Technique in a Biochemist's Toolbox" *J. Chem. Educ.* **2013**, *90*, 203-209.

70. Schönherr, H.; Johnson, J. J.; Lenz, P.; Frank, C. W.; Boxer, S. G. "Vesicle Adsorption and Lipid Bilayer Formation on Glass Studied by Atomic Force Microscopy" *Langmuir*, **2004**, *20*, 11600-11606.

71. Linman, M. J.; Culver, S. P.; Cheng, Q. "Fabrication of Fracture-Free Nanoglassified Substrates by Layer-By-Layer Deposition with a Paint Gun Technique for Real-Time Monitoring of Protein-Lipid Interactions" *Langmuir* **2009**, *25*, 3075-3082.

72. Ghang, Y-J.; Lloyd, J.; Moehlig, M.; Arguelles, J.; Mettry, M.; Zhang, X.; Julian, R.; Cheng, Q.; Hooley, R. J. "Labeled Protein Recognition at a Membrane Bilayer Interface by Embedded Synthetic Receptors" *Langmuir*, **2014**, *30*, 10161-10166.

73. Liu, Y.; Young, M. C.; Moshe, O.; Cheng, Q.; Hooley, R. J. "A Membrane-Bound Synthetic Receptor Promotes Growth of a Polymeric Coating at the Bilayer-Water Interface" *Angew. Chem. Int. Ed.* **2012**, *30*, 7748-7751.

74. Choi, H-J.; Park, Y. S.; Song, J.; Youn, S. J.; Kim, H-S.; Kim, S-H.; Koh, K.; Paek, K. "Structural Properties of the Benzimidazole Cavitand and its Selective Recognition Toward 4-Methylbenzamide Over 4-Methylanilide" *J. Org. Chem.* **2005**, *70*, 5974-5981.

75. Ghang, Y-J.; Perez, L.; Morgan, M.; Si, F.; Hamdy, O.; Beecher, C.; Larive, C.; Julian, R.; Zhong, W.; Cheng, Q.; Hooley, R. J. "Anionic Deep Cavitands Enable the Adhesion of Unmodified Proteins at a Membrane Bilayer" *Soft Matter* **2014**, *10*, 9651-9656.

76. Ghang, Y-J.; Schramm, M. P.; Zhang, F.; Acey, R. A.; David, C. N.; Wilson, E. H.; Wang, Y.; Cheng, Q.; Hooley, R. J. "Selective Cavitand-Mediated Endocytosis of Targeted Imaging Agents into Live Cells" *J. Am. Chem. Soc.* **2013**, *135*, 7090-7093.

Chapter 2: Lipid Bilayer Environments Control Exchange Kinetics of Deep Cavitand Hosts and Enhance Disfavored Guest Conformations

2.1 Introduction

Synthetic receptors can perform selective molecular recognition in complex environments. Deep cavitand **1.13** has been shown to bind guests in supported lipid bilayers (SLB)[1] and the membranes of living cells,[2] though NMR analyses of detailed guest recognition interactions in these environments have been limited. Indirect analyses have shown the recognition capabilities of **1.13** in membrane environments through the use of surface plasmon resonance (SPR) spectroscopy of cavitand:SLB surfaces[3] and capillary electrophoresis (CE) of cavitand:liposome systems.[4] While fluorescence spectroscopy[5] and isothermal calorimetry[6] can also be applied for such studies, NMR spectroscopy would allow more comprehensive studies of the detailed interactions, conformations and exchange rate of guests in the cavity of **1.13**. Guest binding interactions in cavitands have been analyzed using ^{1}H NMR spectroscopy in fast tumbling micelles[7,8,9] as well as urine and blood serum,[10,11] though these simple 1D experiments were limited in the information they divulged. More complex experiments would be needed in order to determine the guest's motion, conformation and exchange rate in these systems.

2.2 Binding Unfavorable Conformations in Lipid Environments

Analyzing host-guest binding interactions via NMR in lipid environments can be complicated if the guest peaks are not shifted enough when bound to avoid being

overlapped by the lipid signals. The appropriate guest must be used for such studies. Guest motion and conformation inside the synthetic host can be studied if the guest displays multiple orientations or conformations while inside the cavity; ^{1}H NMR is preferred for these studies. In order to study in/out kinetics, the guest must be soluble enough in aqueous environment to display peaks for both free and bound guest. A variety of guests were studied for their suitability (Figure 2.1). These guests were obtained from commercial sources or derivatized in one or two steps from commercially available compounds. The simple hydrocarbon cyclooctane **2.1** was selected as well as ^{19}F-containing hydrophobic guests **2.2** and **2.3**. A variety of ^{13}C-enriched guests containing cavitand **1.13**'s preferred binding handle, $RNMe_3^+$ (**2.4**-**2.7**) were also selected for study.

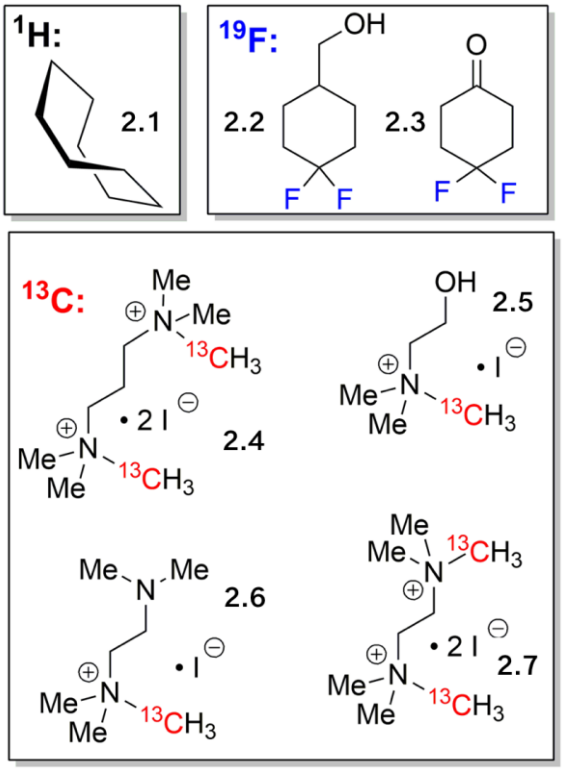

Figure 2.1: Structure of guests containing different labeled nuclei that were used in this study.

Since we were interested in studying guest binding in membrane environments, and natural cell membranes would be challenging to use, we settled on surrogates that are known and used for the NMR studies of membrane-bound biomolecules. The NMR analysis of biomolecular dynamics and structure in membrane bilayers has been studied.[12,13,14,15,16] Magnetically ordered bicelles are good mimics for natural cell membranes as they are very effective at maintaining the bilayer sheet form found in nature.[17,18] Magnetically oriented bicelles allow for solid state NMR (ssNMR) studies due to their ability to align in the magnetic field, but this technique suffers from line broadening effects that can impede accurate analysis. For solution-phase NMR techniques, isotropically tumbling micelles are commonly employed. These micelles are less accurate mimics of the natural environment of the cell membrane, but they are simpler to analyze. Both lipid environments were applied in our host:guest binding analysis due to the ease of accessing both from the same lipid system.

To form the lipid aggregates, a 3.2:1 mix of dimyristoylphosphocholine (DMPC) and diheptylphosphocholine (DHPC) lipids were combined. These lipids are known to form either magnetically oriented bicelles or isotropically disordered micelles depending on temperature.[19,20] As can be seen in Figure 2.2, magnetically ordered bicelles (PC_b) are predominantly formed at 308 K, while decreasing the temperature to 298 K will form disordered isotropic micelles (PC_m). ^{31}P NMR analysis of the system shows a single averaged signal for PC_m while PC_b displays two peaks due to the two orientations of the lipid phosphate groups in the bicelles. The addition of cavitand and guest does not disrupt the structure of the lipid aggregates (Figure 2.2d), so these systems were utilized.

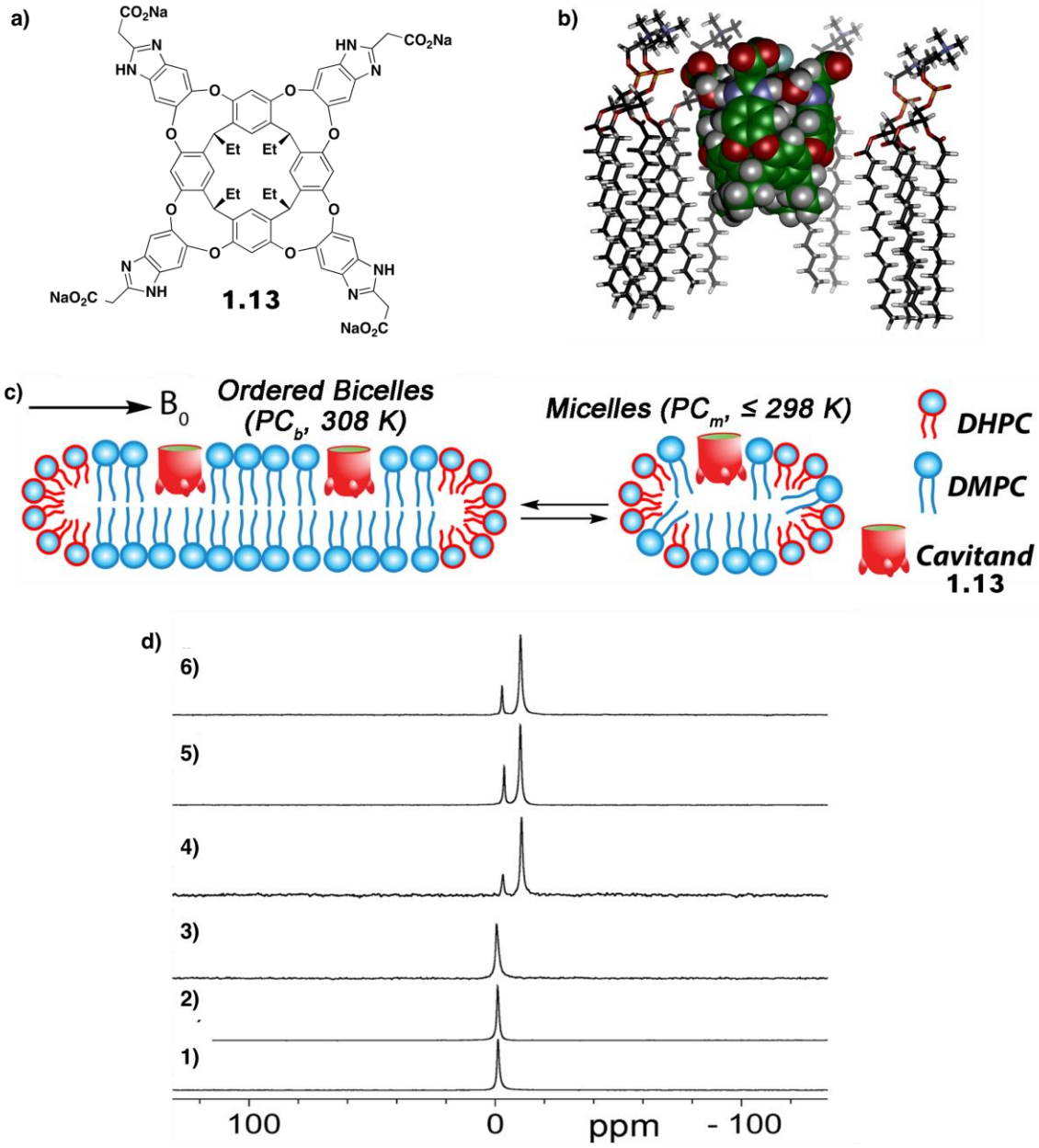

Figure 2.2: a) Structure of tetracarboxylate cavitand **1.13** and b) a representation of **1.13** incorporation into a DMPC lipid monolayer (SPARTAN, AMBER Forcefield); c) Representation of the possible DMPC/DHPC lipid structures of magnetically ordered bicelles and isotropically disordered micelles; d) Temperature dependence of the lipid aggregate. ^{31}P NMR spectra of the DMPC/DHPC aggregates: 1) alone, 283 K; 2) + 5 mM **1.13**, 283 K; 3) + 5 mM **1.13** + 7 mM guest **2.4**, 283 K; 4) alone, 303 K; 5) + 5 mM **1.13**, 303 K; 6) + 5 mM **1.13** + 7 mM guest **2.4**, 303 K. Ratio DMPC/DHPC = 3.2:1, 150 mg mL^{-1} total lipid concentration, 162.07 MHz, 2.5 mM HEPES/D_2O.

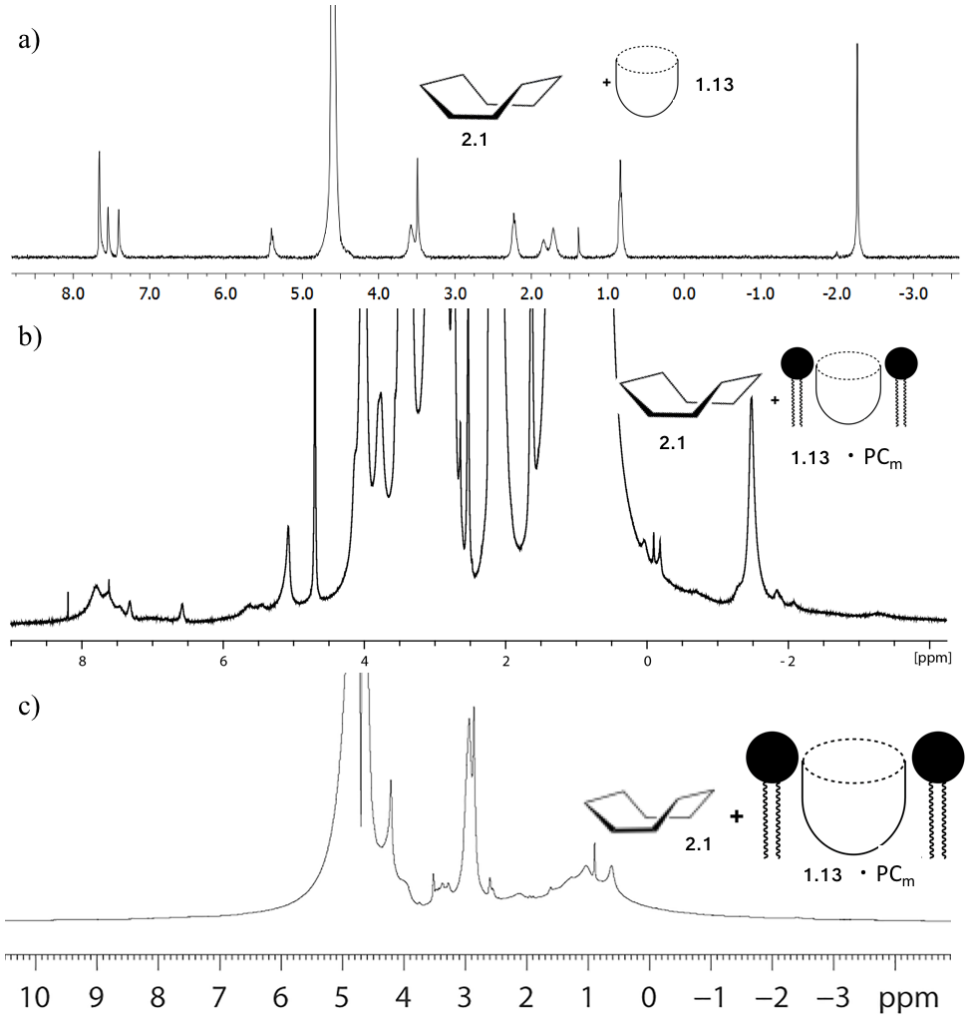

Figure 2.3: ^{1}H NMR spectra of **2.1•1.13** complex: a) in D_2O (400.13 MHz, D_2O, 298 K, [**1.13**] = [**2.1**] = 1.8 mM); b) in PC_m; and c) T_2-filtered ^{1}H NMR spectrum in PC_m (599.88 MHz, 1 mM HEPES/D_2O, 298 K, [**1.13**] = [**2.1**] = 1.8 mM, ratio DMPC/DHPC = 3.2:1, 60 mg/mL total lipid concentration).

Guest binding studies of cyclooctane **2.1** in cavitand **1.13** have been performed in solution. Cyclooctane binds in the cavity of **1.13** with an affinity on the order to 10^4 M^{-1} while displaying a single ^{1}H NMR signal at -1.50 ppm.[21] Due to the guest's rapid tumbling inside the cavity, all 16 of the guest's proton signals average out. NMR spectra of the **2.1•1.13** complex ([**2.1**] = [**1.13**] = 1.8 mM) in D_2O as well as in DMPC:DHPC micelles

were obtained and analyzed. In the micellar environment, cavitand **1.13** binds strongly to **2.1** and is completely incorporated into the aggregates, illustrated by the retained singlet peak of the complex at -1.50 ppm (Figure 2.3a). In order to detect a change in the conformational properties of **2.1**, T2-filtered NMR studies were performed where the temperature of the system was varied, lowering to 283 K. No peaks for unincorporated cavitand or bound guest were seen in the spectra, indicating complete incorporation into the aggregates. Rapid tumbling of the guest in the cavity prevented the analysis of the rate of up/down motion of **2.1** in **1.13**. Studies in bicelles at 308 K gave only broad and undefined peaks with no discrete peaks for either guest or host, even with the application of magic angle spinning (MAS).

Cyclooctane (**2.1**) was not useful for elucidating detailed guest interactions with our host **1.13**, so ^{19}F-containing guests **2.2** and **2.3** were studied. 4,4-difluorocyclohexanemethanol **2.2** and difluorocyclohexanone **2.3** are suitable guests for cavitand **1.13** in aqueous solutions, although they display weaker binding in comparison to equivalent hydrocarbons.[21] To analyze the conformation and in/out guest exchange of these guests in **1.13**, the ^{19}F nuclei must be oriented inside the cavity and display chemical shift changes caused by magnetic anisotropy. Fortunately, this was the case for both fluorinated guests, as can be seen in the ^{19}F NMR spectra of Figure 2.4**,** where the ^{19}F nuclei are shifted upfield by about 2 ppm. These findings also confirmed the orientation of the OH and C=O groups towards the aqueous environment, promoted by favorable H-bonding interactions. The host-guest studies were performed in fast-tumbling micelles at a lipid concentration of

60 mg mL^{-1}. Bicelle studies were not utilized using these guests due to the peak broadening of ^{19}F signals.

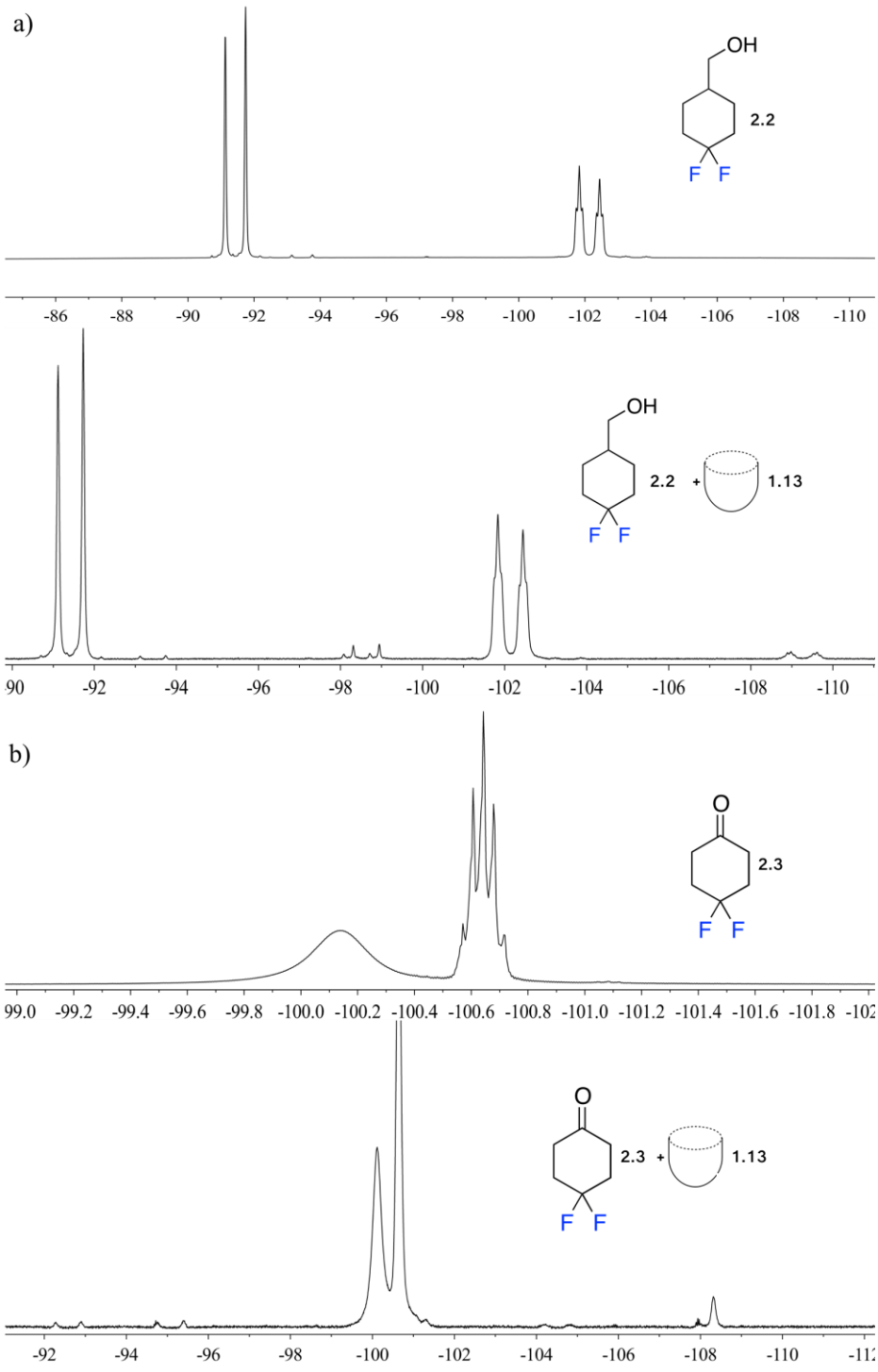

Figure 2.4: a) ^{19}F NMR spectra of guest **2.2** in D_2O and bound in **1.13** (376.50 MHz, D_2O, 298 K, [**1.13**] = 5.8 mM, [**2.2**] = 39.5 mM); b) ^{19}F NMR spectra of guest **2.3** in D_2O and bound in **1.13** (400.13 MHz, D_2O, 298 K, [**1.13**] = 5.8 mM, [**2.3**] = 39.5 mM).

Both fluorinated guests provide useful information on the effects of embedding the host **1.13** in a lipid environment. The ^{1}H NMR spectrum of the **1.13 • 2.2** complex in D_2O revealed two sets of peaks for the bound guest. The chemical shifts of both sets of peaks were close enough to eliminate the possibility of up/down carceroisomers (molecules with hindered rotation within the cavity)[22] as the two guest conformations found in the host:guest complex, and instead confirmed the presence of axial/equatorial ring flip conformers (Figure 2.6d). This unexpected observation provided the opportunity to investigate the effects of lipid environments on the conformations of bound guest.

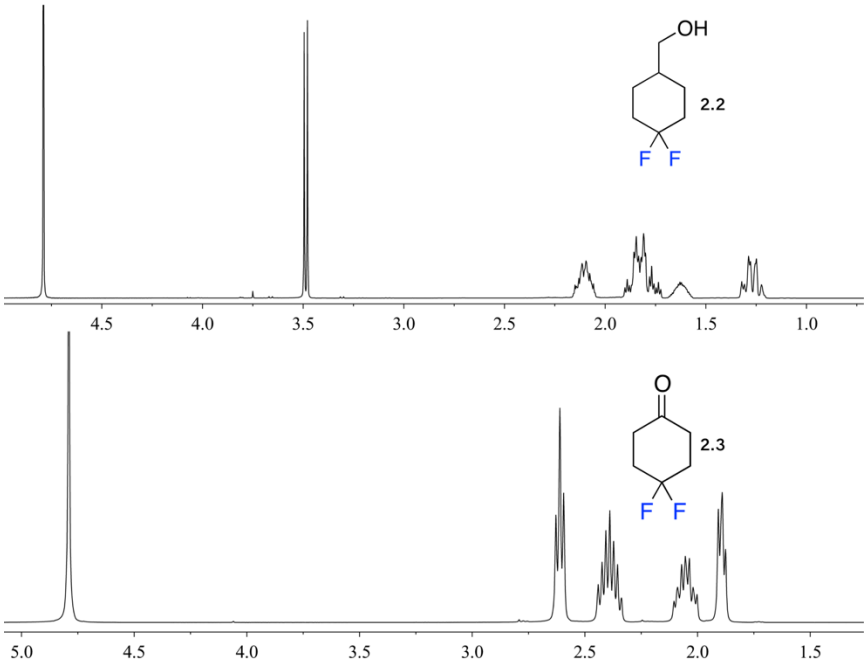

Figure 2.5: ^{1}H NMR spectra of guests **2.2** and **2.3** (400.13 MHz, D_2O, 298 K).

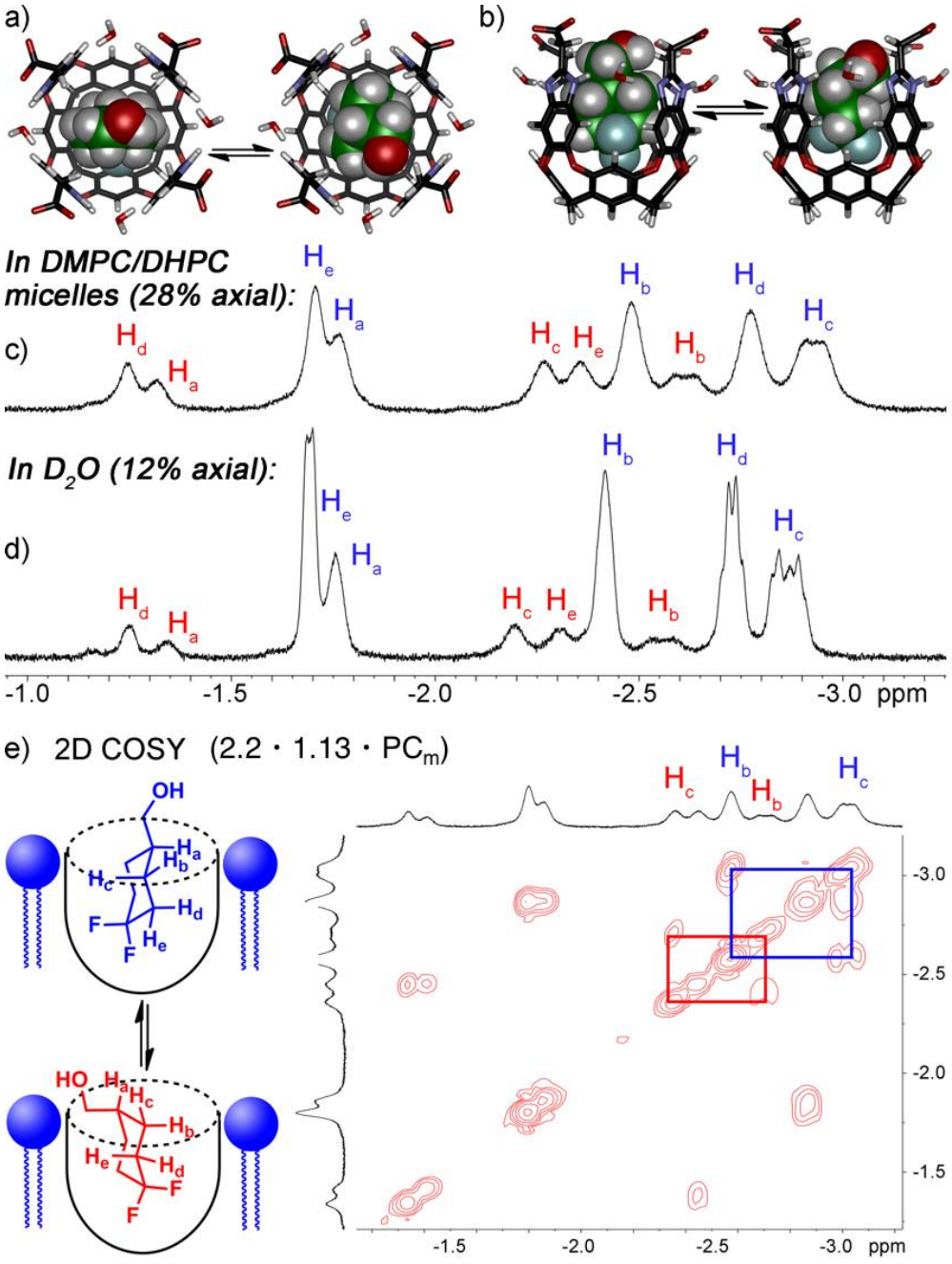

Figure 2.6: The enhanced axial conformation of guest **2.2**. a) and b) The minimized structures of the axial and equatorial host-guest complex (SPARTAN, AMBER forcefield); The upfield region of the ^{1}H NMR spectra of the host-guest complex of **2.2** c) in DMPC/DHPC micelles and d) in D_2O; e) 2D COSY spectrum of the host-guest complex in lipid micelles (700 MHz, 298 K, [1.13] = 5.8 mM, [2.2] = 39.5 mM, ratio DMPC/DHPC = 3.2 : 1, 60 mg mL^{-1} total lipid concentration).

In the absence of cavitand, only one conformation of **2.2** is observed in the ^{1}H or ^{19}F NMR spectra in D_2O. The expected conformation is thought to be that of the lower energy equatorial conformer (Figures 2.4 and 2.5). The ^{19}F NMR spectrum is useful to indicate the presence of <0.5% axial conformer in solution as well as to assign this conformation at the concentrations used. The doublet observed in the ^{19}F NMR of **2.2** corresponds to the equatorial F and shows no visible peak splitting. Due to *trans*-diaxial coupling with the vicinal protons, the axial F shows up as a doublet of triplets, as can be observed in Figure 2.6a. The distinct coupling patterns exhibited by the two fluorines is indicative of slow interconversion between the two conformers. When bound inside the cavity of **1.13**, however, 12% of the present molecules of **2.2** are found in the axial conformation. Molecular modeling of guest **2.2** in the host illustrates that the axial conformer can easily fit in the cavity of host **1.13** and the two separate conformers are clearly visible by utilizing 2D COSY analysis (Figure 2.6e). When the host:guest system of **2.2** is placed in PC_m, a clear indication of the effect of placing the host in lipid environments can be observed. As can be seen in Figure 2.6c, the proportion of axial conformer is increased to 28% when compared to the host:guest complex in solution (12%) and uncomplexed **2.2** (<0.5%).

As with complex **1.13 • 2.2**, studies on the **1.13 • 2.3** system showed the presence of two conformations while only one was observed in free solution (Figures 2.4 and 2.5). The chemical shifts of the protons in bound guest **2.3** do not match the expected signals for up/down carceroisomers and confirm the presence of complexed ketone, **1.13 • 2.3** and the gem-diol product of its hydration, **1.13 • 2.3$_{hyd}$** (Figure 2.7). While the peaks in the ^{19}F

spectrum of the ketone guest **2.3** are close in shift, separation of the two fluorine peaks can be observed due to the distinct axial and equatorial conformations of the all-sp^3 structure of $\mathbf{2.3_{hyd}}$ (Figure 2.4b). The ketone structure is favored over the hydrate in unactivated ketones such as acetone. This is evident as the equilibrium between these two states strongly favors the ketone, however, the presence of electron-withdrawing groups such as halogens shifts the equilibrium towards the hydrate (K_{hyd}(acetone) = 1.4 X 10^{-3}, K_{hyd}(fluoroacetone) = 0.11).[23] In the absence of cavitand, no obvious hydrate is present by NMR analysis of guest **2.3**, indicating that <0.5% hydrate is present in solution at the concentrations used (Figures 2.4 and 2.5). When bound inside the cavity of **1.13**, however, 13% of bound **2.3** can be found in the hydrated form at 298K. Placing the host-guest complex of **2.3** in HMPC/DMPC micelles also shows a preference for the formation of hydrate, similar to the conformational bias seen in the binding of **2.2**. In lipid environment, 23% of bound **2.3** is present in the hydrated state while only 13% is observed for the host-guest complex in D_2O and <0.5% is seen for free guest.

These observations brought up the question of why binding in **1.13** stabilizes guest structures that are normally unfavorable and why this effect is enhanced when the host-guest complex is embedded in lipid aggregates. Cavitand **1.13** can utilize both its cavity and charged upper rim to affect guest binding.[5] The tetracarboxylate rim has been shown to control binding selectivity for functionalized guests in varying pHs[5] and accelerate solvolysis reactions of bound guests.[24] Acidic groups in guests positioned close to the anionic rim of the cavitand exhibit favorable H-bonding interactions, more so than with external bulk water. Guests with properly positioned H-bonding donors such as ammonium

ions,[5,25] thioureas,[5] and even hydroxyl groups[21,5,24,25] have shown stronger affinity for cavitand **1.13** than those with esters, ketones or ethers.[5,24,25] The axial conformer of **2.2** positions its OH group near the anionic rim of **1.13**, increasing the favorability of this conformer when bound in the cavity. The hydrated gem-diol of **2.3** is also able to H-bond with the carboxylates while the ketone is not, explaining the increased favorability of the bound hydrate (Figure 2.7e).

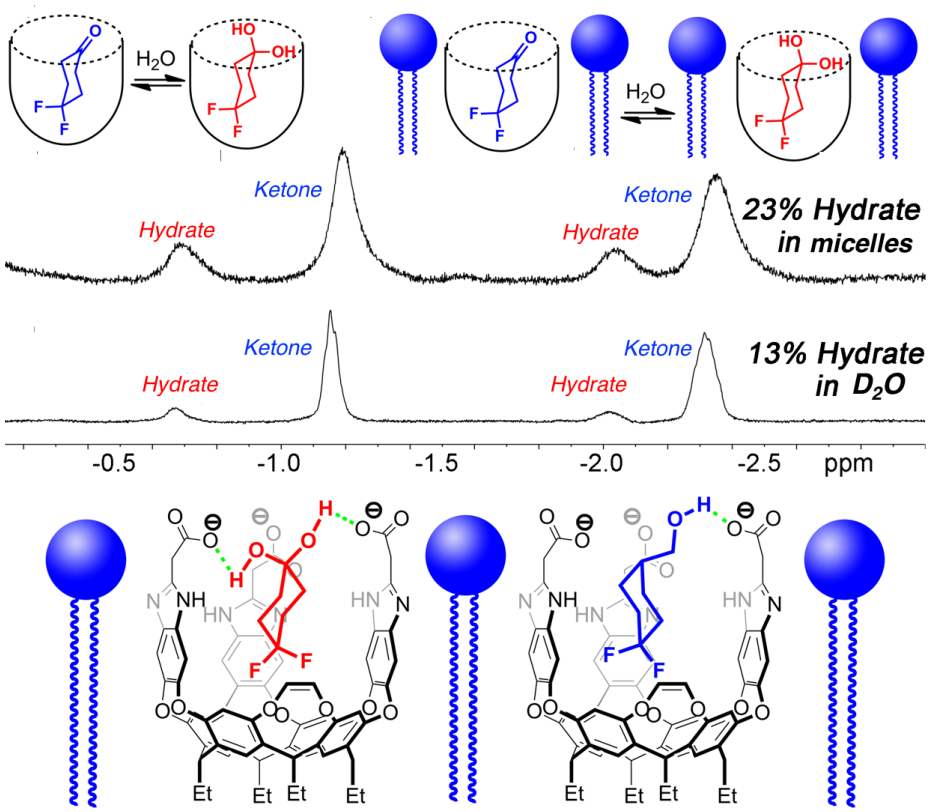

Figure 2.7: The enhanced hydration of guest **2.3**. a and b) Illustration of the equilibrium process. Upfield regions of the ^{1}H NMR spectra of c) **1.13 • 2.3** in DMPC/DHPC micelles and d) **1.30 • 2.3** in D_2O (400 MHz, 298 K, [1.13] = 5.8 mM, [2.3] = 39.5 mM, ratio of DMPC/DHPC = 3.2 : 1, 60 mg mL^{-1} total lipid concentration). e) Illustration of the favorable H-bonding present in axial and equatorial conformations of $\mathbf{2.3_{hyd}}$ in **1.13**.

The increased stability of unexpected guest conformers bound in **1.13** in lipid micelles is not as clear. One possibility could be the creation of a small "hydrophobic" pocket above the cavitand rim while positioned in the bilayer; as has been seen in the binding of cationic proteins to **1.13 • POPC** SLB interface.[4] This "hydrophobic" pocket may somewhat hide the bound guest from the external water, limiting competitive H-bonding interactions, while increasing the effect of H-bonding between the host and guest. There is little hard evidence for this theory due to the lack of concrete information about the position of the cavitand in the lipid micelles used in this study, although the orientation of **1.13** in SLB environments has been indirectly confirmed via SPR studies.[4] A second possibility for the increased stability is that the lipids force the cavitand walls closer to the guest than normally observed in pure water, acting as a "compression sleeve". The walls of cavitand **1.13** are very flexible, and their exact position varies with guest size. The restricted flexing of the cavitand walls while embedded in lipids would strengthen the intermolecular host-guest interactions. This concept has been seen for numerous other encapsulation complexes in both water and organic solvents.[26,27,28,29,30]

2.3 In/Out Exchange Properties of Bound Guests in Lipid Environments

The in/out exchange properties of guests **2.2** and **2.3** in cavitand **1.13** were analyzed in solution and in lipid micelle aggregates in order to shed light on the guest binding behavior in the system, and to elucidate the host-guest kinetics. Kinetic analysis of host-guest systems are usually studied through NMR by taking advantage of magnetization transfer.[31,32,33] Previous ^{1}H-^{1}H EXSY experiments utilizing **1.13** in lipid environments

show the exchange rates of small guests in aqueous solution.[21] However, these studies were not successful in obtaining in/out exchange rates due to the presence of large interfering peaks from the lipids. 2D ^{19}F-^{19}F EXSY is useful for kinetic analysis of guests **2.2** and **2.3** due to the absence of ^{19}F signals in the lipid aggregates. The EXSY studies were performed under the same conditions as the 1D spectra in Figures 2.7 and 2.6. The major diagonal peak present in the 2D ^{19}F-^{19}F EXSY spectra of the host-guest complex of guests **2.2** and **2.3** corresponds to the signals from the free and bound axial F in each molecule. Variable mixing times were applied to the systems: at mixing time = 100 ms, exchange crosspeaks are easily observed, illustrating the in/out exchange process. At a mixing time of 3 ms, however, no crosspeaks are observed. As can be seen in Figure 2.8, the qualitative differences in exchange behavior of **1.13 • 2.2** and **1.13 • 2.3** in D_2O and in lipid micelles are clearly evident. Exchange crosspeaks are clearly visible for **1.13 • 2.2** at τ = 100 ms in D_2O, while only minimal crosspeaks are observed for **1.13 • 2.3** under the same conditions (Figure 2.8a and b). By utilizing longer mixing times, we can observe crosspeaks, indicating a decrease in the exchange rate of **2.2** when host **1.13** is embedded in micelle aggregates. Similarly, the exchange crosspeaks are smaller for **1.13 • 2.3** in the lipid environment, when compared to D_2O at 100 ms (Figure 2.8c and d).

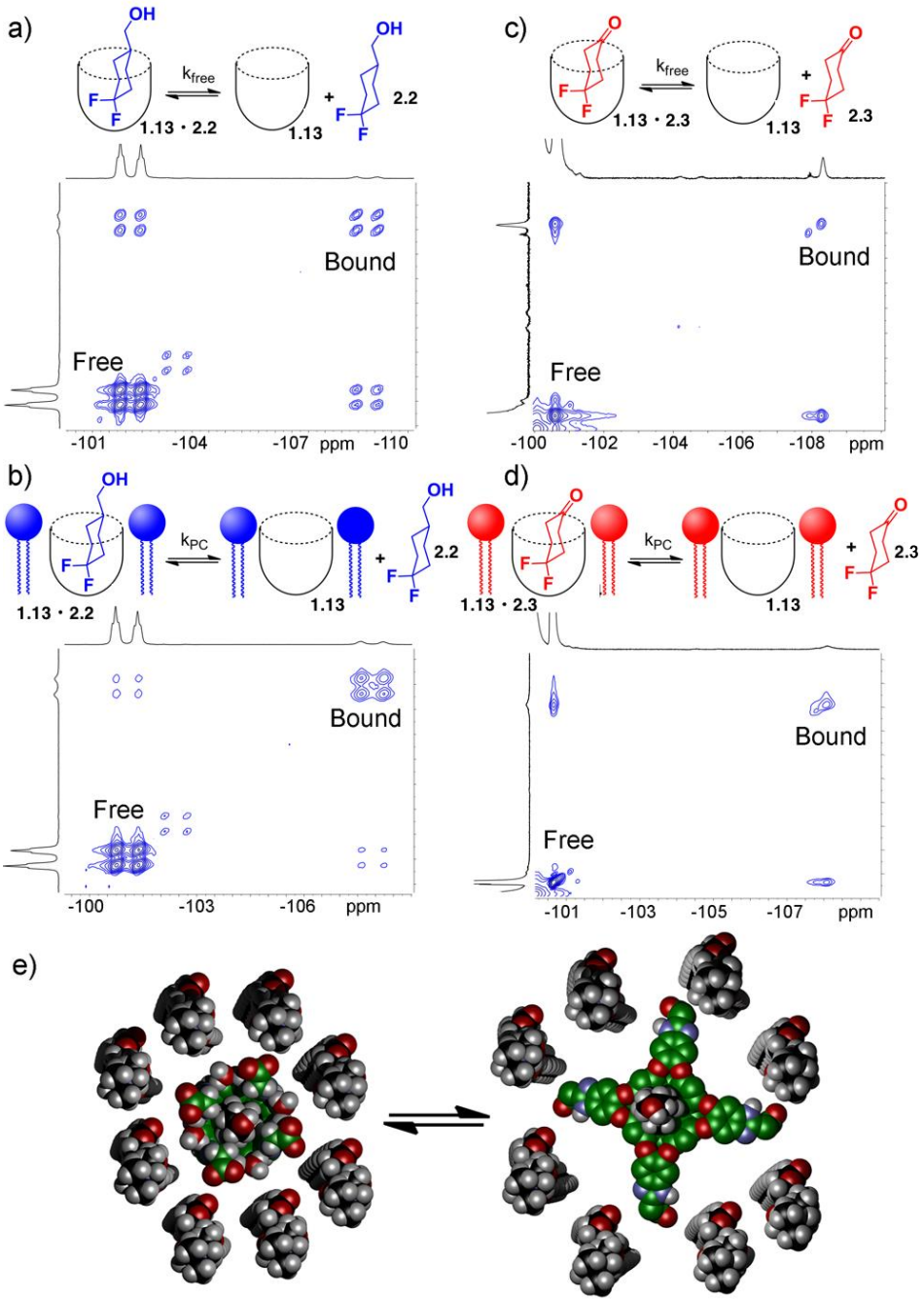

Figure 2.8: In/out exchange of guests **2.2** and **2.3** in **1.13** and **1.13** • PC_m. ^{19}F-^{19}F EXSY NMR spectra at mixing time τ = 100 ms of a) **1.13** • **2.2** in D_2O; b) **1.13** • **2.3** • PC_m; c) **1.13** • **2.3** in D_2O; d) **1.13** • **2.2** • PC_m (376.50 MHz, 298 K, [**1.13**] = 5.8 mM, [**2.2**, **2.3**] = 39.5 mM, ratio DMPC/DHPC = 3.2 : 1, 60 mg mL^{-1} total lipid concentration); e) Representation of the exchange dynamics in cavitand 1 in a DMPC/DHPC lipid bilayer environment.

The quantitation of the exchange rates of fluorinated guests was possible by taking exchange spectra at different mixing times. The relevant sections of the ^{19}F-^{19}F EXSY spectra (at mixing time s = 100 ms) of **1.13 • 2.2** and **1.13 • 2.3** used to determine the exchange rate can be seen in Figure 2.8. There are multiple peaks present in the full spectra due to the diastereotopic geminal fluorines. The axial and equatorial F atoms both show free and bound peaks, which show chemical exchange with each other. NOE crosspeaks can also be observed between the two geminal fluorines of **2.2** while small peaks are also observed due to the other conformer with the CH_2OH group in the axial position. Using this information, and by extracting the 1D slices from the 2D EXSY plots, the in/out exchange rate was determined by fitting the intensity of the four exchange peaks present in Figure 2.8 and fitting them against mixing time. Data was also obtained at higher mixing times (s = 300 ms), however, the multiple methods of magnetization caused inaccuracies in the data fitting so only initial rate regions of the plot were used.

The analysis of the EXSY data was performed by Dr. Beth Caulkins and Prof. Leonard Mueller using a standard two-site exchange model. In this model, the guest can exchange between a free and bound state, A and B, respectively:

$$A \underset{k_b}{\overset{k_f}{\rightleftharpoons}} B$$

k_b represents the exchange constant from B to A, while k_f represents the exchange constant from A to B. At equilibrium, the forward and reverse exchange rates are equal, therefore $k_b[B] = k_f[A]$, or in terms of the equilibrium constant: $\frac{[B]}{[A]} = \frac{k_f}{k_b} = k_{eq}$. The concentration of A can change during the mixing time of the EXSY in three ways: A can become bound

and decrease its contribution to the signal intensity over the mixing time, A can relax due to T_1 and also decrease its intensity, or a bound ligand B can be released, becoming A and adding to its signal intensity. This process can be described by the first-order differential equation $\frac{dA}{dt} = -k_f[A] - \frac{A}{T_{1A}} + k_b[B]\}$. The signal for B varies similarly and is described by the equation $\frac{dB}{dt} = -k_b[B] - \frac{B}{T_{1B}} + k_f[A]$. Each exchange spectrum contains two diagonal peaks, AA and BB, as well as two crosspeaks, AB and BA. The first letter in the designation describes the frequency in f_1 for the EXSY spectrum and the second gives the frequency f_2; for example AB would be the crosspeak at $\{v_A, v_B\}$. The set of coupled, first order, linear differential equations above can be solved using standard methods subject to the following initial conditions at the start of the EXSY mixing time:

AA and AB: $[A(t=0)] = A_0$, $[B(t=0)] = 0$
BB and BA: $[A(t=0)] = 0$, $[B(t=0)] = B_0$

This gives the following expressions for the diagonal and cross peak intensities in terms of the EXSY mixing time (t):

$$AA(t) = A_0 e^{\frac{1}{T_1}} \frac{k_b + e^{(k_b+k_f)t} k_f}{k_b + k_f}^{short\ time} A_0(1 \frac{t}{T_1} k_f t)$$

$$AB(t) = A_0 e^{\frac{1}{T_1}} \frac{(1\ e^{(k_b+k_f)t}) k_f}{k_b + k_f}^{short\ time} A_0\ k_f t$$

$$BB(t) = B_0 e^{\frac{1}{T_1}} \frac{e^{(k_b+k_f)t} k_b + k_f}{k_b + k_f}^{short\ time} B_0(1 \frac{t}{T_1} k_b t)$$

$$BA(t) = B_0 e^{\frac{1}{T_1}} \frac{(1\ e^{(k_b+k_f)t}) k_b}{k_b + k_f}^{short\ time} B_0\ k_b t$$

where it has been assumed that $T_{1A} = T_{1B}$. The initial rate (short time) solutions are shown

to the right. The above set of equations can be fitted to determine k_b and k_f by extracting 1D slices exhibiting the greatest peak intensity from the 2D spectra recorded with different mixing times.

Table 2.1: Exchange rates and barriers for guest exchange in cavitand **1.13** in free solution and DHPC/DMPC lipid micelles.[a]

Guest	k_{free}, s^{-1}	k_{PC}, s^{-1}	$\Delta G^{\ddagger}_{free}$, kcal mol^{-1}	$\Delta G^{\ddagger}_{PC}$, kcal mol^{-1}
2.2	4.2±0.9	1.8±0.8	16.6	17.1
2.3	8.7±1.3	5.2±1.6	16.2	16.5
2.3$_{hyd}$	5.7±0.8	*N/A*	16.4	*N/A*
2.5	*N/A*	3.0±0.2	*N/A*	16.7
2.6	*N/A*	5.7±0.5	*N/A*	16.4

[a] Exchange rates were determined by fitting 2D EXSY crosspeaks. k_{free} = "off" exchange rate k_{-1} of guest from **1.13** in D_2O. k_{free} = "off" exchange rate k_{-1} of guest from **1.13** in PC_m in 1 mM HEPES/D_2O, ratio DMPC/DHPC = 3.2:1, 60 mg mL^{-1} total lipid concentration. [**1.13**] = 5.8 mM, [**2.2**, **2.3**] = 39.5 mM, [**2.5**, **2.6**] = 16 mM. Exchange barriers determined via the Eyring equation.[34]

The exchange analysis results can be observed on Table 1. The rate k_1 (or "k_{off}") for each guest is obtained through the fitting process at identical concentrations and temperatures for each guest in either aqueous solution (k_{free}) or in the micelle environment (k_{PC}). Eyring analysis[25] of the rate constants gives the exchange barriers $\Delta G^{\ddagger}$. The rate was found to be dependent on the nature of the guest and on the external environment. Larger **2.2** shows a k_{free} = 4.2 s^{-1} which is similar to that obtained for cyclooctanol.[21] In lipid environments, the exchange rate drops to k_{PC} = 1.8 s^{-1}, corresponding to an additional 0.5 kcal mol^{-1} of additional barrier presented by the environments surrounding the cavitand

host. This “compression sleeve” effect that enhances the axial conformation of bound **2.2** is also responsible for slowing the in/out exchange rate as well.

Analysis of the EXSY experiments of guest **2.3** showed that $k_{free} = 8.7\ s^{-1}$, similar to the k_{free} obtained for cyclohexanone.[21] In micelles, the exchange rate is slowed to $K_{PC} = 5.2\ s^{-1}$, slightly less than in the case for smaller **2.2**, with an additional barrier of 0.3 kcal mol^{-1}. Since the crosspeaks of the EXSY spectrum were large enough to observe, the analysis of the in/out exchange of the hydrated gem-diol conformation of **2.3** was possible (Figure 2.9). The hydrogen bonding present between $\mathbf{2.3}_{hyd}$ and the rim of **1.13** slows the exchange rate when compared to the ketone conformation, giving $k_{free}(\mathbf{2.3}_{hyd}) = 5.7\ s^{-1}$. Unfortunately, the determination of k_{PC} was not possible for the host-guest complex of $\mathbf{2.3}_{hyd}$ in the lipid environment due to the equivalent crosspeaks being too small to accurately fit.

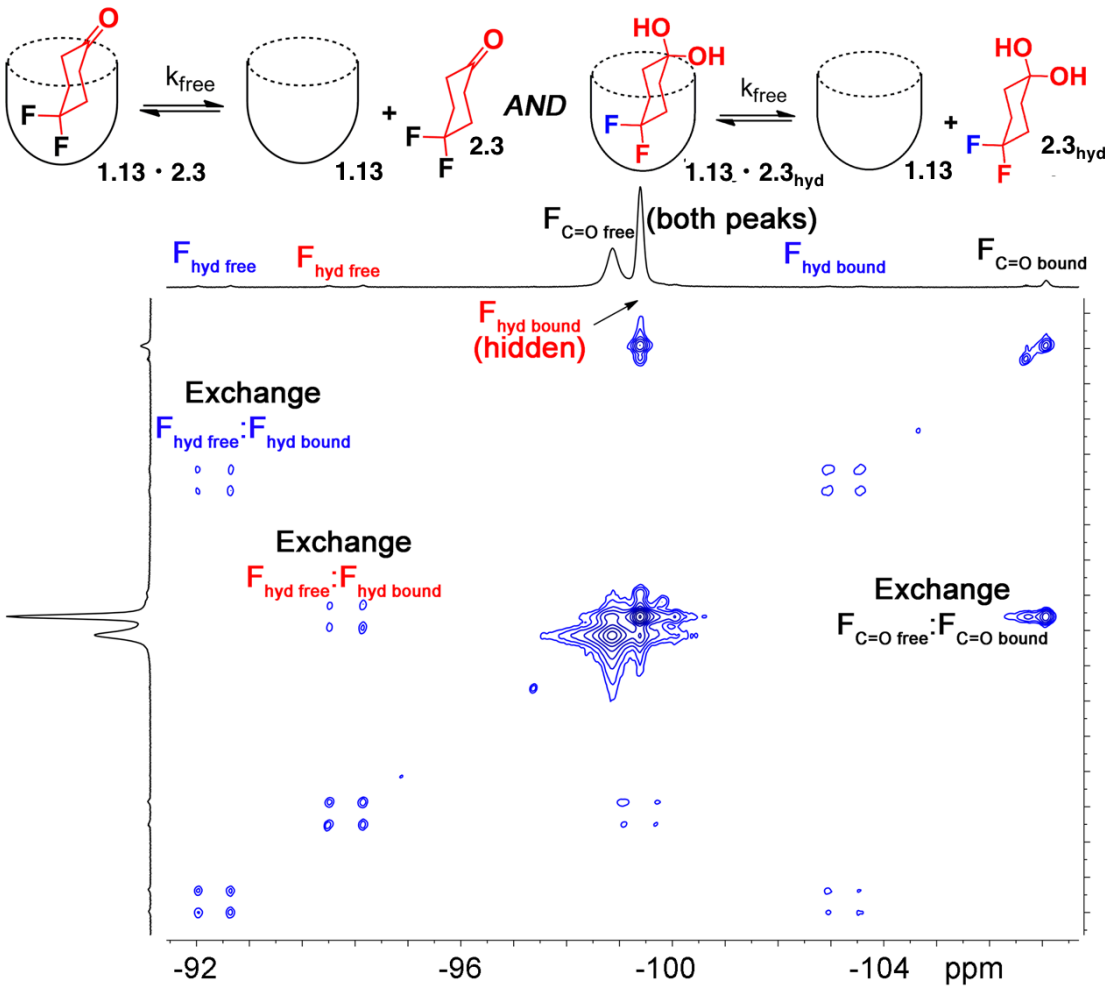

Figure 2.9: Full ^{19}F EXSY spectrum of the cavitand **1.13** guest **2.3** complex in pure D2O with peak assignments (D2O, 150.84 MHz, 298 K, mixing time = 150 ms, [**1.13**] = 5.8 mM, [**2.3**] = 39.5 mM).

2D EXSY NMR studies were also performed on ^{13}C-enriched guests **2.4**-**2.7**. These guests contain ^{13}C-enriched $RNMe_3^+$ groups, to interact with the cavity of **1.13**, and varying groups to interact with the rim. To study guest tumbling as opposed to in/out exchange, symmetrical guests **2.4** and **2.7** were targeted. These guests were unsuccessful candidates due to their inability to bind in cavitand **1.13** in D_2O environment or in the presence of lipids. This showed that the nature of the upper rim of the guests plays a role in guest

recognition. Guests **2.5** and **2.6** were employed due to their asymmetrical nature and ability to take part in H-bonding with the rim of **1.13**. ^{13}C-^{13}C EXSY was used to perform exchange analysis on these guests. The exchange rates obtained for guests **2.5** and **2.6** in micellar environment were very similar to those of the difluorocyclohexanyl guests, which can be seen on Table 1. These results allowed for an estimate of the k_{free} for **2.5** and **2.6** to be on the order of 6 s^{-1} and 10 s^{-1} respectively, assuming the "compression sleeve" effect on the micelle environment is constant.

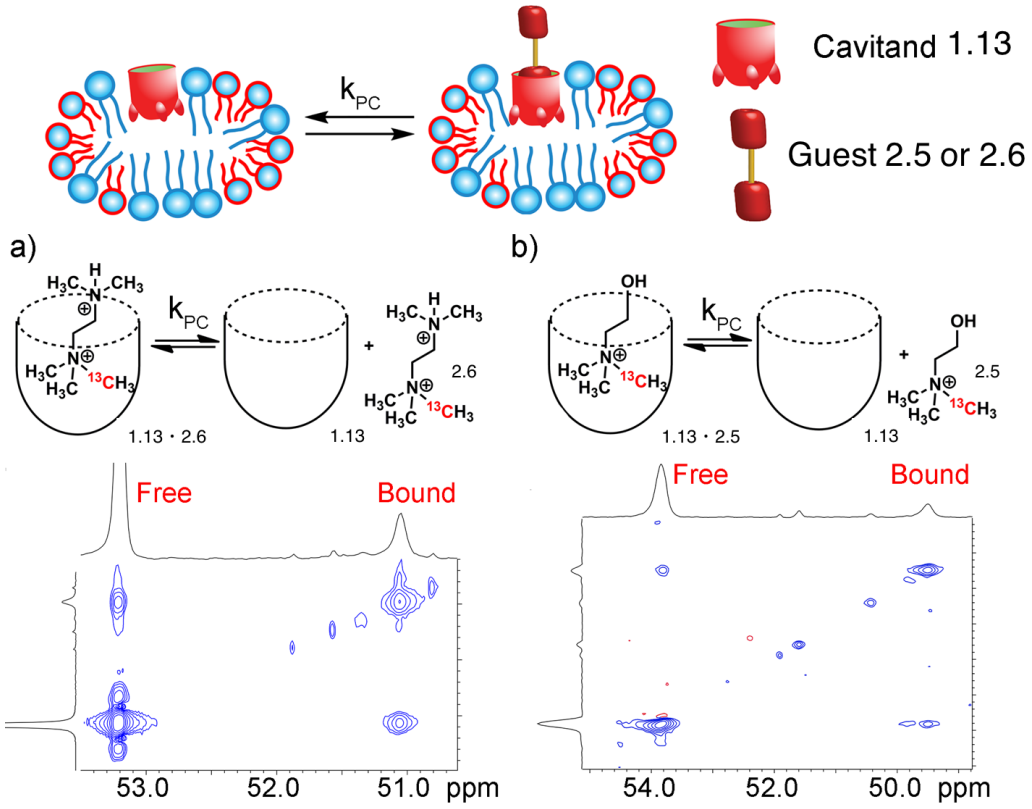

Figure 2.10: In/out exchange of guests **2.5** and **2.6** in **1.13** and **1.13** • PCm. ^{13}C–^{13}C EXSY NMR spectra at mixing time s = 100 ms of (a) **1.13** • **2.6** • PCm; (b) **1.13** • **2.5** • PCm (2.5 mM HEPES/D_2O, 150.84 MHz, 298 K, [**1.13**] = 5.8 mM, [**2.5**, **2.6**] = 16 mM, ratio DMPC/DHPC = 3.2:1, 60 mg mL^{-1} total lipid concentration).

In/out exchange studies using **2.5** and **2.6** in the more relevant, magnetically ordered bicelles was also possible. The signal to noise ratio was poor for guest **2.5**, so studies were performed using **2.6**. These solid-state experiments allowed for the observation of guest **2.6** exchange from the analysis of the exchanging crosspeaks corresponding to the $^{13}CH_3$ signal of bound and free **2.6**. In the bicellar environment, the in/out rate occurs more rapidly and shorter mixing times were required to see guest exchange. Accurate quantitation of the exchange rate in the bicellar system was not possible due to the smaller sample volume requiring a large amount of signal averaging to obtain good signal and required long acquisition time (~ 48 h per spectrum); decomposition of the bicelles occurred after a week at 308 K. Experiments were performed on the same samples in order to avoid changes in concentrations and peak intensity. The spectra obtained were only suitable for qualitative analysis and quantitation of the exchange rate was not possible. Figure 2.11 clearly shows exchange for guest **2.6** and illustrates the power of 2D NMR to analyze host:guest interactions of cavitand **1.13** in different types of lipid aggregates while analyzing the guest kinetics of suitably labeled guests.

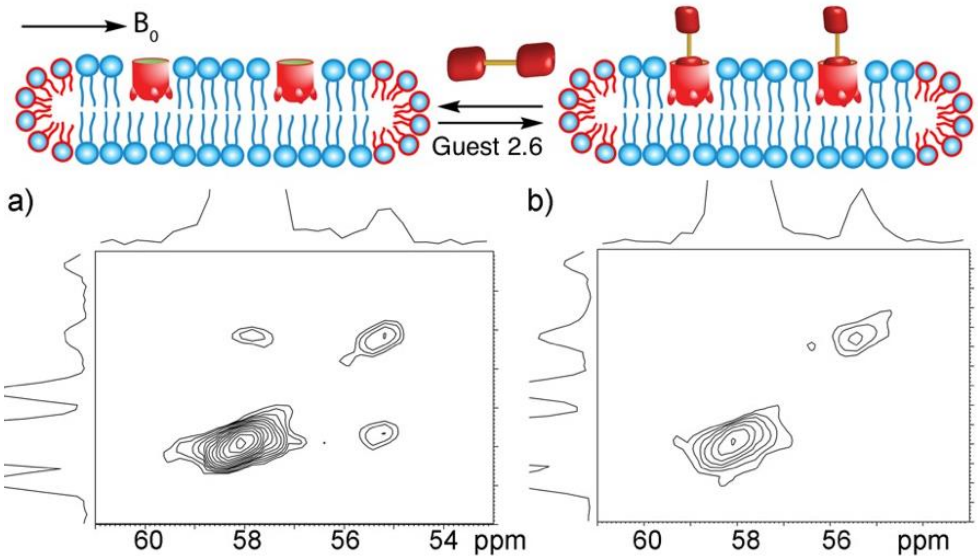

Figure 2.11: In/out exchange of guest **2.6** in the magnetically ordered bicelle system PCb. ^{13}C–^{13}C EXSY NMR spectra at mixing time (a) s = 20 ms; (b) s = 0 ms of **1.13** • **2.6** • PCb; (1 mM HEPES/D_2O, 100.69 MHz, 298 K, [**1.13**] = 20 mM, [**2.6**] = 36 mM, ratio DMPC/DHPC = 3.2 : 1, 150 mg mL^{-1} total lipid concentration).

2.4 Conclusion

The influence of external environment on the recognition properties of **1.13** can be studied using guests with detectable nuclei. ^1H NMR is commonly used to study the conformation and motion of small molecules in confined spaces due to the visible chemical shift changes in comparison to nuclei of ^{19}F and ^{13}C. The effects on small guest molecules by molecules outside of the host were studied and compression of the cavitand **1.13** was shown to enhance its recognition properties by providing an additional barrier to wall opening. This restriction slowed the rate of guest exchange in lipid environments. Unfavorable conformations were also enhanced by the "compression sleeve" effect of restricting guest movement and increasing the interactions between host and guest.

Interactions with the rim of the cavitand allow unstable structures such as hydrated ketone (diol) to exist at a higher rate than in free solution. The compression sleeve effect in lipid environments further increases these interactions and increases the amount of guests found in unfavorable conformations. The guest exchange rates in lipid environments were observed to decrease due to restricted wall flexing, which does not allow the guest to leave the cavity easily.

2.5 References

1. Perez, L.; Ghang, Y.-J.; Williams, P. B.; Wang, Y.; Cheng, Q.; Hooley, R. J. "Cell and Protein Recognition at a Supported Lipid Bilayer Interface via *In Situ* Cavitand-Mediated Functional Polymer Growth." *Langmuir*, **2015**, *31*, 11152–11157.

2. Ghang, Y.-J.; Schramm, M. P.; Zhang, F.; Acey, R. A.; David, C. N.; Wilson, E. H.; Wang, Y.; Cheng, Q.; Hooley, R. J. "Selective Cavitand-Mediated Endocytosis of Targeted Imaging Agents into Live Cells." *J. Am. Chem. Soc.*, **2013**, *135*, 7090–7093.

3. Perez, L.; Mettry, M.; Hinman, S. S.; Byers, S. R.; McKeating, K. S.; Caulkins, B. G.; Cheng, Q.; Hooley, R. J. "Selective Protein Recognition in Supported Lipid Bilayer Arrays by Tailored, Dual-Mode Deep Cavitand Hosts." *Soft Matter*, **2017**, *13*, 3966-3974.

4. Ghang, Y.-J.; Perez, L.; Morgan, M.A.; Si, F.; Hamdy, O.M.; Beecher, C.N.; Larive, C.K.; Julian, R.R.; Zhong, W.; Cheng, Q.; Hooley, R.J. "Anionic Deep Cavitands Enable the Adhesion of Unmodified Proteins at a Membrane Bilayer." *Soft Matter*, **2014**, *10*, 9651-9656.

5. Liu, Y.; Perez, L.; Mettry, M.; Gill, A. D.; Byers, S. R.; Easley, C. J.; Bardeen, C. J.; Zhong, W.; Hooley, R. J. "Site Selective Reading of Epigenetic Markers by a Dual-Mode Synthetic Receptor Array." *Chem. Sci.*, **2017**, *8*, 3960-3970.

6. Wang, K.; Sokkalingam, P.; Gibb, B. C. "ITC and NMR Analysis of the Encapsulation of Fatty Acids Within a Water-Soluble Cavitand and its Dimeric Capsule." *Supramol. Chem.*, **2016**, *28*, 84-90.

7. Schramm, M. P.; Hooley, R. J.; Rebek, J. Jr. "Guest Recognition with Micelle-Bound Cavitands." *J. Am. Chem. Soc.*, **2007**, *129*, 9773-9779.

8. Kim, Y. J.; Lek, M. T.; Schramm, M. P. "pH Influenced Molecular Switching with Micelle Bound Cavitands." *Chem. Commun.*, **2011**, *47*, 9636-9638.

9. Trembleau, L.; Rebek, J. Jr. "Interactions Between Surfactant and Cavitand in Water Blur Distinctions Between Host and Guest." *Chem. Commun.*, **2004**, *40*, 58-59.

10. Ryan, D. A.; Rebek J. Jr. "A Carbohydrate-Conjugated Deep Cavitand Permits Observation of Caviplexes in Human Serum." *J. Am. Chem. Soc.*, **2011**, *133*, 19653-19655.

11. Ryan, D. A.; Rebek J. Jr. "^{1}H NMR Detection of Small Molecules in Human Urine With a Deep Cavitand Synthetic Receptor." *Analyst*, **2013**, *138*, 1008-1010.

12. Park, S. H.; Das, B. B.; Casagrande, F.; Tian, Y.; Nothangel, H. J.; Chu, M.; Kiefer, H.; Maier, K.; De Angelis, A. A.; Marassi, F. M.; Opella, S. J. "Structure of Chemokine Receptro CXCR1 in Phospholipid Bilayers." *Nature*, **2012**, *491*, 779-783.

13. Gustavsson, M.; Verardi, R.; Mullen, D. G.; Mote, K. R.; Traaseth, N. J.; Gopinath, T.; Veglia, G. "Allosteric Regulation of SERCA by Phosphorylation-Mediated Conformational Shift of Phospholamban." *Proc. Natl. Acad. Sci. U. S. A.*, **2013**, *110*, 17338-17343.

14. Wright, A. K.; Batsomboon, P.; Dai, J.; Hung, I.; Zhou, H.-X.; Dudley, G. B.; Cross, T. A. "Differential Binding of Rimantadine Enantiomers to Influenza A M2 Proton Channel." *J. Am. Chem. Soc.*, **2016**, *138*, 1506-1509.

15. Liang, R.; Swanson, J. M. J.; Madsen, J. J.; Hong, M.; DeGrado, W. F.; Voth, G. A. "Acid Activation Mechanism of the Influenza A M2 Proton Channel." *Proc. Natl. Acad. Sci. U. S. A.*, **2016**, *113*, E6955-E6964.

16. Williams, J. K.; Tietze, D.; Lee, M.; Wang, J.; Hong, M. "Solid-State NMR Investigation of the Conformation, Proton Conduction, and Hydration of the Influenza B Virus M2 Transmembrane Proton Channel." *J. Am. Chem. Soc.*, **2016**, *138*, 8143-8155.

17. Opella, S. J. "Structure Determination of Membrane Proteins in their Native Phospholipid Bilayer Environment by Rotationally Aligned Solid-State NMR Spectroscope." *Acc. Chem. Res.*, **2013**, *46*, 2145-2153.

18. Murray, D. T.; Das, N.; Cross, T. A. "Solid State NMR Strategy for Characterizing Native Membrane Protein Structures." *Acc. Chem. Res.*, **2013**, *46*, 2172-2181.

19. Dürr, U. H. N.; Gildenberg, M.; Ramamoorthy, A. "The Magic of Bicelles Lights Up Membrane Protein Structure." *Chem. Rev.*, **2012**, *112*, 6054-6074.

20. Du¨rr, U. H. N.; Soong, R.; Ramamoorthy, A. "When Detergent Meets Bilayer: Birth and Coming of Age of Lipid Bicelles." *Prog. Nucl. Magn. Reson. Spectrosc.*, **2013**, *69*, 1-22.

21. Hooley, R. J.; Van Anda, H. J.; Rebek, J. Jr. "Extraction of Hydrophobic Species into a Water-Soluble Synthetic Receptor." *J. Am. Chem. Soc.*, **2007**, *129*, 13464-13473.

22. Timmerman, P.; Verboom, W.; Vanveggel, F. C. J. M.; Vanduynhoven, J. P. M.; Reinhoudt, D. N. A. "A Novel Type of Steroisomerism in Calix[4]arene-Based

Carceplexes." *Angew. Chem., Int. Ed.*, **1994**, *33*, 2345-2348.

23. Carey, F. A.; Sundberg, R. J. in "Advanced Organic Chemistry Part A: Structure and Mechanisms", Springer, **2008**.

24. Hooley, R. J.; Gavette, J. V.; Mettry, M.; Ajami, D.; Rebek, J. Jr. "Unusual Orientation and Reactivity of Alkyl Halides in Water-Soluble Cavitands." *Chem. Sci.*, **2014**, *5*, 4382-4387.

25. Biros, S. M.; Ullrich, E. C.; Hof, F.; Trembleau, L.; Rebek, J. Jr. "Kinetically Stable Complexes in Water: The Role of Hydration and Hydrophobicity." *J. Am. Chem. Soc.*, **2004**, *126*, 2870-2876.

26. Davis, A. V.; Fiedler, D.; Seeber, G.; Zahl, A.; van Eldik, R.; Raymond, K. N. "Guest Exchange Dynamics in an M_4L_6 Tetrahedral Host." *J. Am. Chem. Soc.*, **2006**, *128*, 1324-1333.

27. Tang, H.; de Oliveira, C. S.; Sonntag, G.; Gibb, C. L.; Gibb, B. C.; B öhne, C. "Dynamics of Supramolecular Capsule Assembly with Pyrene." *J. Am. Chem. Soc.*, **2012**, *134*, 5544-5547.

28. Rudkevich, D. M.; Hilmersson, G.; Rebek, J. Jr. "Self-Folding Cavitands." *J. Am. Chem. Soc.*, **1998**, *120*, 12216-12225.

29. Zhang, D.; Ronson, T. K.; Mosquera, J.; Martinez, A.; Guy, L.; Nitschke, J. R. "Anion Binding in Water Drives Structural Adaptation in an Azaphosphatrane-Functionalized $Fe^{II}{}_4L_4$ Tetrahedron." *J. Am. Chem. Soc.*, **2017**, *139*, 6574-6577.

30. Scarso, A.; Onagi, H.; Rebek, J. Jr. "Mechanically Regulated Rotation of a Guest in a Nanoscale Host." *J. Am. Chem. Soc.*, **2004**, *126*, 12728-12729.

31. Perrin, L; Dwyer, T. J. "Application of Two-Dimensional NMR to Kinetics of Chemical Exchange." *Chem. Rev.*, **1990**, *90*, 935- 967.

32. Sandstrom, J. " Dynamic NMR Spectroscopy" *Academic Press: London*, **1982**, *96*, 380.

33. Bain, A. D. "Chemical Exchange in NMR." *Prog. Nucl. Magn. Reson. Spectrosc.*, **2003**, *43*, 63-103.

34. Anslyn, E. V.; Dougherty, D. A. in "Modern Physical Organic Chemistry." *University Science Books*, Sausalito, California, **2006**.

Chapter 3: Selective Protein Recognition in Supported Lipid Bilayer Arrays by Tailored, Dual-Mode Deep Cavitand Hosts

3.1 Introduction

Lipidation is a common technique used to incorporate biomolecules into supported lipid bilayers (SLB).[1] Covalent modification is required to attach the target molecule to hydrophobic molecules such as fatty acids.[2] The application of this technique has allowed for the incorporation of a range of species into SLBs including small molecules,[3] nucleotides,[4] proteins,[1] glycopeptides,[5] glycopolymers,[6] and even whole living cells.[7] The lipidation process can become synthetically challenging with larger targets due to solubility and purification challenges associated with larger biomolecules. The use of synthetic receptor cavitands allows for the circumvention of this challenge while adhering biomolecules to SLBs. Due its amphiphilic properties, cavitand **1.13** can insert itself into lipid bilayers while retaining its selectivity; the cavity orients itself outward onto the water-lipid interface (Figure 3.1).[8] The binding behavior of water soluble deep cavitand **1.13** has been explored via NMR analysis, where the rate of guest exchange was found to decrease when embedded in lipids.[9] These studies have established cavitands as receptors capable of performing molecular recognition in membrane environments.

Water-soluble deep cavitand **1.13** has been utilized for the immobilization of proteins on the surface of SLBs (Figure 3.1).[8,10] Cavitand **1.13** is capable of molecular recognition via two different modes of interaction. The open-ended cavity in **1.13** allows for selective recognition of substituted trimethylammonium salts (-R-NMe_3^+) due to

cation-π interactions between the guest and the electron-rich aromatic pocket of the cavitand.[11] Proteins modified to contain a R-NMe_3^+ binding handle have been efficiently immobilized on SLBs via these pocket-based interactions.[10] The negative carboxylate groups on the cavitand rim also allow for interactions via both H-bonding and charge interactions, causing the immobilization of native cationic proteins on SLBs.[11] The electrostatic interactions of the cavitand rim are magnified in membrane environments (relative to aqueous solution),[9,12] enhancing salt bridge interactions between the cavitand and anionic proteins such as trypsin.[10] For native protein immobilization, cavitand **1.13** is selective for cationic proteins with high isoelectric points (pI). To increase the scope of native protein adhesion on our SLB surface, varied functionalization on the cavitand rim is required.

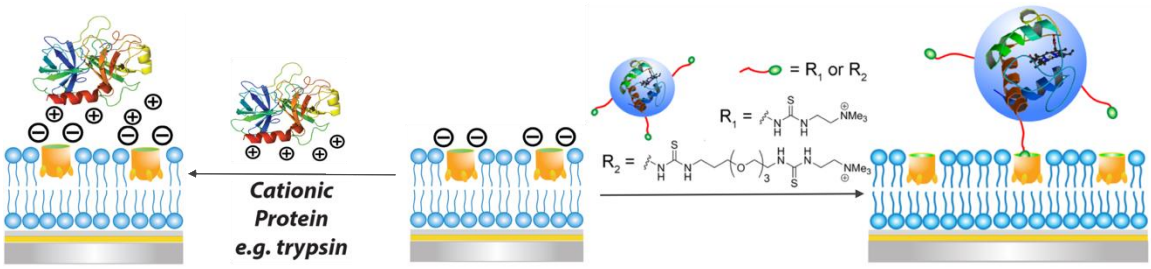

Figure 3.1: Native protein and (-R-NMe_3^+) derivatized protein immobilization by cavitand **1.13** at the water:SLB interface.

The two modes of recognition of cavitand **1.13** had only been utilized separately. In this study, we were interested in combining both modes of recognition into a single binding event for increased efficiency in target discrimination. We can create diverse and

complex interactions by tailoring guests that exploit these two modes of binding with variably functionalized cavitands. Finally, the employment of microarray technology allows us to visualize the selectivity in microarray format via SPR imaging (SPRi).

3.2 Functionalizing the Cavitand Rim to Obtain a Cationic Synthetic Receptor

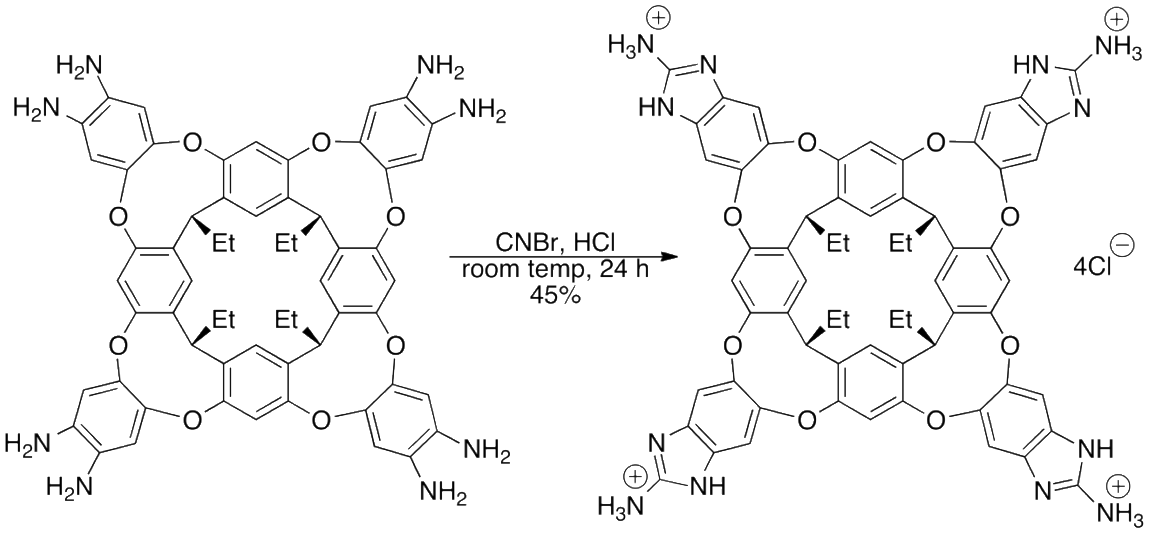

Figure 3.2: Synthesis of cationic cavitand **3.1** by the condensation of cyanogen bromide with octaamine cavitand **1.9**.

Cavitands **1.13** and **1.16** have been previously employed for recognition studies in membrane environments. Neutral cavitand **1.16** does not contain a charge at its rim and is a good control for electrostatic-based binding studies. To invert the native protein selectivity of **1.13**, aminobenzimidazole cavitand **3.1**[8,14] was obtained by reacting octaamine **1.9** with cyanogen bromide (Figure 3.2).[15] Cationic cavitand **3.1** displays millimolar solubility in water and contains four positively charged ammonium groups on

the rim. The cavity of **3.1** is exactly the same as that of **1.13** and **1.16**: it is an aromatic, hydrophobic pocket with selectivity for ($RNMe_3^+$) groups. To test the abilities of **3.1** as a synthetic membrane receptor, cavitand **3.1** was exposed to a SLB in order to analyze whether incorporation of the receptor was possible.

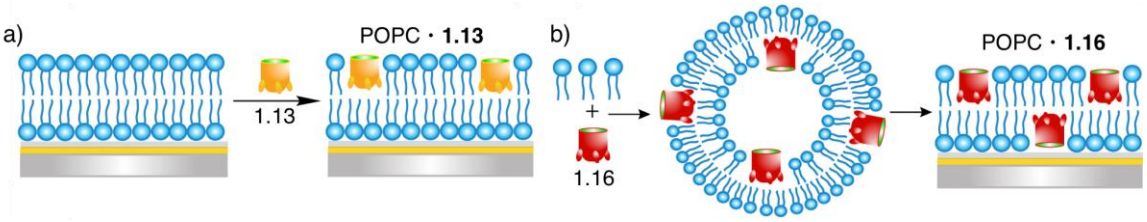

Figure 3.3: Formation of POPC • cavitand surface. Incorporation of a) **1.13** and b) **1.16** into a SLB.

A supported lipid bilayer was formed by the injection of 1-palmitoyl-2-oleoyl-sn-glycero-3-phosphocholine (POPC) vesicles atop a clean, nanoglassified gold substrate through a flowcell apparatus.[10] Subsequent injection of a 1.8 mM, 10% DMSO solution of either cavitand **3.1** or **1.13** in water generated a cavitand-impregnated SLB ready for recognition studies (Figure 3.3a). Due to its hydrophobicity, **1.16** is not soluble enough to inject into the system and needs to be incorporated into lipid vesicles beforehand. These vesicles can then be exposed to the nanoglassified surface to form a **1.16**-impregnated SLB (Figure 3.3b). Real-time SPR analysis of the surface can confirm the SLB formation and cavitand incorporation. SPR sensorgrams of cavitand-impregnated SLBs showed that the incorporation of **3.1** was not as efficient as that of **1.13**. Cavitand **3.1** gives a resonance angle change ($\Delta\theta$) of about $0.1^o \pm 0.011$ when incorporated into the lipid bilayer, while **1.13** exhibits a resonance angle change double that of **3.1** (Figure 3.4a and 3.4b). Although

inefficient, the incorporation of **3.1** into SLBs is effective and its adhesion properties of native proteins was studied and compared to cavitands **1.13** and **1.16**.

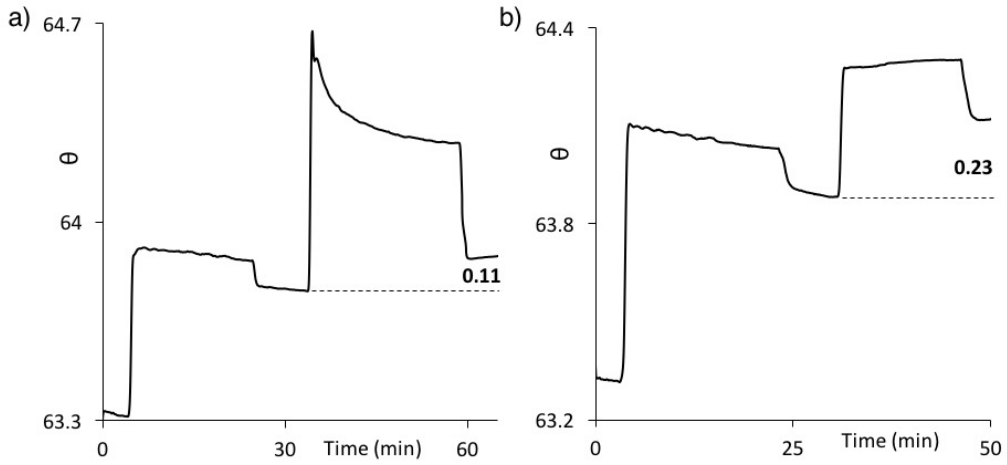

Figure 3.4: SPR sensorgrams depicting the incorporation of cavitand a) **3.1** and b) **1.13** into a POPC SLB.

3.3 Native Protein Binding

Since anionic cavitand **1.13** showed affinity toward cationic proteins, cationic **3.1** was expected to bind anionic proteins. The overall charge of a protein is dependent upon its isoelectric point (pI), which is defined as the pH at which the protein is neutral. At a pH lower than the pI of the protein, the overall charge will be positive, whereas at a pH higher than the pI, the overall charge will be negative. Using this information, we selected a variety of proteins ranging in pI values and size. Table 3.1 shows the different proteins used and their response upon exposure to the POPC • **3.1** and POPC • **1.13** surfaces. Cavitand **1.16** showed no adhesion to proteins of either cationic or anionic nature due to

the lack of electrostatic interactions between that protein and the rim of the cavitand. The POPC SLB also showed no immobilization of either anionic or cationic proteins in the absence of cavitand (Figure 3.5a and 3.5b).[8]

Table 3.1: Charge/H-bonding-based immobilization of native, unmodified proteins of varying size and charge at the POPC•Cavitand interface.

Protein	MW (kDa)	pI	$\Delta\theta_{cav\ \mathbf{1.13}}{}^{a}$ (°)	$\Delta\theta_{cav\ \mathbf{3.1}}{}^{a}$ (°)
Cytochrome *c*	12.4	10.5	0.13±0.020	0.03±0.002
Trypsin	23.3	10.5	0.32±0.004	0.04±0.004
Avidin	69	10.5	0.55±0.022	0.12±0.006
Streptavidin	53	5.0	0.03±0.002	0.12±0.001
Tryptophan Synthase	143	5.06	0.00±0.003	0.10±0.003
BSA	66.4	4.8	0.00±0.000	0.00±0.000

[a] $\Delta\theta_{cav}$ (°) = resonance angle change upon native protein immobilization in the presence of either cavitand **1.13** or **3.1**. Protein injection medium: 10 mM PBS buffer (pH 7.4), injected [**1.13**/**3.1**] = 1.6 mM; [protein] = 15 μM.

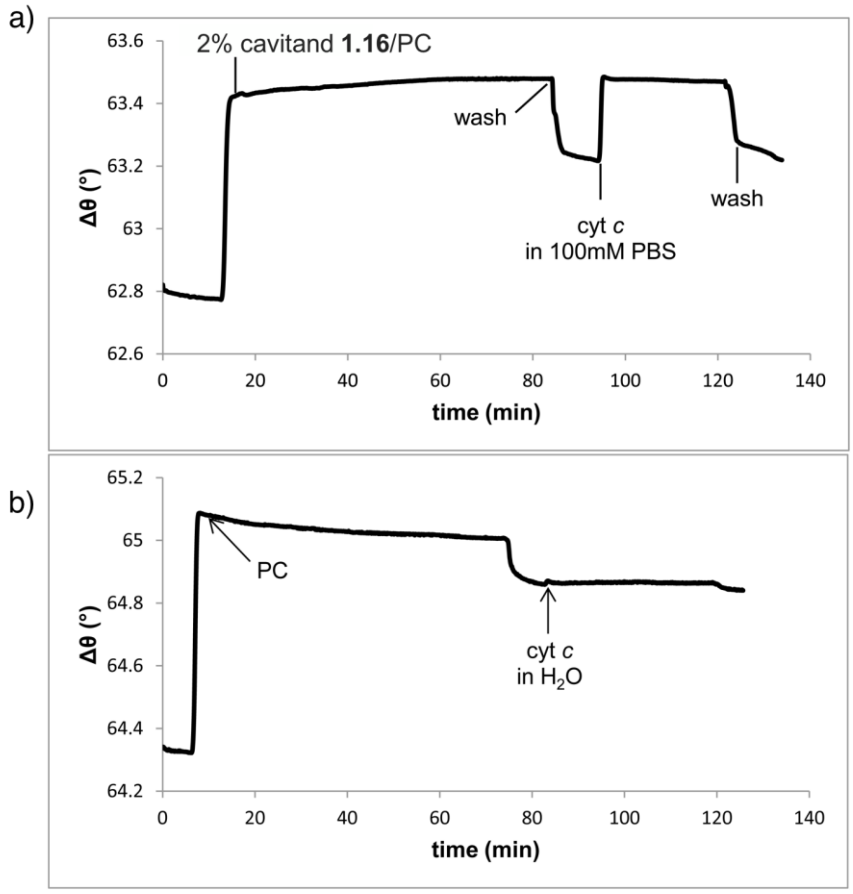

Figure 3.5: SPR sensorgram of the introduction of protein cytochrome *c* onto a) SLB•**1.16** surface[8] and b) SLB surface.

Proteins, in 10mM PBS buffer solution at pH 7.4, were injected onto the POPC•cavitand surface. Lower ionic strength solutions showed better protein adhesion due to charge/H-bonding-based interactions. As expected, and as seen on Table 3.1 and Figure 3.6a, cationic cavitand **3.1** displayed affinity towards anionic proteins while the opposite affinity was observed for cavitand **1.13** (Figure 3.6b). Cationic proteins such as trypsin (pI= 10.5) showed minimal protein adhesion to the surface containing **3.1**. Trypsin displayed a resonance angle change of $0.04^{o} \pm 0.004$, indicating minimal adhesion to the

POPC•**3.1** surface (Figure 3.7a). Cationic trypsin is repelled by the rim of positively charged **3.1**, this unfavorable interaction prevents adhesion. In contrast, the negatively charged cavitand **1.13** strongly immobilizes trypsin, producing a resonance angle change consistent with the size of the protein under examination. Larger proteins caused a bigger signal change relative to smaller sized proteins. The POPC•cavitand surface displays micromolar affinities to complementary-charged proteins. Simple K_d studies via SPR saturation mode analysis were not possible in this system due to the complex and multivalent interactions between the host and guest, but previous studies of the cavitand **1.13** adhesion of cytochrome *c* in a vesicle-based system showed a K_d of 7.6 μM using CE analysis.[10]

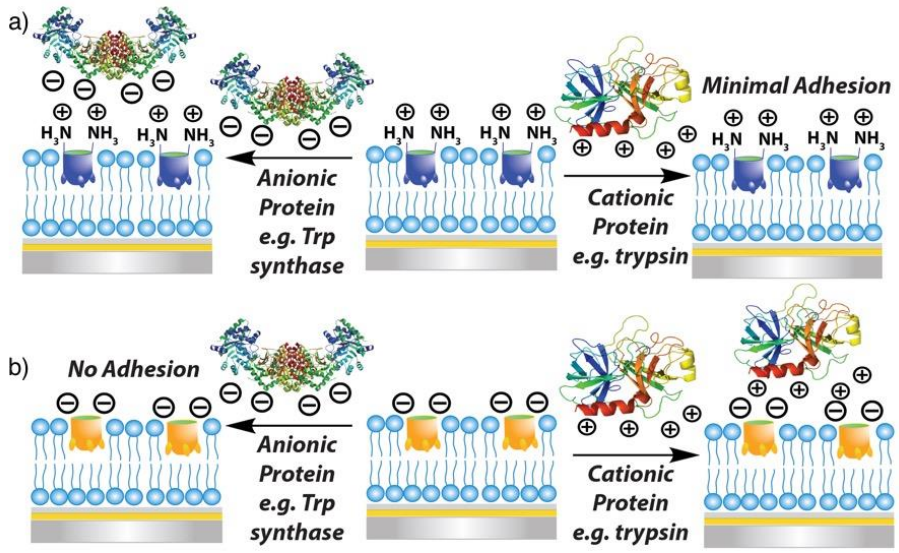

Figure 3.6: Interactions between anionic protein tryptophan synthase and cationic protein trypsin in POPC SLB containing a) cavitand **3.1** and b) cavitand **1.13**.

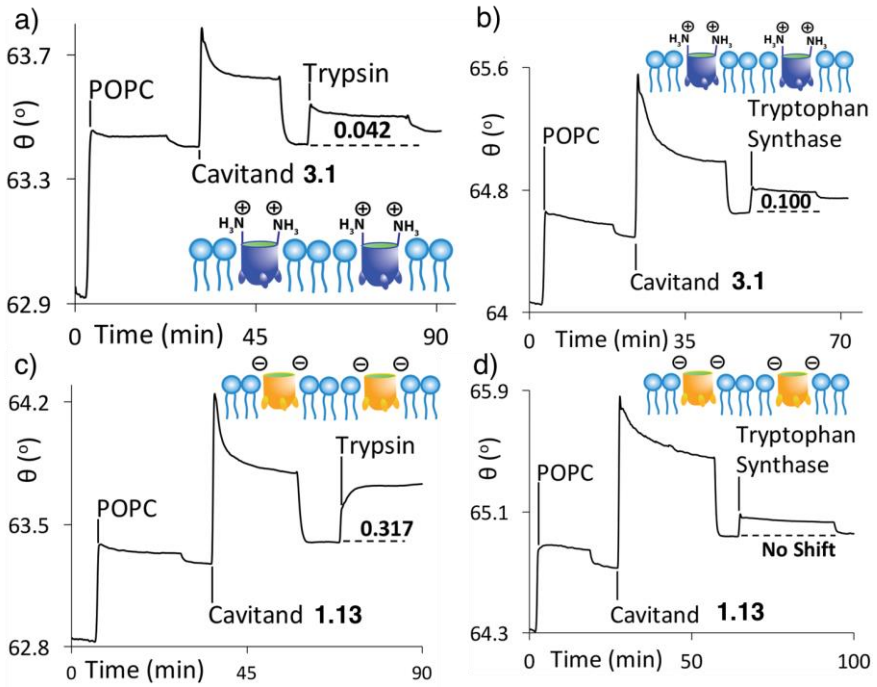

Figure 3.7: SPR sensorgrams of the interactions between POPC•**3.1** and a) cationic trypsin and b) anionic tryptophan synthase as well as the interactions between POPC•**1.13** and c) trypsin and d) tryptophan synthase.

Anionic proteins showed the opposite response when exposed to the POPC • **3.1** surface. Tryptophan synthase has a pI of 5.06, making it negatively charged in our experimental conditions at pH 7. In the presence of negatively charged **1.13**, no adhesion was observed (Figure 3.7d). When injected into the POPC • **3.1** surface, however, a resonance angle change of $0.10^{o} \pm 0.003$ was observed (Figure 3.7b). Even though tryptophan synthase is a much larger protein than cytochrome *c* or trypsin, it exhibits a relatively small resonance angle change when adhered to the POPC • **3.1** surface. This is due to the inefficient incorporation of cavitand **3.1** into the supported lipid bilayer. The smaller amount of incorporated **3.1** on the SLB surface leads to a smaller resonance angle

change upon exposure to anionic proteins. The native protein adhesion was efficient, remaining even after rinsing the surface with nanopure water. The pI of the protein is not the only predictor of protein immobilization on our cavitand-impregnated supported lipid bilayer. Bovine serum albumin (BSA) is a lipophilic protein, which prevents it from binding efficiently to the cavitand surface. BSA was poorly bound by all cavitands in our studies, despite possessing an overall negative charge.

3.4 Tailored Dual-Mode Guest Recognition

After exploring the abilities of the cavitand rim at adhering native proteins in a membrane environment, the host's dual-mode recognition capabilities were explored by combining rim adhesion with the host binding abilities of the cavity. Guest molecules **3.2** – **3.6** were designed to fit in the pocket of the cavitand while also interacting with the rim (Figure 3.8). Cavitands are known to bind guests containing substituted R-NMe_3^+ binding handles and most guests containing $Me_3N^+CH_2CH_2$- groups will bind in the cavity, irrespective of the nature of the external group.[12,13,17] Carnitine[17] and phosphocholines[18] are two exceptions that fail to bind in cavitand **1.13**. These two guests contain a negative charge positioned near the carboxylate rim of **1.13** when inserted in the cavity, and the anion-anion interactions between the guest and rim abolish any positive interactions between the R-NMe_3^+ group and the aromatic cavity. Carnitine and phosphocholines can bind to neutral cavitand **1.16** due to the absence of repelling charge at its rim. This proves that the functionality at the upper rim of the cavitand plays a role in the binding affinity of guests.

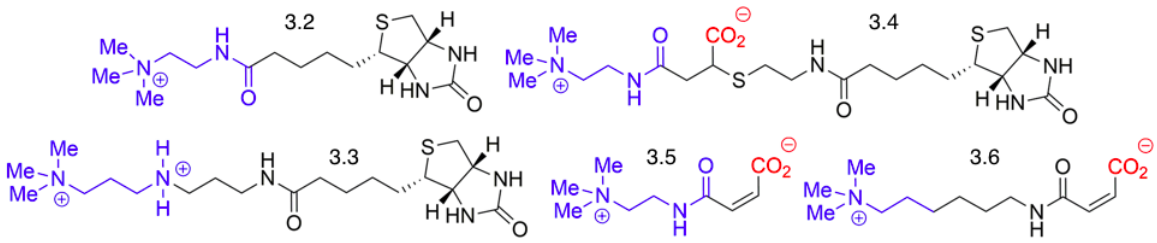

Figure 3.8: Cavitand guests containing the $RNMe_3^+$ handle for pocket binding and a charge placed around the rim of the cavitand to interact with the rim of anionic cavitand **1.13** and cationic **3.1**.

The various tailored guests allow for either direct or indirect protein adhesion. Guests **3.2** – **3.4** contain a biotin epitope which is displayed at the SLB:water interface when bound in the cavitand. The large protein avidin binds strongly to biotin, which can be immobilized by the POPC • cavitand • guest complex. This is a better strategy for the interrogation of guest binding using SPR. As previously stated, large molecules adhering to the surface cause a larger signal increase. Since the guest molecules are relatively small, they can cause ambiguity on whether binding occurred when a minuscule signal is produced. Since the K_a of biotin • avidin is extremely high, and avidin is a large sized protein, a significant signal change will be produced upon binding. The signal change can be solely attributed to the cavitand • guest interactions, and since the size and hydrophobicity of avidin are constant, any signal variation will be due to host • guest affinity. Apart from the biotin and $NMe_3^+CH_2CH_2$- groups, guests **3.3** and **3.4** vary in their internal structure to allow charge interactions with the charged rim of cavitands **1.13** and **3.1** (Figure 3.9a). Guest **3.2**[12] is a control as it does not possess a charge in its structure. Guest **3.3** contains an amine group three atoms away from the $RNMe_3^+$ binding handle,

which is positioned directly at the cavitand rim. In a neutral, aqueous environment, the amine exists mainly as an ammonium ion R-NH_3^+, which favorably interacts through electrostatic interactions and H-bonding with the rim of **1.13** (Figure 3.9c). In the presence of cavitand **3.1**, guest **3.3** will experience unfavorable interactions due to a charge mismatch with the cationic rim. Guest **3.4** is expected to display inverse selectivity as that of **3.3** since it positions a negative carboxylate group near the rim of the cavitand. This anionic group will cause **3.3** to experience a charge mismatch with **1.13**, while producing favorable interactions with **3.1** (Figure 3.9b).

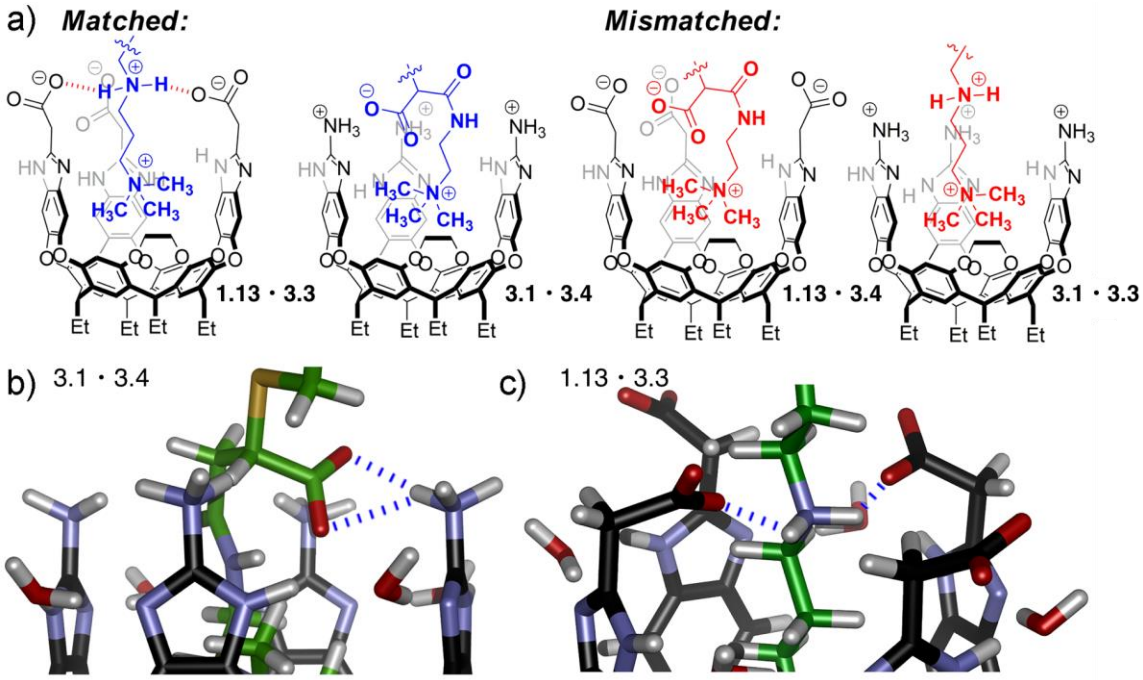

Figure 3.9: (a) Representations of the dual-mode recognition system, illustrating matched and mismatched secondary interactions between guests and the cavitands' upper rims; (b and c) close-up views of the upper rim portion of minimized structures of ''matched'' **3.1 • 3.4** and **1.13 • 3.3**, respectively (SPARTAN, AM1 forcefield).

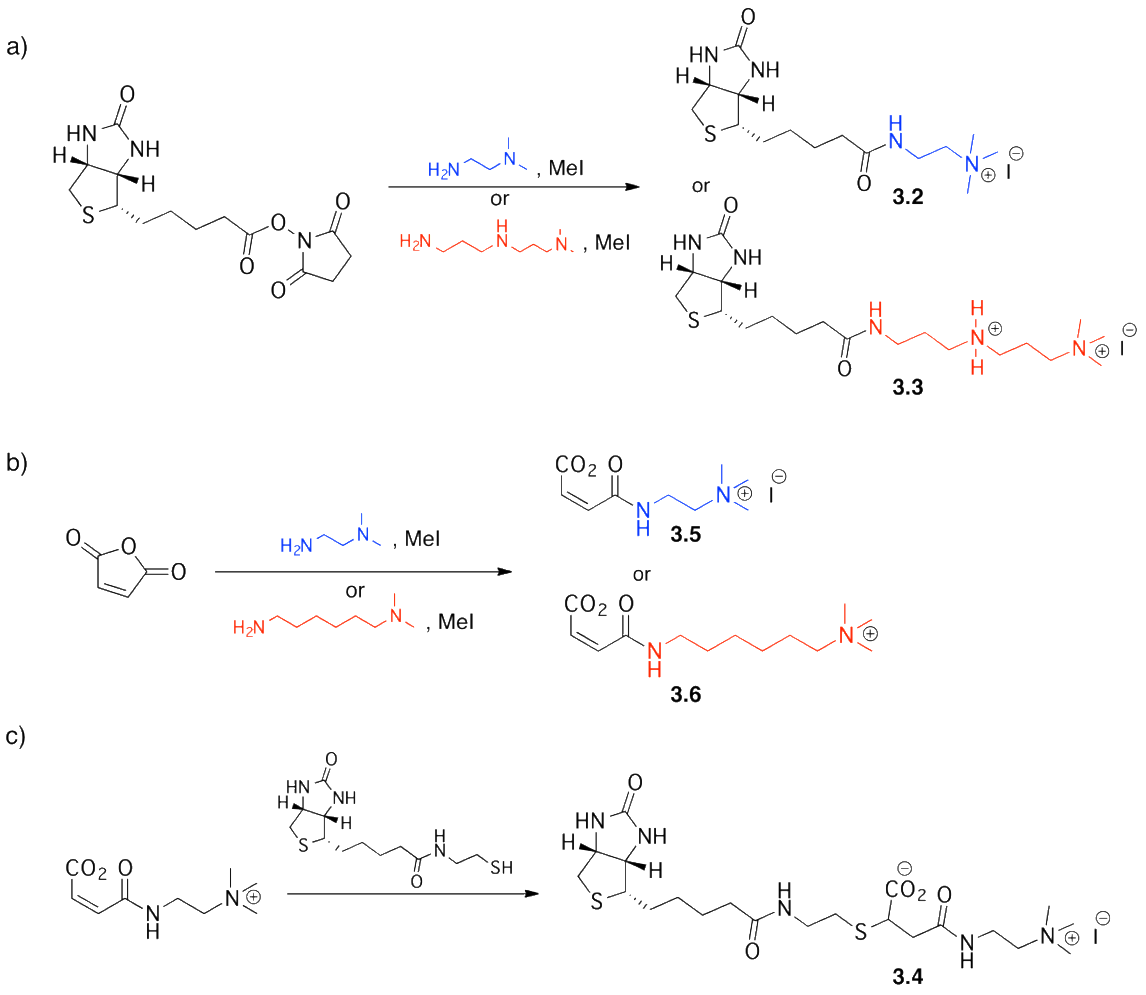

Figure 3.10: a) Synthesis of biotinylated guests **3.2** and **3.3** b) Synthesis of tailored guest handles placing a negative charge near the rim of the cavitand **3.5** and **3.6**; and c) Synthesis of biotinylated guest **3.7**.

The biotin moiety was introduced to guests **3.2** and **3.3** by reacting NHS-biotin with the corresponding amine (N,N-dimethylethylenediamine for **3.2** and N,N-dimethylpropylenediamine for **3.3**), followed by methylation to form the R-NMe_3^+ binding handle (Figure 3.10a). Guests **3.5** and **3.6** were formed by the reaction of maleic anhydride with corresponding amine, followed by methylation (Figure 3.10b). The reaction of guest

3.5 with a thiolated biotin derivative via Michael addition allowed for the formation of **3.4**, containing a negative charge for cavitand rim interaction (Figure 3.10c).

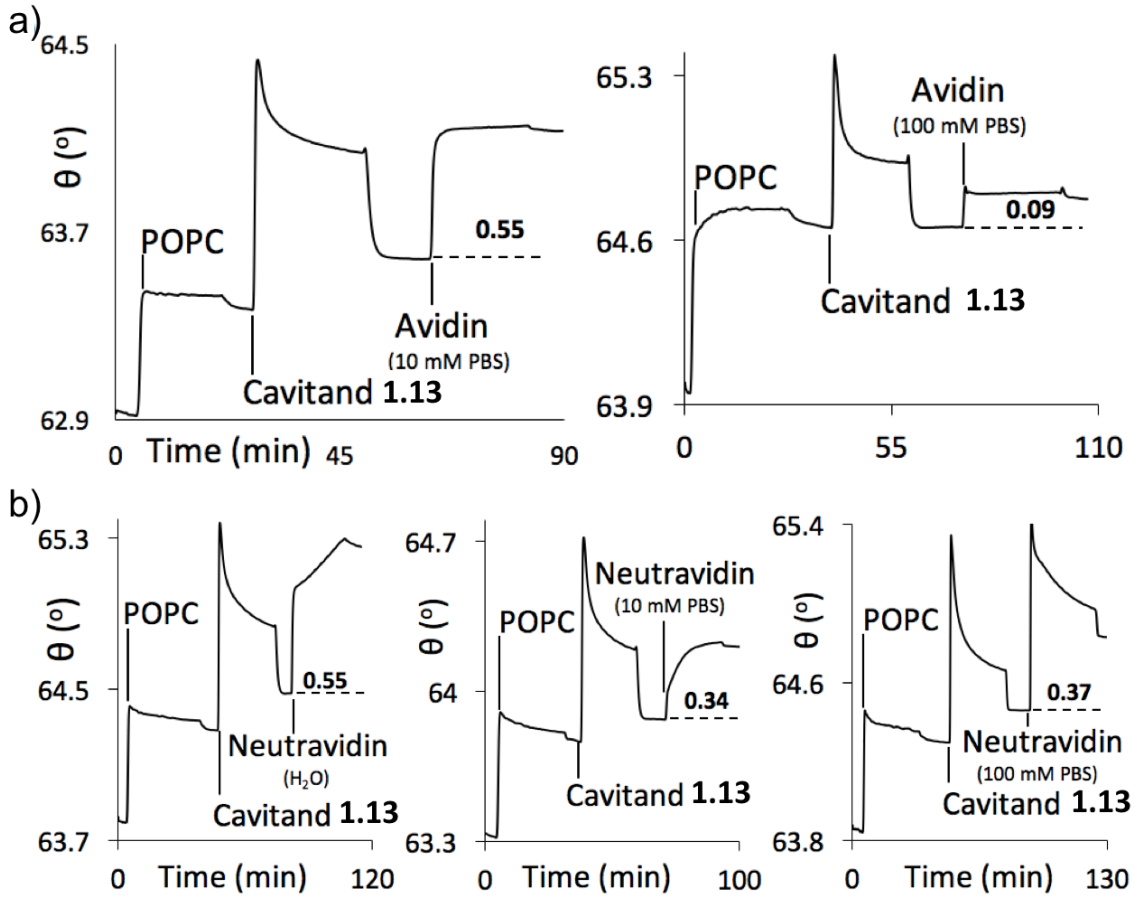

Figure 3.11: a) SPR sensorgrams showing immobilization of avidin by the POPC•**1.13** interface. Avidin immobilization is observed in both 10mM and 100 mM PBS injection medium; b) SPR sensorgrams showing immobilization of neutravidin by the cavitand POPC•**1.13** interface. Neutravidin is immobilized in injection medium of H_2O, 10 mM and 100 mM PBS.

In order to perform accurate analysis of the dual-mode binding process shown in Figure 3.9, any background adhesion of the target proteins with the POPC • cavitand

surface via charge/ H-bonding must be minimized. Avidin was shown to be unsuitable for our studies due to strong background adhesion to cavitand **1.13**, even in high salt concentrations. Figure 3.11a shows the SPR sensorgrams of the immobilization of avidin on a POPC • **1.13** surface with significant resonance angle change, even at a high salt concentration of 100 mM PBS. Neutravidin showed much sharper angle shifts when introduced into the POPC • **1.13** surface in varying salt concentrations (Figure 3.11b). Streptavidin, which also binds biotin efficiently, showed no background affinity for the POPC • **1.13** surface while showing minimal affinity for POPC • **3.1** (Figure 3.12). Due to these results streptavidin was chosen as the target protein.

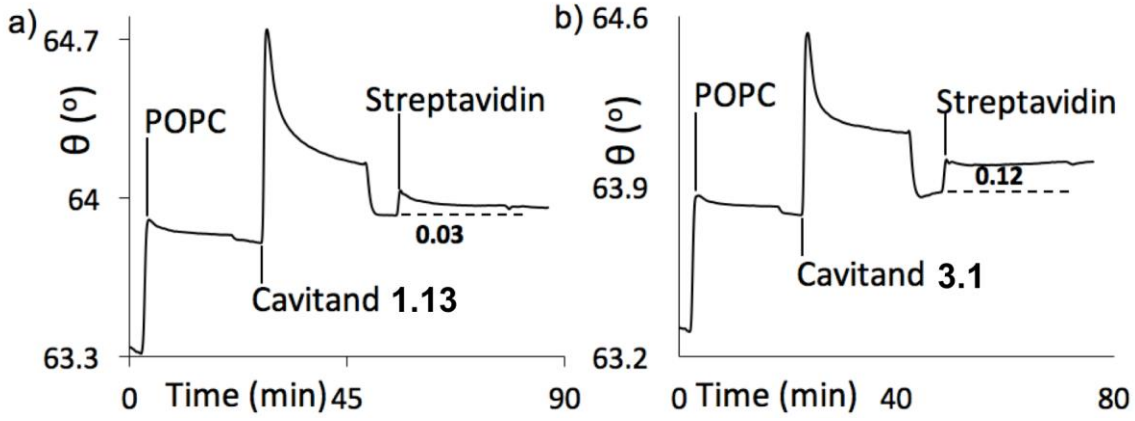

Figure 3.11: SPR sensorgrams showing immobilization of streptavidin at the a) POPC•**1.13** interface and b) POPC•**3.1** interface.

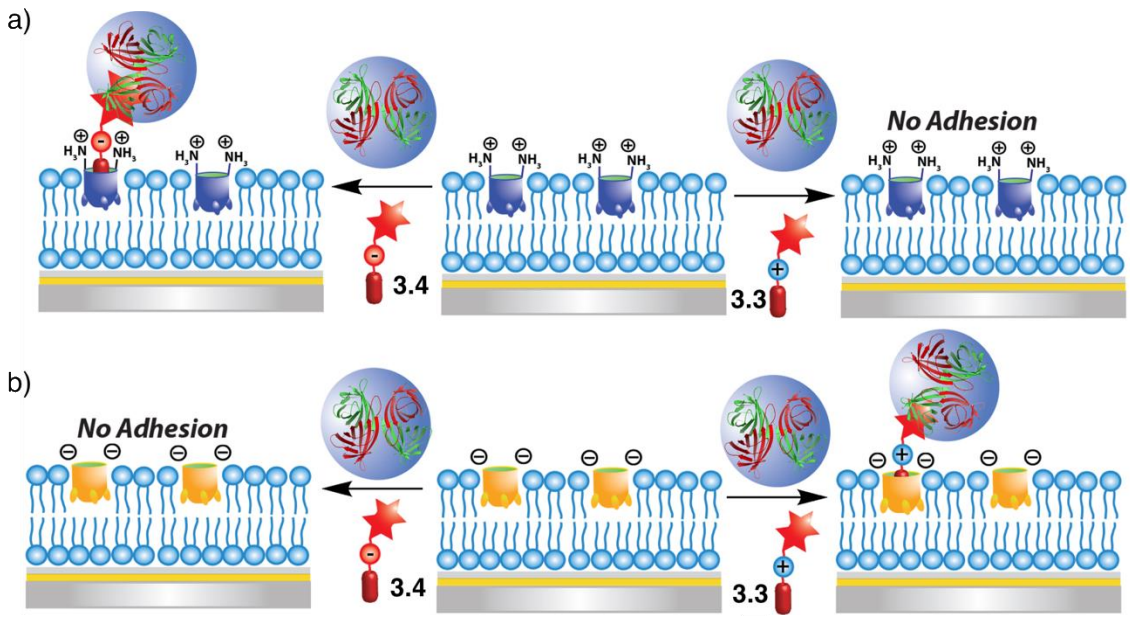

Figure 3.12: Dual-mode binding studies using tailored guests **3.3** and **3.4** to trap avidin in the presence of a) cationic cavitand **3.1** and b) anionic cavitand **1.13**.

Dual-mode binding studies were performed using guests **3.3** and **3.4** in the presence of either cavitand **1.13** or **3.1**. Guests **3.3** and **3.4** contain the biotin epitope and should be able to immobilize streptavidin to the SLB via complementary electrostatic interactions between the guest and rim of the cavitand (Figure 3.12). These experiments were performed by injecting 100 μL of a 1 mg mL^{-1} guest solution in nanopure water onto the POPC•cavitand surface. After incubating and washing away any unbound guest, streptavidin (15 μM) was introduced to the SLB system. Cationic amine-based guest **3.3** illustrates the dual-mode guest binding selectivity well. In the presence of anionic cavitand **1.13**, guest **3.3** shows effective immobilization of streptavidin while causing a resonance angle shift of $0.26^{o} \pm 0.004$ (Figure 3.13b). The charge matching between the cationic

amine in the guest and the anionic rim of the cavitand allow for complementary interactions, leading to effective guest immobolization. In the presence of cationic cavitand **3.1**, guest **3.3** displays minimal streptavidin adhesion while effecting a resonance angle change of only $0.06^{o} \pm 0.007$ (Figure 3.12e). The lower SPR response is due to ineffective guest adhesion by cavitand **3.1**; the cationic amine group on guest **3.3** is repelled from the positively charged rim of the cavitand. Although guest **3.3** contains the R-NMe_3^+ binding handle required for cavity incorporation, the repulsive forces between of the charge mismatch prevent incorporation and therefore streptavidin adhesion.

Dual-mode binding studies were also performed using anionic tailored guest **3.4**. Guest **3.4** places an anionic group near the rim of the cavitand when bound in the pocket. As expected, in the presence of cavitand **1.13**, guest **3.4** failed to adhere streptavidin to the SLB surface (Figure 3.13c). Again, this result is due to charge repulsions between the negative carboxylates on the rim of cavitand **1.13** and on guest **3.4**. In the presence of cavitand **3.1**, however, binding of guest **3.4** was indirectly observed through the immobilization of streptavidin, which caused a resonance angle change of $0.10^{o} \pm 0.007$ (Figure 3.13f). It is evident that cavitand **3.1** is not as efficient at adhering streptavidin in comparison to **1.13**. To prove this, studies employing the use of neutral biotin guest **3.2** were performed in the presence of both **1.13** and **3.1**. Guest **3.2** does not display a charge near the rim of the cavitand when it is bound in the cavity, and should theoretically bind in the cavity of either host. Unfortunately, guest **3.2** positions the biotin group much closer to the water-bilayer interface relative to guests **3.3** and **3.4**, causing streptavidin binding to suffer from steric clashes with the POPC bilayer. This accounts for the relatively smaller

change in resonance angle observed in the presence of this guest (Figure 3.13a and 3.13d). The SPR sensorgrams of Figure 3.13b and 3.13e confirmed that cavitand **1.13** is a far more effective host than **3.1**; cavitand **1.13** exhibits a resonance angle change of $0.22^{o} \pm 0.004$ while cavitand **3.1** shows a change of $0.04^{o} \pm 0.003$ due to streptavidin adhesion.

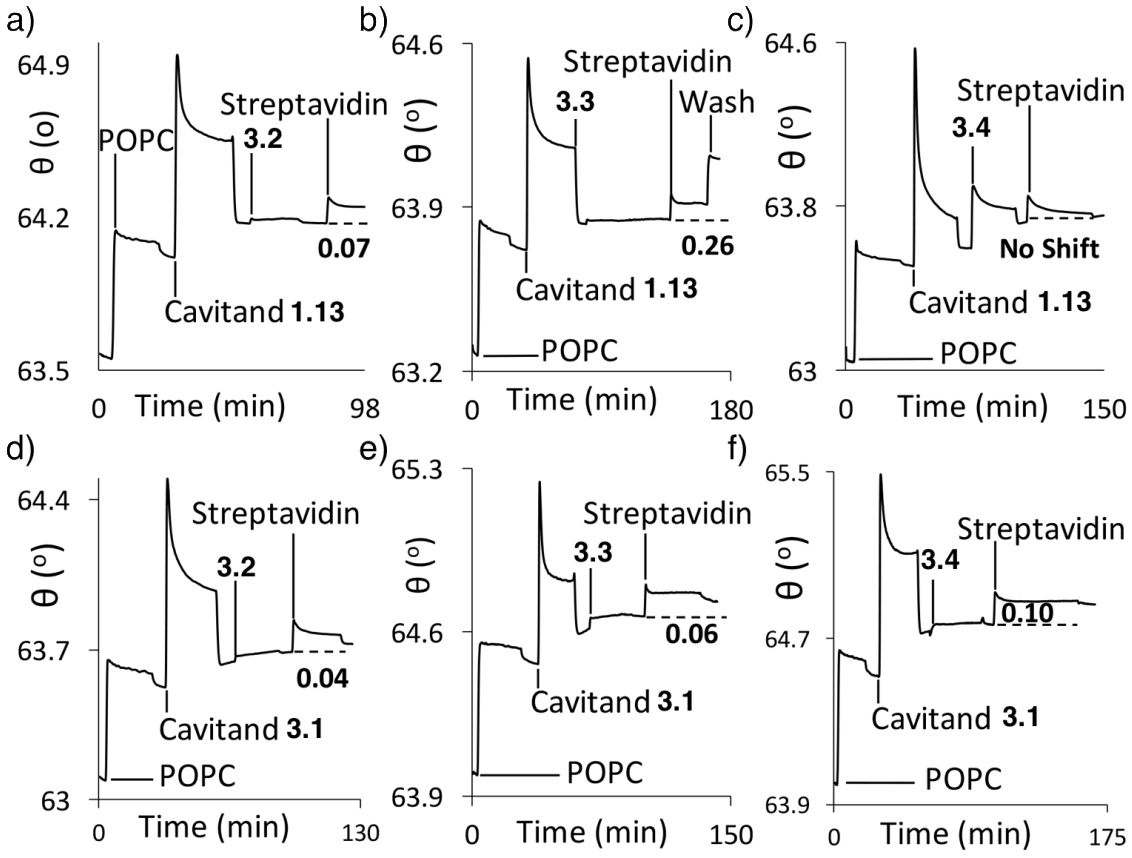

Figure 3.13: SPR sensorgrams of the variable interactions of streptavidin at the POPC interface with anionic cavitand **1.13** and (a) control guest **3.2**; (b) matched guest **3.3**; (c) mismatched guest **3.4**, or with cationic cavitand **3.1**, and (d) control guest **3.2**; (e) mismatched guest **3.3**; (f) matched guest **3.4**. Protein injection medium: 100 mM PBS buffer.

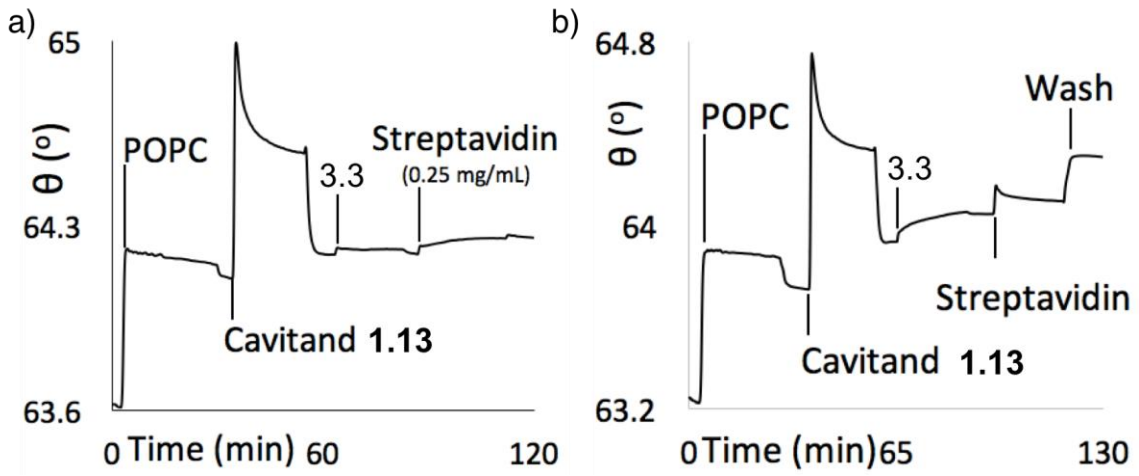

Figure 3.14: a) SPR sensorgram showing immobilization of streptavidin in 10 mM PBS (0.25 mg/mL) by the POPC • **1.13** • **3.3** interface; b) SPR sensorgrams showing immobilization of streptavidin in 10 mM PBS by the POPC • **1.13** • **3.3** interface by increasing the injection time from 2 minutes and 35 seconds to 3 minutes and 30 seconds.

The sensorgram of the adhesion of avidin by dual-mode binding guests **3.3** and **3.4** immobilized by cavitand **1.13** displayed an unusual characteristic. After incubation, and during the rinsing of excess streptavidin from the POPC • **1.13** • guest surface, a sharp increase in signal was observed instead of the characteristic decrease in signal (Figure 3.13b). The reason for this phenomenon is not evident, as this behavior is not observed with other strongly binding proteins described here or in other publications.[8,19,20] In an attempt to prevent this second binding event during rinsing, different experimental conditions were explored. Lowering the concentration of the avidin solution injected into the system did not work, as a sharp increase in signal was still observed (Figure 3.14a). Increasing the incubation time of avidin to allow the binding process enough time to complete was also unsuccessful (Figure 3.14b). Even though the second adhesion event is

still present, the qualitative selectivity of the guest binding is not affected; guest **3.3** matches and binds efficiently to cavitand **1.13** and mismatches with **3.1**.

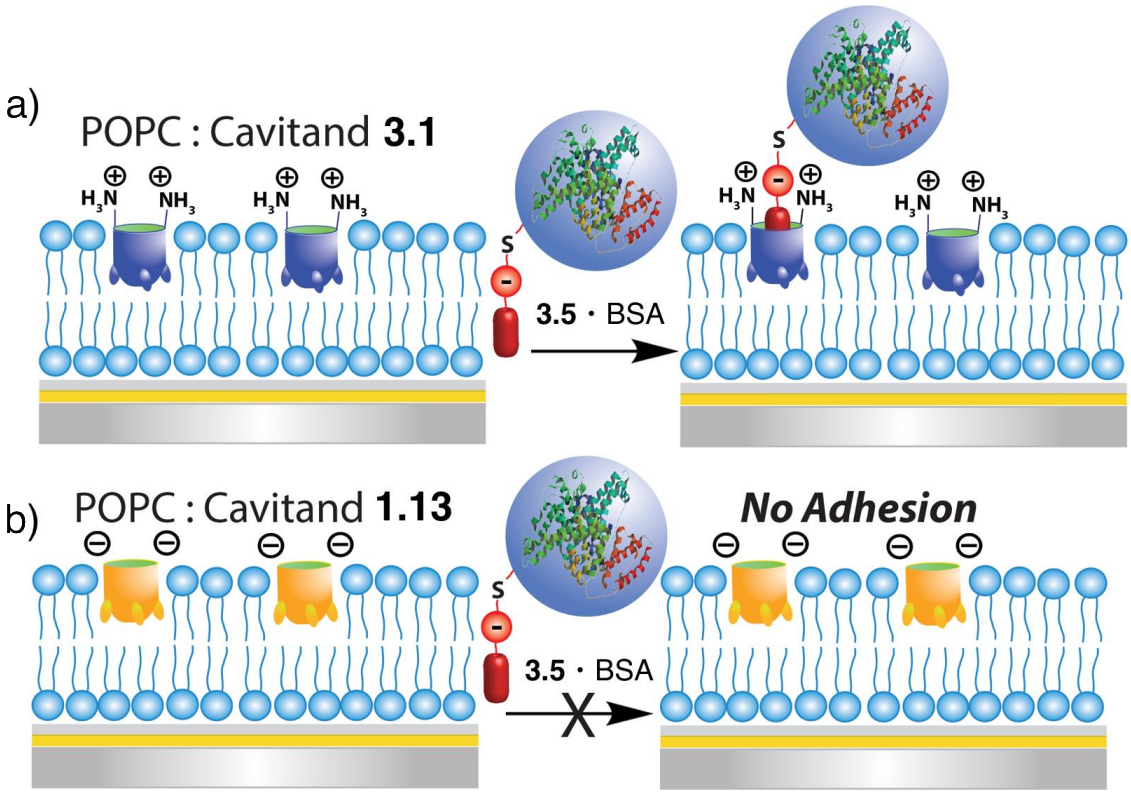

Figure 3.15: Selective dual mode recognition of covalently labeled BSA in the presence of: a) cationic cavitand **3.1** and b) anionic cavitand **1.13**.

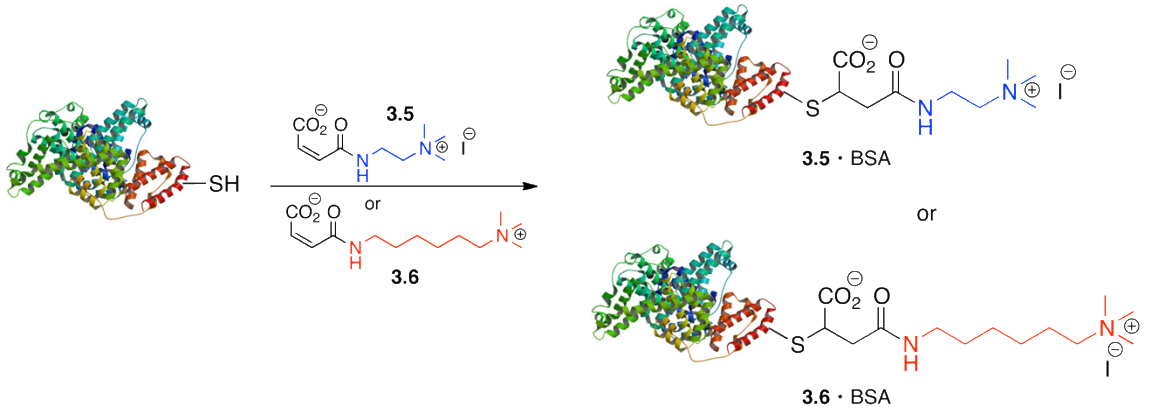

Figure 3.16: Derivatization of surface cysteine residue of BSA with guests **3.5** and **3.6** to form **3.5•**BSA and **3.6•**BSA.

Apart from using an epitope-containing guest to immobilize proteins on our surface via cavitand, a binary complex can be formed by covalently derivatizing proteins with the $RNMe_3^+$ binding handle. This method has been previously utilized for the immobilization of proteins on a SLB surface.[10] The covalent modification of proteins to form a binary complex that utilizes both modes of cavitand binding is possible with guest **3.5** (Figure 3.15). The formation of dual-mode binding guest **3.4** from maleamic acid-containing **3.5** via thiolate Michael reaction suggests that cysteine residues on proteins can also be reacted with **3.5**. BSA was suitable for our studies because it contains only one cysteine residue on its surface, and does not display adhesion in its native form to cavitands **1.13**, **1.16**, or **3.1**. BSA was reacted with either **3.5** or **3.6** in buffered solution over two hours in order to form **3.5** • BSA and **3.6** • BSA respectively (Figure 3.16). The two labeled BSA guests vary in length and **3.5** • BSA places a negative charge near the rim of the cavitand when bound

inside the pocket. Guest **3.6** • BSA is longer and therefore does not participate in dual-mode binding with the cavitand, making it a good control.

Both BSA guests were introduced onto the POPC•cavitand surface and the results are shown in Figure 3.17. The binding of guest **3.5** • BSA was highly selective, showing no affinity for the cavitand **1.13**-impregnated bilayer and strong adhesion in the presence of cavitand **3.1** (Figure 3.15a). Due to the negative carboxylate group placed near the rim of **1.13**, **3.5** • BSA experiences repulsive forces from the charge mismatch. These forces prevent the binding of **3.5** • BSA on the SLB surface. Due to complementary charge matching interactions with cavitand **3.1** in the bilayer, guest **3.5** • BSA displays a resonance angle change of $0.20^{o} \pm 0.023$. Interestingly, no immobilization was observed in the presence of neutral cavitand **1.16**. Cavitand **1.16** does not display a charge at its rim and would be expected to immobilize guest **3.5** • BSA using cavity-based recognition. Neutral host **1.16** has been shown to immobilize proteins labeled with longer oligoethyleneglycol-containing $RNMe_3^+$ handles,[10] but due to the short length of **3.5** • BSA, no adhesion was observed (Figure 3.17a). Guest **3.6** • BSA positions the negative carboxylate group further away from the rim, preventing dual-mode binding interactions. This longer guest is flexible, and so it can bend to afford some charge-matching interactions between its negative carboxylate and the cationic rim of cavitand **3.1**. These interactions are not as efficient compared to those between cavitand **3.1** and shorter guest **3.5**, where the complementarily charged groups are in close proximity. As was expected, a lower response ($0.14^{o} \pm 0.020$) was observed for guest **3.6**•BSA in the presence of a **3.1**-impregnated SLB

while no immobilization was observed in the presence of negative **1.13** or neutral **1.16** (Figure 3.17b).

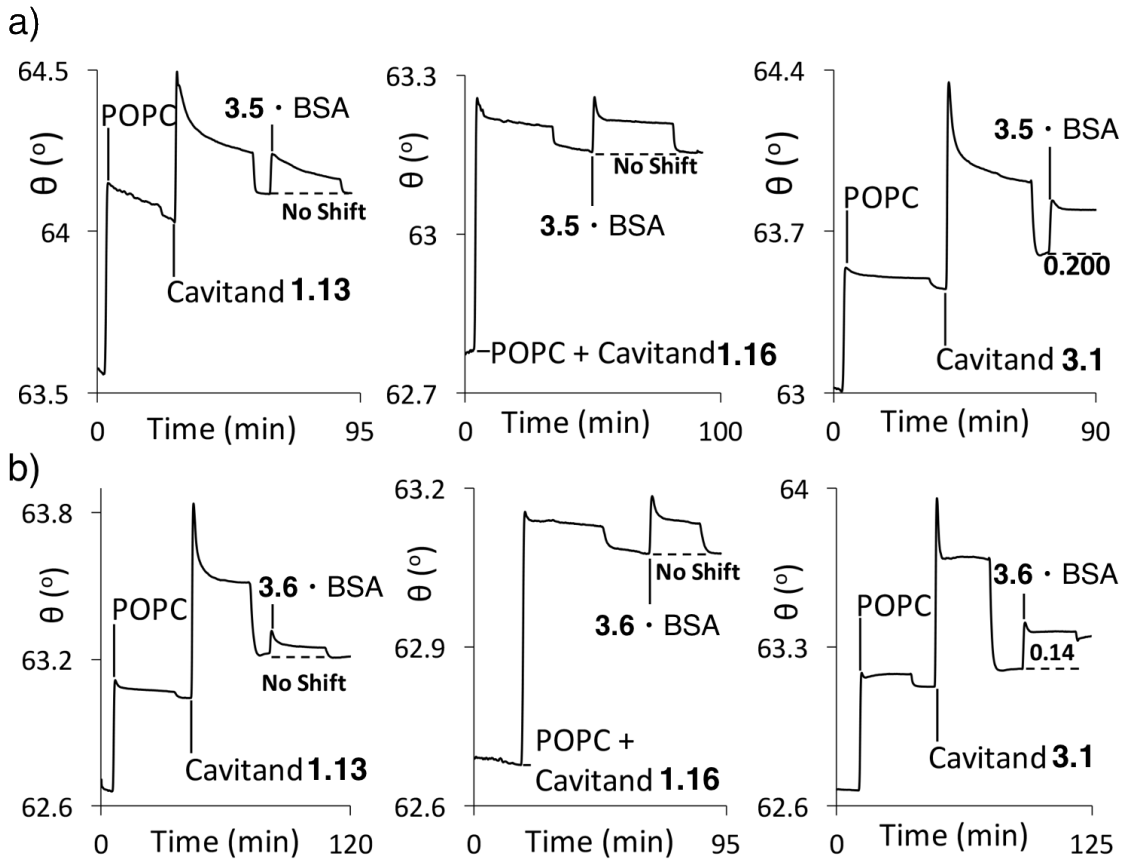

Figure 3.17: SPR sensorgrams of the variable interactions of: (b) the **3.5** • BSA conjugate; (c) the **3.6** • BSA conjugate at the POPC interface with cavitands **1.13**, **1.16** and **3.1**. Protein injection medium: 10 mM PBS buffer.

Since guests **3.5** • BSA and **3.6** • BSA both form a 1:1 complex with the host molecule **3.1**, the determination of guest binding affinity (K_d) under saturation mode analysis was possible in order to illustrate the effect of charge matching on the system. Increasing concentrations (0.1-15 μM) of either guest were injected over the POPC • **3.1**

surface and the shift in resonance angle was recorded. The equation $AB_{eq} = AB_{max}(1/(1 + \frac{K_d}{[A]})$ was applied, where AB_{eq} is the average response obtained for guest binding and [A] is the concentration of guest injection. AB_{max}/AB_{eq} was plotted against 1/[A], where the slope is equivalent to K_d, and so dissociation constants were obtained for **3.5** • BSA and **3.6** • BSA (Figure3.18). A K_d of 0.29 $\pm$ 0.01 μM was afforded for guest **3.5** • BSA, while a K_d of 1.1 $\pm$ 0.01 μM was observed for **3.6** • BSA. These measurements illustrate the correlation between the qualitative changes in resonance angle change and binding affinity; a larger change signifies larger binding affinity. The affinities observed for these guests are similar to those of NMe_3^+-derivatized macromolecules for host **1.13**, which are on the order of micromolar.

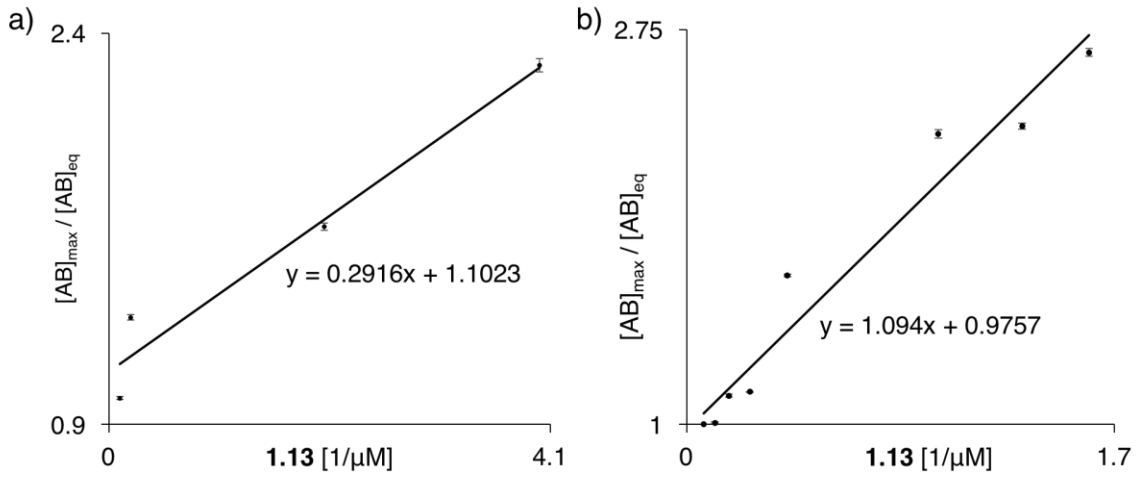

Figure 3.18: Binding affinity (K_d) determination using saturation mode analysis of increasing concentrations (0.1-15 μM) of guests a) **3.5** • BSA and b) **3.6** • BSA. AB_{max}/AB_{eq} was plotted against **1.13**[1/μM] and where the slope is equivalent to K_d.

3.5 Selective Recognition *via* Cavitand Arrays

The tunable, selective recognition of proteins by variably functionalized cavitands in POPC supported lipid bilayers can be applied to array-based detection. Through microarray technology, we can build individual, separated corrals, each containing membrane bilayer environments. The array system can be utilized for high throughput analyte sensing, although the reproducible construction of bilayer arrays has proven to be challenging.[16] Small molecule hosts have not been previously studied in membrane bilayer arrays. SPR imaging (SPRi)[21] was utilized in order to visualize the adhesion events occurring at the arrayed surface. SPRi analysis would allow us to detect guest binding of arrayed, cavitand-impregnated SLB.

The membrane corrals (800 X 800 μm) can be fabricated on calcinated silicate chips by conventional cleanroom lithographic procedures. Trehalose vitrified POPC vesicles were utilized to form SLB arrays.[22] The membrane environment was deposited using a high precision nanoliter delivery system, allowing the individual wells to be properly segregated from one another. The SLB arrays were dried before being placed on the SPRi flowcell, where they were rehydrated before incorporating the desired cavitand (**1.13** or **3.1**) by injection into the system. After cavitand incubation and rinsing, protein was injected, incubated and washed. Using SPRi software, areas on each array spot were selected for analysis. SPRi sensorgrams were generated by averaging the signal of the selected spots. For clarity, each chip was arrayed with a single type of cavitand (**1.13** or **3.1**). A cooled 12-bit CCD camera was mounted to capture images of the surface in order to visualize the binding events. Surface adhesion can be visualized by the lightening of the

array spots on the SPRi chip while no change in the shade of the spots indicates no binding (Figure 3.19). Difference images (displaying a black background) allow for maximized visibility and were also taken in our experiments.

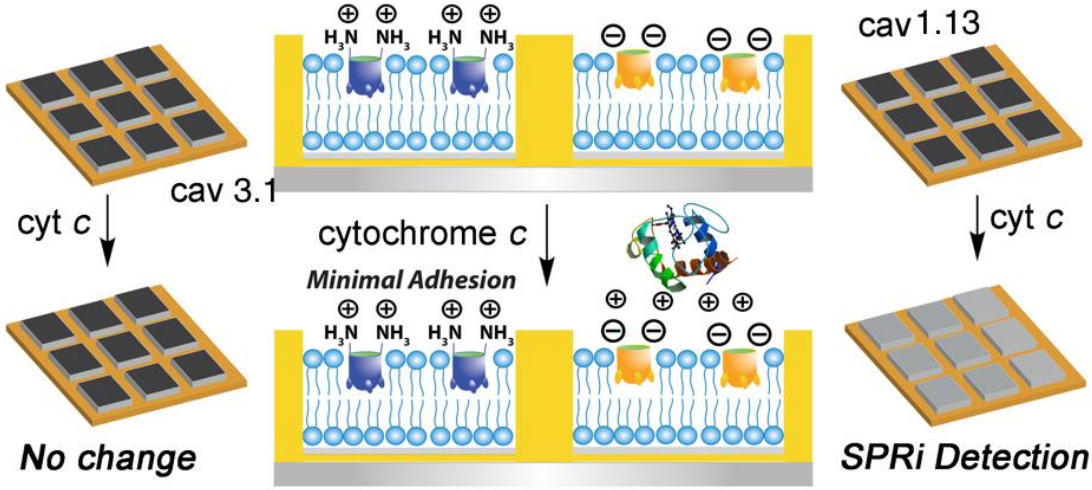

Figure 3.19: Selective charge-based native protein recognition in SLB array.

The interaction of cationic proteins with our synthetic hosts were visualized using SPRi as well. Cytochrome *c* was injected into an arrayed system containing either **1.13** or **3.1** (Figure 3.20a and 3.20b respectively). As expected, after incubation and rinsing, cytochrome *c* was immobilized by the POPC•**1.13** arrayed surface. This result was visually confirmed by the lightening of the array spots, which are indicative of a change in resonance angle at the surface and therefore confirm the adhesion event. The difference image obtained also confirms this result (Figure 3.20a). The arrayed POPC • **3.1** surface failed to adhere cytochrome *c* after its injection, incubation and rinsing. Due to repulsions

with the rim, cationic **3.1** fails to bind the protein and does not display a change in resonance angle via SPRi. As can be seen in Figure 3.20b, there is no change in the shade of the array spots and the difference image shows no change either. These results were reproduced with a different cationic protein, trypsin. As can be seen in Figure 3.21, due to repulsions, no SPRi signal was observed in the presence of cavitand **3.1** while an evident change is observed in the presence of **1.13**.

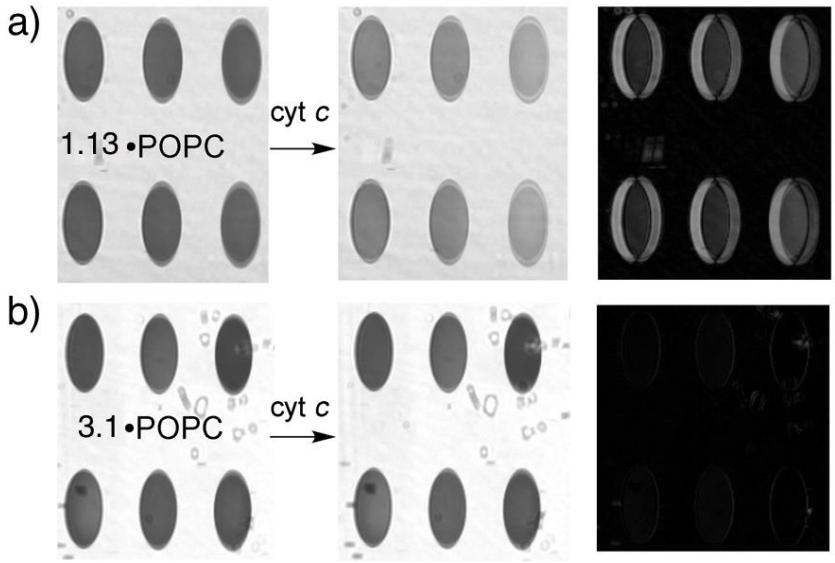

Figure 3.20: SPRi difference images of the interactions of b) cytochrome *c* and POPC•**1.13** array surface and c) cytochrome *c* and POPC•**3.1** array surface.

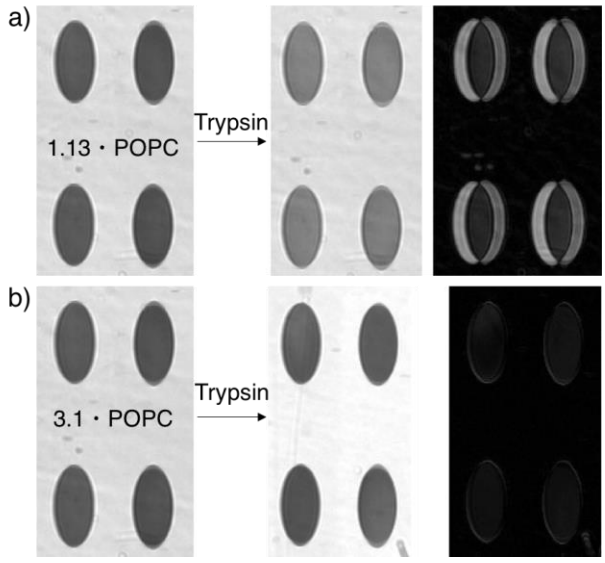

Figure 3.21: SPRi and difference images of the interactions of a) trypsin and the POPC•**1.13** array surface and b) trypsin and the POPC•**3.1** array surface.

The dual-mode binding recognition was also visualized using SPRi. The adhesion of streptavidin by the POPC • **3.1** • **3.3** surface was evident by the large change in signal on the SPRi sensorgram, including the second binding event during the rinsing process (Figure 3.22a). The SPRi images of the arrayed surface also show a change in the shade of the membrane corrals, establishing SPRi as a plausible analytical tool for dual-mode binding recognition of proteins, although not as efficient as native protein recognition. The SPRi sensorgrams confirmed our previous studies, showing that cavitand **3.1** does not bind guest **3.3** due to a charge mismatch between the rim of the cavitand and the cationic amine on the guest (Figure 3.22b). The inability to immobilize streptavidin on the surface was evident by the enduring shade of the array spots, even after guest and protein injections.

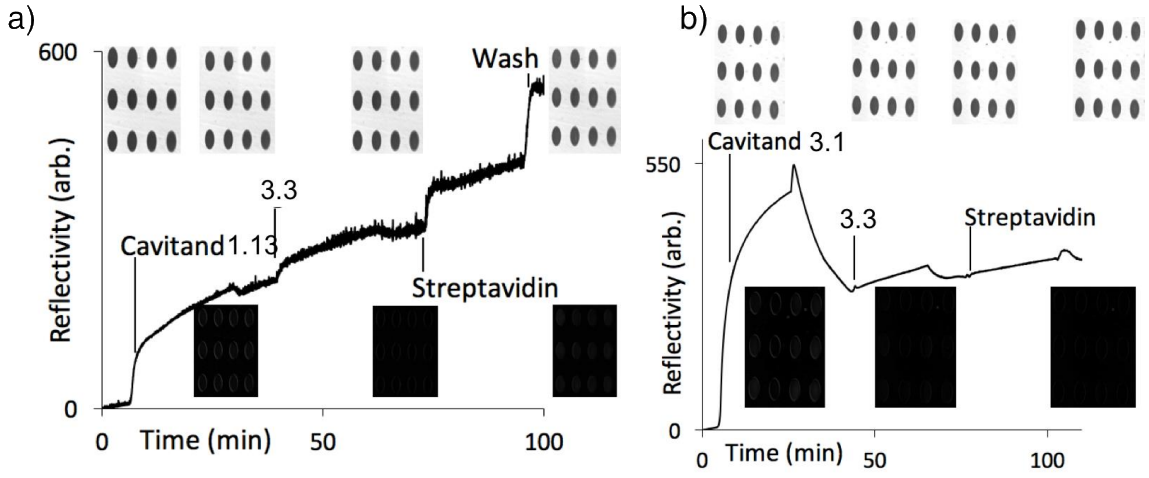

Figure 3.22: a) Mean SPR sensorgram of the array spots showing immobilization of streptavidin in 10 mM PBS by the POPC • **1.13** • **3.3** array surface.

3.6 Conclusion

The binding versatility of cavitands in supported lipid bilayers was demonstrated by their dual-mode binding abilities. The variety of host:guest interactions can be multiplied by synthesizing cavitands that display varying charges on their upper rim. Both the upper rim and the cavity of the host can be exploited in order to allow selective, tailored molecular recognition by varying mechanisms. By combining both recognition elements in a single guest molecule, their selectivity can be greatly enhanced. These guests can be utilized to bind larger structures such as proteins, or be covalently attached to immobilize the protein directly. Each recognition mechanism is selective and the mismatched upper rim interactions can outcompete the highly favorable interactions between the cavity and R-NMe_3^+ species. Previous studies showed that cavitands were highly selective for R-NMe_3^+ groups; adding a second component to their recognition allows for discrimination

between guests that display identical R-NMe_3^+ binding handles. This recognition system can also be applied to SLB array systems and can be visualized in real time using SPRi. Utilizing this recognition system would allow for the construction of complex cell membrane-mimicking environments with multiple components utilizing cavitands.

3.7 References

1. Brunsveld, L.; Kuhlmann, K.; Alexandrov, K.; Wittinghofer, A.; Goody, R. G.; Waldmann, H. "Lipidated Ras and Rab peptides and proteins - Synthesis, Structure, and Function." *Angew. Chem. Int. Ed.,* **2006**, *45*, 6622−6646.

2. Nodolski, M. J.; Linder, M. E. "Protein lipidation." *FEBS Journal.,* **2007**, *274*, 5202–5210.

3. Boonyarattanakalin, S.; Martin, S. E.; Dykstra, S. A.; Peterson, B. R. "Synthetic Mimics of Small Mammalian Cell Surface Receptors." *J. Am. Chem. Soc.,* **2004**, *126*, 16379−16386.

4. Zope, H. R.; Versluis, F.; Ordas, A.; Voskuhl, J.; Spaink, H. P.; Kros, A. "In Vitro and In Vivo Supramolecular Modification of Biomembranes Using a Lipidated Coiled-Coil Motif." *Angew. Chem., Int. Ed.,* **2013**, *52*, 14247−14251.

5. Godula, K.; Rabuka, D.; Nam, K. T.; Bertozzi, C. R. "Synthesis and Microcontact Printing of Dual End-Functionalized Mucin-like Glycopolymers for Microarray Applications." *Angew. Chem., Int. Ed.,* **2009**, *48*, 4973−4976.

6. Rabuka, D.; Forstner, M. B.; Groves, J. T.; Bertozzi, C. R. "Noncovalent Cell Surface Engineering: Incorporation of Bioactive Synthetic Glycopolymers into Cellular Membranes." *J. Am. Chem. Soc.*, **2008**, *130*, 5947−5953.

7. Groves, J. T.; Mahal, L. K.; Bertozzi, C. R. "Control of Cell Adhesion and Growth with Micropatterned Supported Lipid Membranes." *Langmuir*, **2001**, *17*, 5129−5133.

8. Ghang, Y.-J.; Perez, L.; Morgan, M. A.; Si, F.; Hamdy, O. M.; Beecher, C. N.; Larive, C. K.; Julian, R. R.; Zhong, W.; Cheng, Q.; Hooley, R. J. "Anionic Deep Cavitands Enable the Adhesion of Unmodified Proteins at a Membrane Bilayer." *Soft Matter*., **2014**, *10*, 9651–9656.

9. Perez, L.; Mettry, M.; Caulkins, B. G.; Mueller, L. J.; Hooley, R. J. "Lipid Bilayer Environments Control Exchange Kinetics of Deep Cavitand Hosts and Enhance Disfavored Guest Conformations." *Chem. Sci.*, **2018**, *9*, 1836-1845.

10. Ghang, Y.-J.; Lloyd, J.; Moehlig, M.; Arguelles, J.; Mettry, M.; Zhang, X.; Julian, R.; Cheng, Q.; Hooley, R. J. "Labeled Protein Reconition at a Membrane Bilayer Interface by Embedded Synthetic Receptors." *Langmuir*., **2014**, *30*, 10161-10166.

11. Hof, F.; Trembleau, L.; Ullrich, E. C.; Rebek, J. Jr. “Acetylcholine Recognition by a Deep, Biomimetic Pocket.” *Angew. Chem., Int. Ed.*, **2003**, *42*, 3150–3153.

12. Liu, Y.; Perez, L.; Mettry, M.; Gill, A. D.; Byers, S. R.; Easley, C. J.; Bardeen, C. J.; Zhong, W.; Hooley, R. J. “Site Selective Reading of Epigenetic Markers by a Dual-Mode Synthetic Receptor Array.” *Chem. Sci.*, **2017**, *8*, 3960–3970.

13. Liu, Y.; Liao, P.; Cheng, Q.; Hooley, R. J. “Protein and Small Molecule Recognition Properties of Deep Cavitands in a Supported Lipid Membrane Determined by Calcination-Enhanced SPR Spectroscopy.” *J. Am. Chem. Soc.*, **2010**, *132*, 10383–10390.

14. Soberats, B.; Sanna, E.; Martorell, G.; Rotger, C.; Costa, A. “Programmed Enzyme-Mimic Hydrolysis of a Choline Carbonate by a Metal-Free 2-Aminobenzimidazole-Based Cavitand.” *Org. Lett.*, **2014**, *16*, 840-843.

15. Ballester, P.; Shivanyuk, A.; Rafai Far, A.; Rebek, J. Jr. “A Synthetic Receptor for Choline and Carnatine.” *J. Am. Chem. Soc.*, **2002**, *124*, 14014–14016.

16. Hinman, S. S.; Ruiz, C. J.; Drakakaki, G.; Wilkop, T. E.; Cheng, Q. “On-Demand Formation of Supported Lipid Membrane Arrays by Trehalose-Assisted Vesicle Delivery for SPR Imaging.” *ACS Appl. Mater. Interfaces*., **2015**, *7*, 17122–17130.

17. Biros, S. M.; Ullrich, E. C.; Hof, F.; Trembleau, L.; Rebek, J. Jr. “Kinetically Stable Complexes in Water: The Role of Hydration and Hydrophobicity.” *J. Am. Chem. Soc.*, **2004**, *126*, 2870–2876.

18. Trembleau, L.; Rebek, J. Jr. “Helical Conformation of Alkanes in a Hydrophobic Cavitand.” *Science*., **2003**, *301*, 1219–1220.

19. Ghang, Y.-J.; Lloyd, J. J.; Moehlig, M. P.; Arguelles, J. K.; Mettry, M.; Zhang, X.; Julian, R. R.; Cheng, Q.; Hooley, R. J. “Labeled Protein Recognition at a Membrane Bilayer Interface by Embedded Synthetic Receptors.” *Langmuir*, **2014**, *30*, 10161–10166.

20. Perez, L.; Ghang, Y.-J.; Williams, P. B.; Wang, Y.; Cheng, Q.; Hooley, R. J. “cell and Protein Recognition at a Supported Lipid Bilayer Interface via *In Situ* Cavitand-Mediated Functional Polymer Growth.” *Langmuir*, **2015**, *31*, 11152–11157.

21. Wilkop, T.; Wang, Z. Z.; Cheng, Q. “Analysis of Mu-Contact Printed Protein Patterns by SPR Imaging with a LED Light Source.” *Langmuir*, **2004**, *20*, 11141−11148.

22. Hinman, S. S.; Ruiz, C. J.; Drakakaki, G.; Wilkop, T. E.; Cheng, Q. "On-Demand Formation of Supported Lipid Membrane Arrays by Trehalose-Assisted Vesicle Delivery for SPR Imaging." *ACS Appl. Mater. Interface*s., **2015**, *7*, 17122-17130.

Chapter 4: Cell and Protein Recognition at a Supported Lipid Bilayer Interface via *In Situ* Cavitand-Mediated Functional Polymer Growth

4.1 Introduction

Water-soluble deep cavitands have the ability of adhering molecules ranging in size from small, such as choline,[1,2,3] to larger biomolecules like proteins while embedded in supported lipid bilayers.[4,5,6] In order to effectively bind large macromolecules at the water:membrane interface, a large surface area is needed for good affinity. Polymeric structures on the cell surface play crucial roles in protection and communication, and often these polymers incorporate recognition motifs that allow for cell signaling, transport and adhesion events.[7,8] There are multiple examples of synthetic polymers used for recognition in both cellular[9,10,11] and synthetic membrane environments.[12,13,14] These recognition motifs are often built by covalently attaching a preformed polymer to lipids found in bilayers, vesicles or cells. The limitation for such structures, however, is their solubility in aqueous environments. To avoid the synthetic challenge of forming a functional polymer and introducing it to a membrane environment, *in situ* polymerization can be applied.

Atom transfer radical polymerization (ATRP)[15,16] is a mild way of forming a polymer *in situ*. Cavitand-mediated polymer growth via this method is possible at a supported lipid bilayer (SLB) by the noncovalent recognition and display of a suitable ATRP initiator.[17,18] By derivatizing an alkyl halide ATRP initiator with the ($-R\text{-}NMe_3^+$) cavitand binding handle, guest **1.17** is obtained and is able to facilitate polymerization at a SLB surface. ATRP is tolerant to aqueous conditions and can be performed without damaging the supported lipid bilayer, making it ideal for membrane environments. By

varying the monomers used for ATRP, different functionalities can be imparted to the surface. Hydrophobic poly(methyl methacrylate) (MMA), hydrophilic poly(2-hydroxyethyl methacrylate) (HEMA) and bioadhesive poly(biotin-2-aminoethyl methacrylate) (biotin-AEMA) were all formed using cavitand-anchored ATRP at a SLB (Figure 1.13).[17] The scope of this method is limited to small monomers: larger, more functionalized polymers were not formed due to solubility issues in buffered aqueous solution. Highly water-soluble saccharide-linked methacrylates showed weaker affinity for the cavitands in the bilayer and were easily washed away from the surface. These issues limit the formation of functional polymers with interesting properties. A solution to this dilemma would be to functionalize the freshly formed polymer *in situ* and impart it with bioadhesive properties. There are a multitude of methods to post-synthetically modify poly(HEMA),[15] however these methods are not amenable to aqueous environments. An amine-functionalized polymer would be the ideal candidate for post-synthetic modification, although there are many challenges in forming such a structure.

4.2 Forming an Amine-Functionalized Polymer

An amine-functionalized polymer is desirable due to its nucleophilic nature. Primary amines are capable of performing a wide variety of reactions, and are commonly used in biomolecule derivatizations.[19] The ability of amines to function and react in aqueous environments is also a benefit since the cavitand-impregnated SLB is in an aqueous setting. The amine functionality would allow for the tailoring of the polymer to immobilize biorelevant targets, which could lead to the possibility of creating complex cell

surface mimics. There are few known examples of bioorthogonally reactive species that are tolerant to the bilayer environment,[19] and since amines are one of them, this group was selected to decorate our polymer.

Polymer formation on the membrane surface is promoted by anchoring trimethylammonium-tagged initiator **1.17** via cavitand **1.13** to the supported lipid bilayer, exposing the initiator's reactive end at the water:bilayer interface. Subsequent injection of a mixture of suitable monomer and CuBr•bipy catalyst forms the polymer (Figure 4.1). The polymer formed extends from the supported lipid bilayer and is held in place by multiple noncovalent contacts between the initiator and the cavitand embedded in the SLB. Aminoethyl methacrylate (AEMA) **4.1** is the monomer used to form an amine-functionalized polymer. The formation of the membrane surface and its components are monitored using surface plasmon resonance (SPR) spectroscopy.[20,21]

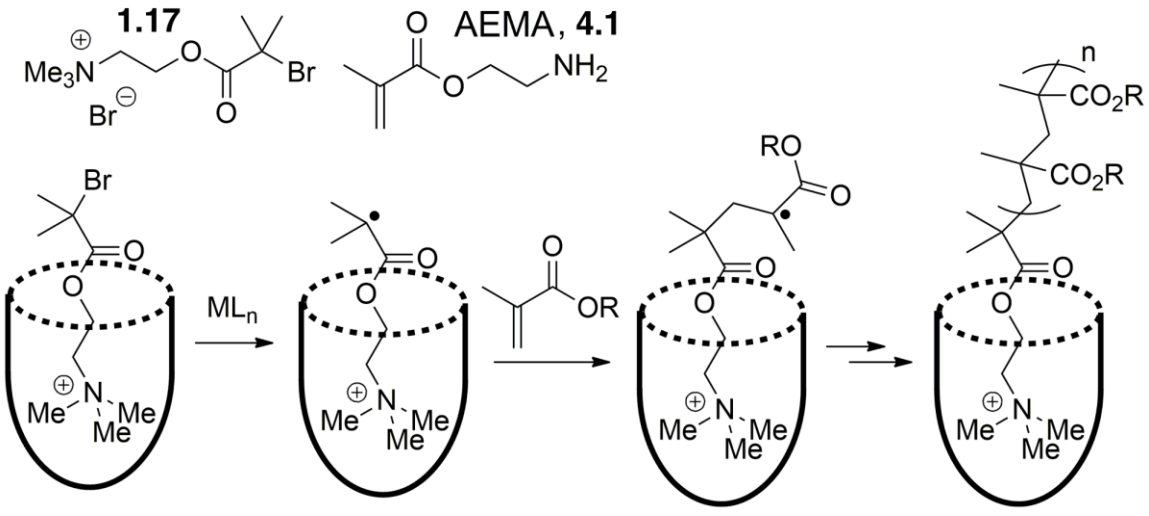

Figure 4.1: Initiator guest, **1.17** and AEMA monomer **4.1** and a representation of the ATRP process.

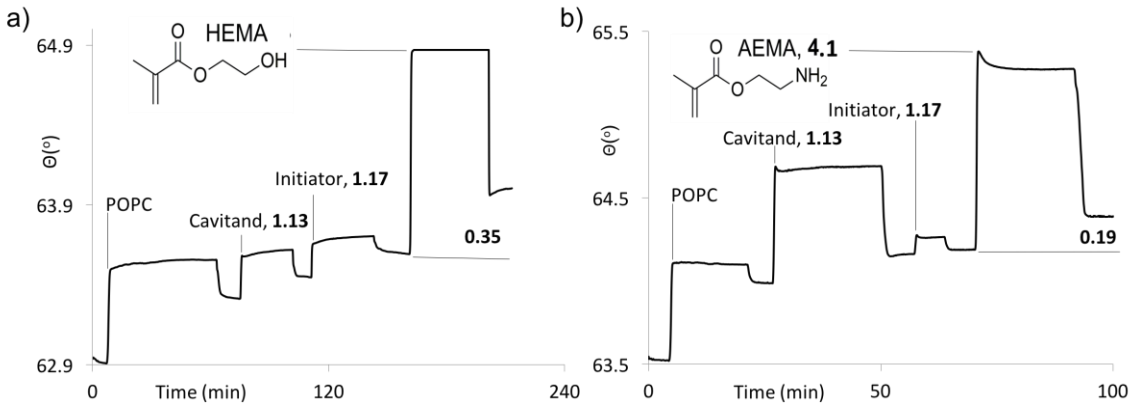

Figure 4.2: *In situ* ATRP polymer formation of a) poly(HEMA) and b) poly(AEMA).

Due to their strong coordination to metals, amines are not well suited for ATRP. ATRP utilizes a transition metal catalyst, which AEMA **4.1** is able to leach off and cause high polydispersity and turnover numbers. Because of this, ATRP does not function efficiently in the formation of amine polymers.[15,16] Using the catalyst conditions for previously formed polymers,[17] an AEMA polymers was successfully grown on our membrane surface (Figure 4.2a). The growth of the AEMA polymer was not as efficient when compared to previously established poly(HEMA) (Figure 4.2b). Fortunately, a large polymer is not needed for the purposes of the desired studies. Narrow polydispersities are unimportant and a small reactive polymer patch is all that is needed to allow for *in situ* reactivity at the bilayer surface. The polymerization of AEMA **4.1** was investigated further in order to optimize the conditions for optimal growth. Although a large polymer is not needed, the capabilities of this polymer and its formation are not well known and their investigation was undertaken.

4.3 Amine Polymer Growth Optimization

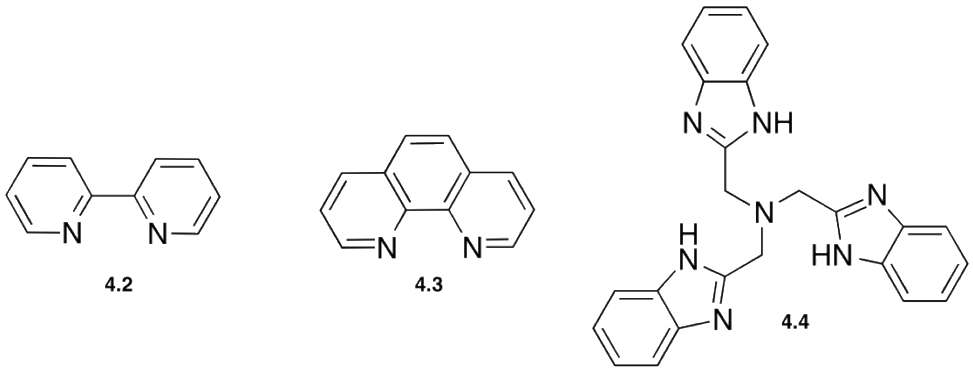

Figure 4.3: Ligands used for the transition metal catalyst optimization of AEMA polymerization: 2,2-bipyridine (bipy) **4.2**, 9,10-phenantrholine (phen) **4.3**, and tris(benzimidazole)-triethyleneamine (tbte) **4.4**.

Since amines are poor substrates for ATRP, the catalyst system was varied to find a metal:ligand complex that would facilitate polymerization and minimize catalyst leaching. There are multiple catalysts capable of ATRP using methacrylate monomers.[15] In the cavitand-anchored formation of polymers performed by Liu et. al., CuBr•bipy is the transition metal catalyst used. Combinations of three ligands, 2,2-bipyridyl (bipy) **4.2**, 9,10-phenanthroline (phen) **4.3**, and tris(benzimidazole)triethyleneamine (tbte) **4.4**, and two metal salts ($FeCl_2$ and CuBr) were tested for ATRP effectiveness (Figure 4.3) and ascorbic acid was added to the catalyst system as a reductant. Phen **4.3** and bipy **4.2** are both bidentate and therefore coordinate to the metal catalyst in a similar manner. Ligands **4.2** and **4.3** are more weakly coordinating than tbte **4.4**. Ligand **4.4** can occupy four

coordination sites on the metal center, competing with and potentially limiting the coordination of AEMA, therefore preventing inactivation due to catalyst leaching. The polymerization was performed by injecting a 0.7 M solution of AEMA monomer along with 15 mM catalyst complex (1:2 ligand:metal ratio) in 10 mM phosphate buffered saline (PBS). The amount of polymerization was observed via SPR as the change in resonance angle after washing away any unreacted monomer.

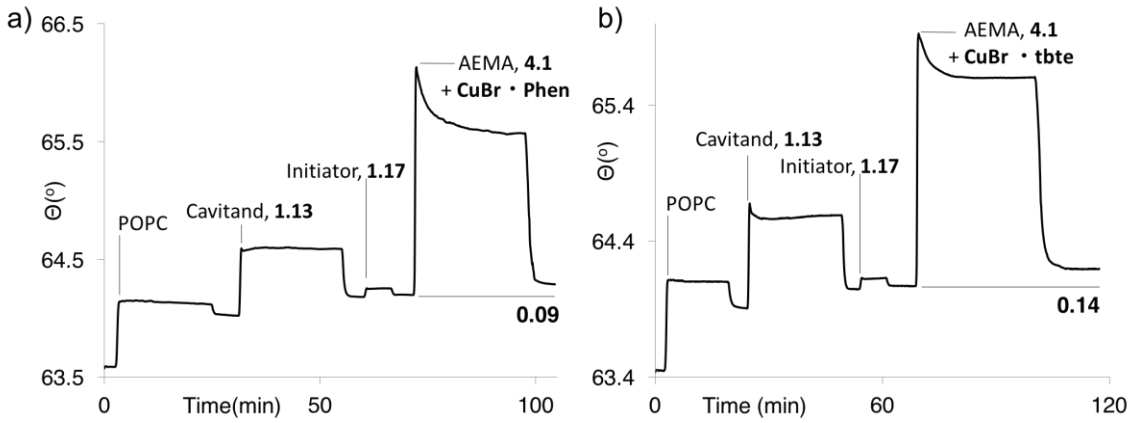

Figure 4.4: SPR sensorgrams of the polymerization of AEMA utilizing the catalyst: a) CuBr•phen and b) CuBr•tbte.

The typical resonance angle shift observed when using the established CuBr•Bipy catalyst system was approximately $\Delta\theta = 0.19°$ (Figure 4.2b). Using CuBr as the transition metal, the ligand was varied to see the effect on AEMA polymerization. Interestingly, the CuBr•phen and CuBr•tbte catalysts were less effective than CuBr•bipy (Table 4.1). This was unexpected since the CuBr complex with bidentate **4.3** gave a resonance angle shift of

0.09°, much lower than that of CuBr•bipy (Figure 4.4a). The more tightly coordinated CuBr•tbte displayed a low shift as well ($\Delta\theta = 0.14^{o}$), making CuBr•bipy the preferred catalyst system when utilizing copper (Figure 4.4b). The metal salt was also varied to $FeCl_2$. Due to the lower toxicity of Fe(II), $FeCl_2$ can be beneficial for the application of this method in biological systems. $FeCl_2$ was as effective as CuBr in catalyzing the polymerization of AEMA **4.1**. Relative to the copper salt, $FeCl_2$ provided a smaller variation between the three different ligands used (Table 4.1). The most effective iron complex was $FeCl_2$•phen, giving an SPR resonance angle change of 0.20^{o} (Figure 4.5b), this is comparable to the original CuBr•bipy system. Using ligands **4.2** and **4.4** with the $FeCl_2$ salt gave comparable results, although not as efficient at those in the presence of ligand **4.3** (Figure 4.5). Although the polymerization of **4.1** was not improved, a new catalyst system compatible to biological environments was established.

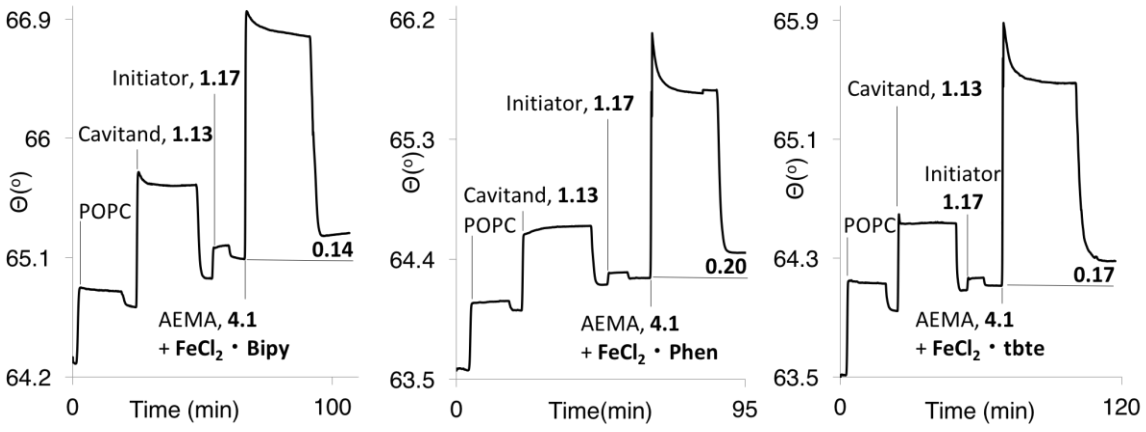

Figure 4.5: SPR sensorgrams of the polymerization of AEMA utilizing different catalysts: a) $FeCl_2$•bipy; b) $FeCl_2$•phen and c) $FeCl_2$•tbte.

Table 4.1: Variation of metal salt and ligand of the ATRP transition metal catalyst for optimization of poly(AEMA) growth.

Ligand	ΔΘ, L•CuBr (^{o})	ΔΘ, L•$FeCl_2$ (^{o})
2,2'- bipyridyl (Bipy), **4.2**	0.20 ± 0.03	0.14 ± 0.03
1,10-phenanthroline (Phen), **4.3**	0.09 ± 0.01	0.20 ± 0.01
Tris(benzimidazole)triethyleneamine (tbte), **4.4**	0.14 ± 0.02	0.17 ± 0.02

Other variables were tested in the optimization process including monomer concentration, incubation time as well as initiator-monomer ratio. Varying the concentration of monomer injected into the system did not greatly affect the size of poly(AEMA) formed. A 0.7 M solution of monomer **4.1** produced a 0.19^o resonance angle shift (Figure 4.2b). The polymerization was not increased even in the presence of a large excess of monomer with respect to bound initiator. The concentration of **4.1** was further varied in increments from 0.7 M to 1.4 M, however, no appreciable difference in resonance angle was observed upon polymerization (Figure 4.6). Next, the monomer incubation time was altered in hopes of improving the polymerization. The standard incubation time is 20 minutes and it was increased to 60, then 90 minutes. Once again, no appreciable increase in polymerization was observed as the resonance angle shift observed was similar to that of a 20 minute incubation (Figure 4.7). These results hinted to the relatively rapid catalyst inactivation due to the coordinating and reducing nature of AEMA.

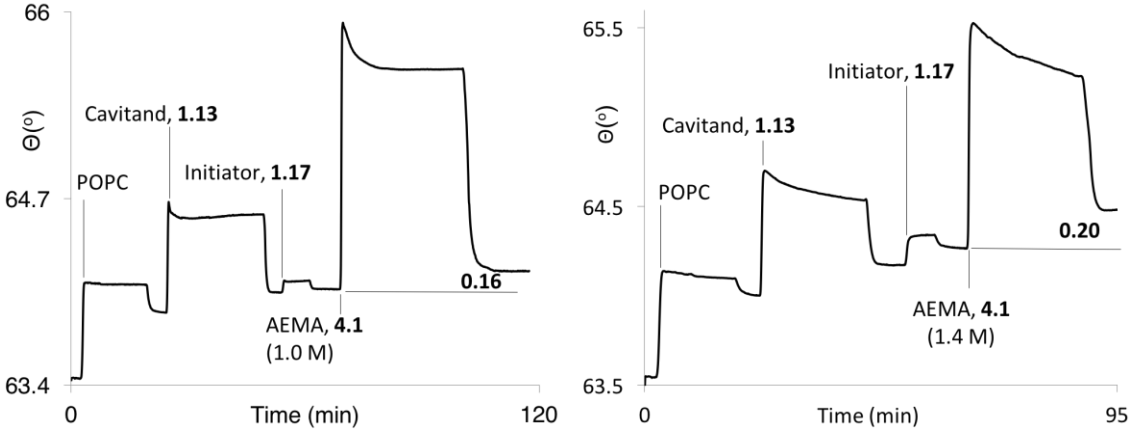

Figure 4.6: SPR sensorgrams of the injection of varying AEMA **4.1** concentrations for the optimization of polymerization on the SLB.

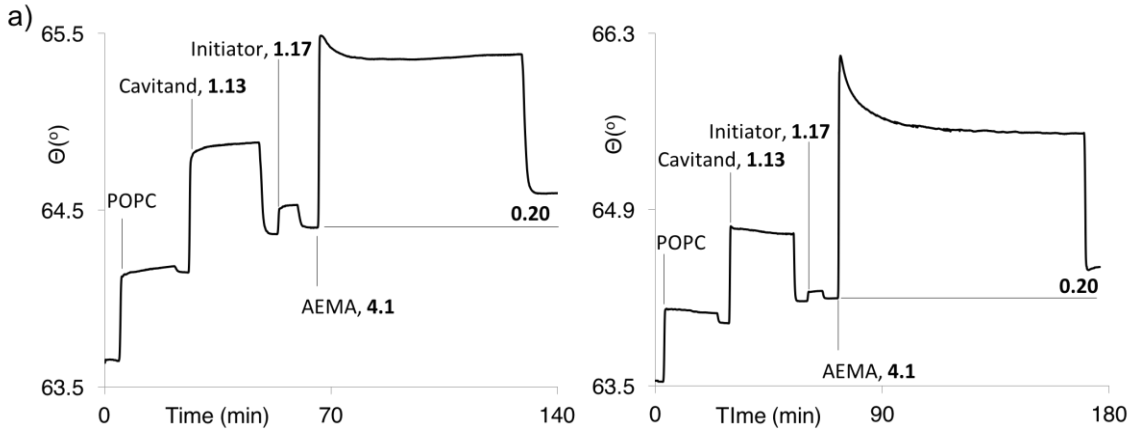

Figure 4.7: Cavitand-mediated ATRP of AEMA **4.1** with incubation times of a) 60 minutes and b) 90 minutes.

Altering the concentration of initiator **1.17** from 15 mM also failed at improving the size of poly(AEMA) (Figure 4.8a). The cavitand host **1.13** is believed to be saturated with initiator before ATRP due to the dissociation constant of (-$RNMe_3^+$) guests in a POPC

bilayer being on the order of micromolar.[5] Although it is difficult to determine the exact concentration of cavitand **1.13** embedded in the membrane, studies of vesicles preloaded with 2% cavitand gave a similar amount of guest recognition as injecting the typical 0.7 g/mL **1.13**.[4] Increasing the concentration of injected cavitand from 0.7 mg/mL to 2 mg/mL did not help increase AEMA **4.1** polymerization (Figure 4.8b). Finally, the living nature of the AEMA polymerization was tested. ATRP is a living polymerization and allows further polymer growth when additional monomer and catalyst are injected into the system.

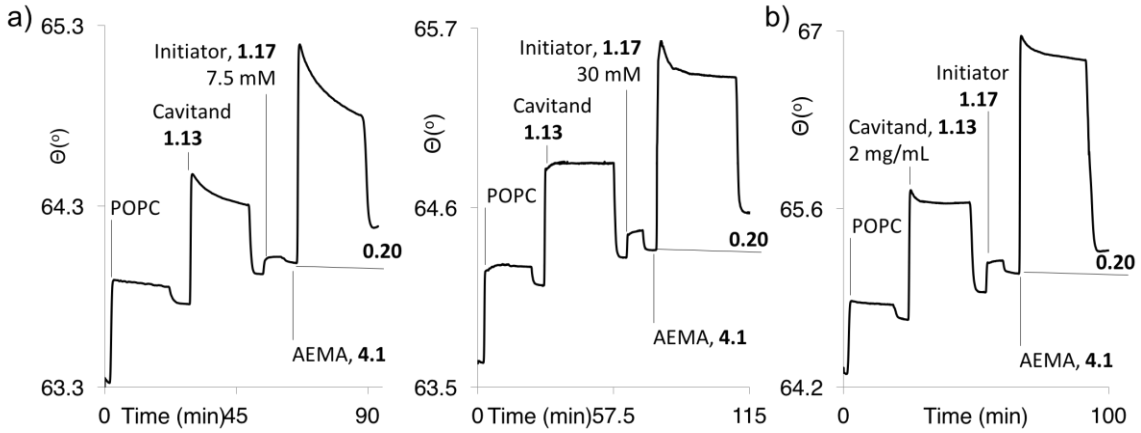

Figure 4.8: Cavitand-mediated ATRP of AEMA **4.1** with a) varying initiator **1.17** concentrations and b) cavitand **1.13** concentration of 2 mg/mL.

Previously, the ATRP of HEMA displayed living characteristics in a bilayer environment, the size of poly(HEMA) increased multiple times following monomer injections.[17] This process was not successful for AEMA **4.1**. After the initial polymerization, subsequent injections of monomer **4.1** and catalyst were introduced but no

observable increase in resonance angle was observed by SPR analysis (Figure 4.9). The amine groups not only inactivate the catalyst mixture after initial reaction, they also terminate the living polymerization process and therefore limit further reaction at the membrane surface. This inactivation event limits the polymerization of AEMA to the formation of microscale polymer patches.

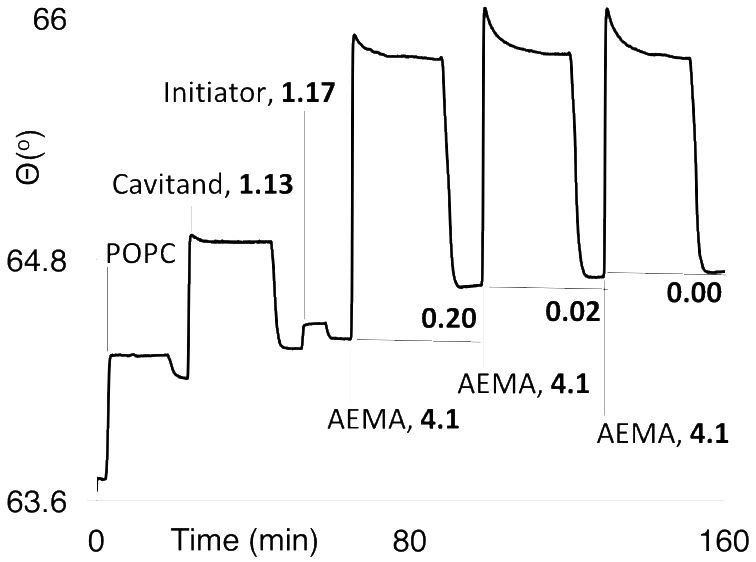

Figure 4.9: Testing of the living polymerization abilities of poly(AEMA).

Although the polymerization is consistent, there is variation in the polymer size between individual runs. Based on SPR response, there is a resonance angle change variation of $\pm 0.04^{o}$. Although the polymerization was not successfully optimized to increase the size of the amine-functionalized structure, the thin polymer layer formed is perfectly suited for further derivatization at the bilayer interface. There was also no

observed disruption of the membrane upon polymerization and the surface is now decorated with multiple primary amine groups ready for derivatization. To establish the functionality of poly(AEMA), several *in situ* reactions were explored.

4.4 Reacting and Visualizing the Amine Polymer

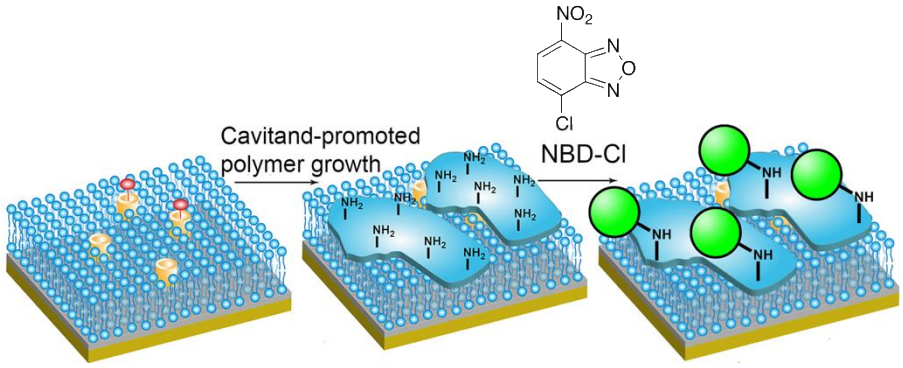

Figure 4.10: Cavitand-promoted aminopolymer growth followed by *in situ* functionalization.

The *in situ* reactivity of poly(AEMA) was tested using amine-reactive 4-chloro-7-nitrobenzofurazan (NBD-Cl) (Figure 4.10). The use of this reagent provided the added advantage of an alternate method for characterizing the polymer. SPR provides evidence of polymerization at the SLB surface, but other methods are not amenable to our membrane system. Poly(AEMA) cannot be isolated for postsynthetic characterization. Removing the polymer from the surface by washing is not possible and surface analysis techniques such as X-ray Photoelectron Spectroscopy (XPS) or Infrared Spectroscopy (IR) are not applicable to the complex lipid bilayer environment. Mass spectrometry (MS) analysis is

also not an option for the characterization of poly(AEMA). It is possible to strip the bilayer from the surface along with the cavitand and polymer, but the presence of the charged POPC lipids complicates and renders MS analysis useless. NBD-Cl fluoresces upon reaction with amines, therefore, upon *in situ* reaction it imparts fluorescent properties onto poly(AEMA).

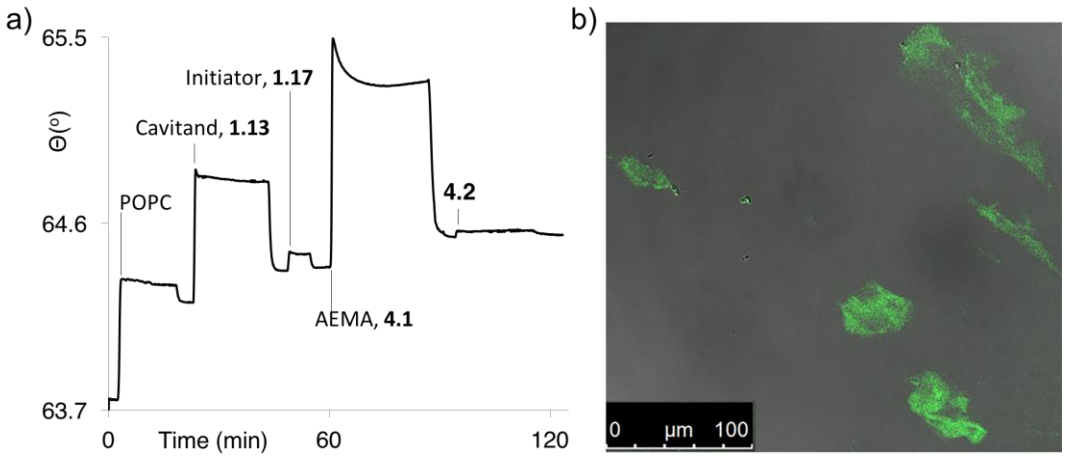

Figure 4.11: a) SPR sensorgram of the aminopolymer reaction with NBD-Cl; b) Confocal microscopy image of the dyed polymer at the membrane surface.

After polymer formation on the cavitand-impregnated SLB surface, a 1 mg/mL NBD-Cl aqueous solution was introduced into the system. The fluorophore was incubated for 20 minutes before washing off any excess NBD-Cl. A small resonance angle change was observed, which was consistent with the reaction of poly(AEMA) and the low molecular weight NBD-Cl (Figure 4.11a). In order to verify the *in situ* functionalization of poly(AEMA), confocal microscopy studies of the fluorescent surface were performed. The calcinated gold chip containing the functionalized SLB surface was carefully removed

from the flow cell before confocal microscopy analysis. Confocal microscopy analysis revealed the presence of individual fluorescent patches, indicating successful derivatization of the poly(AEMA) surface. These studies not only allowed for the visualization of the polymer, but also quantitation of the polymer patch sizes (Figure 4.11b). The poly(AEMA) patches vary in size and partially coat the bilayer interface while leaving the membrane surface undisrupted. The ATRP of AEMA **4.1** appears to form discrete, micrometer-sized polymer patches atop the SLB due to the fluid nature of the anchoring cavitand **1.13**, which displays lateral diffusion similar to that of POPC lipids.[22]

While poly(AEMA) displays incomplete surface coverage, the polymerization process is quite variable and different coverage patterns can be observed with different runs. This variability as well as the small size of the patches between experiments is consistent with the inefficient ATRP process of the AEMA **4.1** monomer. It is possible, however, that the reaction with water-sensitive NBD-Cl does not occur to completion with the aminopolymer. Even though a large excess of fluorophore is used for testing, NBD-Cl is poorly water soluble, which could lead to localized reaction at the polymer surface. The formation of poly(AEMA) is far more consistent via SPR analysis than it is through confocal microscopy analysis, indicating variability of polymer patch sizes, though they do form consistently. Compared to poly (AEMA), poly(HEMA) and poly(MMA) provide full, consistent surface coverage due to the more efficient polymerization process of the corresponding monomers.[17]

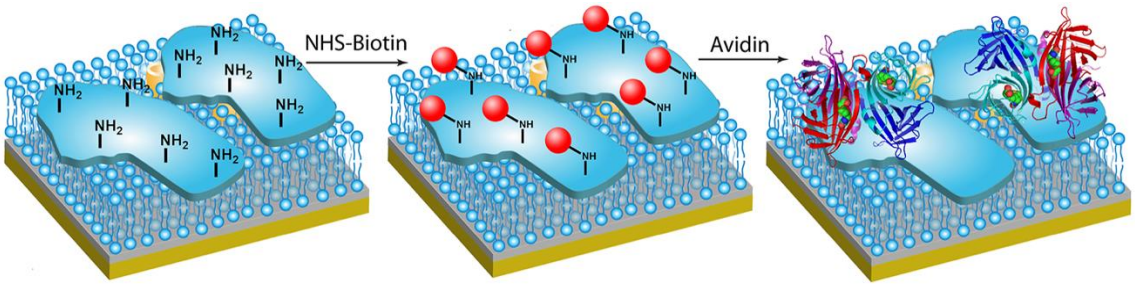

Figure 4.12: The functionalization of poly(AEMA), imparting it with bioadhesive properties, allowing it to perform protein immobilization.

Even though the size of the poly(AEMA) patches is variable, their synthesis is consistent, and this indicates that they are capable of performing *in situ* reactions at the membrane surface. The next step was to investigate whether these functional polymer patches are capable of more challenging *in situ* reactions. As can be seen in Figure 4.12, the poly(AEMA) surface can be imparted with bioadhesive properties through the functionalization with an amine-reactive epitope followed by protein recognition. The amine-functionalized polymer was derivatized with avidin-binding biotin groups through the injection of N-hydroxysuccinimide (NHS)-derivatized biotin atop the surface. As with the NBD-Cl reaction, a small resonance angle change was observed upon reaction of NHS-biotin. A 10% DMSO solution of 1 mg/mL NHS-biotin was injected into the SPR flow cell and incubated before rinsing away any unbound reagent. This was followed by a 1 mg/mL buffered solution of avidin, which was incubated and rinsed to remove any unbound protein. As can be seen in Figure 4.13a, a larger resonance angle change was observed via SPR due to the larger size of the protein ($\Delta\theta = 0.35°$). This indicated that the polymer

successfully immobilized proteins at the surface, confirming its bioadhesive properties. This protein recognition process only occurs when the polymer is functionalized with the biotin epitope. When the process is repeated with underivatized biotin, which is incapable of reacting with the amine-functionalized polymer, no avidin adhesion is observed (Figure 4.13b). Biotin has no affinity for poly(AEMA) under the buffered conditions used for its injection, and is easily washed away after its incubation. There are also no charge-based interactions between the cationic polymer surface and avidin (Figure 4.13c), confirming that the polymer must be reacted in order to impart protein adhesion properties.

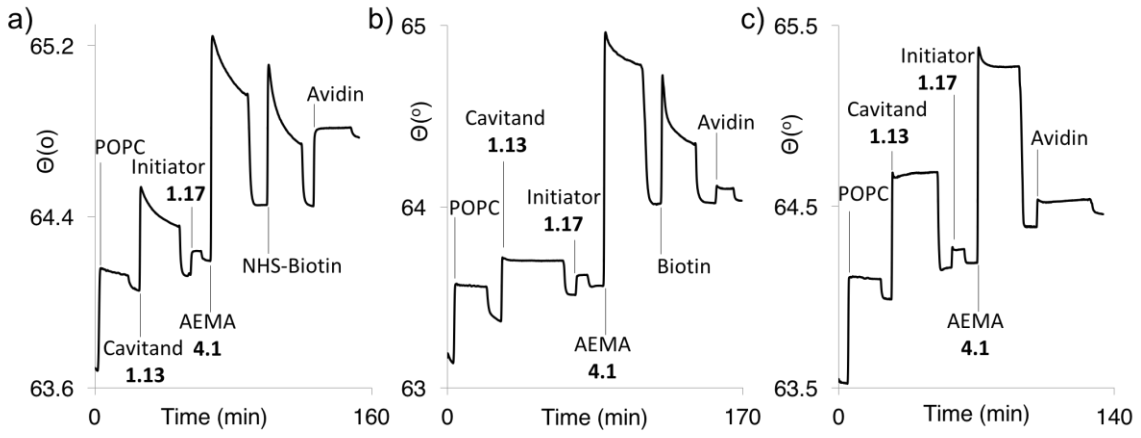

Figure 4.13: SPR sensorgrams of: a) *In situ* recognition of avidin by biotin functionalized poly(AEMA); b) control experiment with unactivated biotin; c) control experiment showing the incompatibility of avidin with unfunctionalized poly(AEMA).

4.5 Cell Adhesion Properties of AEMA Polymer

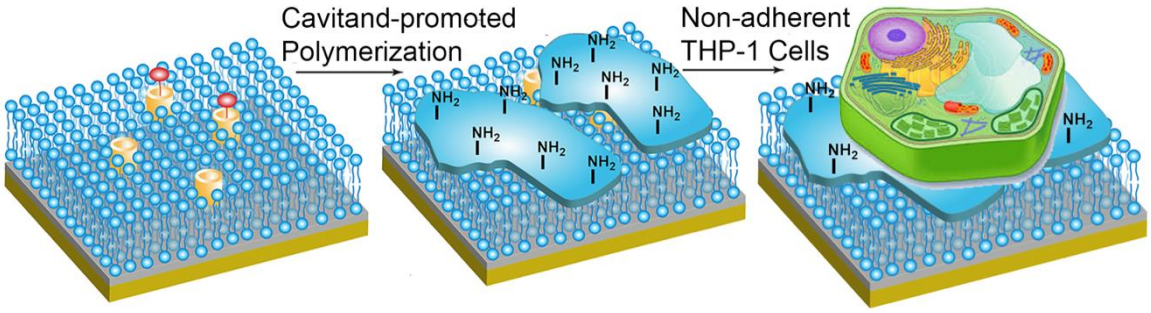

Figure 4.14: The immobilization of nonadherent THP-1 cells at the cationic poly(AEMA) surface.

The amine groups displayed on the cavitand-anchored polymer are cationic under the pH 7.4 buffered conditions of the SLB system. This allows for the application of poly(AEMA) in multiple ways, apart from functionalization via nucleophilic reactions. Cationic graft polymers are well-known to adhere to living cells and mediate target transport,[19] this suggests that poly(AEMA) is capable of recognizing large structures such as cells on the SLB surface (Figure 4.14). Eukaryotic cells have little to no affinity for hydrophobic surfaces or to POPC bilayers,[23] meaning that our polymer construct is necessary for adhering live cells. The thin layer of poly(AEMA) would also serve as protection for the somewhat fragile SLB, while also acting as a "glue" capable of adhering cells. The cell adhering properties of cavitand-anchored poly(AEMA) were tested using human monocytic THP-1 cells, which are nonadherent. These cells were grown in RPMI growth medium before being centrifuged to form a pellet and removal of the high salt medium. The THP-1 cells were then rinsed with 10 mM PBS buffer before being suspended

in either 10 mM PBS buffer or deionized water. The cells were diluted to a cell density of 7.5 X 10^6 cells/mL before being injected into the SPR flow cell for analysis.

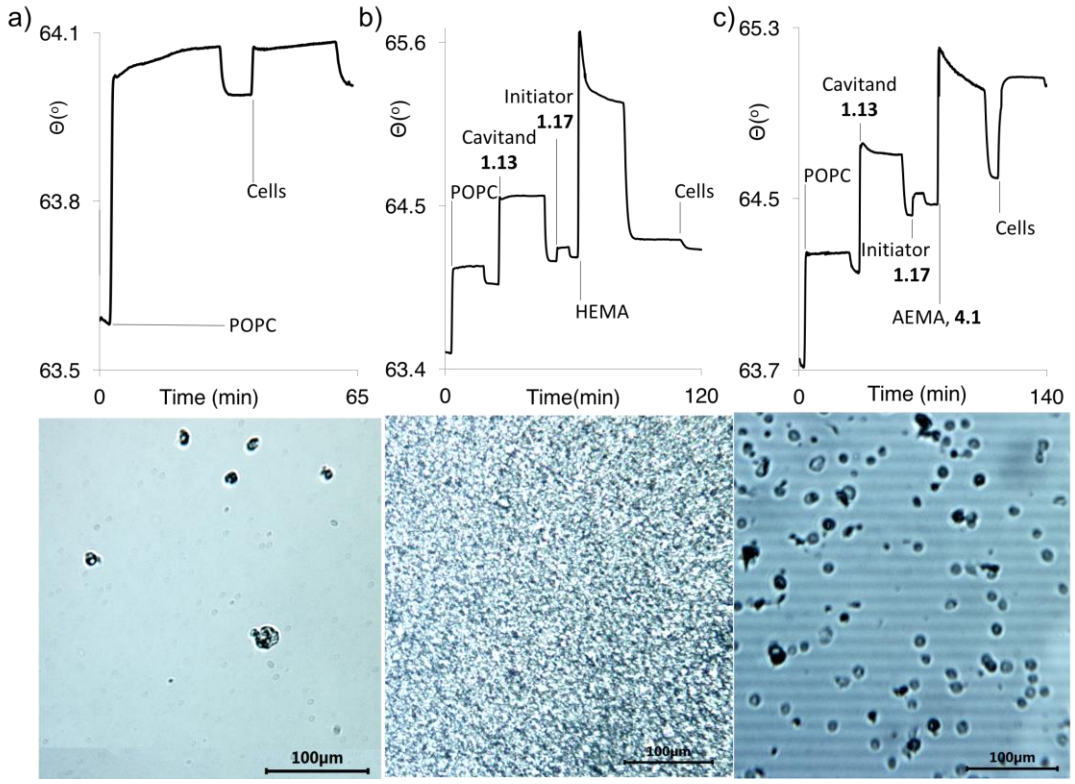

Figure 4.15: SPR sensorgram and microscope image of nonadherent THP-1 cell recognition at: a) pristine POPC bilayer; b) neutral, hydrophilic poly(HEMA) coated surface, and c) cationic poly(AEMA) coated surface.

The cell-adhering properties of three different systems were tested in order to illustrate the selectivity of the cationic poly(AEMA) surface: an intact POPC bilayer, a neutral, hydrophilic poly(HEMA) surface, and the cationic poly(AEMA) system. As can be seen in Figure 4.15a, the pristine POPC bilayer interface showed minimal response in the presence of THP-1 cells. In order to take a visible light microscopy images of the

surface, the chip was removed from the flow cell after washing. Special attention was paid to prevent the removal of the aqueous environment around the bilayer in order to prevent defects in the fragile SLB. Through microscope analysis, it is evident that very few cells adhered to the bilayer. The cells in the microscope images were most likely attached to the silica surface underneath the bilayer as opposed to the SLB itself.[17] Similar results were recorded in the presence of neutral, hydrophilic poly(HEMA), where no cell adhesion was observed. As previously mentioned, the polymerization of HEMA is much more efficient than that of AEMA **4.1** and therefore produces a thicker, more complete coating at the SLB surface. This thick poly(HEMA) coating did not display any affinity toward the non-adherent THP-1 cells as can be seen in the microscope image of this surface, though the polymer fibrils are visible (Figure 4.15b). Finally, as predicted, the cationic poly(AEMA) surface was exposed to the non-adherent cells and successfully immobilized them. As can be seen in Figure 4.15c, after injection, incubation and rinsing, there is a large resonance angle change observed for the SPR sensorgram of this system, indicating immobilization of the cells by the polymer. These results were confirmed by visualization of the SPR chip under the microscope, after careful removal from the flow cell. The cells are smaller than the poly(AEMA) patches that were visualized in Figure 4.11b and are therefore spaced randomly atop the cationic surface. The immobilization of non-adherent cells by the cationic poly(AEMA) was reproducible, though the display pattern of the cells on the surface was variable. This random display pattern is consistent with the uncontrolled polymer growth process. The cells were not removed from the surface after excessive rinsing in the flow cell with PBS buffer, proving that the adhesion between cationic

poly(AEMA) and the cells is robust. The injection medium was varied and the results were consistent, the cells remained adhered on the cationic surface in the presence of either pure water or higher ionic strength buffer. Due to the small size of THP-1 cells relative to the AEMA polymer patches, a large enough cationic surface area is provided for the efficient immobilization of the nonadherent cells.

4.6 Conclusion

Through these studies, the versatile binding abilities of membrane-embedded cavitands were expanded by the use of functional polymers. Cavitand **1.13** is able to promote polymerization of amine containing AEMA **4.1** at a SLB interface. This polymerization process is formed in a controlled and repeatable manner and can be further functionalized to impart bioadhesive properties. Although the amine functionality prevents the growth of a large polymer via ATRP, the formation of micrometer sized poly(AEMA) patches are observed at the water:bilayer interface. These poly(AEMA) patches can be reacted with NBD-Cl *in situ* and visualized under fluorescence microscopy. The polymer patches can also be reacted to display epitopes for protein binding and behave as "molecular glue" for the immobilization of nonadherent cells on the surface, due to the cationic nature of poly(AEMA). The application of the nontoxic $FeCl_2$ ATRP catalyst indicates that this method of *in situ* reactivity can be applied in cell surface engineering for the controlled creation of complex cell surface mimics.

4.7 References

1. Hof, F.; Trembleau, L.; Ullrich, E. C.; Rebek, J., Jr. "Acetylcholine Recognition by a Deep, Biomimetic Pocket." *Angew. Chem. In. Ed.*, **2003**, *42*, 3150-3153.

2. Biros, S. M.; Ullrich, E. C.; Hof, F.; Trembleau, L.; Rebek, J., Jr. "Kinetically Stable Complexes in Water: The Role of Hydration and Hydrophobicity." *J. Am. Chem. Soc.*, **2004**, *126*, 2870-2876.

3. Hooley, R. J.; Van Anda, H. J.; Rebek, J., Jr. "Extraction of Hydrophobic Species into a Water-Soluble Synthetic Receptor." *J. Am. Chem. Soc.*, **2007**, *129*, 13464-13473.

4. Ghang, Y.-J.; Lloyd, J.; Moehlig, M.; Arguelles, J.; Mettry, M.; Zhang, X.; Julian, R.; Cheng, Q.; Hooley, R. J. "Labeled Protein Reconition at a Membrane Bilayer Interface by Embedded Synthetic Receptors." *Langmuir*, **2014**, *30*, 10161-10166

5. Ghang, Y.-J.; Perez, L.; Morgan, M. A.; Si, F.; Hamdy, O. M.; Beecher, C. N.; Larive, C. K.; Julian, R. R.; Zhong, W.; Cheng, Q.; Hooley, R. J. "Anionic Deep Cavitands Enable the Adhesion of Unmodified Proteins at a Membrane Bilayer." *Soft Matter*, **2014**, *10*, 9651–9656.

6. Perez, L.; Ghang, Y.-J.; Williams, P. B.; Wang, Y.; Cheng, Q.; Hooley, R. J. "Labeled Protein Recognition at a Membrane Bilayer Interface by Embedded Synthetic Receptors." *Langmuir*, **2015**, *31*, 11152–11157.

7. Peterson, B. R. "Synthetic Mimics of Mammalian Cell Surface Receptors: Prosthetic Molecules that Augment Living Cells." *Org. Biomol. Chem.*, **2005**, *3*, 3607–3612.

8. Groves, J. T.; Mahal, L. K.; Bertozzi, C. R. "Control of Cell Adhesion with Micropatterned Supported Lipid Membranes." *Langmuir*, **2001**, *17*, 5129 – 5133.

9. Wilson, J. T.; Krishnamurthy, V. R.; Cui, W.; Qu, Z.; Chaikof, E. L. "Noncovalent Cell Surface Engineering with Cationic Graft Copolymers." *J. Am. Chem. Soc.*, **2009**, *131*, 18228−18229.

10. Kozlovskaya, V.; Zavgorodnya, O.; Chen, Y.; Ellis, K.; Tse, H. M.; Cui, W.; Thompson, J. A.; Kharlampieva, E. "Ultrathin Polymeric Coatings Based on Hydrogen-Bonded Polyphenol for Protection of Pancreatic Islet Cells." *Adv. Funct. Mater.*, **2012**, *22*, 3389−3398.

11. Niikura, K.; Nambara, K.; Okajima, T.; Kamitani, R.; Aoki, S.; Matsuo, Y.; Ijiro, K. “Artificial Polymeric Receptors on the Cell Surface Promote the Efficient Cellular Uptake of Quantum Dots.” *Org. Biomol. Chem.*, **2011**, *9*, 5787−5792.

12. Hubert, D. H. W.; Jung, M.; German, A. L. “Vesicle Templating,” *Adv. Mater.*, **2000**, *12*, 1291−1294.

13. Fukuda, H.; Diem, T.; Stefely, J.; Kezdy, F. J.; Regen, S. L. “Polymer-Encased Vesicles Derived from Dioctadecyldimethylammonium Methacrylate.” *J. Am. Chem. Soc.*, **1986**, *108*, 2321−2327.

14. Jayasuriya, N.; Bosak, S.; Regen, S. L. “Supramolecular Surfactants: Polymerized Bolaphiles Exhibiting Extraordinarily High Membrane-Disrupting Activity.” *J. Am. Chem. Soc.*, **1990**, *112*, 5851− 5854.

15. Ouchi, M.; Terashima, T.; Sawamoto, M. “Transition Metal- Catalyzed Living Radical Polymerization: Toward Perfection in Catalysis and Precision Polymer Synthesis.” *Chem. Rev.*, **2009**, *109*, 4963−5050.

16. Matyjaszewski, K.; Tsarevsky, N. V. “Nanostructured Functional Materials Prepared by Atom Transfer Radical Polymerization.” *Nat. Chem.*, **2009**, *1*, 276−288.

17. Liu, Y.; Young, M. C.; Moshe, O.; Cheng, Q.; Hooley, R. J. “A Membrane-Bound Synthetic Receptor Promotes Growth of a Polymeric Coating at the Bilayer-Water Interface.” *Angew. Chem., Int. Ed.*, **2012**, *51*, 7748−7751.

18. Perez, L.; Ghang, Y-J; Williams P. B.; Wang, Y.; Cheng, Q.; Hooley, R. J. "Cell and Protein Recognition at a Supported Bilayer Interface via In Situ Cavitand-Mediated Functional Polymer Growth." *Langmuir*, **2015**, *31*, 11152-11157.

19. Sletten, E. M.; Bertozzi, C. R. “Bioorthogonal Chemistry: Fishing for Selectivity in a Sea of Functionality.” *Angew. Chem., Int. Ed.*, **2009**, *48*, 6974−6998.

20. Bakhtiar, R. “Surface Plasmon Resonance Spectroscopy: A Versatile Technique in a Biochemist’s Toolbox.” *J. Chem. Educ.*, **2013**, *90*, 203-209.

21. Linman, M. J.; Abbas, A.; Cheng, Q. “Interface Design and Multiplexed Analysis with Surface Plasmon Resonance (SPR) Spectroscopy and SPR Imaging.” *Analyst*., **2010**, *135*, 2759-2767.

22. Liu, Y.; Liao, P.; Cheng, Q.; Hooley, R. J. “Non-Covalent Molecular Recognition of Proteins at a Bilayer Interface by Self- Folding Synthetic Receptors.” *J. Am. Chem. Soc.*, **2010**, *132*, 10383− 10390.

23. Groves, J. T.; Mahal, L. K.; Bertozzi, C. R. “Control of Cell Adhesion and Growth with Micropatterned Supported Lipid Membranes.” *Langmuir*, **2001**, *17*, 5129−5133.

Chapter 5: Cavitands in Indicator Displacement Assays and Inside Cells

5.1 Introduction

The different modes of interaction of the synthetic host molecule, cavitand **1.13** allows for its efficient use in host:guest indicator displacement assays (IDA). Indicator displacement assays allow for the detection and differentiation of specific analytes and are a popular method for utilizing synthetic receptors as optical sensors.[1] Indicator displacement assays function by reversibly binding an indicator molecule to a receptor before introducing a competitive analyte that displaces the indicator, causing an optical signal that can be recorded.[2] Indicator displacement assays are a more selective approach for detection when compared to methods that require the design of sensing structures such as graphene oxides,[3,4] or the construction of highly specific antibodies for immunoassays.[5] IDAs can be applied to the sensing of proteins[6] and in particular, IDAs are a method for sensing protein post-translational modifications (PTM) [7,8,9] by utilizing CX4 and CB7. Indicator displacement assays have also been utilized in live cells for the detection of the uptake of bioorganic analytes.[7]

An important requirement for IDA systems is for the analyte to have an affinity to the receptor that is better or comparable to that of the indicator to the receptor. The interaction between the dye and receptor is dependent on the functionality and shape of both host and guest. Luckily, deep cavitands have an affinity for trimethylammonium groups (-R-NMe_3^+) which can be easily attached to common, commercial fluorophores.

Binding affinities for soft cationic guests vary between mM and μM, with (-R-NMe_3^+) species such as acetylcholine showing the greatest affinity.[10] Using deep cavitand receptors, and a fluorescent indicator containing the (-R-NMe_3^+) binding handle, a variety of molecules can be detected. There are a variety of naturally-occurring guests that contain the (-R-NMe_3^+) functional group, and can be detected by the cavitand sensor, Lysine trimethylation, a type of PTM on histones, produces cationic methylammonium groups that fit well inside the pocket of the cavitand.[11] More complex discrimination of guests can occur by varying the functionality on the rim and feet of the cavitand in order to promote more complex interactions.[12] Cavitand **1.13** has shown selective recognition of a wide variety of substrates in aqueous,[13] biomimetic membrane,[14] and living cell environments[15] and has even been utilized as a sensing agent for acetylcholine.[16] This chapter explores the use of cavitand synthetic receptors in IDAs for varying targets ranging from PTMs to metals as well as inside HeLa cells.

5.2 Fluorescein Displacement Sensor

Cavitand **1.13** exhibits unusual assembly behavior when binding mildly hydrophobic (-R-NMe_3^+)-containing guests. In the presence of small molecules such as choline, a 1:1 complex is observed while larger guests that protrude out of the cavity can cause the cavitand to aggregate into larger assemblies.[16] This aggregation behavior observed upon target binding introduced the possibility of a new strategy for IDA. By tailoring the desired indicator molecule to contain the (-R-NMe_3^+) binding handle, excellent selectivity for the desired dye can be attained. The challenge would be to find an

appropriate indicator dye that quenches upon binding in the cavitand (due to aggregation) and turn back on when released (Figure 5.1).

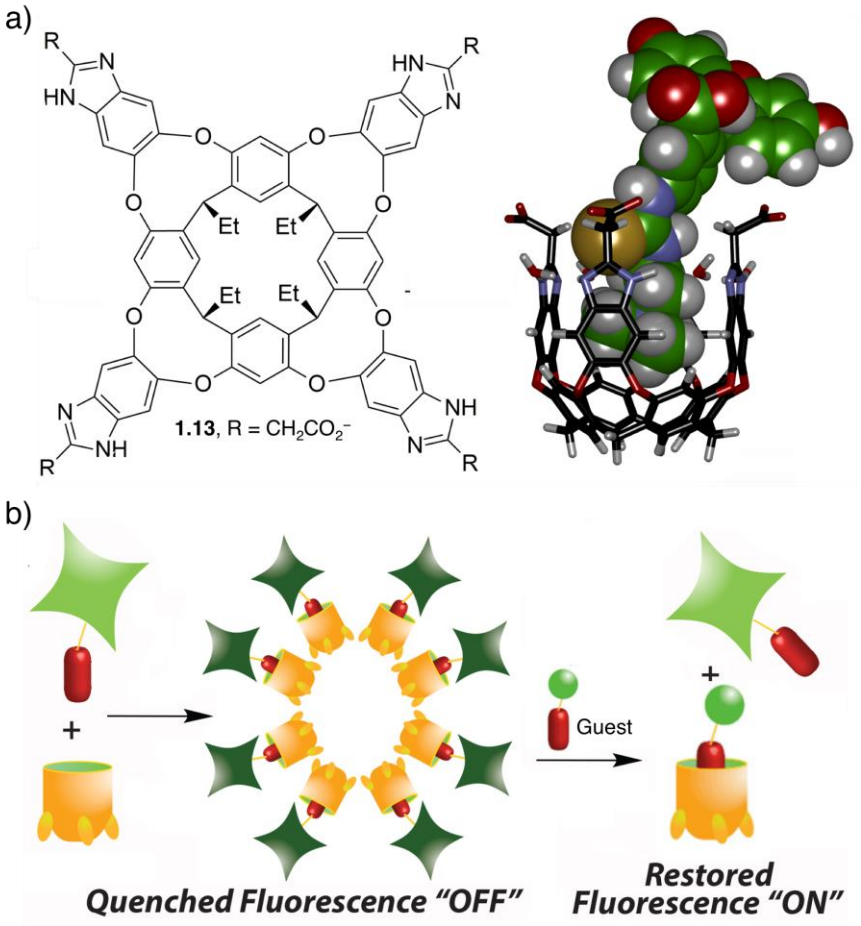

Figure 5.1: a) Structure of cavitand **1.13** and the minimized model of the **1.13 • 5.1** host:guest complex (SPARTAN); b) The aggregation-based sensing system.

Important qualities in an indicator dye for the IDA are water solubility and emission at long wavelengths for simple sensing. A small range of water soluble fluorescein-based dyes were tested to determine their affinity for cavitand **1.13** as well as their potential quenching range. Guests **5.1** - **5.3** vary in the methylation state of the terminal nitrogen and

were synthesized in one or two steps form commercial fluorescein isothiocyanate (Figure 5.2). Fluorescein guest **5.1** is a well-established guest for cavitand **1.13** in lipid bilayer environments[17] and has even been transported and imaged inside cells.[18] Underivatized fluorescein and guests **5.2** and **5.3** were expected to show significantly smaller affinities to **1.13** due to shape mismatch and charge-fitting within the cavity.

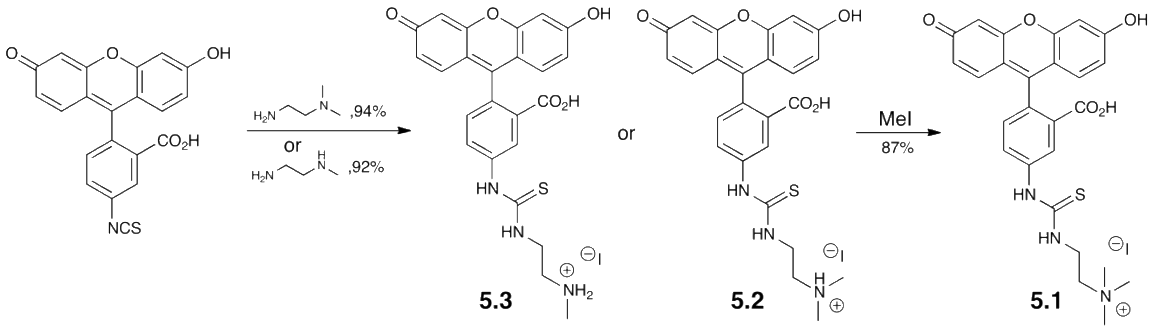

Figure 5.2: Synthesis of fluorescein guests **5.1** - **5.3**.

As can be seen in Figure 5.3, fluorescein and derivatized guests **5.2** and **5.3** behave very differently from guest **5.1** upon addition of increasing concentrations of cavitand **1.13** in phosphate buffered saline (PBS). Minimal changes in fluorescence were observed in the presence of monomethylated ($-NH_2Me^+$) guest **5.3** and underivatized fluorescein, while dimethylated ($-NHMe_2^+$) guest **5.2** showed slight quenching. In the presence of trimethylated ($-NMe_3^+$) guest **5.1**, however, a significant decrease in fluorescence is observed, reaching maximal quenching in the presence of 20 μM of **1.13**. At this cavitand concentration, a 70% loss in fluorescence is observed and a dissociation constant of 17 ± 10 μM was obtained for the **1.13** • **5.1** complex. The dissociation constants for fluorescein

and guests **5.2** and **5.3** were at least 10 times larger than that of **5.1**, indicating weak binding due to shape mismatch in the pocket of the cavitand.[17]

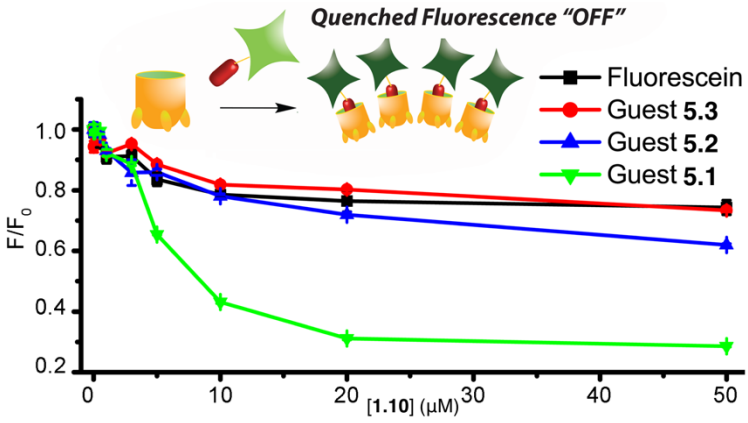

Figure 5.3: Aggregation based quenching. Relative fluorescence of guests **5.1**-**5.3** at 3 μM with increasing concentrations of **1.13** in PBS buffer (10 mM phosphate, 150 mM NaCl, pH 7.4).

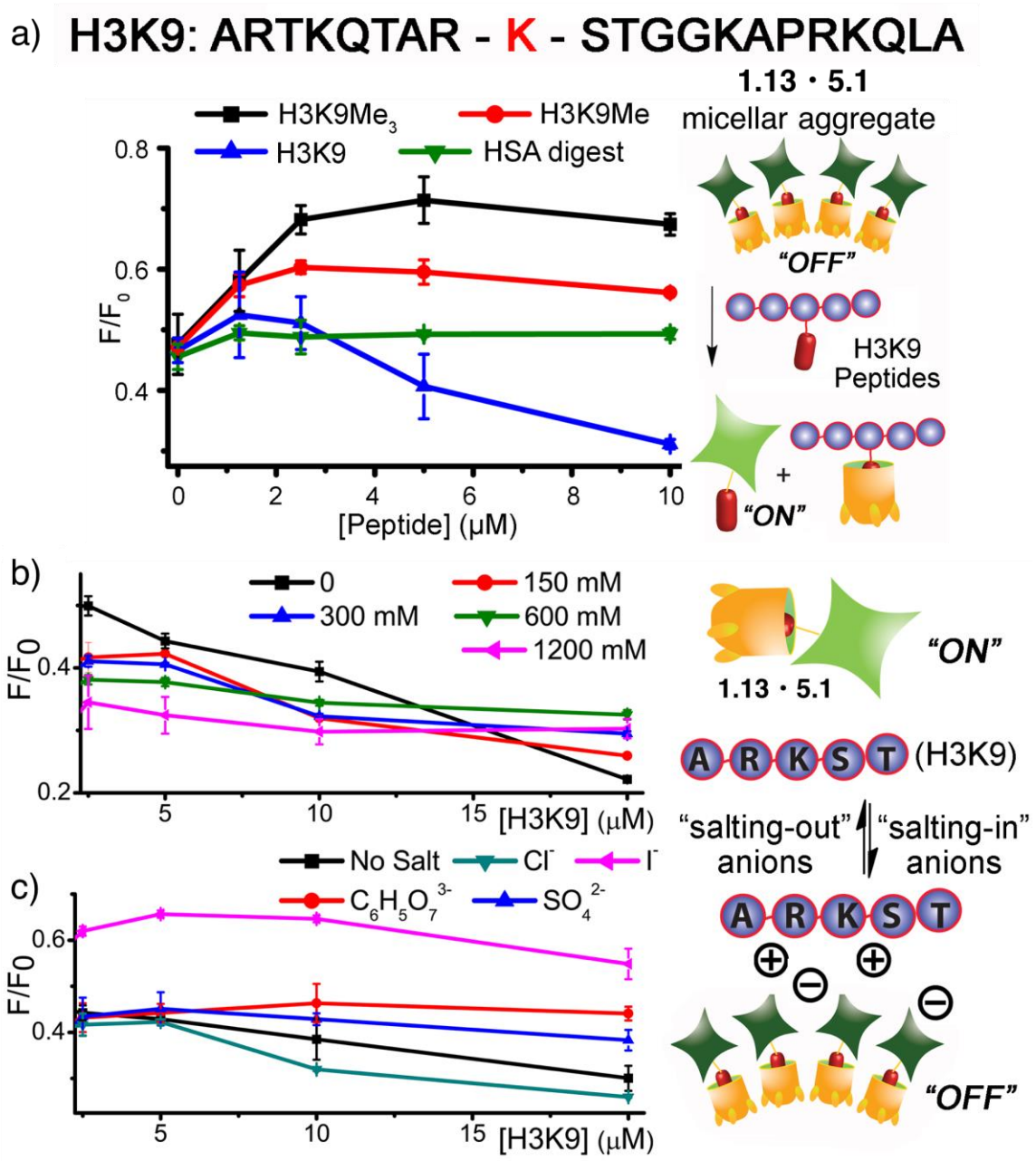

Figure 5.4: a) H3 primary amino acid sequence and fluorescence recovery induced by mixing modified (H3K9Me, H3K9Me3) or unmodified (H3K9) histone peptides (H3, 1−21), or the protease digest of human serum albumin (HSA) with the sensor system (PBS buffer, 20 μM **1.13**, 3 μM **5.1**); Hofmeister-dependent aggregation. Effect of varying b) [NaCl] and c) anion type with [X−] = 150 mM on the fluorescence of the sensor (18 μM **1.13**, 3 μM **5.1**).

Since the dissociation constant for the **1.13 • 5.1** was about 17 μM, only strongly binding substrates should be able to displace, and turn on the fluorescent guest, making this host:guest complex a selective sensor. Trimethylammonium salts are the strongest bound guests for cavitand **1.13** due to the favorable cation-π interactions, this should make the sensor capable of detecting lysine methylation PTMs. Yang Liu tested the sensor on H3 peptide fragments, whose primary amino acid sequence can be seen in Figure 5.4a. This sensor proved to be selective for trimethylated NMe_3^+ guests as some fluorescence recovery was observed for the monomethylated peptide (H3H9Me) and none was observed for the native H3. The addition of protease digest from human serum albumin (HSA digest) did not alter the fluorescence signal of the sensor, proving to be robust in systems that mimic cell extraction.

The effect on fluorescence quenching induced by H3K9 on the **1.13 • 5.1** sensor in the presence of both "salting-in" (chaotropic) and "salting out" (kosmotropic) anions was also tested (Figure 5.4b and c). As can be seen in Figure 5.4b, the quenching was decreased in higher NaCl concentrations due to reduced electrostatic interactions between the cationic peptide and the **1.13 • 5.1** complex. This process has been observed in the binding disruption of cationic proteins with cavitand **1.13** in membrane bilayers.[18] Surprisingly, in the presence of "salting out" salts such at citrate, less fluorescence quenching is observed due to a lowered amount of aggregation with the cationic H3K9 (Figure 5.4c). This result was due to chaotropes, which cause increased binding of sodium ions to the external anionic carboxylates, reducing the net charge of **1.13** (as has been observed by Gibb with his anionic host),[19] therefore reducing the electrostatic attraction between H3K9 and

cavitand **1.13**. Chloride was the least effective additive while iodide increased the baseline fluorescence significantly, this may be due to the soft iodide anion having some affinity for the cavity itself[19] and competitively displacing **5.1** while regenerating fluorescence. The ability of this sensor to differentiate between methylation states of lysine residues also allowed for its successful application in the monitoring of enzymatic activity of N-methyltransferase and lysine demethylase.

5.3 Rhodamine Displacement Sensor

In order to make the cavitand IDA sensor more efficient, more variables were introduced to the host and guest system. Rhodamine guest **5.4** was synthesized and utilized as an additional indicator dye and cavitands **1.16** and **3.1** were introduced to diversify the interactions of guests with the variably functionalized rims (Figure 5.5). These receptors and dyes were utilized to form an array that provides multi-mode recognition to maximize signal differences from small variations in guest molecules. This technique has been previously utilized to create a "chemical nose" for small molecules in a variety of optical sensing applications.[20,21] The combined responses from the selective interactions between the individual receptors and target molecules can create a fingerprint for each molecule that can be analyzed using a variety of multi-variate statistic tools such as principal component assay (PCA)[22,23] or linear discriminant analysis (LDA).[24] This multivariable sensor was applied in order to selectively discriminate between highly similar small molecular targets as well as positional variations in histone peptides displaying lysine methylation, phosphorylation and acetylation PTMs.

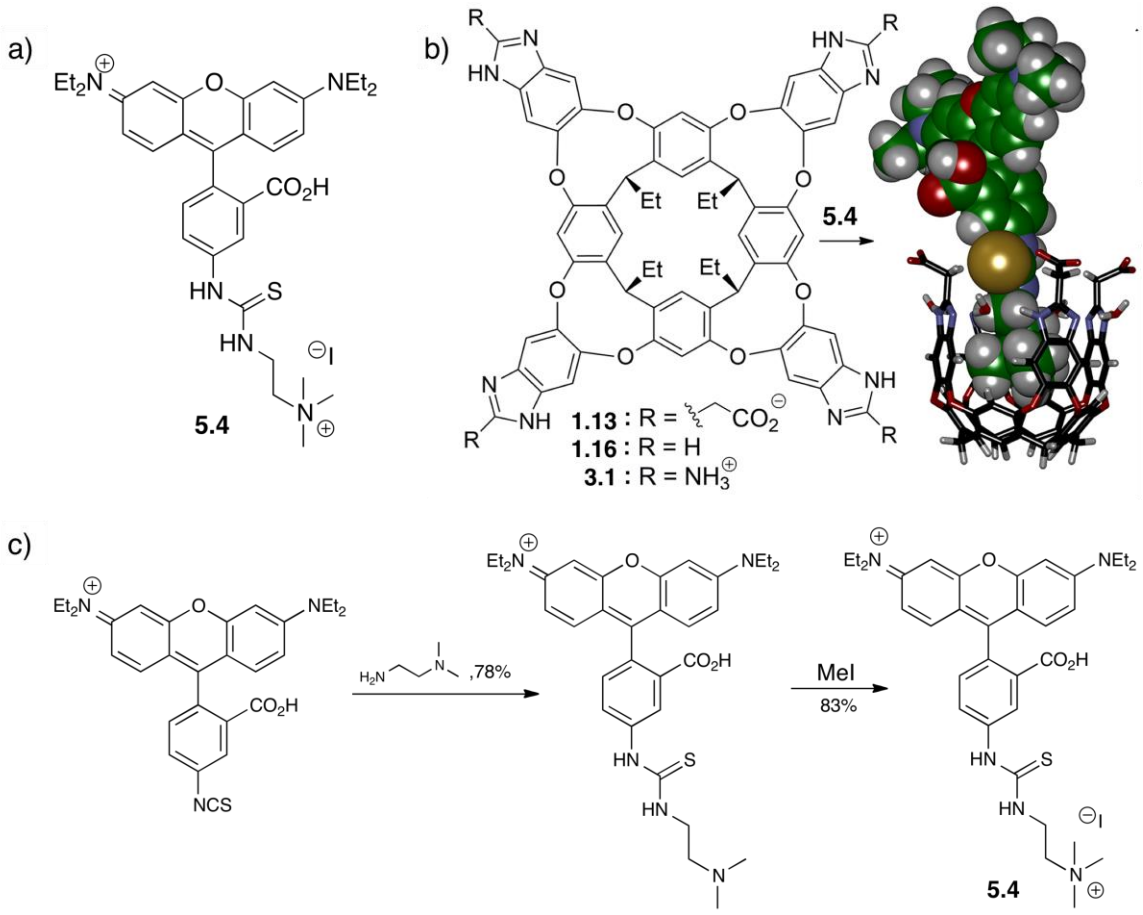

Figure 5.5: a) structure of rhodamine B guest **5.4**; b) The structure of hosts **1.13**, **1.16** and **3.1** and the incorporation of guest **5.1** inside the cavity of the cavitand (SPARTAN); c) synthesis of rhodamine guest **5.4**.

Before the discrimination studies were performed, the binding abilities of rhodamine B guest **5.4** with cavitands **1.13**, **1.16** and **3.1** were studied. Even though the structure of **5.4** is very similar to that of fluorescein guest **5.1**, the binding behavior of these two molecules is very different. The binding of guest **5.4** in cavitands **1.13**, **1.16** and **3.1** is stronger than that of guest **5.1** and occurs upon simple 1:1 complexation as opposed to the aggregative mechanism displayed by **5.1**. A strong loss in fluorescence was observed when

guest **5.4** (3 μM) was mixed with cavitands **1.13**, **1.16** and **3.1** due to photoinduced electron transfer (Figure 5.6a). [25] Cavitands **1.16** and **3.1** showed stronger fluorescence quenching at higher cavitand concentrations compared to **1.13**. The pH of the system was also varied, since the protonation state of the negative and positive cavitands varies with pH (Figure 5.6b). Negative cavitand showed the greatest affinity for guest **5.4** at pH 5 while cavitands **1.16** and **3.1** displayed greater affinities at higher pHs. All three cavitands showed strong affinities with guest **5.4** and their varying affinities at varying pHs allows for the sensor to create pH responsive guest recognition. This system is also biocompatible since these studies were performed in aqueous buffered solutions. The high affinities of cavitands towards guest **5.4** would also allow for more accurate sensing, as only strongly binding targets will cause a displacement.

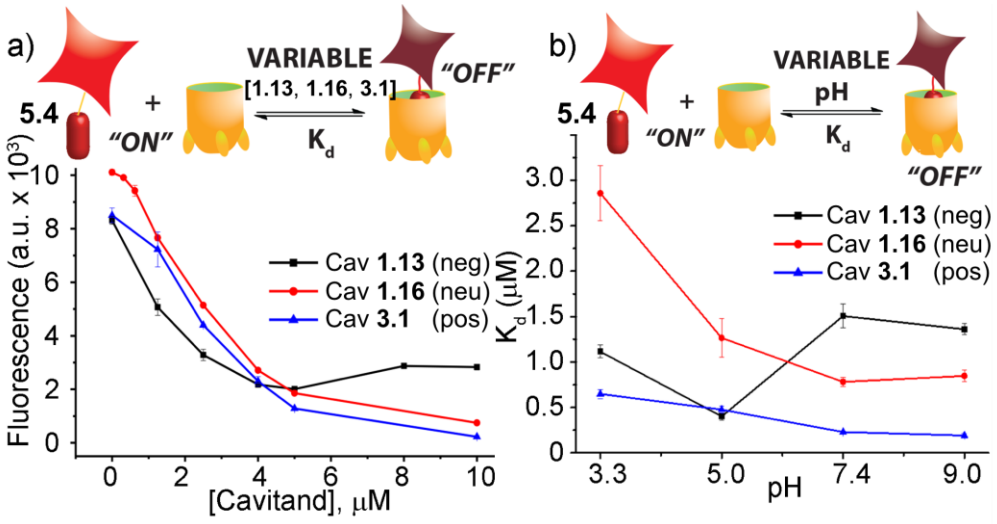

Figure 5.6: a) Fluorescence quenching of 3 mM guest **5.4** with varying cavitand [**1.13**, **1.16**, **3.1**] in 80 mM phosphate buffer, pH = 7.4; b) pH-dependent affinity of guest **5.4** for cavitands in 80 mM different buffers (citrate buffer, pH = 3.3; phosphate buffer, pH = 5.0; phosphate buffer, pH = 7.4; carbonate buffer, pH = 9.0).

5.4 Selectivity of Displacement Sensor

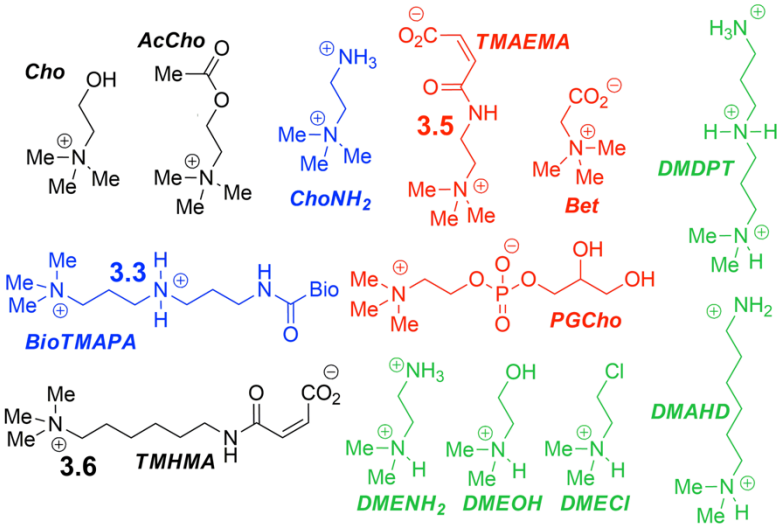

Figure 5.7: Small molecule guests to test the scope of discrimination of the IDA sensor.

Yang Liu was also able to test the scope of the array and evaluate its efficiency at discriminating between molecules with extremely small differences, the guests in Figure 5.7. These compounds vary in the binding handle, the guests colored in green contain a (-$NHMe_2^+$) group while the rest have the (-NMe_3^+) functionality. Other variations in guests allowed them to interact with the cavitand's rim by placing a charge near the (-R-NMe_3^+) handle, lipophilic chains or H-bonding groups. The array was composed of the three cavitands, the two fluorescent guests at different pHs (pH 3.3, 5.0, 7.4 and 9.0 for **5.4** and 7.4 and 9.0 for guest **5.1**) to give a total of 14 different variables. The screening seen in Figure 5.8 a-d shows the efficiency of the sensor at discriminating between very similar molecules. Choline (Cho) and cholamine ($ChoNH_2$) were effectively discriminated against

despite only differing in the terminal group. The effect of varying the pH and cavitand is also illustrated in the sensing of very similar molecules. The PCA plot in figure 5.8e illustrates the variety of individual effects at play in the system: from pH dependent affinity of the fluorophores for different cavitands, to guest matching and mismatching with the upper rim of the cavitand, as well as aggregation effects. The displacement percentages measured with the rhodamine sensor were subjected to PCA in order to obtain the scores plot. The three "strongest binders" (R-NMe_3^+ containing guests Cho, AcCho and BioTMAPA) locate in the upper-right panel, well separated from the R-$NHMe_2^+$ guests and the more weakly bound R-NMe_3^+ guests.

The rhodamine sensor was also successfully capable of discriminating between various PTMs from peptides derived from histone H3. The 14 peptides illustrated in Figure 5.9a varied in methylation state at K9 from 0/1/2/3 methyl groups (K9Me_0-K9Me_3) to the position of the trimethylation PTM on the backbone. Non-methylation PTMs were also tested such as lysine acetylations and serine/threonine phosphorylations including the presence of single, double or triple modifications. The pH of the sensor was varied from neutral (pH 7.4) to basic (pH 9.0) and only rhodamine guest **5.4** was applied along with cavitands **1.13**, **1.16** and **3.1**. PCA analysis of the data obtained shows successful discrimination between PTMs such as acetylations and methylation (Figure 5.9b) as well as peptides with varying methylation sites (Figure 5.9c). This sensor was also able to effectively discriminate between methylations at the same site but in peptides of varying lengths (Figure 5.9d) as well as varying PTMs (Figure 5.9e).

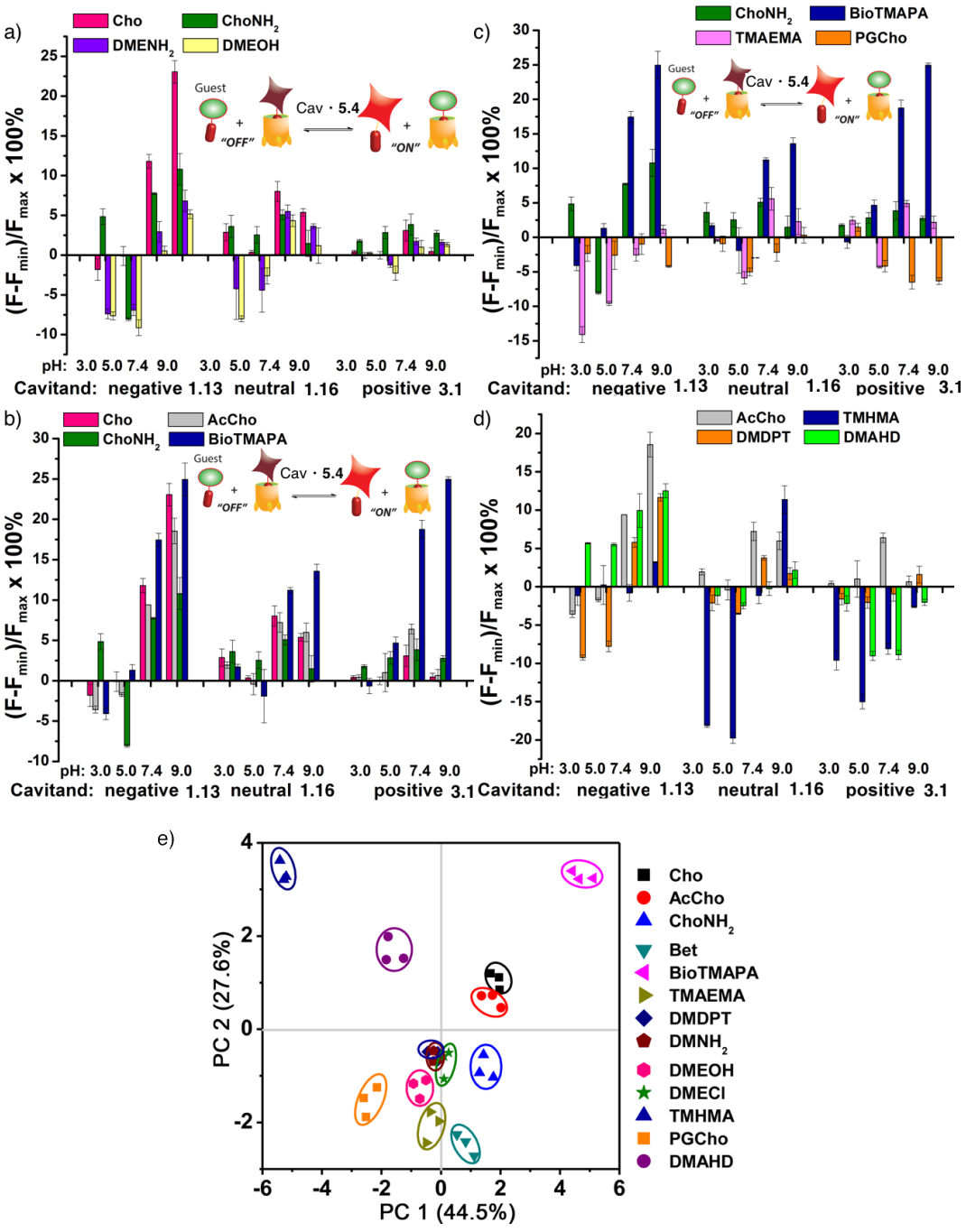

Figure 5.8: Small molecule indicator displacement. a) (R-NMe_3^+) vs. (R-$NHMe_2^+$) discrimination for guests; (b) discrimination between highly similar (R-NMe_3^+) guests; c) discrimination between anionic and cationic (R-NMe_3^+) guests; d) discrimination between neutral and lipophilic guests. Error bars calculated from three repeat experiments. For negative **1.13**, [guest **5.4**] = 3 mM and [cavitand **1.13**] = 4 mM, and for neutral **1.16** and positive **3.1**, [guest **5.4**] = 3 mM, [cavitand **1.16** or **3.1**], = 5 mM. [small molecule] = 100 mM.

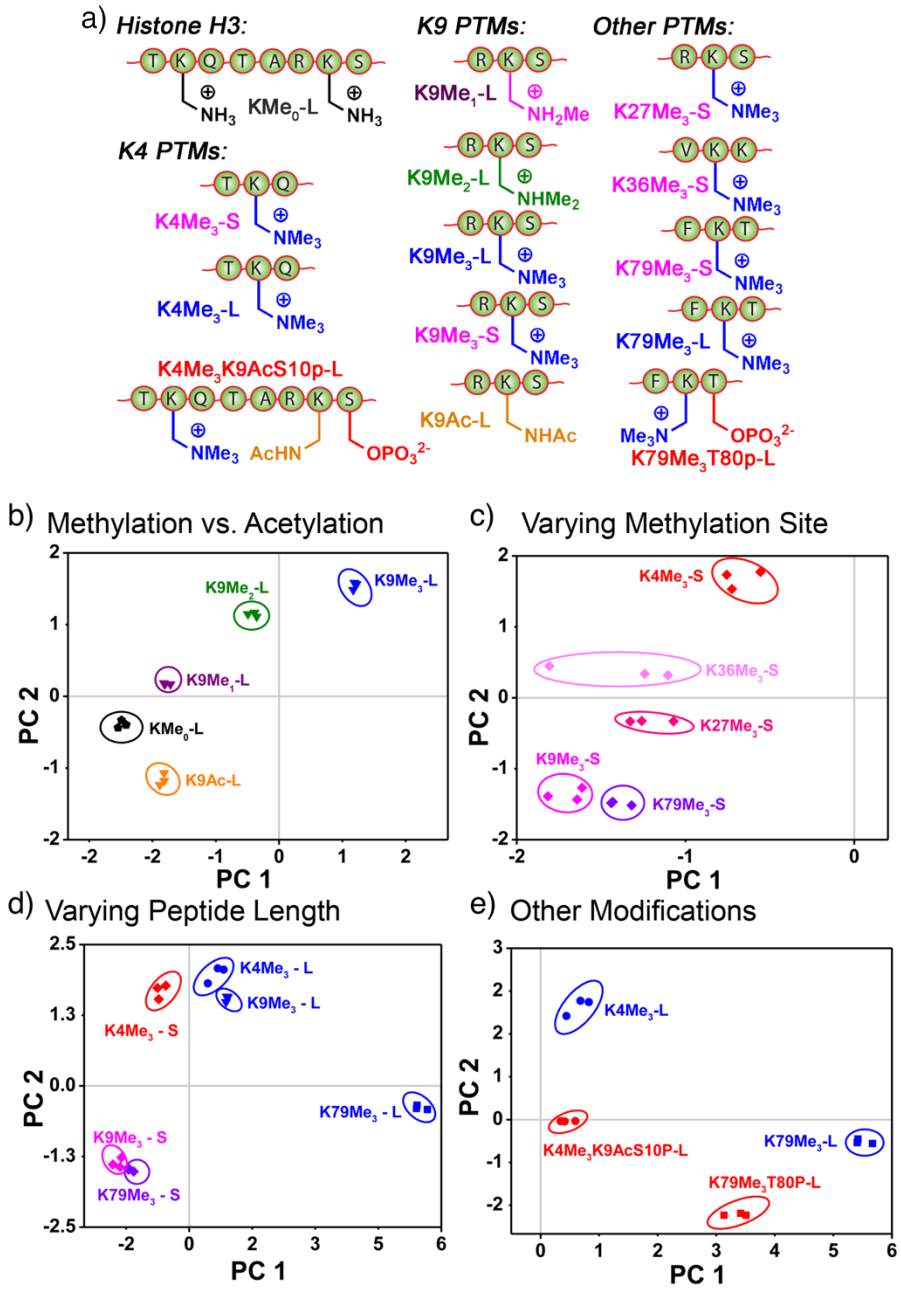

Figure 5.9: a) Variably modified peptides used in this study. L = 20/21 amino acid residues. S = 10–15 amino acid residues; Peptide discrimination PCA. Zoom-in scores plot for peptides b) with various degrees of methylation or acetylation; c) with varying methylation sites; d) with different peptide lengths; e) with phosphorylation and/or acetylation near the trimethylated site. The error ellipses were obtained at 95% confidence interval.

5.5 Metal Sensing

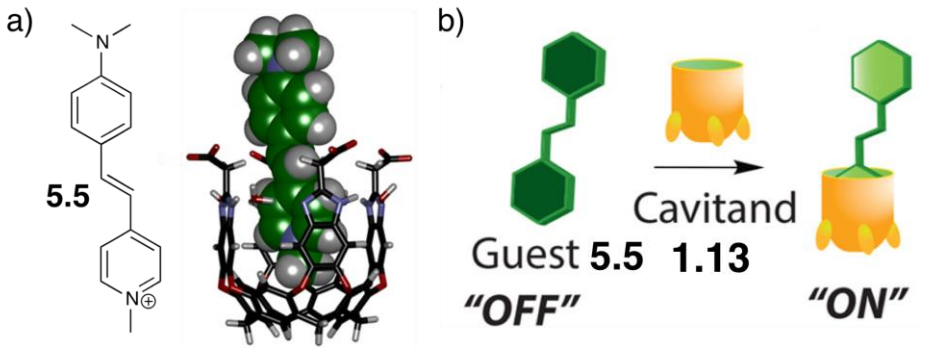

Figure 5.10: a) Structure of DSMI **5.5** and its incorporation into the cavitand pocket; b) illustration of the turn-on and turn-off fluorescence detection processes.

The cavitand IDA was also utilized as a heavy metal sensor. This is a useful application since heavy metals such as mercury, lead and chromium pose a threat to the environment[26] and human health.[27,28] Electrochemical[29,30] and small molecule metal sensors[31,32] can be used to detect heavy and rear earth (RE) metals, however their selectivity and sensitivity is limited. The four carboxylate groups on the rim of **1.13** are in close proximity to each other and are free to rotate and chelate a metal ion, this would allow for effective metal binding in aqueous solution.

Since fluorescein guest **5.1** was not effective as a sensor component, it was replaced by trans-4-[4-(dimethylamino)styryl]-1-methylpyridinium iodide (DSMI) **5.5** (Figure 5.10a). DSMI is capable of incorporating into the cavitand's pocket due to its size, shape and charge profile. This guest is well-known to display enhanced fluorescence in hydrophobic environments such as in host molecules hexasulfonatocalix[6]arene[35,36] or

cucurbit[7]uril.[36] Upon binding to cavitand **1.13**, DSMI displays a fluorescence increase, as opposed to the quenching nature of rhodamine B guest **5.4** (Figure 5.10).

Alkaline earth metals (Ca^{2+}, Mg^{2+}), early transition metals (MN^{2+}-Cu^{2+}), group IIB/IVA transition metals (Zn^{2+}, Cd^{2+}, Hg^{2+}, Pb^{2+}), rare earth metals (La^{3+}, Ce^{3+}, Er^{3+}) and actinides (Th^{4+}, UO_2^{2+}) were tested. The lanthanides and actinides (La^{3+}, Ce^{3+}, Er^{3+} and Th^{4+}) were very well distinguished at pH 5.5 and showed a large fluorescence recovery. A very different response profile was observed for the same sensor at pH 7.4 as can be observed in Figure 5.11b. Almost 100% loss of fluorescence was observed for Fe^{2+}, Co^{2+}, Ni^{2+}, Cu^{2+} and UO_2^{2+} in the presence of the **1.13 • 5.5** sensor at pH 7.4 (20 μM **1.13**, 1.5 μM **5.5** in 20 mM Tris). Minimal change in fluorescence was observed in the presence of the alkaline earth metals, Mn^{2+}, as well as the group IIB transition metals while the lanthanides and actinides caused a loss in fluorescence varying from 30% (La^{3+}, Er^{3+}, Th^{4+}) to 70% (Ce^{3+}). The fluorescence of guests **5.4** and **5.5** did not change significantly upon addition of 50 μM metal in the absence of cavitand **1.13**, this indicated that the sensor is based on a host-mediated process.

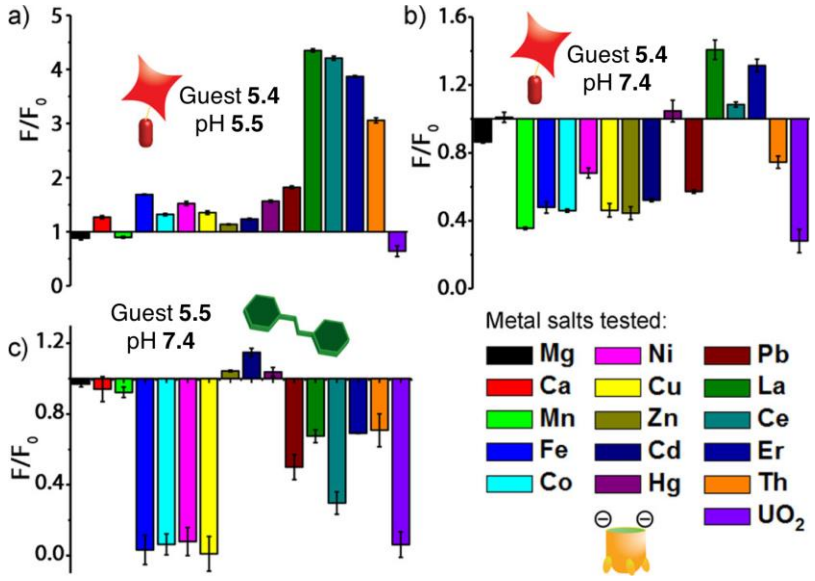

Figure 5.11: Fluorescence response change on metal addition to host-fluorophore complexes. [metal] = 50 μM; sensor **1.13 • 5.4**: [**1.13**] = 4 μM, [**5.4**] = 3 μM in (a) 20 mM Tris (pH 7.4) or (b) Bis-Tris (pH 5.5) titrated to the corresponding pH with nitric acid, (c) Sensor **1.13 • 5.5**: [**1.13**] = 20 μM, [**5.5**] = 1.5 μM, in 20 mM Tris (pH 7.4).

The mode of interaction between the metal salts and cavitand **1.13** are due to the carboxylate groups on the host's rim. Even though carboxylate groups are weakly coordinating, they are in suitable proximity to each other to allow chelating interactions with large metal ions in the presence and absence of guests **5.4** and **5.5**.[37] The freely rotating carboxylates allow bidentate metal binding in multiple orientations: In the presence of guest, the metals can be positioned away from the cavity (Figure 5.11a), while in the absence of guest the metal resides above the cavity (Figure 5.11b). The chelating metal lowers the affinity of the fluorophores in the cavity of **1.13** due to steric interactions between the metal and protruding guest. This model explains the minimal effect by small alkali and alkaline earth metals such as Mg^{2+} and Na^{+} since they are less favorably chelated

and do not interfere with the fluorophore binding.

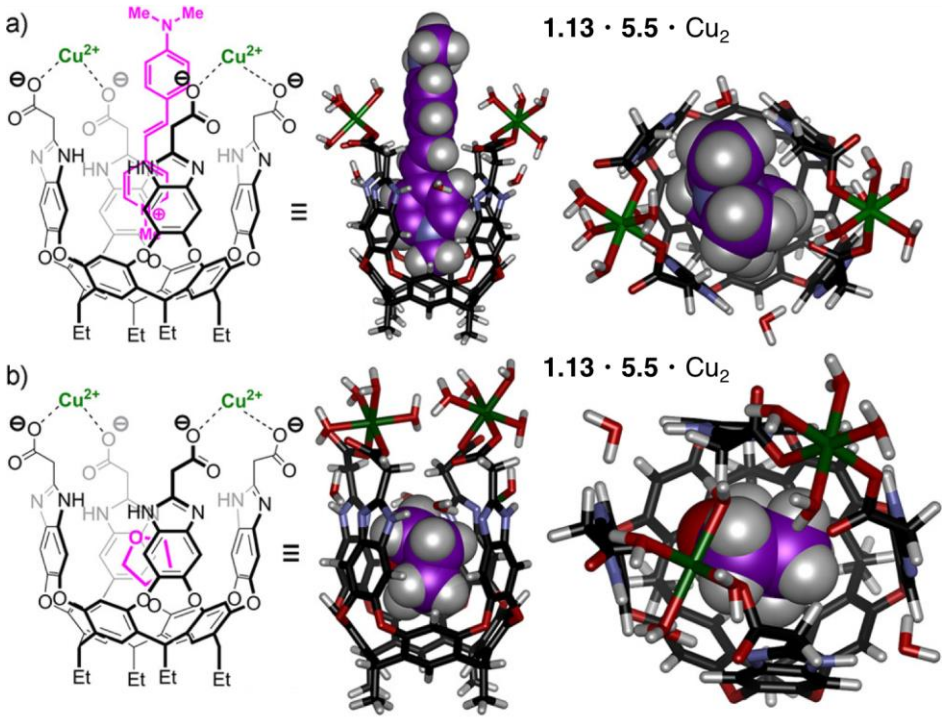

Figure 5.12: Minimized structures of (a) **1.13 • 5.5 •** Cu_2 and (b) **1.13 •** THF **•** Cu_2, indicating the effect on metal orientation in the presence of large and small guests (SPARTAN, AM1 force field).

The data obtained was subjected to LDA since each sensor is able to respond to multiple metals that induce subtle fluorescence changes depending on their type and concentration. The LDA plot for fluorescence profiles obtained from guests **5.4** and **5.5** in the absence of cavitand can be seen in Figure 5.13a. Since the metals interact with the cavitand and not the guests, no separation is observed between the metals with the exception of UO_2^{2+} which has a strong native quenching ability. Excellent metal discrimination is obtained using a 3-component cavitand-fluorophore sensor array (using

the data from Figure 5.11), which can be seen in Figure 5.13b. Even the metals with the highest structural similarity (La^{3+}, Ce^{3+}, Er^{3+} and Th^{4+}) were very well separated by this minimal sensor. Figure 5.13c also shows the scores plot for the full 7-factor sensor array which includes the cavitand complex of **1.16** and **3.1** with guest **5.4** at two pHs. This extended array also gave good separation between the metals, although discrimination among the IIA/IIB cluster was poorer.

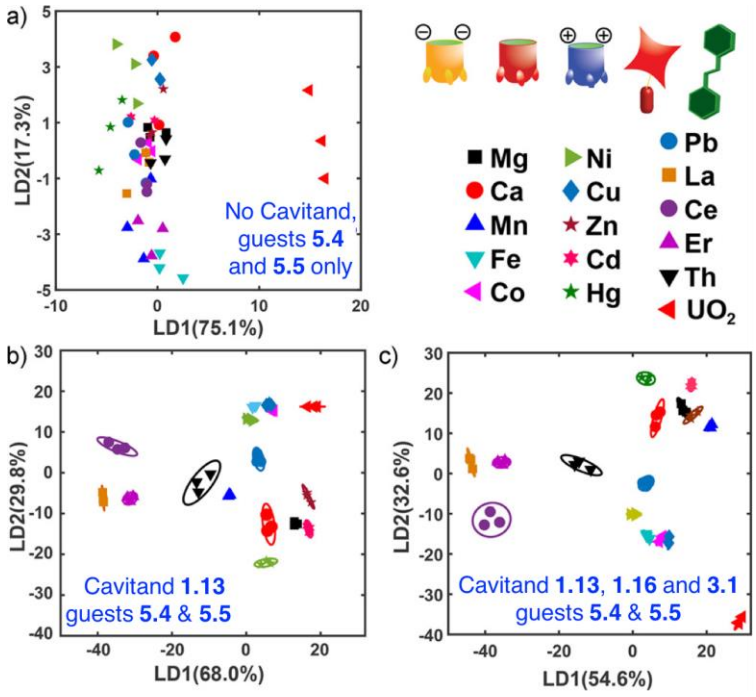

Figure 5.13: Metal salt identification via linear discriminant analysis: (a) scores plot of the metal screen with a cavitand-free screen,[**5.4**]=3μM, [**5.5**] = 1.5 μM; (b) scores plot of the metal screen with the 3 factor sensor array containing **1.13 • 5.4** ([**1.13**] = 4 μM, [**5.4**] = 3 μM) in pH 7.4 or pH 5.5 buffer, and sensor **1.13 • 5.5** ([**1.13**] = 20 μM, [**5.5**] = 1.5 μM, pH 7.4); (c) scores plot of the metal screen with the 7 factor sensor array containing **1.13 • 5.4**/**1.16 • 5.4** /**3.1 • 5.4** ([**1.13**] = 4 μM, [**1.16**] = 3 μM, [**3.1**] = 3 μM, [**5.4**] = 3 μM) in pH 7.4 or pH 5.5 buffer, and sensor **1.13 • 5.5** ([**1.13**] = 20 μM, [**5.5**] = 1.5 μM, pH 7.4). pH 7.4 = 20 mM Tris, pH 5.5 = 20 mM Bis-Tris.

5.6 Sensing in Cells

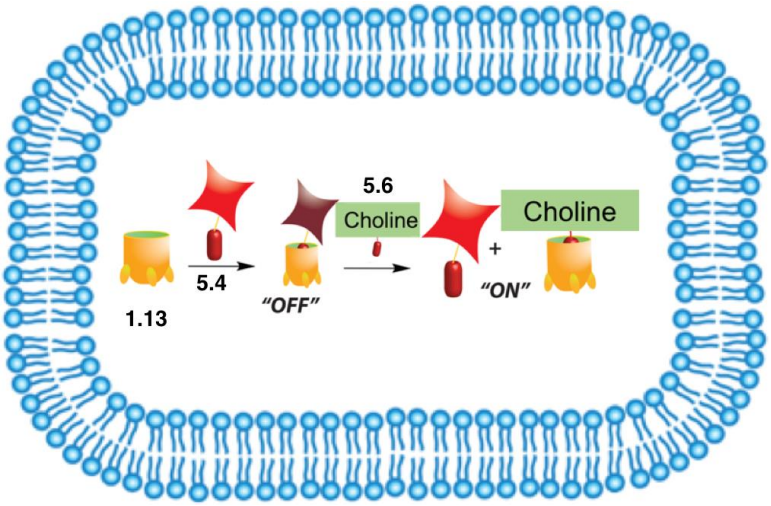

Figure 5.14: The cavitand **1.13**:fluorescent guest **5.4** sensor utilized as an IDA for choline uptake inside cells.

Previous research has shown that cavitand **1.13** is capable of inserting itself into both synthetic[14] and actual cell membranes.[15] Previous work by Ghang et. al. showed that cavitand **1.13** is also capable of transporting small molecules into cells via cavitand-mediated endocytosis.[15] Confocal microscopy can be utilized to track the cavitand within cells, however direct visualization of the host molecule is not possible. A fluorophore-tagged cavitand would be ideal for this purpose, but this molecule has proven difficult to synthesize. Guest **5.1** was first used to visualize the cavitand within a supported lipid bilayer via confocal fluorescence microscopy.[14] This same guest was then utilized with cavitand **1.13** and transported into human cervical cancer (HeLa) cells. These results were confirmed by comparing results in the presence and absence of cavitand, which determined

the efficiency of cavitand **1.13** at successfully transporting small molecules such as **5.1** inside cells. Nau et. al. have successfully performed IDA inside live cells by utilizing a host:guest complex composed of the macrocycle p-sulfonatocalix[4]arene and lucigenin (LCG).[7] Successful detection of the uptake of choline was monitored inside live Chinese hamster ovary (CHO) cells using this IDA sensor. The change in fluorescence between bound and unbound guest **5.4** is more significant than that of fluorescein guest **5.1** and its sensing mechanism is also much simpler (1:1 binding as opposed to aggregative quenching). This allows for the use of rhodamine guest **5.4** in a possible IDA sensor inside live cells. Since rhodamine guest **5.4** is also fluorescent and has a similar structure to **5.1**, it should also be able to be transported into cells via cavitand-mediated endocytosis. By incubating cells with both cavitand **1.13** and guest **5.4**, followed by a displacer molecule such as choline, studies similar to Nau et. al. to detect the intake of choline inside cells should be possible (Figure 5.14).

5.7 Rhodamine Guest Transport into Cells

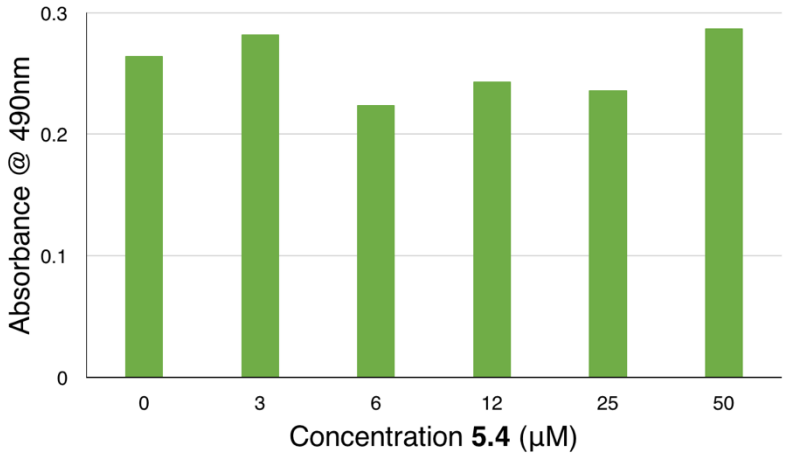

Figure 5.14: Sulforhodamine B (SRB) assay testing the cytotoxicity of rhodamine guest **5.4** inside HeLa cells. HeLa cells treated with varying concentrations of **5.4** (0-60 μM) for 24 hr. Results are an average of a triplicate assay.

In order to perform the IDA cell studies, the molecules being transported into the cells have to be tested for toxicity. Previously studies have shown that cavitand **1.13** does not pose a danger to cells at a concentration of 1 μM or lower. Using 1 μM of cavitand **1.13** does not display membrane permeability, which is needed in order to transport guests into cells. At concentration of 10 μM or higher, a 75% or lower cell proliferation is observed, indicating that cavitand shows little cytotoxicity.[14] Studies testing the cytotoxicity of guest **5.4** were also performed. As can be seen in Figure 5.14, the rhodamine guest posed no danger to cells at any concentration ranging from 0 to 60 μM. Before performing the IDA, the efficiency of guest **5.4** permeability into cells was tested in the presence and absence of cavitand **1.13**. Human cervical cancer cells (HeLa) were utilized

for these studies, which were seeded on a glass cover slip in a 24-well plate for 24 h at 37ºC before adding guest **5.4** and cavitand **1.13**. The HeLa cells were incubated with 50 μM rhodamine guest **5.4** in the presence or absence of 50 μM cavitand **1.13** for 1 h or 24 h. Confocal fluorescence microscopy and differential interference contrast (DIC) microscopy were then used in order to visualize the HeLa cells. DIC, cell nuclei (λ_{ex} = 405 nm), and fluorescent guest **5.4** (λ_{ex} = 550 nm) images were combined in order to located the **1.13** • **5.4** complex within the cells. As can be seen in Figure 5.15, in the absence of cavitand, no fluorescence is detected after incubation for one h while a slight amount of fluorescence can be seen after 24 h. Upon addition of cavitand **1.13**, an increase in fluorescence can be seen at both one and 24 h. These results indicate that deep cavitand **1.13** increases the efficiency of cell uptake of guest **5.4**.

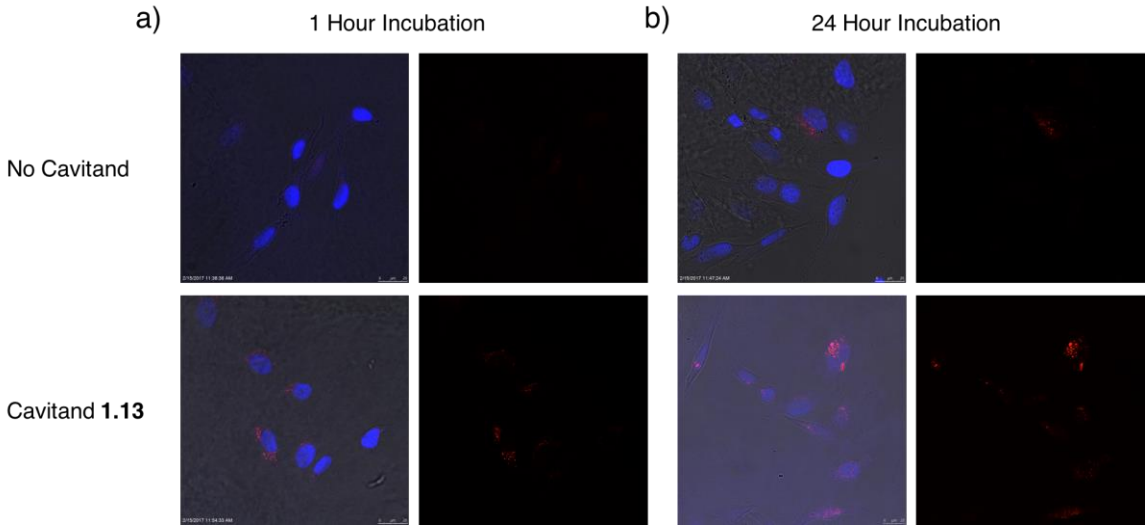

Figure 5.15: DIC/confocal fluorescence microscopy images of HeLa cells incubated with 50 μM cavitand **1.13** and 50 μM fluorescent guest **5.4** with incubation times of a) 1 h and b) 24 h.

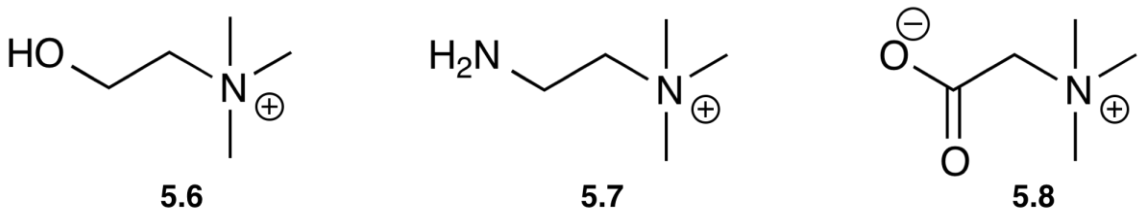

Figure 5.15: Displacer guests: choline **5.6**, cholamine **5.7** and betaine **5.8**.

Next, the IDA inside live cells was tested using the **1.13 • 5.4** sensor. After incubating HeLa cells with both cavitand **1.13** and guest **5.4** for 24 h, a displacer guest was introduced to the cells and incubated for one h. Displacers such as choline **5.6**, cholamine **5.7** and betaine **5.8** were utilized and can be seen in Figure 5.15. This sensor would be used in order to detect the uptake of these molecules by the HeLa cells. Trimethylammonium guests **5.6-5.8** are good guests for cavitand **1.13** with a binding affinity on the order of up to 10^5 M^{-1}. When the displacer molecules are taken up by the cells, they should be able to displace the rhodamine guest from the cavity of **1.13**, increasing the fluorescence. As can be seen in figure 5.16, upon the addition and incubation of choline **5.6**, an increase in fluorescence within the cells is indeed observed. This indicated the successful uptake of choline into HeLa cells followed by the displacement of the fluorescent guest **5.4** within the cells. Cholamine **5.7** and betaine **5.8** did not show efficient turn-on fluorescence after incubation with fluorophore-host incubated cells (Figure 5.16). Cholamine showed a negligible increase in fluorescence when incubated with HeLa cells containing the fluorophore guest complex and the presence of betaine **5.8** produced less fluorescence than in the absence of displacer. Betaine contains a negative carboxylate group opposite the

cavitand binding handle (-R-NMe_3^+) which can interact negatively with the negatively charged rim of cavitand **1.13**. This may prevent displacer molecule **5.8** from efficiently displacing the fluorescent guest and therefore "turning on" the signal.

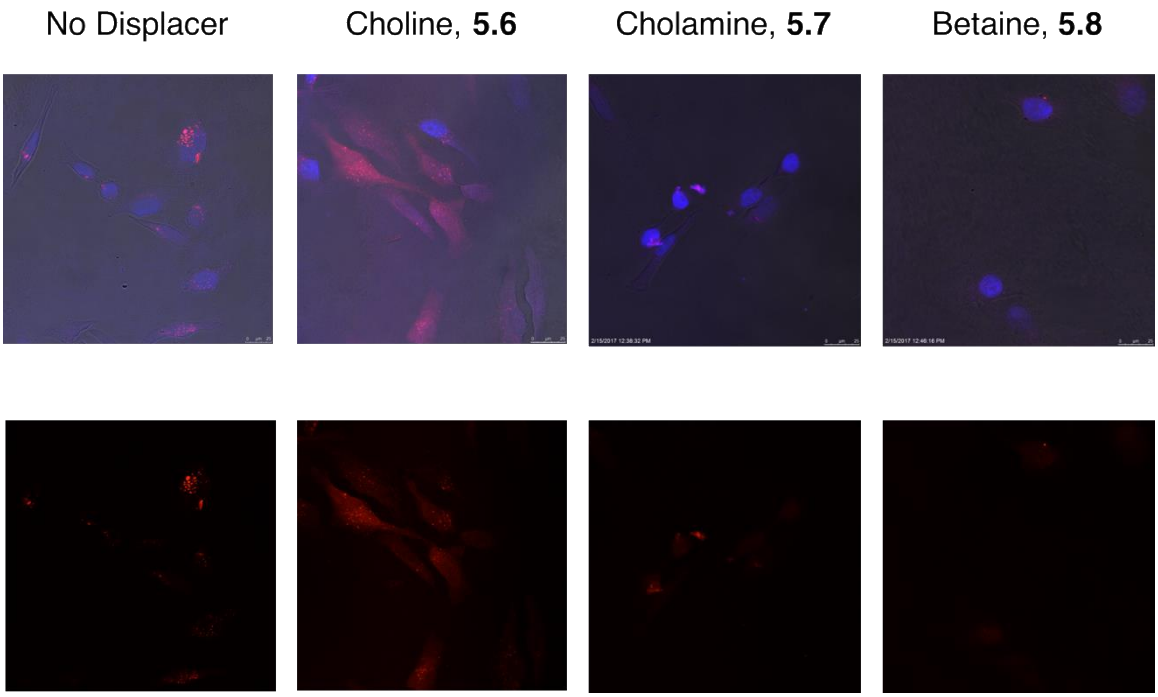

Figure 5.16: DIC/confocal fluorescence microscopy images of HeLa cells incubated with 50 μM cavitand **1.13** and 50 μM fluorescent guest **5.4** followed by 1 mM displacer guest **5.6**, **5.7** or **5.8**.

The ability of other cavitands at transporting guests across the membrane of cells was also tested. HeLa cells were incubated with guest **5.4** in the presence of cavitand **1.16** as well as cavitand **3.1** followed by addition of displacer molecule **5.6**. The results of the addition and incubation of choline with the cavitand-fluorophore impregnated HeLa cells can be observed in Figure 5.17. In the presence of the positively charged cavitand **3.1** a

visible increase in fluorescence can be observed while in the presence of the neutral rimmed cavitand **1.16** there is a negligible increase. These results showed the ability of variable cavitands to be used in IDA inside live cells.

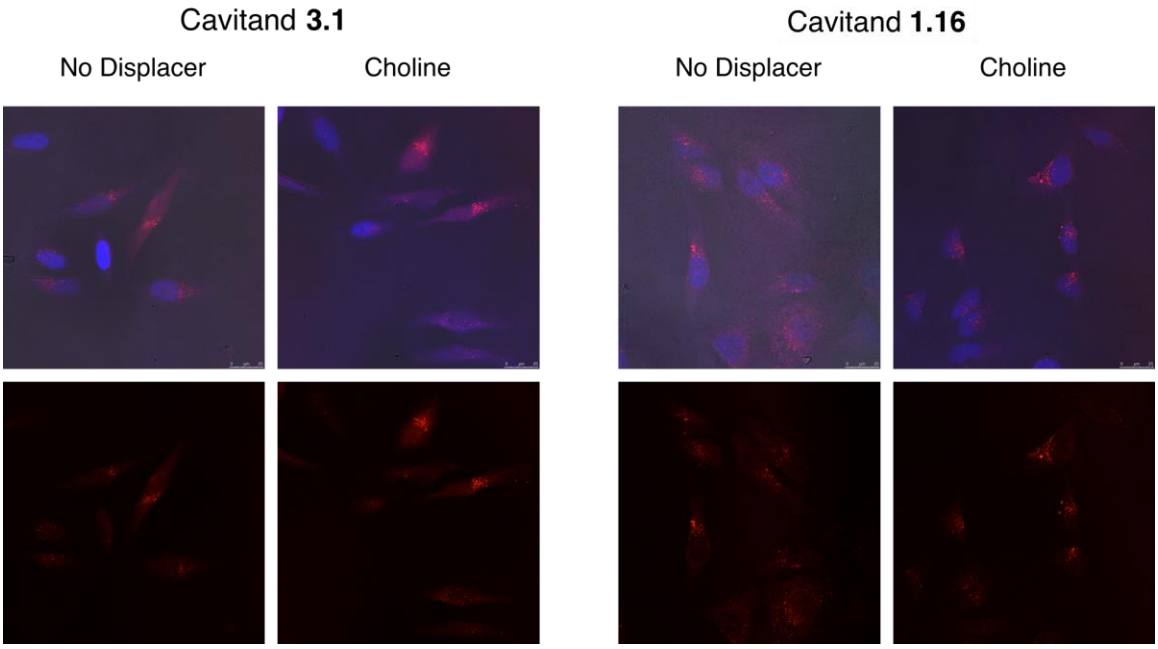

Figure 5.17: DIC/confocal fluorescence microscopy images of HeLa cells incubated with 50 μM cavitand **1.16** or **3.1** and 50 μM fluorescent guest **5.4** followed by choline displacer **5.6**.

5.8 Conclusion

The use of cavitands in indicator displacement assays has been shown in this chapter. The use of fluorescent guests and their interactions with cavitands allows for the detection of signal changes upon molecule detection. By varying the functionalities on the rim of the cavitand different interactions with guests and the surrounding environment can occur. This is helpful in producing varying interactions with desired target molecules and

creating diverse fluorescent signals. The cavitand IDA can be utilized to sense molecules differing not only in overall structure, but also molecules with slight structural differences. The detection of the uptake of molecules utilizing cavitand IDAs proved efficient for choline **5.6**. By further functionalizing the cavitand's feet and rim, more diverse sensors can be formed using deep cavitands.

5.5 References:

1. Nguyen, B.T.; Anslyn, E. V. "Indicator-Displacement Assays." *Coord. Chem. Rev.*, **2006**, *250*, 3118-3127.

2. Nguyen, B. T.; Wiskur, S. L.; Anslyn, E. V. "Using Indicator-Displacement Assays in Test Strips and to Follow Reaction Kinetics." *Org. Lett.*, **2004**, *6*, 2499-2501.

3. Wang, Y.; Li, Z. H.; Hu, D. H.; Lin, C. T.; Li, J. H.; Lin, Y. H. "Aptamer/Graphene Oxide Nanocomplex for *in situ* Molecular Probing in Living Cells." *J. Am. Chem. Soc.*, **2010**, *132*, 9274 – 9276.

4. Sun, X.; Liu, Z.; Welsher, K.; Robinson, J. T.; Goodwin, A.; Zarix, S.; Dai, H. "Nano-Graphene Oxide for Cellular Imaging and Drug Delivery." *Nano Res.*, **2008**, *1*, 203-212.

5. Mire-Sluis, A. R.; Barret, Y. C.; Devanarayan, V.; Koren, E.; Liu, H.; Maia, M.; Parish, T.; Scott, G.; Shankar, G.; Shores, E.; Swanson, S. J.; Taniguchi, G.; Weirda, D.; Zukerman, L. A. "Recommendations for the Design and Optimization of Immunoassays Used in the Detection of Host Antibodies Against Biotechnology Products." *J. Immunol. Methods.*, **2004**, *289*, 1-16.

6. Jeong, H. S.; Choi, S. M.; Kim, H. W.; Park, J. W.; Park, H. N.; Park, S. M.; Jang, S. K.; Rhee, Y. M.; Kim, B. H. "Fluorescent Peptide Indicator Displacement Assay for Monitoring Interactions Between RNA and RNA Binding Proteins." *Mol. BioSyst.*, **2013**, *9*, 948-951.

7. Norouzy, A.; Azizi, Z.; Nau, W. M. "Indicator Displacement Assays Inside Live Cells." *Angew. Chem., Int. Ed.*, **2015**, *54*, 792−795.

8. Ghale, G.; Nau, W. M. "Dyamically Analyte-Responsive Macrocyclic Host-Fluorophore Systems." *Acc. Chem. Res.*, **2014**, *47*, 2150−2159.

9. Biedermann, F.; Hathazi, D.; Nau, W. M. "Associative Chemosensing by Fluorescent Macrocycle-Dye Complexes-A Versatile Enzyme Assay Platform Beyond Indicator Displacement." *Chem. Commun.*, **2015**, *51*, 4977−4980.

10. Hof, F.; Trembleau, L.; Ullrich, E. C.; Rebek, J. Jr. "Acetylcholine Recognition by a Deep, Biomimetic Pocket." *Angew. Chem., Int. Ed.*, **2003**, *42*, 3150–3153.

11. Davidson, V. L. “Protein-Derived Cofactors. Expanding the Scope of Post-Translational Modifications.” *Biochemistry.*, **2007**, *46*, 5283−5292.

12. Perez, L.; Mettry, M.; Hinman, S. S.; Byers, S. R.; McKeating, K. S.; Caulkins, B. G.; Cheng, Q.; Hooley, R. J. “Selective Protein Recognition in Supported Lipid Bilayer Arrays by Tailored, Dual-Mode Deep Cavitand Host.” *Soft Matter.*, **2017**, *13*, 3966-3975.

13. Biros, S. M.; Ullrich, E. C.; Hof, F.; Trembleau, L.; Rebek, J., Jr. “Kinetically Stable Complexes in Water: The Role of Hydration in Hydrophobicity.” *J. Am. Chem. Soc.*, **2004**, *126*, 2870−2876.

14. Liu, Y.; Liao, P.; Cheng, Q.; Hooley, R. J. “Protein and Small Molecule Recognition Properties of Deep Cavitands in a Supported Lipid Membrane Determined by Calcination-Enhanced SPR Spectroscopy.” *J. Am. Chem. Soc.*, **2010**, *132*, 10383-10390.

15. Ghang, Y.-J.; Schramm, M. P.; Zhang, F.; Acey, R. A.; David, C. N.; Wilson, E. H.; Wang, Y.; Cheng, Q.; Hooley, R. J. “Selective Cavitand-Mediated Endocytosis of Targeted Imaging Agents into Live Cells.” *J. Am. Chem. Soc.*, **2013**, *135*, 7090−7093.

16. Li, V.; Ghang, Y.-J.; Hooley, R. J.; Williams, T. J. “Non-Covalent Self Assembly Controls the Relaxivity of Magnetically Active Guests.” *Chem. Commun.*, **2014**, *50*, 1375-1377.

17. Liu, Y.; Perez, L.; Mettry, M.; Easley, C.J.; Hooley, R. J.; Zhong, W. "A Self-Aggregating Deep Cavitand Acts as a Fluorescence Displacement Sensor for Lysine Methylation." *J. Am. Chem. Soc.*, **2016**, *138*, 10746-10749.

18. Ghang, Y.-J.; Perez, L.; Morgan, M. A.; Si, F.; Hamdy, O. M.; Beecher, C. N.; Larive, C. K.; Julian, R. R.; Zhong, W.; Cheng, Q.; Hooley, R. J. “Anionic Deep Cavitands Enable the Adhesion of Unmodified Proteins at a Membrane Bilayer.” *Soft Matter*, **2014**, *10*, 9651-9656.

19. Carnegie, R. S.; Gibb, C. L.; Gibb, B. C. “Anion Complexation and the Hofmeister Effect.” *Angew. Chem., Int. Ed.*, **2014**, *53*, 11498-11500.

20. A. Hennig, H. Bakirci and W. M. Nau, Nat. Methods, 2007, 4, 629-632

21. You, L.; Zha, D.; Anslyn, E. V. “Recent Advances in Supramolecular Analytical Chemistry Using Optical Sensing.” *Chem. Rev.*, **2015**, *115*, 7840-7892.

22. Jiang, Z.; Le, N. D. B.; Gupta, A.; Rotello, V. M. “Cell Surface-Based Sensing with Metallic Nanoparticles.” *Chem. Soc. Rev.,* **2015**, *44*, 4264-4274.

23. Ashby J.; Flack, K.; Jimenez, L. A.; Duan, Y.; Khatib, A.-K.; Somlo, G.; Wang, S. E.; Cui, X.; Zhong, W. “Distribution Profiling of Circulating MicroRNAs in Serum.” *Anal. Chem.*, **2014**, *86*, 9343-9349.

24. Jurs, P. C.; Bakken, G. A.; McClelland, H. E. “Computational Methods for the Analysis of Chemical Sensor Array Data From Volatile Analytes.” *Chem. Rev.*, **2000**, *100*, 2649-2678.

25. Liu, Y.; Perez, L.; Mettry, M.; Gill, A. D.; Byers, S. R.; Easley, C. J.; Bardeen, C. J.; Zhong, W.; Hooley, R. J. “Site Selective Reading of Epigenetic Markers by Dual –Mode Synthetic Receptor Array.” *Chem. Sci.*, **2017**, *8*, 3960-3970.

26. Weiss, D. J.; Rehkaemper, M.; Schoenberg, R.; McLaughlin, M.; Kirby, J.; Campbell, P. G. C.; Arnold, T.; Chapman, J.; Peel, K.; Gioia, S. “Application of Nontraditional Stable-Isotope Systems to the Study of Sources and Fate of Metals in the Environment.” *Environ. Sci. Technol.*, **2008**, *42*, 655-664.

27. Traudt, E. M.; Ranville, J. F.; Meyer, J. S. “Acute Toxicity of Ternary Cd-Cu-Ni and Cd-Ni-Zn Mixtures to *Daphnia Magna*: Dominant Metal Pairs Change along a Concentration Gradient.” *Environ. Sci. Technol.*, **2017**, *51*, 4471-4481.

28. Nys, C.; Versieren, L.; Cordery, K. I.; Blust, R.; Smolders, E.; De Schamphelaere, K. A. C. “Systematic Evaluation of Chronic Metal-Mixture Toxicity to Three Species and Implications for Risk Assesment.” *Environ. Sci. Technol.*, **2017**, *51*, 4615-4623.

29. Cui, L.; Wu, J.; Ju, H. “Electrochemical Sensing of Heavy Metal Ions with Inorganic, Organic, and Bio-Materials.” *Biosens. Bioelectron.*, **2015**, *63*, 276-286.

30. Saidur, M. R.; Aziz, A. R. A.; Basirun, W. J. “Recent Advances in DNA-Based Electrochemical Biosensors for Heavy Metal Ion Detection: A Review.” *Biosens. Bioelectron.*, **2017**, *90*, 125-139.

31. Bakirci, H.; Koner, A. L.; Nau, W. M. “Binding of Inorganic Cations by p-sulfonatocalix[4]arene Monitored Through Competitive Fluorophore Displacement in Aqueous Solution.” *Chem. Commun.*, **2005**, *43*, 5411-5413.

32. Aoki, S.; Kagata, D.; Shiro, M.; Takeda, K.; Kimura, E. “Metal Chelation-Controlled Twisted Intramolecular Charge Transfer and Its Application to Fluorescent Sensing of Metal Ions and Anions.” *J. Am. Chem. Soc.*, **2004**, *126*, 13377-13390.

33. Liu, Y.; Perez, L.; Gill, A. D.; Mettry, M.; Li, L.; Wang, Y.; Hooley, R. J.; Zhong, W. "Site-Selective Sensing of Histone Methylation Enzyme Activity via an Arrayed Supramolecular Tandem Assay." *J. Am. Chem. Soc.*, **2017,** *139, 10964-10967.*

34. Korbakov, N.; Timmerman, P.; Lidich, N.; Urbach, B.; Sa’ar, A.; Yitzchaik, S. “Acetylcholine Detection at Micromolar Concentrations with the Use of an Artificial Receptor-Based Fluorescence Switch.” *Langmuir*, **2008**, *24*, 2580-2587.

35. Fernańdez-Abad, S.; Pesseĝo, M.; Basílio, N.; García-Río, L. “Counterion-Controlled Self-Sorting in an Amphiphilic Calixarene Micellar System.” *Chem. Eur. J.*, **2016**, *22*, 6466-6470.

36. Sun, S.; Yuan, Y.; Li, Z.; Zhang, S.; Zhang, H.; Peng, X. “Interaction of Hemicyanine Dye and its Derivative with DNA and Curcubit[7]uril.” *New J. Chem.*, **2014**, *38*, 3600-3605.

37. Mettry, M.; Moehlig, M. P.; Hooley, R. J. “Synthesis, Guest Binding, and Metal Coordination of Functionalized Self-Folding Deep Cavitands.” *Org. Lett.*, **2015**, *17*, 1497-1500.

Chapter 6: Steroid Sensing

6.1 Introduction

Because cavitands can interact with molecules in varying manners, they are good hosts for the use in sensors and have been utilized to detect analytes such as metal cations[1] and post-translational modifications (PTM)[2]. Steroids are present in all biological systems, playing important roles in maintaining membrane fluidity as well as acting as messengers.[3,4,5] Steroids act as hormones[6] in the body and are commonly employed for medicinal uses[7] such as anti-inflammatory drugs and contraceptives, as well as performance enhancing purposes.[8] A vast number of structurally diverse steroids and their metabolites can be found in biofluids.[9,10] Mass spectrometry is commonly employed for steroid detection, however the employment of this technique is complicated by the presence of metabolites of similar size and identical mass.[11,12,13] Steroids are highly hydrophobic in nature and steroid binding-receptors rely heavily on the hydrophobic effect. Synthetic receptors such as calixarenes,[14] cyclophanes[15] and cyclodextrins[16] can effectively trap steroid molecules within their hydrophobic cavities. Although these hosts can bind these hydrophobic structures, they suffer from lack of selectivity between different steroids. Cucurbiturils have been recently employed for the detection of steroids via IDA and up to nanomolar steroid binding has been reported,[17] however, derivatized cucurbiturils are synthetically challenging to obtain.[18] Even though steroids do not contain the trimethylammonium (-R-NMe_3^+) binding handle that is most favorable for selective cavitand pocket recognition,[19] cavitands can be utilized to detect these structures through

an aggregation-based sensor system. Previous studies using cavitand receptors have shown their ability at detecting small changes in structure in highly similar molecules.[20] This same concept can be applied to steroids with highly similar structures. The success of cavitands in sensors is derived from their diverse modes of interaction with desired analytes.[1,21] The hydrophobic, aromatic pocket allows for the binding of guests of proper size that are cationic as well as hydrophobic while the negative charge on the water-soluble deep cavitand **1.13** also allows for electrostatic interactions between host and analyte.[22]

6.2 Steroid Sensor Optimization

The main components of the steroid sensor are tetracarboxylate cavitand **1.13**, and two cationic fluorescent guests: fluorescein **5.1** and trans-4-[4-(dimethylamino)styryl]-1-methylpyridinium iodide (DSMI) **5.5** (Figure 6.1) as well as cationic metals. The two fluorescent, reporter molecules have micromolar affinity to cavitand **1.13** and have been previously used in the selective array-based sensing of modified histone peptides.[16,18]

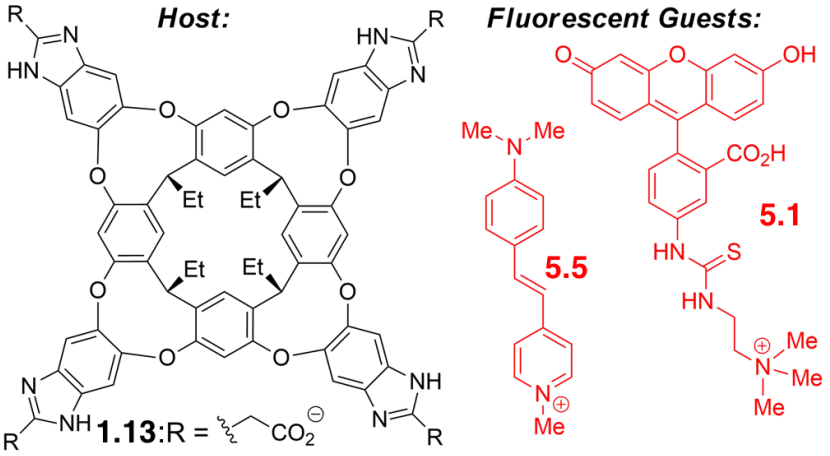

Figure 6.1: Structure of sensor components, cavitand host **1.13** and fluorophore guests **5.1** and **5.5**.

The sensing mechanism is different depending on the fluorescent guest used. DSMI guest **5.5** experiences an increase in fluorescence when bound in the cavity of **1.13**[17] while fluorescein guest **5.1** displays quenching due to aggregation.[1] The fluorescence response of the system changes depending on the surrounding environment. Varying the pH or adding ions such as cationic metal salts can alter the fluorescence signal. Aggregation of the cavitand:fluorophore complex alters the fluorescence response, therefore, molecules capable of altering the aggregation of the system could be selectively sensed by the host:fluorophore:metal complex. As previously stated, steroids are hydrophobic in nature and are capable of introducing themselves into lipid environments. The addition of steroids to the host:fluorophore:metal complex environment has the possibility of altering the interactions of the system and causing a change in the fluorescence signal emitted. Six steroids with minimal structural differences were tested using the cavitand sensor (Figure 6.2). Steroid hormones estrone (EO), β-estradiol (EOL) and progesterone (PG) vary at the 17 position as well as in the A ring, while anabolic androgenic steroids stanozolol (STA), 17-α-methyltestosterone(MT) and methandienone (MD) vary only at the A ring. STA, MT and MD are also synthetic steroids used as performance enhancers.[6]

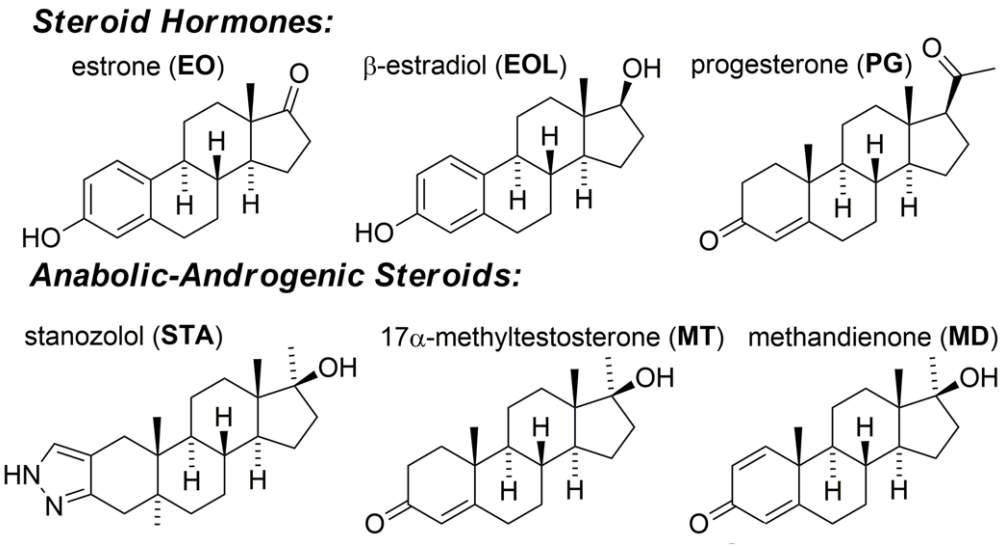

Figure 6.2: The steroid substrates used, displaying their structural similarities.

Initial studies were performed in order to see the effect of steroid addition to fluorophore **5.1**. As can be seen in Figure 6.3, the change in fluorescence response is not only dependent on the steroid but also the pH and buffer used. Tris and PBS buffers maintain a pH of 7.4 while the pH of the Bis-Tris buffer is 5.5. The addition of all six steroids to **5.1** does not change the fluorescence signal significantly at pH 5.5 (in Bis-Tris). The same is true in Tris buffer (pH 7.4), except in the presence of estradiol, which causes an increase in fluorescence over double that of the fluorophore alone. In PBS buffer EO, PG and MD also cause significant increase in fluorescence.

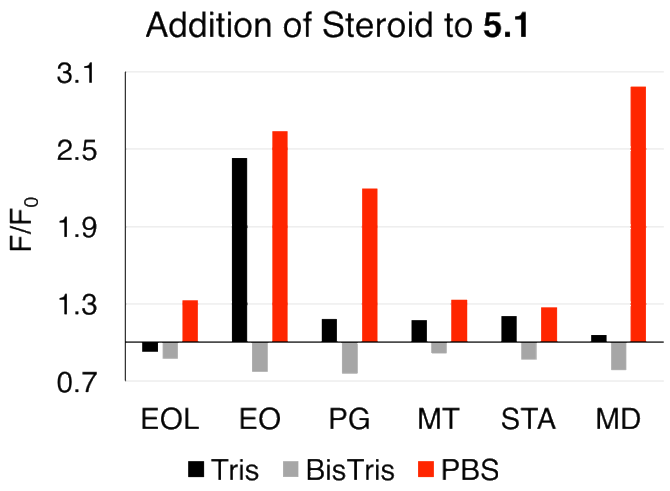

Figure 6.3: The effect of steroid addition on the fluorescence response of fluorophore guest **5.1**. [**5.1**] = 3 μM, pH of Tris and PBS = 7.4 and pH of Bis-Tris = 5.5. The signal is normalized to the fluorescence of **5.1** alone.

Next, the effect of steroid addition to the cavitand **1.13**: guest **5.1** complex was also studied in the same three buffers at varying pHs. The fluorescence response was normalized to the emission of the cavitand **1.13**: fluorophore **5.1** complex as can be seen in Figure 6.4. Similar quenching patterns as in the absence of cavitand **1.13** (Figure 6.3) are observed in Tris, pH 7.4 and Bis Tris, pH 5.5. In the presence of Tris (pH 7.4), EO, once again, causes a large increase in fluorescence in the presence of cavitand while the other steroids cause negligible changes. This signal change is due to the interaction between the fluorophore and steroid (Figure 6.4a). In PBS, the presence of cavitand causes an increase in fluorescence signal for EO, PG, STA and MD while EOL and MT experience a slight quenching (Figure 6.4b) and an overall quenching pattern is observed in the presence of Bis-Tris, pH 5.5 (Figure 6.4c).

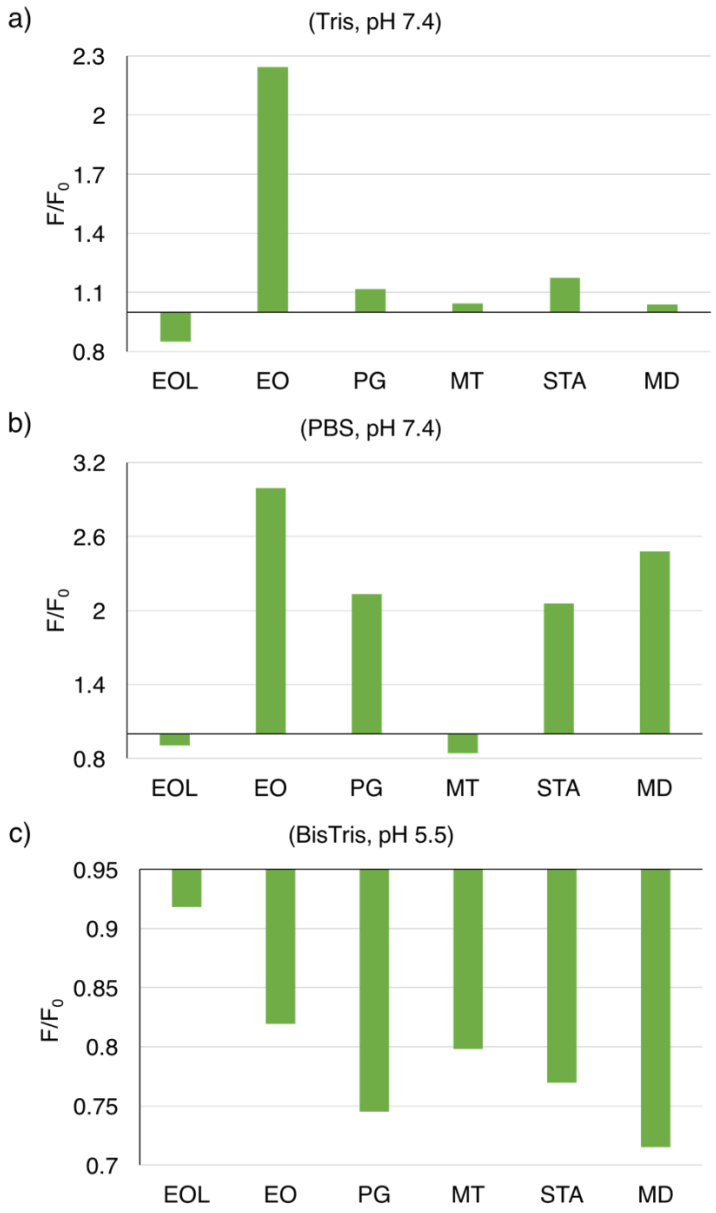

Figure 6.4: The effect of steroid addition to the **1.13 • 5.1** complex in a) Tris buffer, pH 7.4; b) PBS buffer, pH 7.4; c) Bis Tris buffer, pH 5.5. [**1.13**] = 20 μM, [**5.1**] = 3 μM, pH of Tris and PBS = 7.4 and pH of Bis Tris = 5.5. The signal is normalized to the fluorescence of the **1.13 • 5.1** complex.

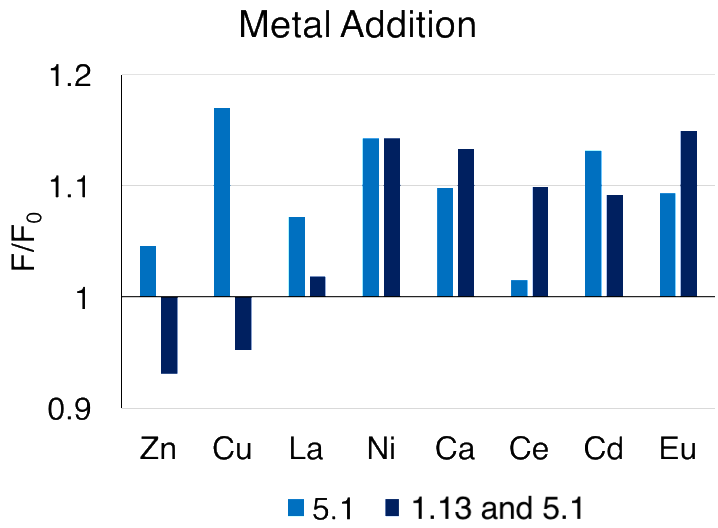

Figure 6.5: The effect of metal addition addition to the **5.1** and the **1.13 • 5.1** complex in tris buffer, pH 7.4. [**1.13**] = 20 μM, [**5.1**] = 3 μM, [Metal] = 50 μM. The signal is normalized to the fluorescence of the **1.13 • 5.1** complex.

Next, a metal screen was performed in order to analyze the effect of steroid addition to the cavitand:fluorophore:metal complex. Previous studies have shown the effects of metals on the cavitand **1.13**:rhodamine guest (**5.4**) complex. Since fluorescein experiences a similar quenching mechanism as rhodamine, studies were performed for guest **5.1** in order to observe the effect of metals on the aggregative **1.13 • 5.1** complex (Figure 6.5). Eight metals were tested for their quenching effects on the sensor, these metals varied from early (Zn^{2+}, Cu^{2+}, Ni^{2+}) and late (Cd^{2+}) transition metals, alkaline earth (Ca^{2+}) and rare earth metals (La^{3+}, Ce^{3+}, Eu^{3+}). All of these metals displayed the ability to bind to the rhodamine fluorophore:cavitand complex, although with varying affinities in aqueous solution: Cu^{2+} has a K_d of 8 μM while Ni^{2+} has a K_d of 80 μM. The quenching abilities of the metal ions also vary as can be seen in Figure 6.5. While Zn^{2+} and Cu^{2+} cause a quenching effect in the

presence of cavitand, the other metals display an increased fluorescence under the same conditions.

Finally, the effects of the steroid solvent were tested in order to see whether the sensor is affected in its presence. The hydrophobic steroids do not dissolve in water, so solvents such as dimethylsulfoxide (DMSO) or dimethoxyethane (DME) are employed in order to make the steroid solutions. DMSO was initially used for the sensor studies, however, the steroids used are commercially available dissolved in DME. An overall quenching pattern can be observed upon steroid addition in the presence of either solvent to the cavitand:fluorophore:metal complex. In DMSO, a slight fluorescence increase is observed in the presence of europium (Eu^{3+}) while the same is true for copper (Cu^{2+}) in DME. The fluorescence increase in each case is negligible, however, and the amount of quenching for the rest of the metals varies slightly depending on the solvent (Figure 6.6). Similar studies were also performed by Adam Gill using DSMI guest **5.5** in order to determine the solvent and metal effects on the fluorophore: cavitand sensor (see Chapter 7). DSMI guest **5.5** works better in the sensor, it displays a greater change in fluorescence (up to 11-fold increase) when exposed to the sensor components. Using these observations, the optimized sensor conditions were obtained and steroid sensing studies were performed.

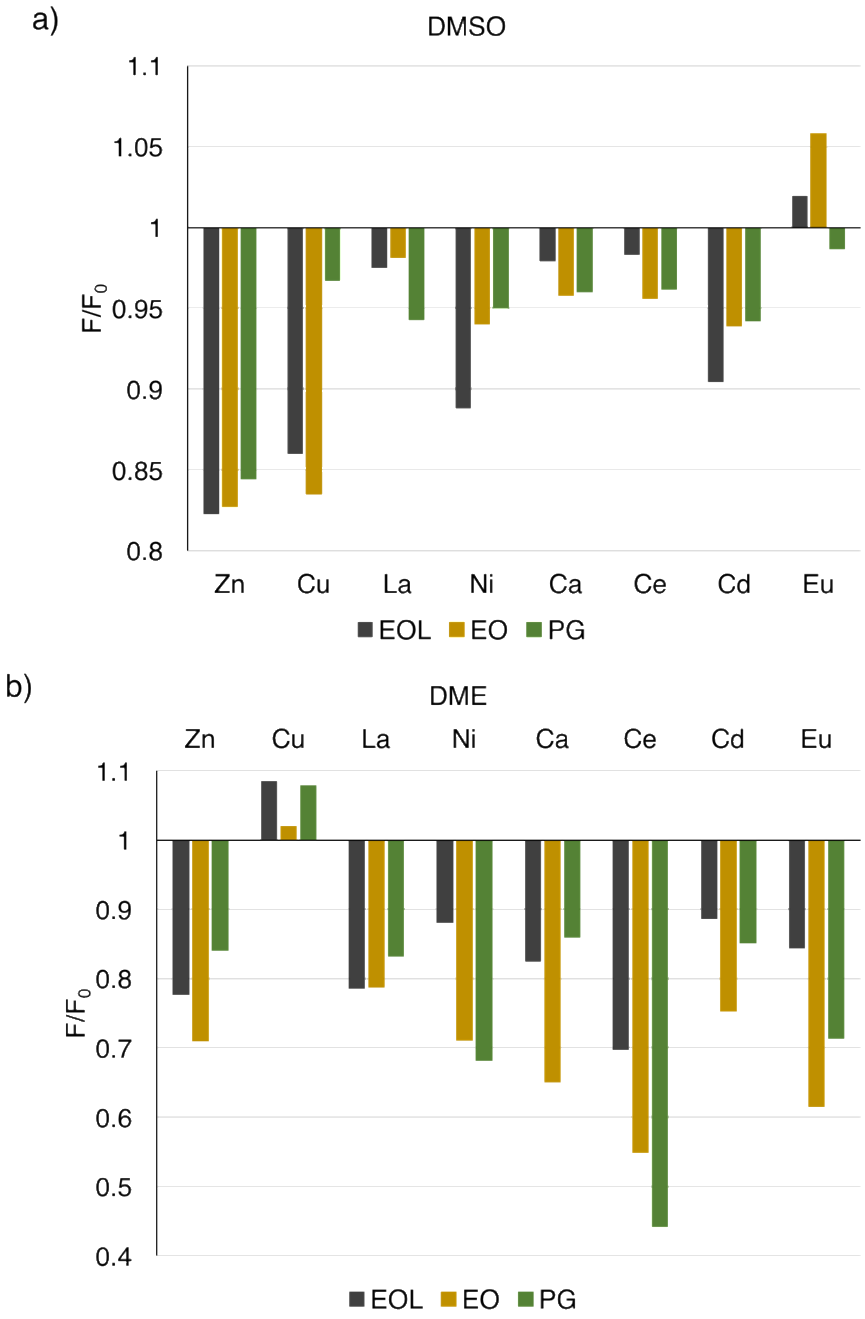

Figure 6.6: The effect of steroid addition to the **1.13 • 5.1 •** metal complex in tris buffer, pH 7.4 in the presence of 10 % a) DMSO and b) DME. [**1.13**] = 20 μM, [**5.1**] = 3 μM, [Metal] = 50 μM [steroid] = 100 μM. The signal is normalized to the fluorescence of the **1.13 • 5.1 •** metal complex.

6.3 Steroid Sensing

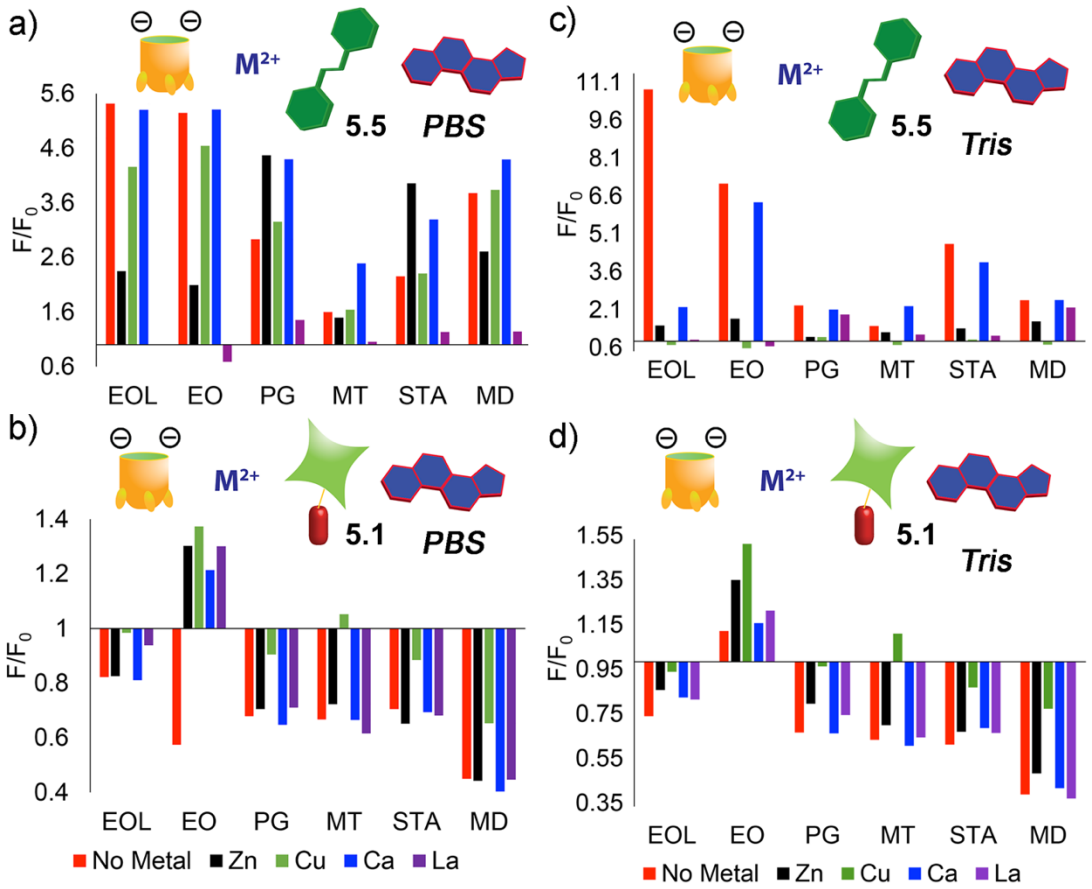

Figure 6.7: Fluorescence response changes upon addition of steroid to the **1.13 • 5.1/5.5 •** Metal sensor in varying buffer conditions. a) Cavitand **1.13**, guest **5.5**, metals Cu^{2+}, Zn^{2+}, La^{3+} and Ca^{2+} in PBS buffer; b) Cavitand **1.13**, guest **5.1**, metals Cu^{2+}, Zn^{2+}, La^{3+} and Ca^{2+} in PBS buffer; c) Cavitand **1.13**, guest **5.5**, metals Cu^{2+}, Zn^{2+}, La^{3+} and Ca^{2+} in tris buffer; d) Cavitand **1.13**, guest **5.1**, metals Cu^{2+}, Zn^{2+}, La^{3+} and Ca^{2+} in tris buffer.

As can be seen in Figure 6.7, different fluorescence responses were obtained upon addition of steroid to the cavitand:fluorophore complex in the absence and presence of metal. The red bars in Figure 6.7 display the fluorescence change upon steroid addition to the cavitand:fluorophore complex in the absence of metal. Upon addition of varying heavy

metals, the fluorescent signals emitted are differentiated depending on the metal introduced. The metals utilized for these studies (Zn, Cu, Ca and La) were chosen after performing a metal screen (Figure 6.5 and 6.6) on both fluorophores **5.1** and **5.5**. An overall increase in fluorescence is observed upon steroid addition to the DSMI **5.5** sensor. EOL addition to the **1.13 • 5.5** complex (in the absence of metal) in Tris buffer causes an 11-fold increase in fluorescence, observed in Figure 6.7c. In comparison, the fluorescein (**5.1**) sensor displayed an overall quenching effect upon steroid addition (Figure 6.7 b/d). In particular, a 70% loss of fluorescence was observed upon addition of MD in the presence of Tris buffer (Figure 6.7d).

As can be seen in Figure 6.7, the sensor's multiple component combinations cause diverse signal changes. These responses can be analyzed using linear discriminant analysis to create a scatter plot showing the discrimination between the varying steroids. The sensor components were varied in order to analyze their importance and effect on the fluorescence response of the sensor. As can be seen in Figure 6.8, experiments were performed in both the presence and absence (Figure 6.8 a) of cavitand host **1.13** as well as in the presence of a single fluorophore (Figure 6.8 b/c) and with the full components (Figure 6.8d). The full array is composed of cavitand **1.13**, the two fluorophore guests **5.1** and **5.5**, four metals (Zn^{2+}, Cu^{2+}, Ca^{2+}, La^{3+}) as well as two buffer conditions (PBS and Tris) at pH 7.4.

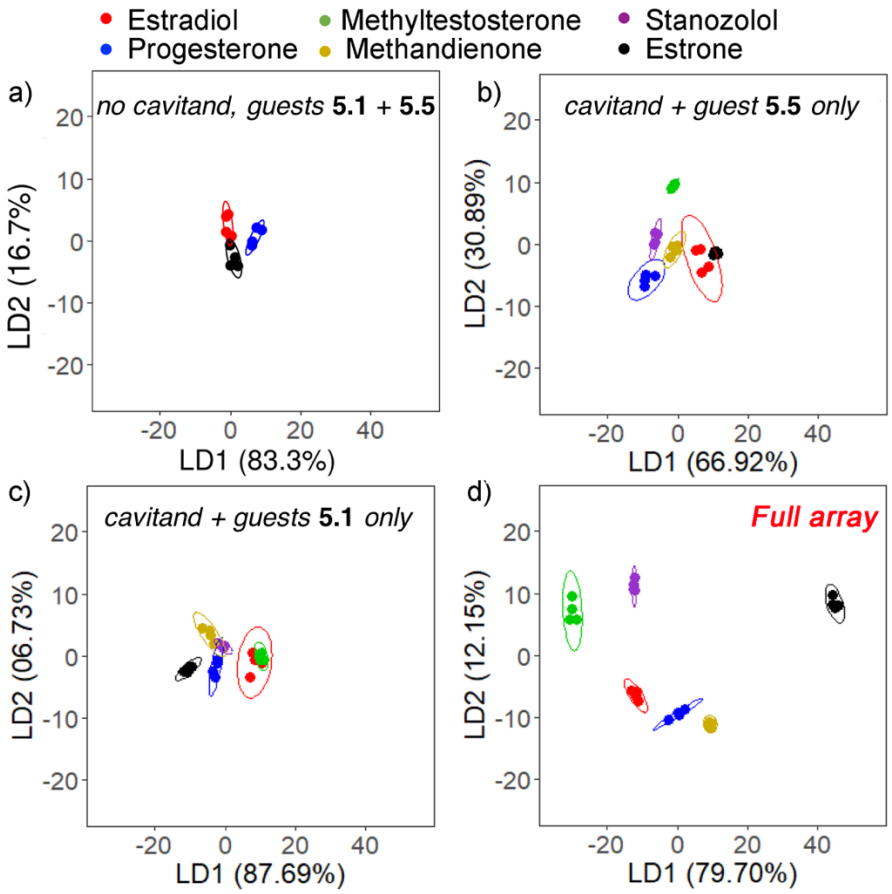

Figure 6.8: LDA scores plots of the selective steroid sensing with: a) no cavitand, guests **5.1** and **5.5**, Cu^{2+}, Zn^{2+}, La^{3+}, Ca^{2+}, 20 mM PBS, pH =7.4 (8 components); b) cavitand **1.13**, guest **5.5**, Cu^{2+}, Zn^{2+}, La^{3+}, Ca^{2+}, 20 mM PBS, pH =7.4 (5 components); c) cavitand **1.13**, guest **5.1**, Cu^{2+}, Zn^{2+}, La^{3+}, Ca^{2+}, 20 mM PBS, pH =7.4 (5 components); d) cavitand **1.13**, guest **5.1** or **5.5**, Cu^{2+}, Zn^{2+}, La^{3+}, Ca^{2+}, 20 mM PBS, pH =7.4, 20 mM Tris, pH =7.4, or 20mM BisTris, pH = 5.5 (30 components). [Steroids] = 100 µM, [**1.13**] = 20 µM, [**5.1**] = 3.0 µM, [M^{2+}] = 50 µM, [**5.1**] = 1.5 µM. The error ellipses were obtained at 95% confidence interval.

The cavitand host **1.13** is essential for the steroid sensor, as can be seen in Figure 6.8a, where no discrimination is observed between EO, EOL and PG in the absence of cavitand **1.13**. Steroid discrimination is also more efficient in the presence of both fluorescent hosts, as can be seen by comparison of Figure 6.8d to 6.8b/c. Full separation is observed using the full 30-component sensor, even between steroids that are very similar

in structure such as MD and MT which differ only by a double bond. To simplify our steroid sensor array, the number of components were varied further in order to determine a minimal combination that would still yield efficient discrimination. As can be seen in Figure 6.8, cavitand **1.13** and both fluorophores are necessary for efficient steroid discrimination, therefore these two components are essential to the minimal array.

In the absence of metals, steroid discrimination is not as efficient, especially between MD, STA and PG (Figure 6.9a). The addition of a single metal (Cu^{2+}), to give a 4-component system did not yield overall efficient discrimination. Although EOL, EO and MT were separated more efficiently, MD, STA and PG were still overlapped. The addition of another metal (Zn^{2+}), to give a 5-component array, effected complete steroid separation, as can be seen in Figure 6.9c. Of course, as is expected, increasing the number of components (adding another metal) gives even better discrimination and separation between the similarly structured steroids (Figure 6.9d), but only 5-components are necessary for complete differentiation of steroids.

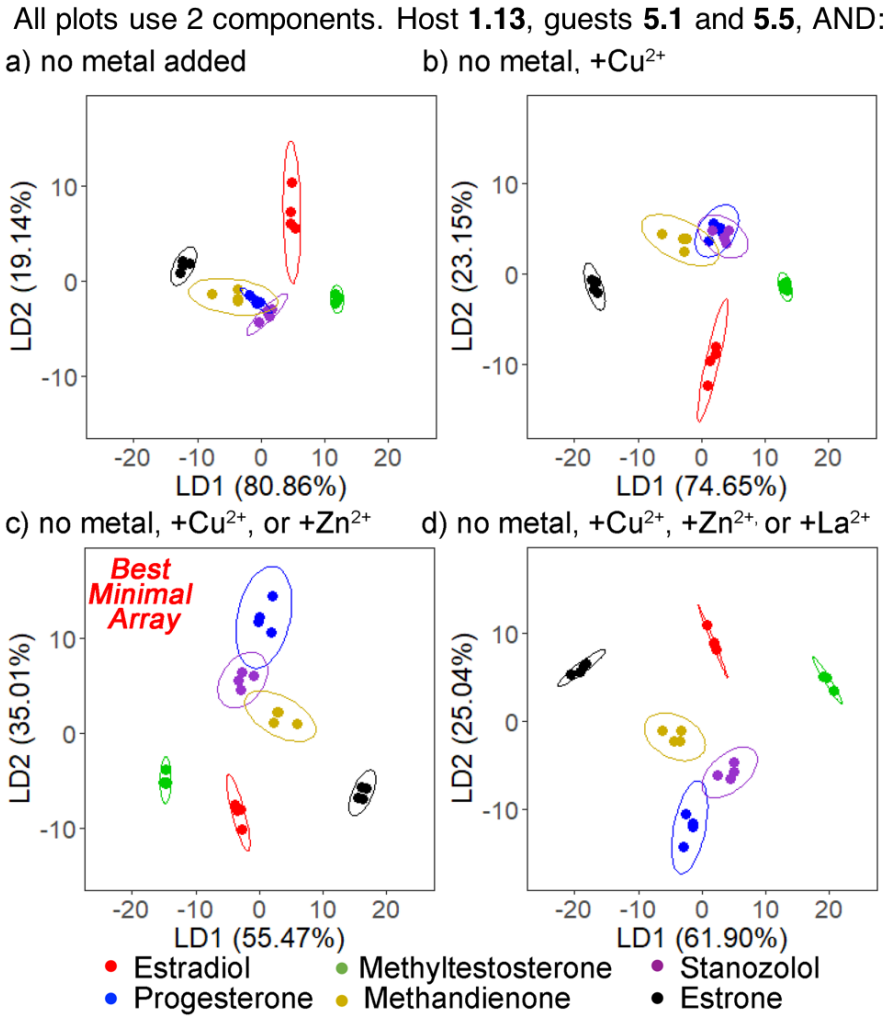

Figure 6.9: LDA scores plots of the selective steroid sensing with: a) cavitand **1.13**, guest **5.1** or **5.5**; b) cavitand **1.13**, guest **5.1** or **5.5**, Cu^{2+}; c) cavitand **1.13**, guest **5.1** or **5.5**, Cu^{2+}, Zn^{2+}; d) cavitand **1.13**, guest **5.1** or **5.5**, Cu^{2+}, Zn^{2+}, La^{3+}, 20 mM PBS, pH =7.4, [steroids] = 100 μM, [**1.13**] = 20 μM, [**5.1**] = 3.0 μM, [M^{2+}] = 50 μM, [**5.5**] = 1.5 μM. The error ellipses were obtained at 95% confidence interval.

The minimal 5-component array was then tested in a biological setting, human urine. The procedure was performed just as it was in the buffered solutions and the components used were cavitand **1.13**, guests **5.1** and **5.5**, no metal, Zn^{2+} and Cu^{2+}, and human urine as the medium. The fluorescence responses were subjected to LDA and the

data can be observed in Figure 6.10. The biological and multicomponent nature of human urine makes it a complex system to perform the steroid sensing studies. As can be seen in Figure 6.10a, the discrimination between steroids was not as efficient in this complex medium when compared to the controlled buffered system. The sensor was not able to discriminate between stanozolol (STA) and methyltestosterone (MT), which were colocalized on the LDA plot. Good discrimination was observed between the highly similar MT and MD, however. It should be possible to obtain complete separation between the steroids in urine if the number of sensor components were increased, however, this study only utilized the minimal array.

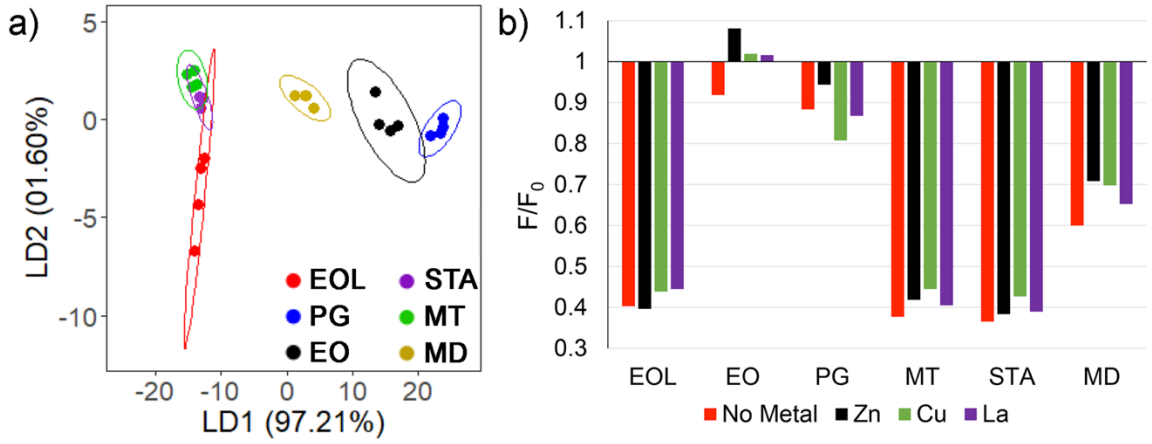

Figure 6.10: Discrimination between steroids in urine. a) LDA scores plots of the selective steroid sensing in urine with the minimal array, cavitand **1.13**, guest **5.1** or **5.5**, Cu^{2+}, Zn^{2+}; b) fluorescence response changes upon addition of 100 μM steroid to the individual **1.13** • **5.1** • Metal sensor in urine. [Steroids] = 100 μM, [**1.13**] = 20 μM, [**5.1**] = 3.0 μM, [M^{2+}] = 50 μM, [**5.5**] = 1.5 μM. The error ellipses were obtained at 95% confidence interval.

The efficacy of the cavitand • fluorophore • metal sensor array at discriminating between highly similarly structured steroids, even in biological medium, is due to the multiple interactions between all the sensor components. Even though the steroids do not bind the cavity of the host (see chapter 7) and are not able to displace the fluorophore guest, they are still able to cause a fluorescence signal change by increasing the aggregation between the cavitand • fluorophore complex. The emission profiles of the cavitand complex of both **5.1** and **5.5** are controlled by their self-aggregation, and adding steroid to the system increases this aggregation, as can be seen in Figure 6.11, and therefore increases the fluorescence emission of **1.13 • 5.5** while further quenching that of **1.13 • 5.1**. The steroids cause minimal changes in emission in the presence of only the fluorophore, with the exception of estradiol which increased the emission significantly in the presence of **5.1**.

The addition of metal ions to the system can cause a decrease in fluorescence via multiple pathways. The metal ions have the ability of complexing to the rim of the cavitand, decreasing the affinity of the fluorescent guest in the pocket of the cavitand. NMR studies were performed in the presence of metals (see chapter 7) and showed that the metals also further enhance the aggregation process, effecting fluorescence signal change. Different metals showed varying affinities and quenching patterns of the cavitand • fluorophore complex. Filled shell metals such as Zn^{2+} displayed minimal quenching compared to Cu^{2+} which fully quenches both fluorophore guests. The addition of metal ions modulate the fluorescence response of the cavitand • fluorophore complex to steroids in the aggregated state. The varying responses, and therefore fluorescence variation between metals allows for the selectivity using LDA. Even though the cavitand • fluorophore complex has the

ability to detect steroids individually, the addition of varying metals ions allows for signal modulation and therefore selective discrimination between the similar steroid structures.

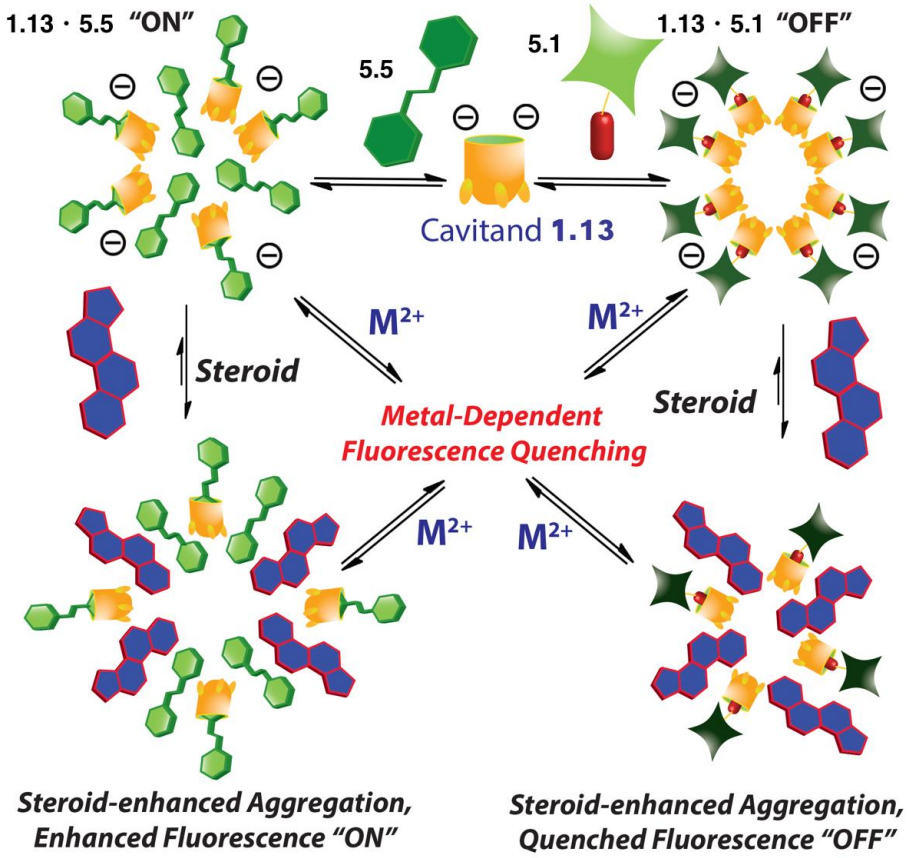

Figure 6.11: Illustration of the possible aggregation modes of the **1.13 • 5.1/5.5/M^{2+}** complexes, and the effects of steroid addition on the emission profiles.

6.4 Conclusion

A steroid sensor with the ability to differentiate between highly similar structures such as 17-a-methyltestosterone (MT) and methandienone (MD) was developed using cavitand **1.13** and fluorescent hosts **5.1** and **5.5**. The multiple modes of interaction between the cavitand and sensor components enhances the efficiency of the sensor. Using its pocket, the cavitand can bind the cationic fluorescent hosts, which cause aggregative fluorescent quenching in the case of **5.1** and an increase in fluorescence for **5.5**. The addition of steroid causes a further increase in aggregation which then increases the signal change effected by the aggregation of the cavitand • fluorophore complex. By adding metals into the system, a decrease in fluorescence can be observed due to the metal decreasing the affinity of the fluorophore guest in the pocket of the cavitand as well as increased aggregation of the sensor components. The combination of the different sensor components and the analysis of the data using LDA allows for the efficient discrimination between the different steroids. The more components are added to the system, the better discrimination is attained. Preliminary studies determined that cavitand **1.13** and both fluorophores are necessary for better steroid discrimination. The application of only two metals (Zn^{2+} and Cu^{2+}) give the best minimal array, which was utilized in human urine to show the application of the steroid sensor in biological settings such as urine.

6.5 References

1. Liu, Y.; Mettry, M.; Gill, A. D.; Perez, L.; Zhong, W.; Hooley, R. J. "Selective Heavy Element Sensing with a Simple Host: Guest Fluorescent Array" *Anal. Chem.* **2017**, *89*, 11113-11121.

2. Liu, Y.; Perez, L.; Mettry, M.; Easley, C. J.; Hooley, R. J.; Zhong, W. "A Self-Aggregating Deep Cavitand Acts as a Fluorescence Displacement Sensor for Lysine Methylation" *J. Am. Chem. Soc.* **2016***, 138,* 10746-10749.

3. Tsai, M.; O'Malley, B.W. "Molecular Mechanisms of Action of Steroid/Thyroid Receptor Superfamily Members" *Annu. Rev. Biochem.* **1994**, *63*, 451-486.

4. Whiting, K. P.; Restall, C. J.; Brain, P. F. "Steroid Hormone-Induced Effects on Membrane Fluidity and Their Potential Roles in Non-Genomic Mechanisms" *Life Sci.* **2000**, *67*, 743-757.

5. Brann, D. W.; Hendry, L. B.; Mahesh, V. B. "Emerging Diversities in the Mechanism of Action of Steroid Hormones" *J. Steroid Biochem. Mol. Biol.* **1995**, *52(2)*, 113-133.

6. Hall, J. M.; Couse, J. F.; Korach, K. S. "The Multifaceted Mechanisms of Estradiol and Estrogen Receptor Signaling" *J. Biol. Chem.* **2001**, *276*, 36869-36872.

7. Turgeon, J. L.; McDonnell, D. P.; Martin, K. A.; Wise, P. M. "Hormone Therapy: Physiological Complexity Belies Therapeutic Simplicity" *Science* **2004**, *304*, 1269-1273.

8. Franke, W. W.; Berendonk, B. "Hormonal Doping and Androgenization of Athletes: A Secret Program of the German Democratic Republic Government" *Clin. Chem.* **1997**, *43*, 1262-1279.

9. Catlin, D. H.; Hatton, C. K.; Starcevic, S. H. "Issues in Detecting Abuse of Xenobiotic Anabolic Steroids and Testosterone by Analysis of Athletes' Urine" *Clin. Chem.* **1997**, *43*, 1280-1288.

10. Mareck, U.; Geyer, H.; Opfermann, G.; Thevis, M.; Schänzer, W. "Factors Influencing the Steroid Profile in Doping Control Analysis" *J. Mass Spectrom.* **2008**, *43*, 877-891.

11. Schänzer, W.; Donike, M. "Metabolism of Anabolic Steroids in Man: Synthesis and Use of Reference Substances for Identification of Anabolic Steroid Metabolites" *Anal. Chim. Acta* **1993**, *275*, 23-48.

12. Saugy, M.; Cardis, C.; Robinson, N.; Schweizer, C. “Test Methods: Anabolics” *Best Pract. Res. Cl. En.* **2000**, *14*, 111-133.

13. Ayotte, C.; Goudreault, D.; Charlebois, A. “Testing for Natural and Synthetic Anabolic Agents in Human Urine” *J. Chromatogr. B Biomed. Sci. Appl.* **1996**, *687*, 3-25.

14. Rekharsky, M. V.; Inoue, Y. “Complexation Thermodynamics of Cyclodextrins” *Chem. Rev.* **1998**, *98*, 1875-1917.

15. Bohmer, V. “Calixarenes, Macrocycles with (Almost) Unlimited Possibilities” *Angew. Chem. Int. Ed., Engl.* **1995**, *34*, 713-745.

16. Diederich, F. “Complexation of Neutral Molecules by Cyclophane Hosts” *Angew. Chem. Int. Ed.* **1988**, *27*, 362-386.

17. Lazar, I.; Biedermann, F.; Mustafina, K. R.; Assaf, K. I.; Hennig, A.; Nau, W. M. “Nanomolar Binding of Steroids to Cucurbit[n]urils: Selectivity and Applications” *J. Am. Chem. Soc.* **2016**, *138*, 13022−13029.

18. Lucas, D.; Minami, T.; Iannuzzi, G.; Cao, L.; Wittenberg, J. B.; Anzenbacher, P., Jr.; Isaacs, L. “Templated Synthesis of Glycoluril Hexamer and Monofunctionalized Cucurbit[6]uril Derivatives” *J. Am. Chem. Soc.* **2011**, *133*, 17966-17976.

19. Hof, F.; Trembleau, L.; Ullrich, E. C.; Rebek, J., Jr. “Acetylcholine Recognition by a Deep, Biomimetic Pocket.” *Angew. Chem. In. Ed.* **2003**, *42*, 3150-3153.

20. Liu, Y.; Perez, L.; Mettry, M.; Gill, A. D.; Byers, S. R.; Easley, C. J.; Bardeen, C. J.; Zhong, W.; Hooley, R. J. “Site Selective Reading of Epigenetic Markers by Dual-Mode Synthetic Receptor Array” *Chem. Sci.* **2017**, *8*, 3960-3970.

21. Liu, Y.; Perez, L.; Gill, A. D.; Mettry, M.; Li, L.; Wang, Y.; Hooley, R. J.; Zhong, W. "Site-Selective Sensing of Histone Methylation Enzyme Activity via an Arrayed Supramolecular Tandem Assay" *J. Am. Chem. Soc.* **2017**, *139*, 10964-10967.

22. Ghang, Y-J.; Prez, L.; Morgan, M.; Si, F.; Hamdy, O.; Beecher, C.; Larive, C.; Julian, R.; Zhong, W.; Cheng, Q.; Hooley, R. J. “Anionic Deep Cavitands Enable the Adhesion of Unmodified Proteins at a Membrane Bilayer” *Soft Matter* **2014**, *10*, 9651-9656.

23. Perez, L.; Mettry, M.; Hinman, S. S.; Byers, S. R.; McKeating, K. S.; Caulkins, B. G.; Cheng, Q.; Hooley, R. J. “Selective Protein Recognition in Supported Lipid

Bilayer Arrays by Tailored, Dual-Mode Deep Cavitand Host" *Soft Matter* **2017**, *13*, 3966-3974.

Chapter 7: Experimental

7.1 General Information

1D NMR experiments (^{1}H, ^{13}C, ^{19}F) were performed on a Bruker Avance NEO 400 9.4 T spectrometer with a 5 mm Prodigy CPP BBO BB-H&F z-gradient cryo-probe or a Bruker 14.1 T (600.01 MHz 1H) Avance I spectrometer equipped with a 5 mm BBO Z- grad probe. Micelle (PCm) experiments (^{1}H–^{1}H COSY, ^{2}H–^{2}H EXSY, ^{13}C–^{13}C EXSY, ^{19}F–^{19}F EXSY) were performed on a Bruker Avance NEO 400 9.4 T spectrometer with a 5 mm Prodigy CPP BBO BB-H&F z-gradient cryo-probe, a Bruker 14.1 T (600.01 MHz ^{1}H) Avance I spectrometer equipped with a 5 mm BBO Z-grad probe or a Bruker Avance III 700 16.44 T spectrometer with a 5 mm CP TCI H–C/N-D z-gradient cryo-probe. Magnetically ordered bicelle (PCb) experiments (^{13}C, ^{13}C–^{13}C EXSY) were performed at 9.4 T (400.37 MHz ^{1}H, 100.69 MHz ^{13}C, 162.07 MHz ^{31}P) on a Bruker AVIII spectrometer equipped with a double resonance, 4 mm MAS probe.Obtained NMR were processed using MestReNova by Mestrelab Research S.L. Proton (^{1}H) and carbon (^{13}C) chemical shifts are reported in parts per million (δ) with respect to tetramethylsilane (TMS, $\delta = 0$). Phosphorus (^{31}P) chemical shifts are reported in parts per million (δ), and referenced internally with respect to 85% H_3PO_4. Fluorine (^{19}F) chemical shifts are reported in parts per million (δ), and referenced internally with respect to CF_3COOH. Deuterated NMR solvents were obtained from Cambridge Isotope Laboratories, Inc., Andover, MA, and used without further purification. 1-Palmitoyl-2-oleoyl-*sn*-glycero-3-phosphocholine was purchased from Avanti Polar Lipids (Alabaster, AL). Bradford Protein Assay solution was purchased from Bio-Rad (Hercules, CA). All other materials were obtained from Aldrich Chemical

Company (St. Louis, MO), Fisher Scientific (Fairlawn, NJ), or TCI (Tokyo, Japan) and were used as received. Solvents were dried through a commercial solvent purification system (Pure Process Technologies, Inc.). Dulbecco's Modification of Eagle's Medium (DMEM) and fetal bovine serum (FBS) were purchased from ATCC. The HeLa cell line was purchased from ATCC (Manassas, VA). HeLa cells were maintained in DMEM supplemented with 10 % FBS in a humidified incubator with 5 % CO2 at 37 °C. Human monocytic THP-1 cells were kindly provided by Dr. Yingsheng Wang. THP-1 cells (ATCC TIB-202) were cultured at 37 °C and 5% CO_2 in RPMI 1640 media supplemented with 10% FBS, 100 U/ml penicillin, 100 µg/mL streptomycin, and 50 µM 2-mercaptoethanol. Molecular modeling (semi-empirical calculations) was performed using the AM1 force field using SPARTAN. Cavitand **1.13**[1], **1.16**[2] and **3.1**[3,4] were synthesized according to literature procedures. Surface Plasmon Resonance spectroscopic measurements were performed with a dual-channel SPR spectrometer, NanoSPR6-321 (NanoSPR, Chicago, IL), with a GaAs semiconductor laser light source (λ = 650 nm). The device was equipped with a manufacturer-supplied high-refractive index prism (n = 1.61) and a 30 µL flow cell. Surface interactions at the gold interface were monitored using the resonance angle tracking mode. Mass spectra were recorded on an Agilent 6210 LC TOF mass spectrometer using electrospray ionization with fragmentation voltage set at 115 V and processed with an Agilent MassHunter Operating System. Fluorescence measurements were achieved in a Perkin Elmer Wallac 1420 Victor 2 Microplate Reader (PerkinElmer) with the Ex/Em wavelengths at 530/605 nm or 485/605 nm. Linear Discriminant Analysis (LDA) and confidence ellipses were accomplished with RStudio (Version 1.0.136), an integrated

development environment (IDE) for R (version 3.3.2). Victor2 1420 multilable counter (PerkinElmer, Waltham, MA) was used for Bradford assay and SRB assay. Fluorescence and DIC images of SLB and cells were taken by Confocal Leica SP5 fluorescence microscopy (Buffalo Grove, IL).

Calcinated Chip Preparation: Gold substrates were fabricated with a 2 nm thick chromium adhesion layer, followed by the deposition of a 46 nm thick gold layer via e-beam evaporation on cleaned glass slides. The nanoglassified layers were constructed on the surface based on a previous layer-by- layer protocol:[1] Clean gold substrates were immersed in 10 mM 3-mercaptopropionic acid (MPA) ethanol solution overnight to form a self-assembled monolayer. After extensive rinsing with ethanol and nanopure water and drying with nitrogen gas, modified gold substrates were alternately dipped into poly(allylamine hydrochloride) (MW ~17,500) solution (2 mg/mL, adjusted to pH 8.0) and sodium silicate solution (22 mg/mL, adjusted to pH 9.5) for 1 min to form a layer by layer assembly structure, with sufficient ultrapure water rinsing between layers. This dipping process was repeated five times to build up a multilayer membrane gold chip, followed by calcination in a furnace by heating to 450 °C at a rate of 17 °C per min and allowing cooling to room temperature 4 hours later.

Vesicle Preparation: 1-Palmitoyl-2-oleoyl-*sn*-glycero-3-phosphocholine (POPC) lipid stock solution in chloroform was transferred to a small vial and the organic solvent was purged from the vial with nitrogen gas to form a dry lipid film on the vial wall, which was then rehydrated with 20 mM PBS (150 mM NaCl, pH 7.4) to a lipid concentration of 1 mg/mL. The resuspended lipids were probe sonicated for 20 minutes. The supernatant was

then extruded with 11 passes through a polycarbonate membrane of pore size 100 nm to ensure formation of small unilamellar vesicles. The solution was incubated at 4 °C for at least 1 h before use. For the preparation of vesicle preincorporated with cavitand **1.16**, 1-Palmitoyl-2-oleoyl-*sn*-glycero-3-phosphocholine (POPC) lipid stock solution in chloroform was transferred to a small vial and cavitand **1.16** stock solution in chloroform was added to a final concentration of 2 wt%. The rest of the preparation steps are identical.

7.2 Chapter 2 Experimental

Fitting model for EXSY Experiments:

A standard two-site exchange model is used to analyze the EXSY data. In this model, the guest can exchange between a free and bound state, A and B, respectively:

$$A \underset{k_b}{\overset{k_f}{\rightleftharpoons}} B$$

k_b is the exchange constant from B to A, while k_f is the exchange constant for A to B. At equilibrium, the forward and reverse exchange rates are equal. Therefore, $k_b[B] = k_f[A]$, or in terms of the equilibrium constant:

$$\frac{[B]}{[A]} = \frac{k_f}{k_b} = K_{eq} ,$$

During the mixing time of the EXSY experiment, the concentration of A can change in three ways: first, A can become bound, decreasing its contribution to the signal intensity over the mixing time; second, A can relax due to T_1, also decreasing its intensity; third, a bound ligand B can be released, becoming A and adding to its signal intensity. This can be described by the following first-order differential equation:

$$\frac{d[A]}{dt} = -k_f[A] - \frac{[A]}{T_{1A}} + k_b[B]$$

The signal from B varies in a similar way, giving

$$\frac{d[B]}{dt} = -k_b[B] - \frac{[B]}{T_{1B}} + k_f[A]$$

Each exchange spectrum contains two diagonal peaks, AA and BB, and two crosspeaks, AB and BA; the first letter refers to the frequency in f_1 of the EXSY spectrum, while the second gives the frequency in f_2 (hence AB would be the cross peak at $\{\nu_A, \nu_B\}$). The above set of coupled, first-order, linear differential equations can be solved using standard methods subject to the following initial conditions at the start of the EXSY mixing time:

AA and AB: $[A(t=0)] = A_0$, $[B(t=0)] = 0$

BB and BA: $[A(t=0)] = 0$, $[B(t=0)] = B_0$

giving the following expressions for the diagonal and cross peak intensities in terms of the EXSY mixing time (t):

$$AA(t) = A_0 e^{-t/T_1} \frac{k_b + e^{-(k_b+k_f)t} k_f}{k_b + k_f} \overset{\text{short time}}{\approx} A_0\left(1 - \tfrac{t}{T_1} - k_f t\right)$$

$$AB(t) = A_0 e^{-t/T_1} \frac{\left(1 - e^{-(k_b+k_f)t}\right) k_f}{k_b + k_f} \overset{\text{short time}}{\approx} A_0 k_f t$$

$$BB(t) = B_0 e^{-t/T_1} \frac{e^{-(k_b+k_f)t} k_b + k_f}{k_b + k_f} \overset{\text{short time}}{\approx} B_0\left(1 - \tfrac{t}{T_1} - k_b t\right)$$

$$BA(t) = B_0 e^{-t/T_1} \frac{\left(1 - e^{-(k_b+k_f)t}\right) k_b}{k_b + k_f} \overset{\text{short time}}{\approx} B_0 k_b t$$

where it has been assumed that $T_{1A} = T_{1B}$. The initial rate (short time) solutions are shown to the right. By extracting one-dimensional slices showing the greatest peak intensity from 2D spectra recorded with different mixing times, it is possible to fit the above set of equations and determine both k_b and k_f.

NMR Spectra of New Compounds:

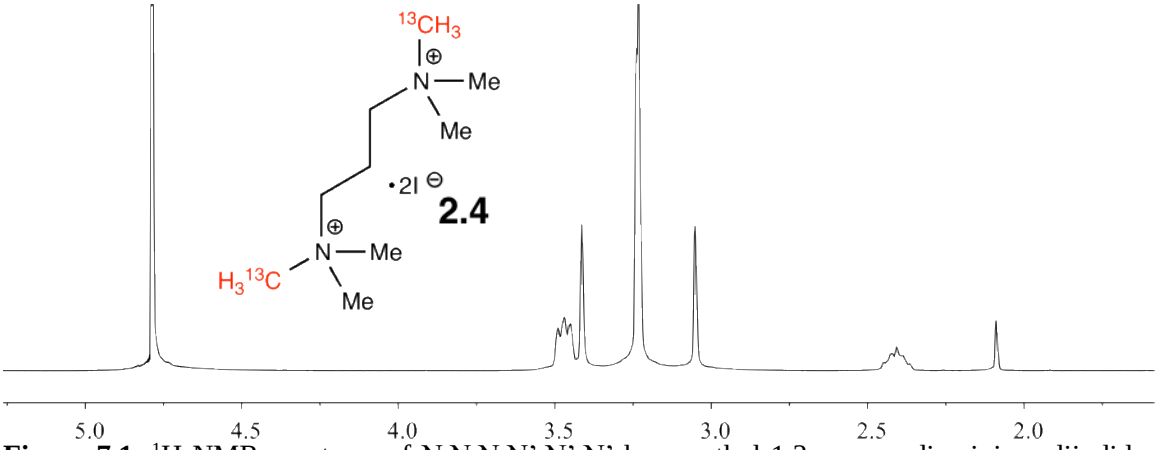

Figure 7.1: ^{1}H NMR spectrum of N,N,N,N',N',N'-hexamethyl-1,3-propanediaminium diiodide-^{13}C guest **2.4** (400.13 MHz, D_2O, 298 K).

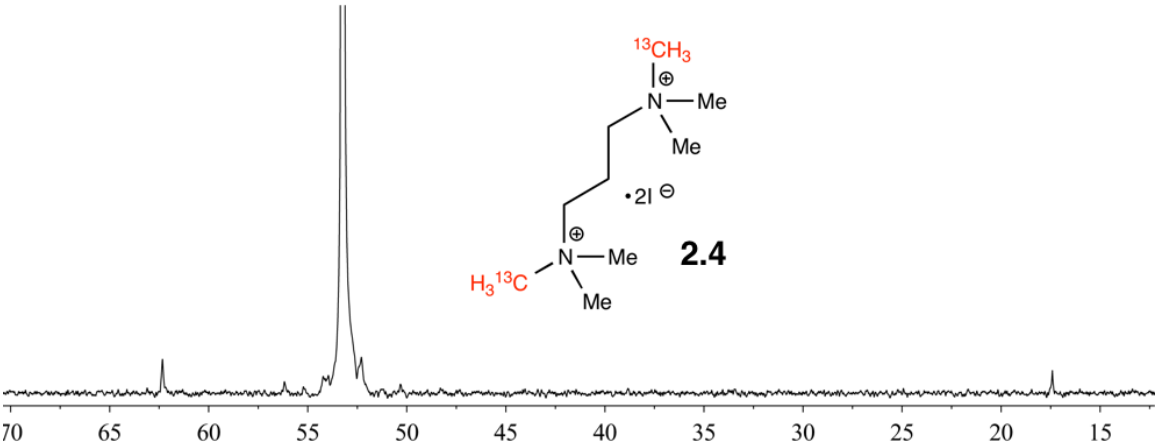

Figure 7.2: ^{13}C NMR spectrum of N,N,N,N',N',N'-hexamethyl-1,3-propanediaminium diiodide-^{13}C guest **2.4** (100.61 MHz, D_2O, 298 K).

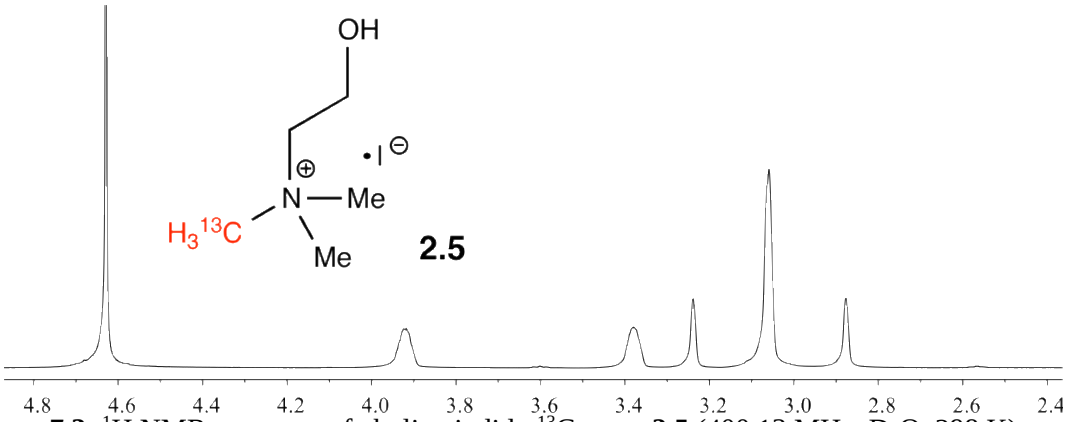

Figure 7.3: ^{1}H NMR spectrum of choline iodide-^{13}C guest **2.5** (400.13 MHz, D_2O, 298 K).

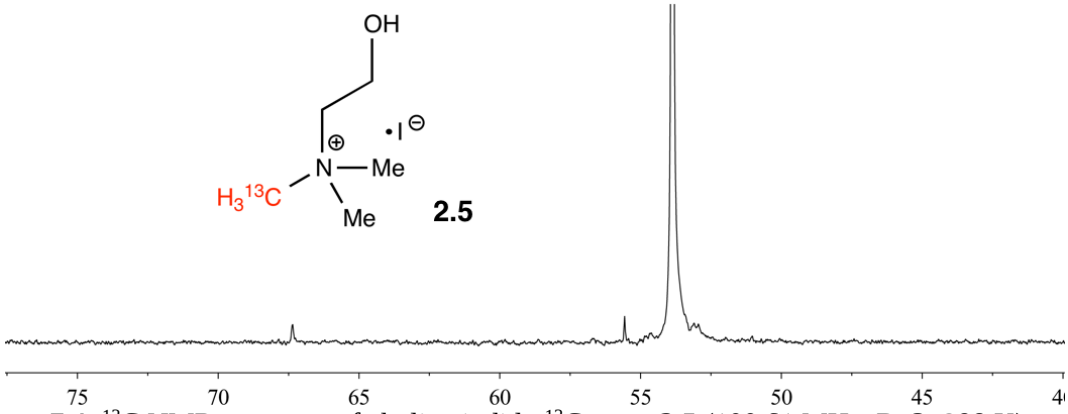

Figure 7.4: ^{13}C NMR spectrum of choline iodide-^{13}C guest **2.5** (100.61 MHz, D_2O, 298 K).

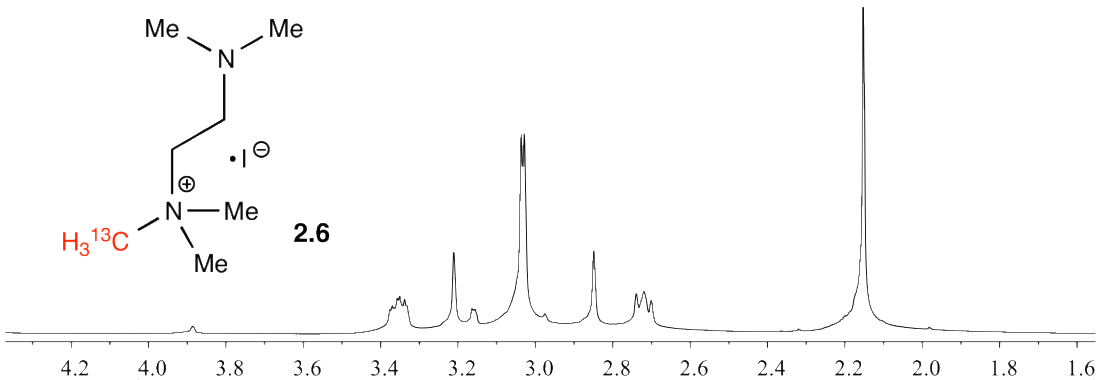

Figure 7.5: ^{1}H NMR spectrum of N,N,N,N',N'-pentamethyl-1,2-ethanediaminium iodide-^{13}C guest **2.5** (400.13 MHz, D_2O, 298 K).

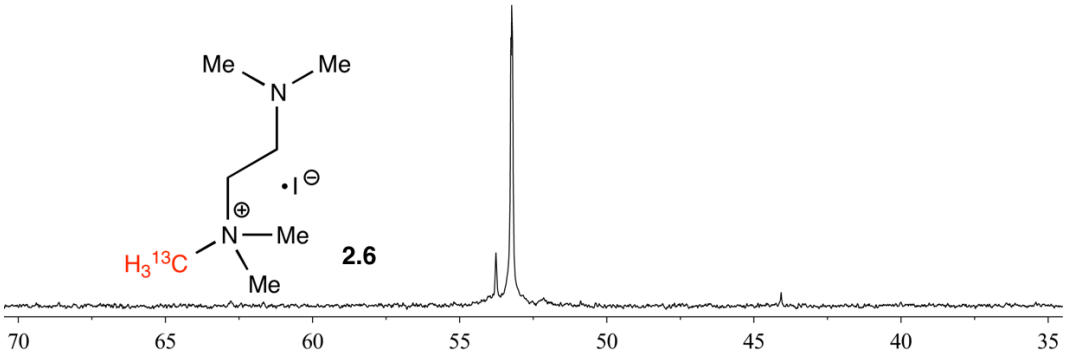

Figure 7.6: ^{13}C NMR spectrum of N, N, N, N', N'-pentamethyl-1,2-ethanediaminium iodide-^{13}C guest **2.5** (100.61 MHz, D_2O, 298 K).

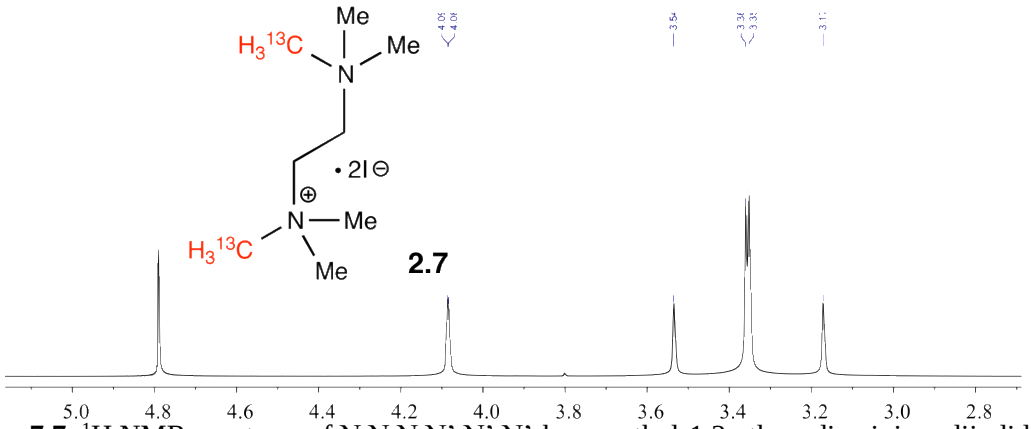

Figure 7.7: ^{1}H NMR spectrum of N,N,N,N',N',N'-hexamethyl-1,2-ethanediaminium diiodide-^{13}C guest **2.7** (400.13 MHz, D_2O, 298 K).

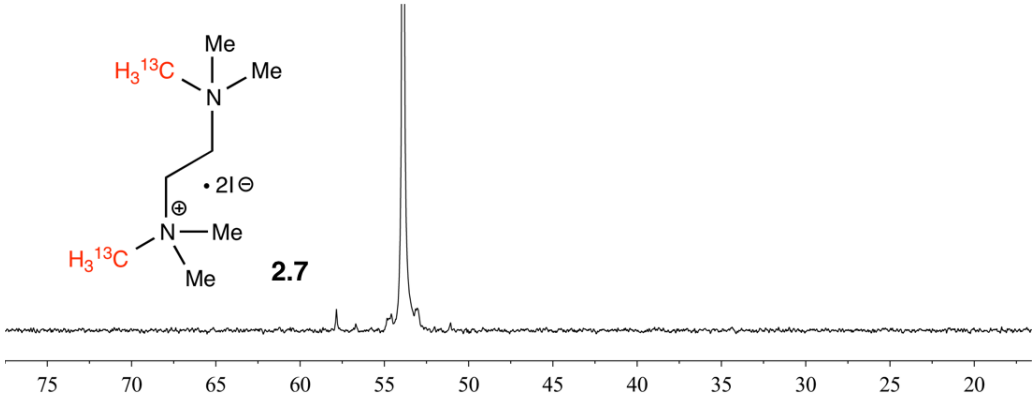

Figure 7.8: ^{13}C NMR spectrum of N,N,N,N',N',N'-hexamethyl-1,2-ethanediaminium diiodide-^{13}C guest **2.8** (100.61 MHz, D_2O, 298 K).

NMR Spectra of Host:Guest Complexes in Free Aqueous Solution:

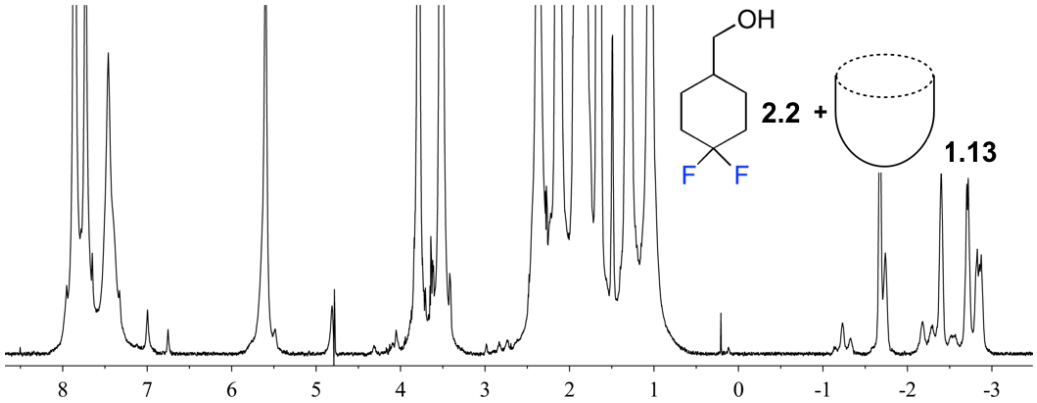

Figure 7.9: ^{1}H NMR spectrum of the **1.13 • 2.2** cavitand-guest complex (400.13 MHz, D_2O, 298 K, [**1.13**] = 5.8 mM, [**2.2**] = 39.5 mM).

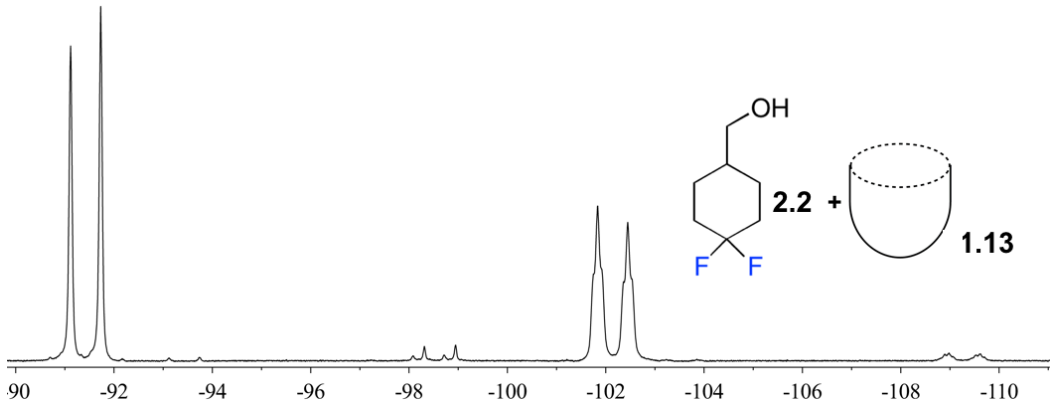

Figure 7.10: ^{19}F NMR spectrum of the **1.13 • 2.2** cavitand-guest complex (376.50 MHz, D_2O, 298 K, [**1.13**] = 5.8 mM, [**2.2**] = 39.5 mM).

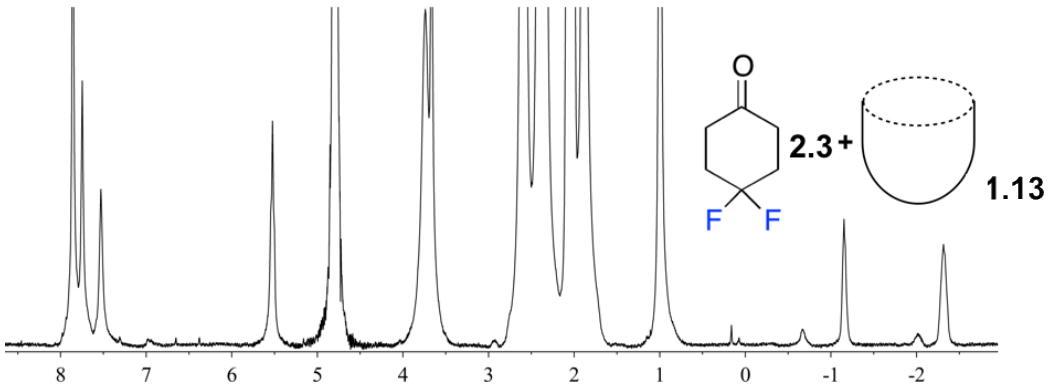

Figure 7.11: ^{1}H NMR spectrum of the **1.13 • 2.3** cavitand-guest complex (400.13 MHz, D_2O, 298 K, [**1.13**] = 5.8 mM, [**2.3**] = 39.5 mM).

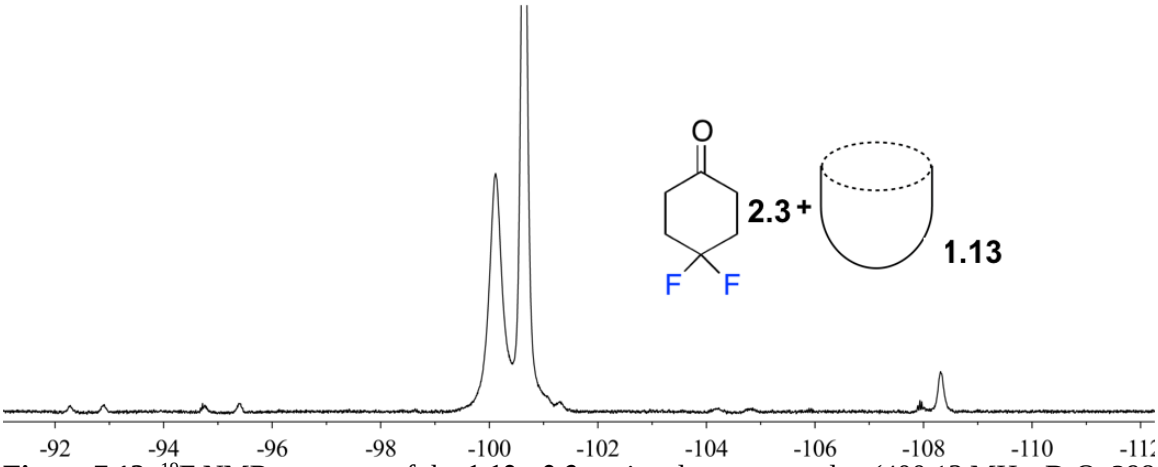

Figure 7.12: ^{19}F NMR spectrum of the **1.12 • 2.3** cavitand-guest complex (400.13 MHz, D_2O, 298 K, [**1.13**] = 5.8 mM, [**2.3**] = 39.5 mM).

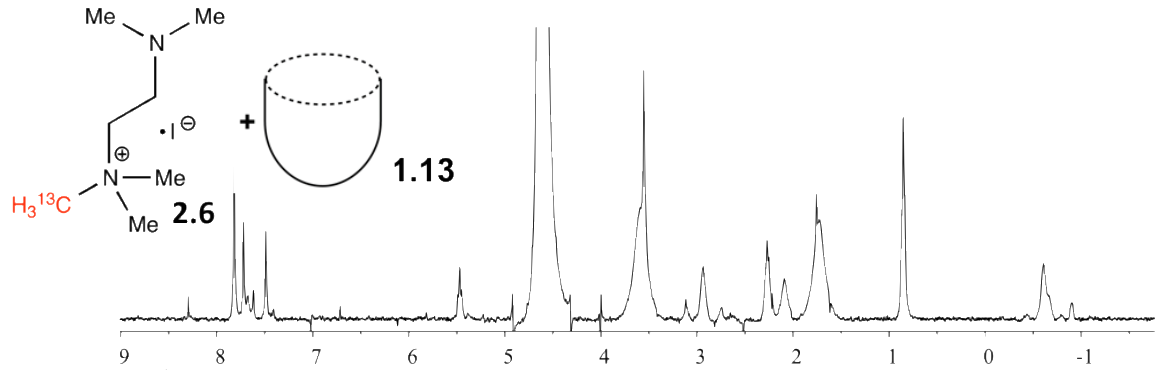

Figure 7.13: ^{1}H NMR spectrum of the **1.13 • 2.6** cavitand-guest complex (400.13 MHz, D_2O, 298 K, [**1.13**] = 1.8 mM, [**2.6**] = 2.2 mM).

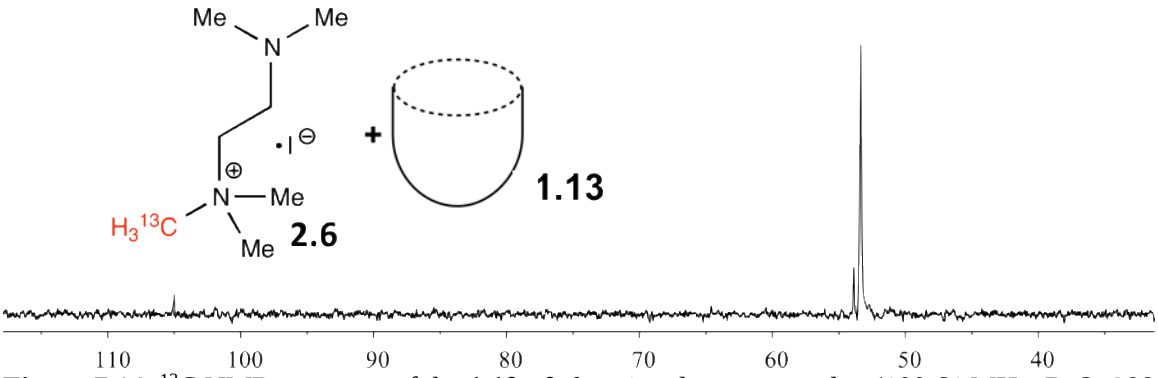

Figure 7.14: ^{13}C NMR spectrum of the **1.13 • 2.6** cavitand-guest complex (100.61 MHz, D_2O, 298 K, [**1.13**] = 1.8 mM, [**2.6**] = 2.2 mM).

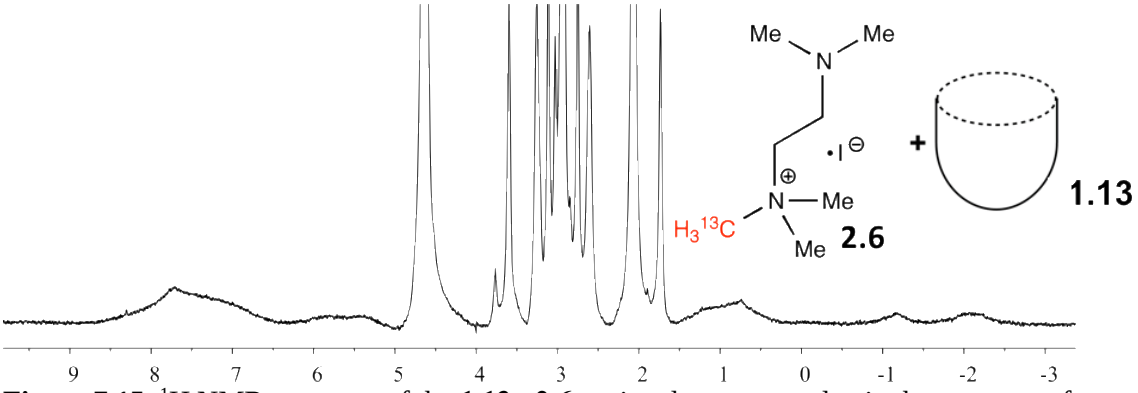

Figure 7.15: ^{1}H NMR spectrum of the **1.13 • 2.6** cavitand-guest complex in the presence of excess **2.6** (400.13 MHz, D_2O, 298 K, [**1.13**] = 1.8 mM, [**2.6**] = 10 mM).

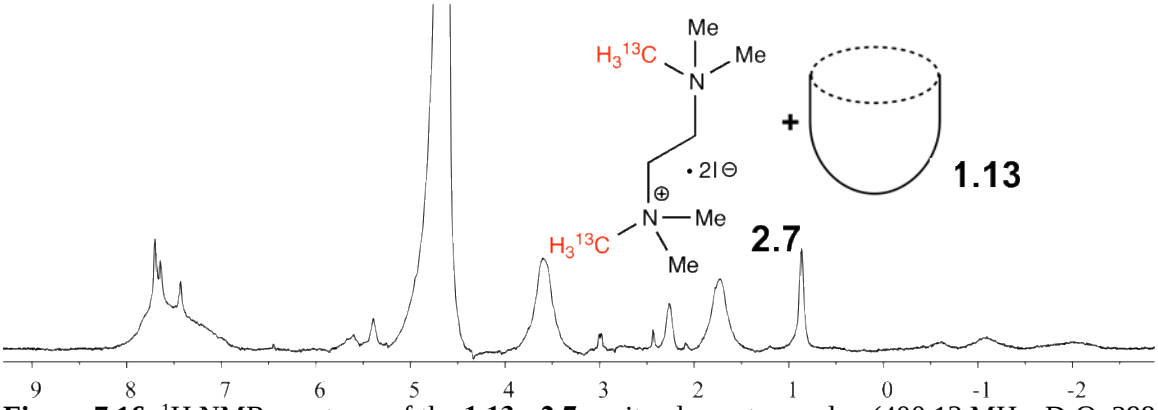

Figure 7.16: ^{1}H NMR spectrum of the **1.13 • 2.7** cavitand-guest complex (400.13 MHz, D_2O, 298 K, [**1.13**] = 1.8 mM, [**2.7**] = 2.2 mM).

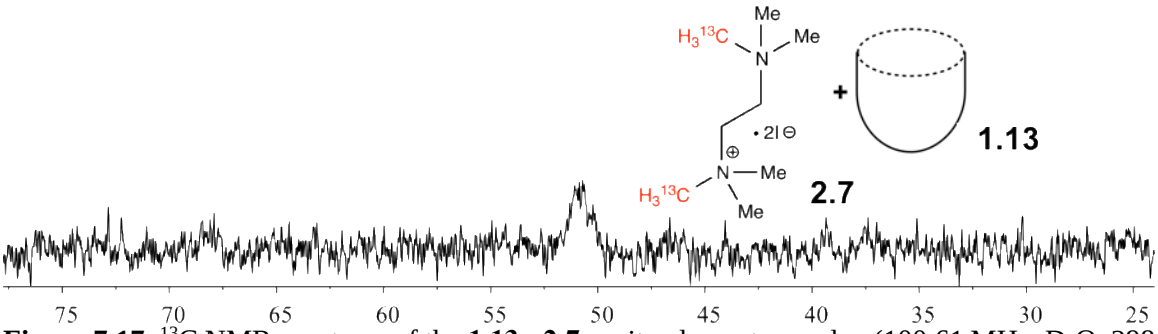

Figure 7.17: ^{13}C NMR spectrum of the **1.13 • 2.7** cavitand-guest complex (100.61 MHz, D_2O, 298 K, [**1.13**] = 1.8 mM, [**2.7**] = 2.2 mM).

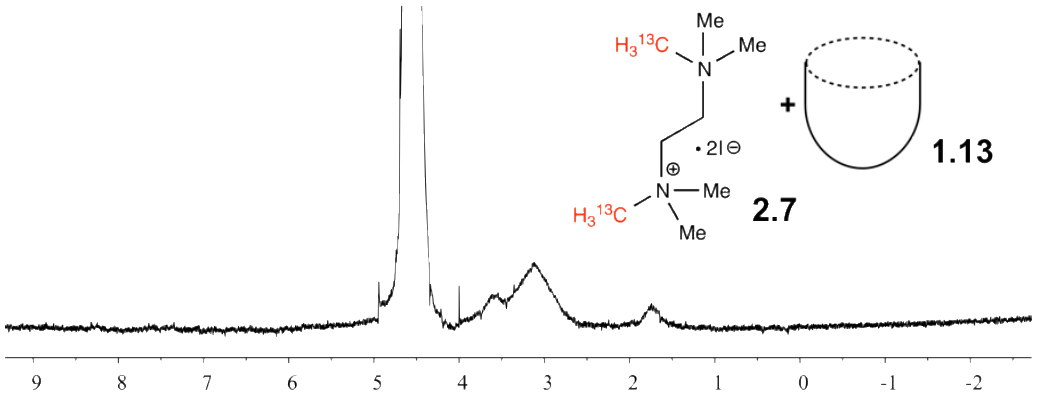

Figure 7.18: ^{1}H NMR spectrum of the **1.13 • 2.7** cavitand-guest complex in the presence of excess **2.7** (400.13 MHz, D_2O, 298 K, [**1.13**] = 1.8 mM, [**2.7**] = 5.5 mM).

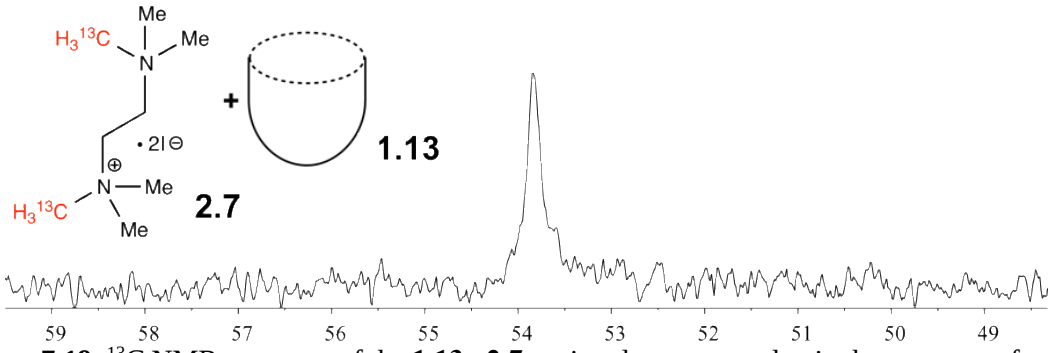

Figure 7.19: ^{13}C NMR spectrum of the **1.13 • 2.7** cavitand-guest complex in the presence of excess **2.7** (100.61 MHz, D_2O, 298 K, [**1.13**] = 1.8 mM, [**2.7**] = 5.5 mM).

NMR Spectra of Host:Guest Complexes in DMPC/DHPC Lipid Micelles:

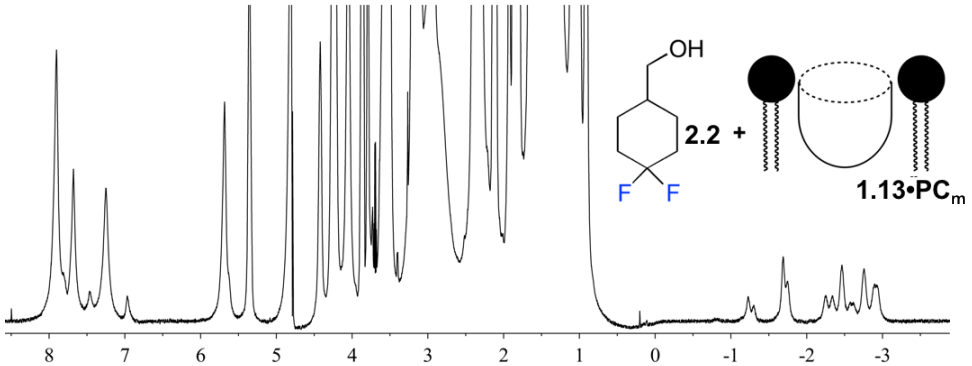

Figure 7.20: ^{1}H NMR spectrum of the cavitand **1.13** • guest **2.2** complex in PC_m micelles (599.88 MHz, 1 mM HEPES/D_2O, 283 K, [**1.13**] = 5.8 mM, [**2.2**] = 39.5 mM, ratio DMPC/DHPC = 3.2:1, 60 mg/mL total lipid concentration).

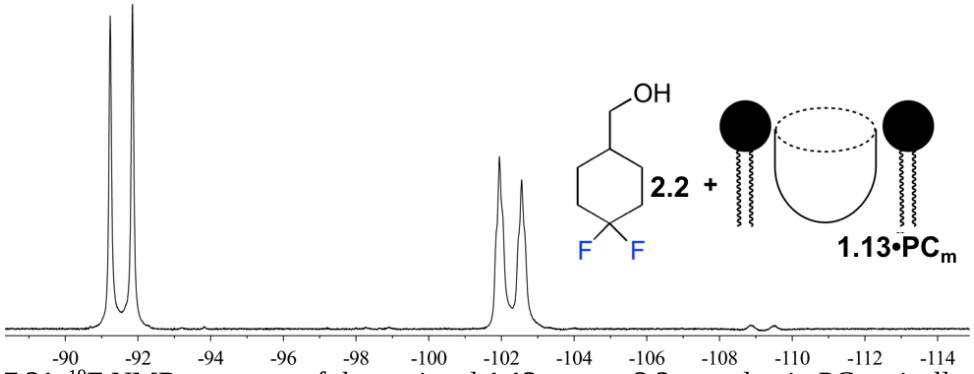

Figure 7.21: ^{19}F NMR spectrum of the cavitand **1.13** • guest **2.2** complex in PC_m micelles (1 mM HEPES/D_2O, 376.50 MHz, 298 K, [**1.13**] = 5.8 mM, [**2.2**] = 39.5 mM, ratio DMPC/DHPC = 3.2:1, 60 mg/mL total lipid concentration).

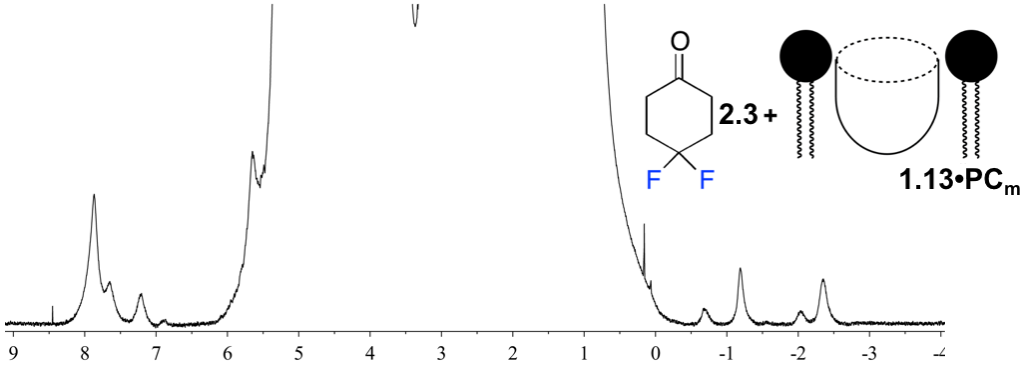

Figure 7.22: ^{1}H NMR spectrum of the cavitand **1.13** • guest **2.3** complex in PC_m micelles (599.88 MHz, 1 mM HEPES/D_2O, 283 K, [**1.13**] = 5.8 mM, [**2.3**] = 39.5 mM, ratio DMPC/DHPC = 3.2:1, 60 mg/mL total lipid concentration).

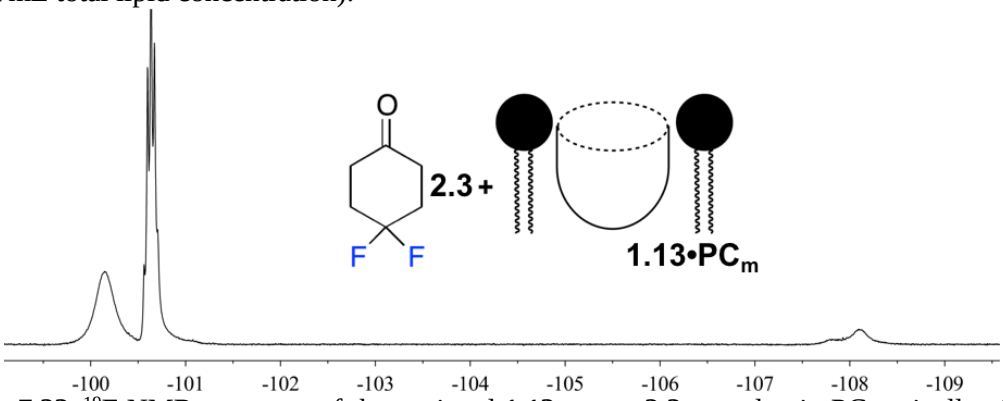

Figure 7.23: ^{19}F NMR spectrum of the cavitand **1.13** •guest **2.3** complex in PC_m micelles **(**1 mM HEPES/D_2O, 376.50 MHz, 298 K, [**1.13**] = 5.8 mM, [**2.3**] = 39.5 mM, ratio DMPC/DHPC = 3.2:1, 60 mg/mL total lipid concentration);

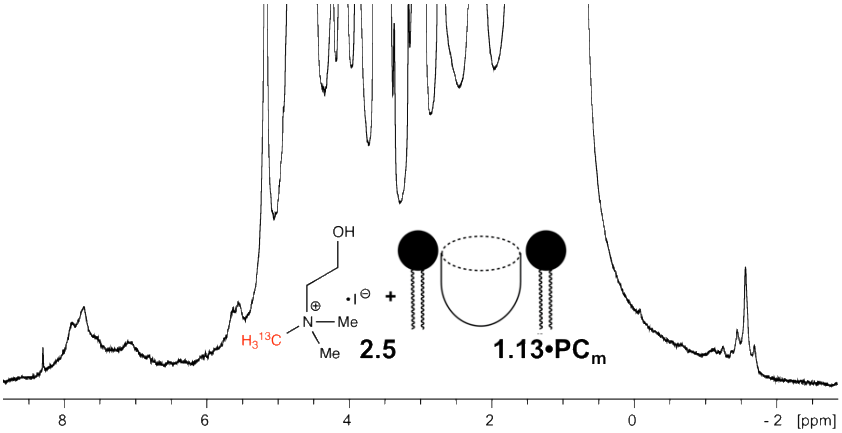

Figure 7.24: ^{1}H NMR spectrum of the **1.13 • 2.5** cavitand-choline complex in DMPC:DHPC lipid micelles (599.88 MHz, 1 mM HEPES/D_2O, 283 K, [**1.13**] = 5.8 mM, [**2.5**] = 16.0 mM, ratio DMPC/DHPC = 3.2:1, 60 mg/mL total lipid concentration).

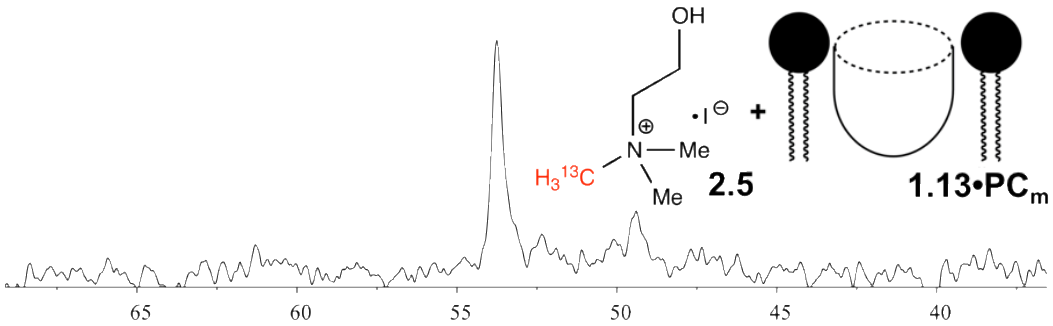

Figure 7.25: ^{13}C NMR spectrum of the **1.13 • 2.5** cavitand-choline complex in DMPC:DHPC lipid micelles (100.61 MHz, 1 mM HEPES/D_2O, 283 K, [**1.13**] = 5.8 mM, [**2.5**] = 16.0 mM, ratio DMPC/DHPC = 3.2:1, 60 mg/mL total lipid concentration).

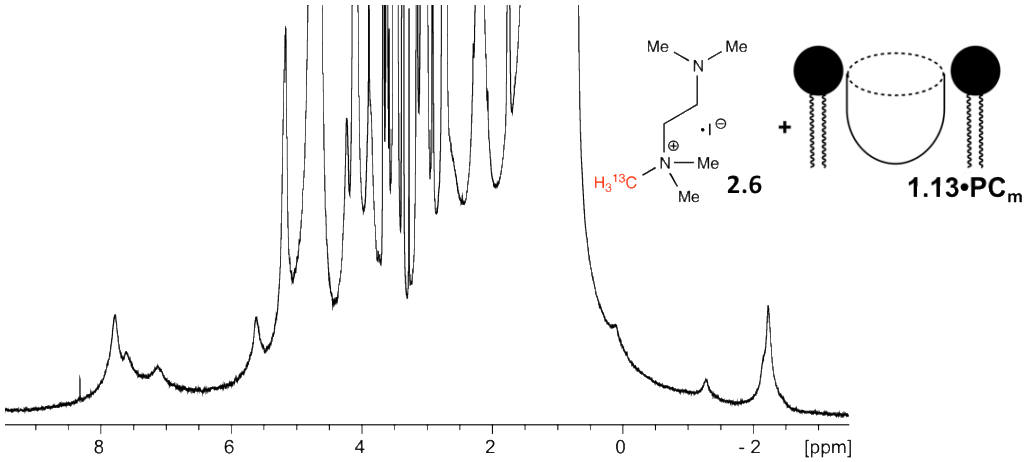

Figure 7.26: ^{1}H NMR spectrum of the **1.13 • 2.6** cavitand-guest complex in DMPC:DHPC lipid micelles (599.88 MHz, 1 mM HEPES/D_2O, 283 K, [**1.13**] = 5.8 mM, [**2.6**] = 16 mM, ratio DMPC/DHPC = 3.2:1, 60 mg/mL total lipid concentration).

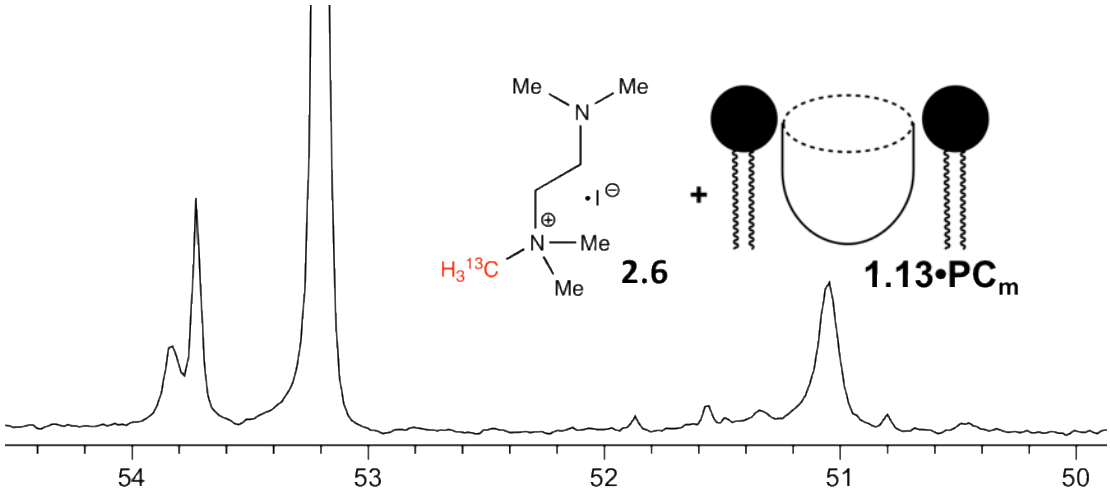

Figure 7.27: ^{13}C NMR spectrum of the **1.13 • 2.6** cavitand-guest complex in DMPC:DHPC lipid micelles (100.61 MHz, 1 mM HEPES/D_2O, 283 K, [**1.13**] = 5.8 mM, [**2.6**] = 16 mM, ratio DMPC/DHPC = 3.2:1, 60 mg/mL total lipid concentration).

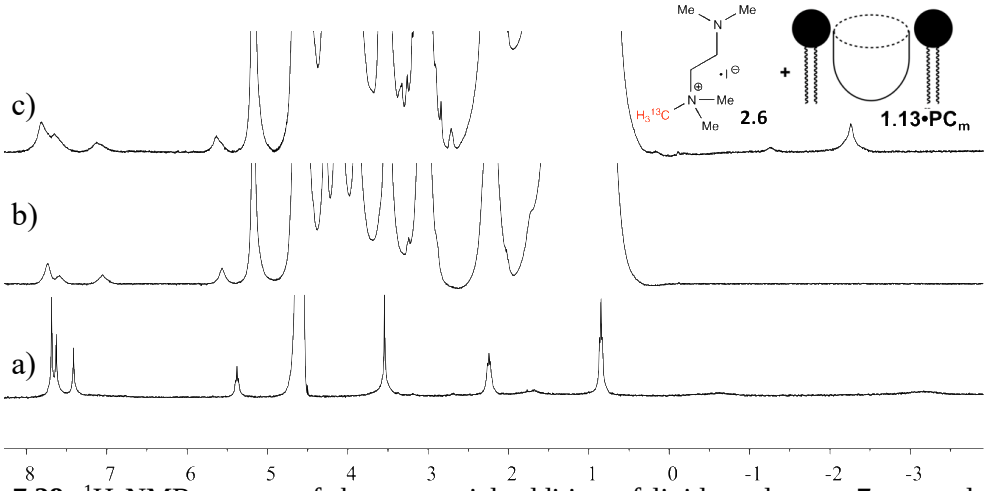

Figure 7.28: ^1H NMR spectra of the sequential addition of lipids and guest **7** to a solution of cavitand **1.13** (400.13 MHz, 1 mM HEPES/D_2O, 298 K). a) 1.8 mM of cavitand **1.13**; b) 1.8 mM of cavitand **1.13** + DMPC/DHPC lipids, ratio DMPC/DHPC = 3.2:1, 60 mg/mL total lipid concentration; c) 1.8 mM of cavitand **1.13** + DMPC/DHPC lipids =2.2 mM guest **2.6**.

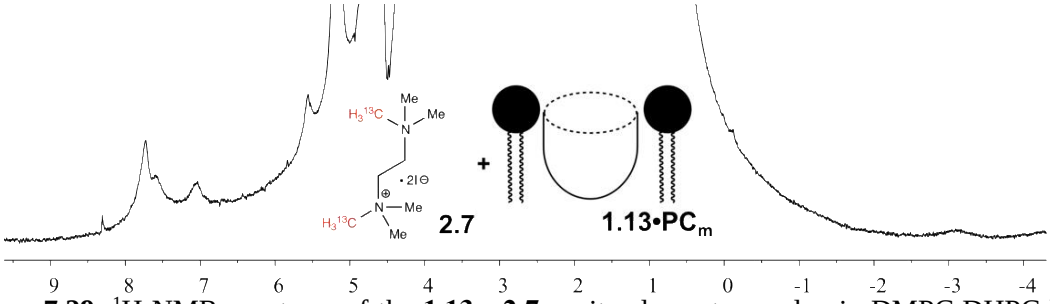

Figure 7.29: ^{1}H NMR spectrum of the **1.13 • 2.7** cavitand-guest complex in DMPC:DHPC lipid micelles (400.13 MHz, 1 mM HEPES/D_2O, 298 K, [**1.13**] = 1.8 mM, [**2.7**] = 5.4 mM, ratio DMPC/DHPC = 3.2:1, 60 mg/mL total lipid concentration).

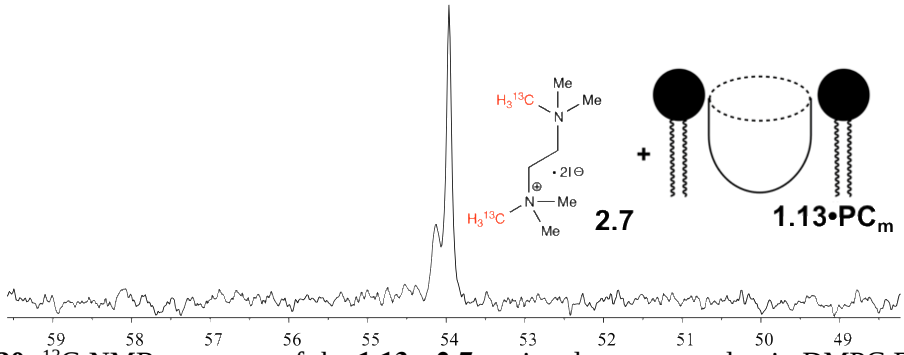

Figure 7.30: ^{13}C NMR spectrum of the **1.13 • 2.7** cavitand-guest complex in DMPC:DHPC lipid micelles (100.61 MHz, 1 mM HEPES/D_2O, 298 K, [**1.13**] = 1.8 mM, [**2.7**] = 5.4 mM, ratio DMPC/DHPC = 3.2:1, 60 mg/mL total lipid concentration).

2D Exchange NMR Spectra in Water and in Lipid Micelles:

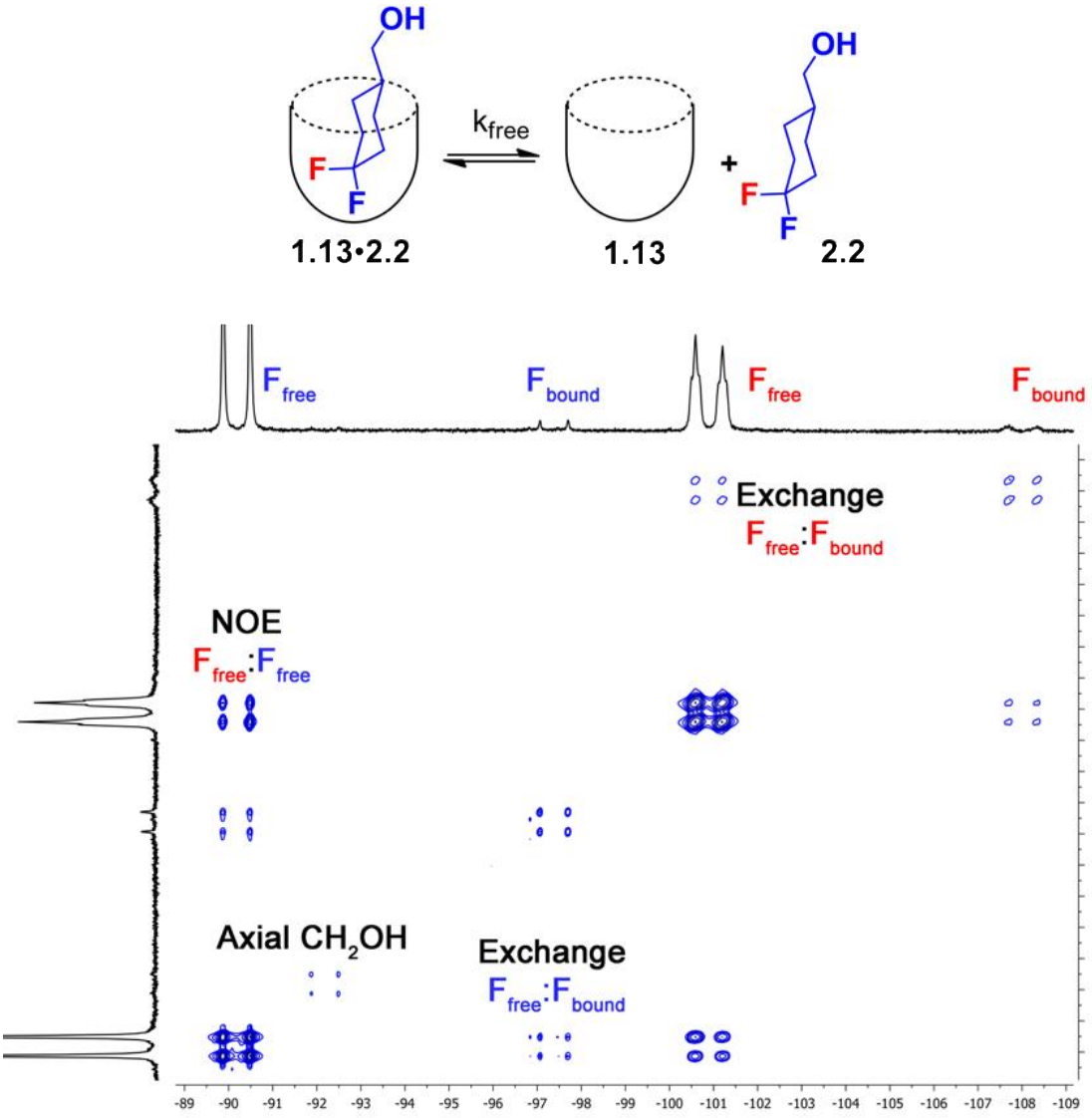

Figure 7.31: Full ^{19}F EXSY spectrum of the cavitand **1.13** • guest **2.2** complex in pure D_2O with peak assignments (D_2O, 150.84 MHz, 298 K, mixing time = 150 ms, [**1.13**] = 5.8 mM, [**2.2**] = 39.5 mM).

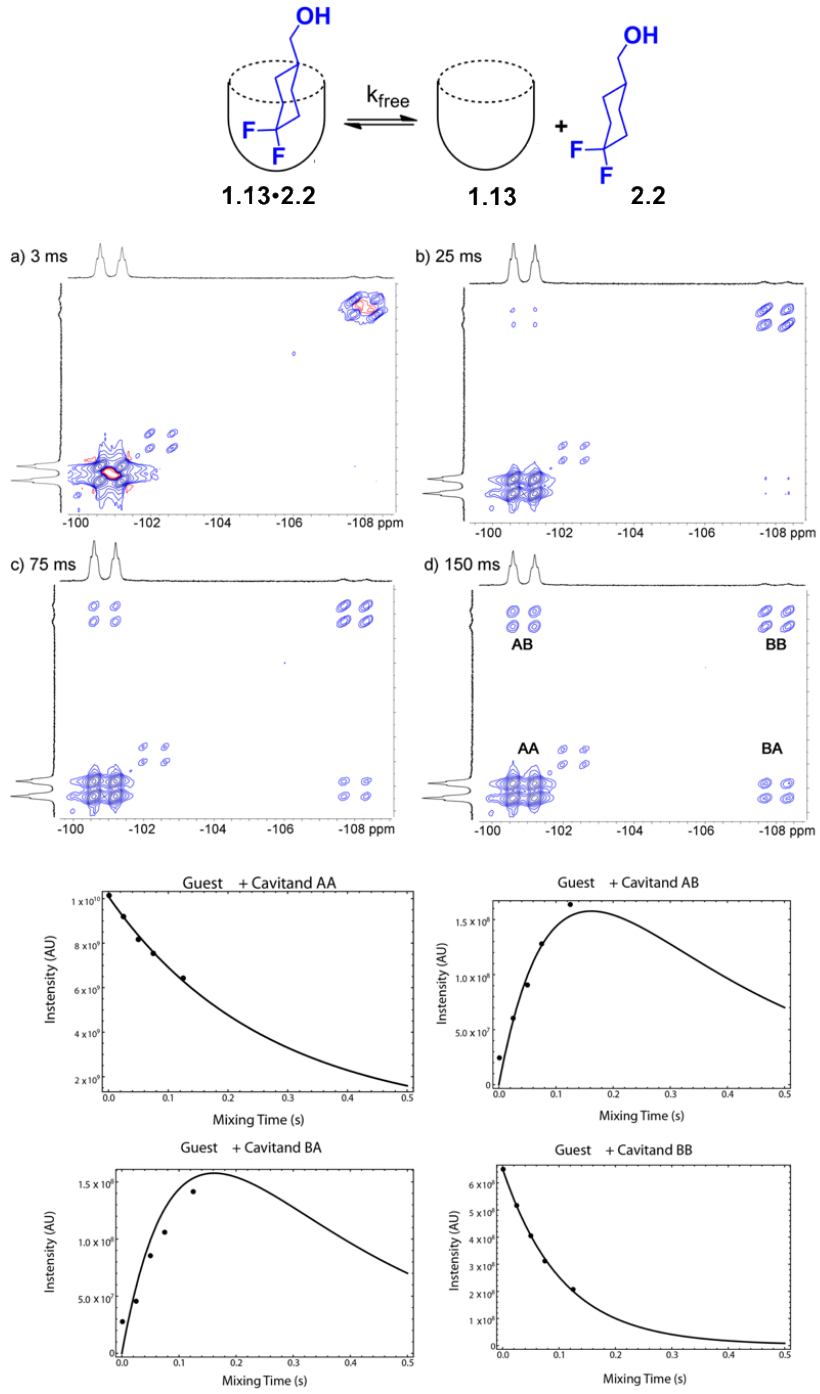

Figure 7.32: Representative ^{19}F EXSY spectra of the cavitand **1.13** •guest **2.2** complex in pure D_2O with varying mixing times (D_2O, 376.50 MHz, 298 K, [**1.13**] = 5.8 mM, [**2.2**] = 39.5 mM); fitted plots of peak intensity correlated with mixing time for each diagonal and crosspeak used to calculate the exchange rate.

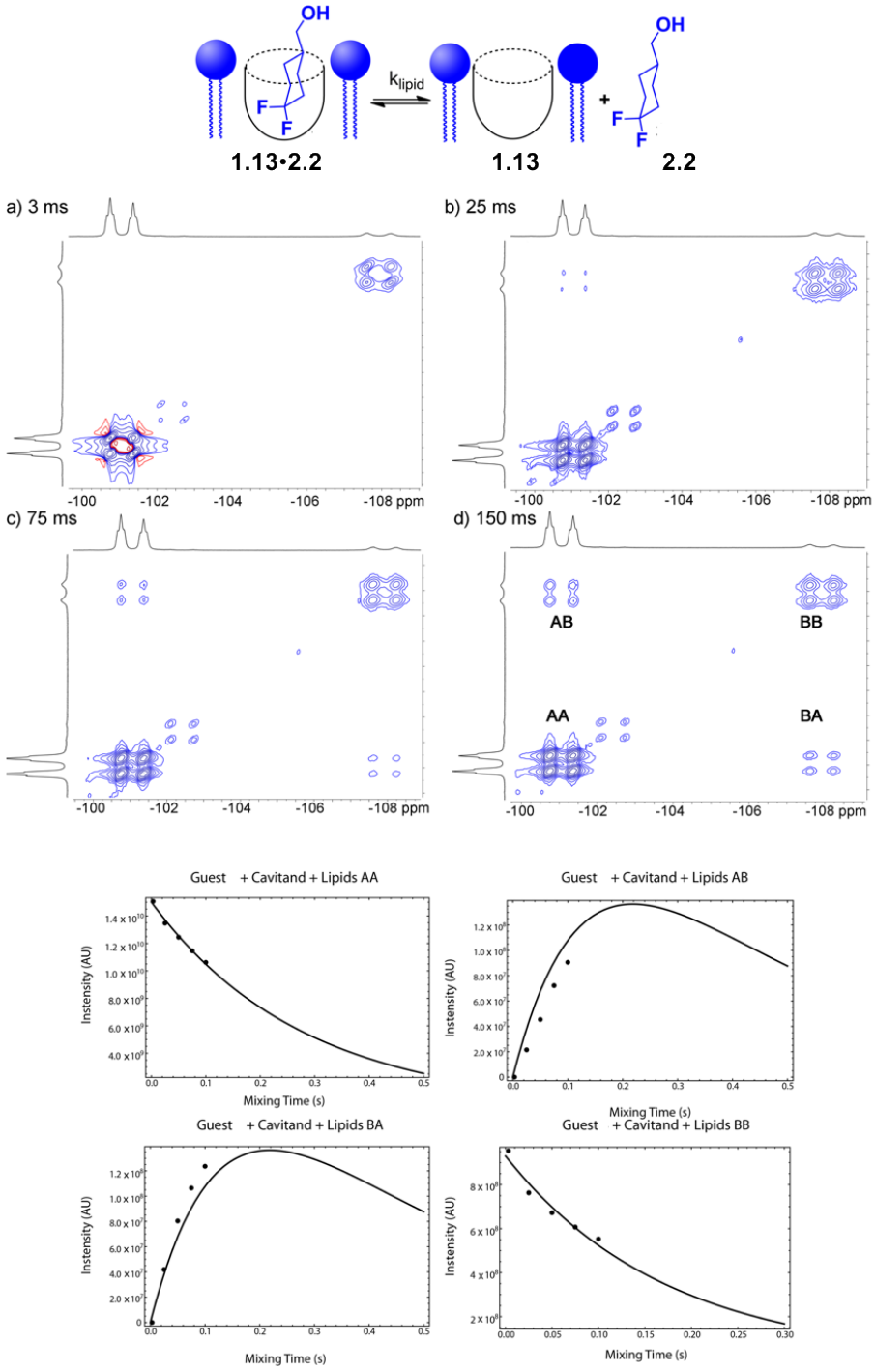

Figure 7.33: Representative ^{19}F EXSY spectra of the cavitand **1.13** • guest **2.2** complex in the PC_m micelles with varying mixing times **(**1 mM HEPES/D_2O, 376.50 MHz, 298 K, [**1.13**] = 5.8 mM, [**2.2**] = 39.5 mM, ratio DMPC/DHPC = 3.2:1, 60 mg/mL total lipid concentration); fitted plots of peak intensity correlated with mixing time for each diagonal and crosspeak used to calculate the exchange rate.

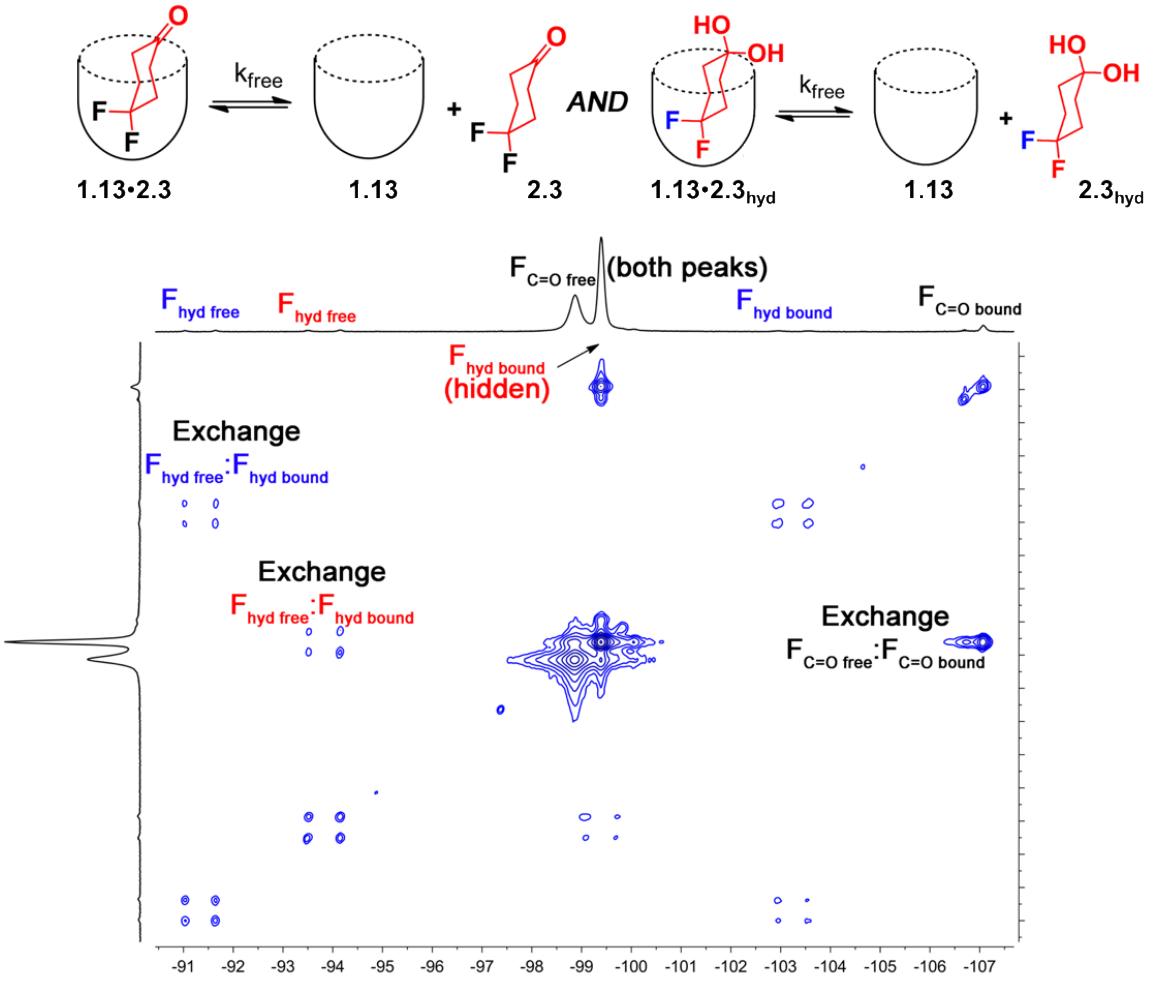

Figure 7.34: Full ^{19}F EXSY spectrum of the cavitand **1.13** • guest **2.3** complex in pure D_2O with peak assignments (D_2O, 150.84 MHz, 298 K, mixing time = 150 ms, [**1.13**] = 5.8 mM, [**2.3**] = 39.5 mM).

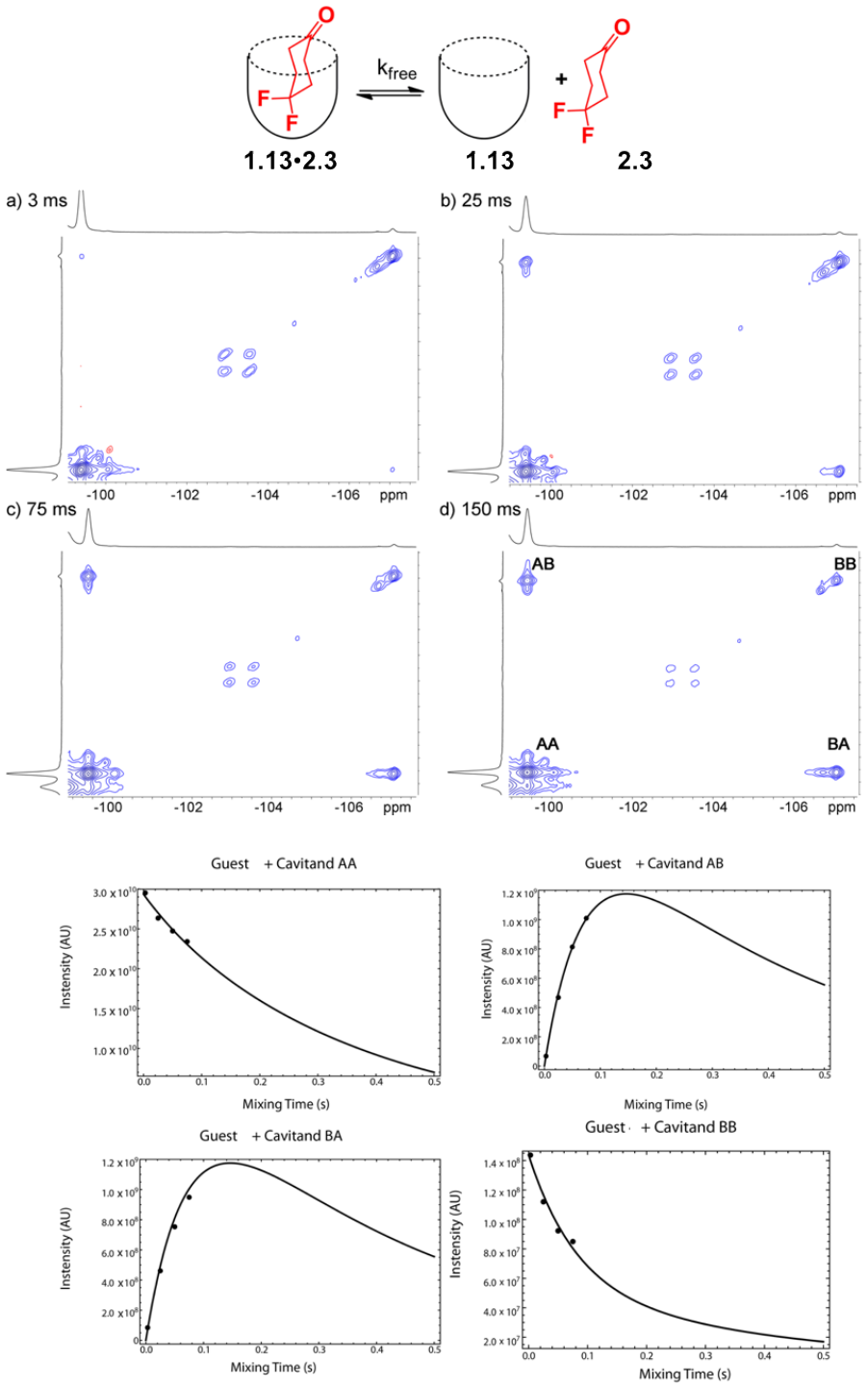

Figure 7.35: Representative ^{19}F EXSY spectra of the cavitand **1.13** • guest **2.3** complex in pure D_2O with varying mixing times (D_2O, 376.50 MHz, 298 K, [**1.13**] = 5.8 mM, [**2.3**] = 39.5 mM); fitted plots of peak intensity correlated with mixing time for each diagonal and crosspeak used to calculate the exchange rate.

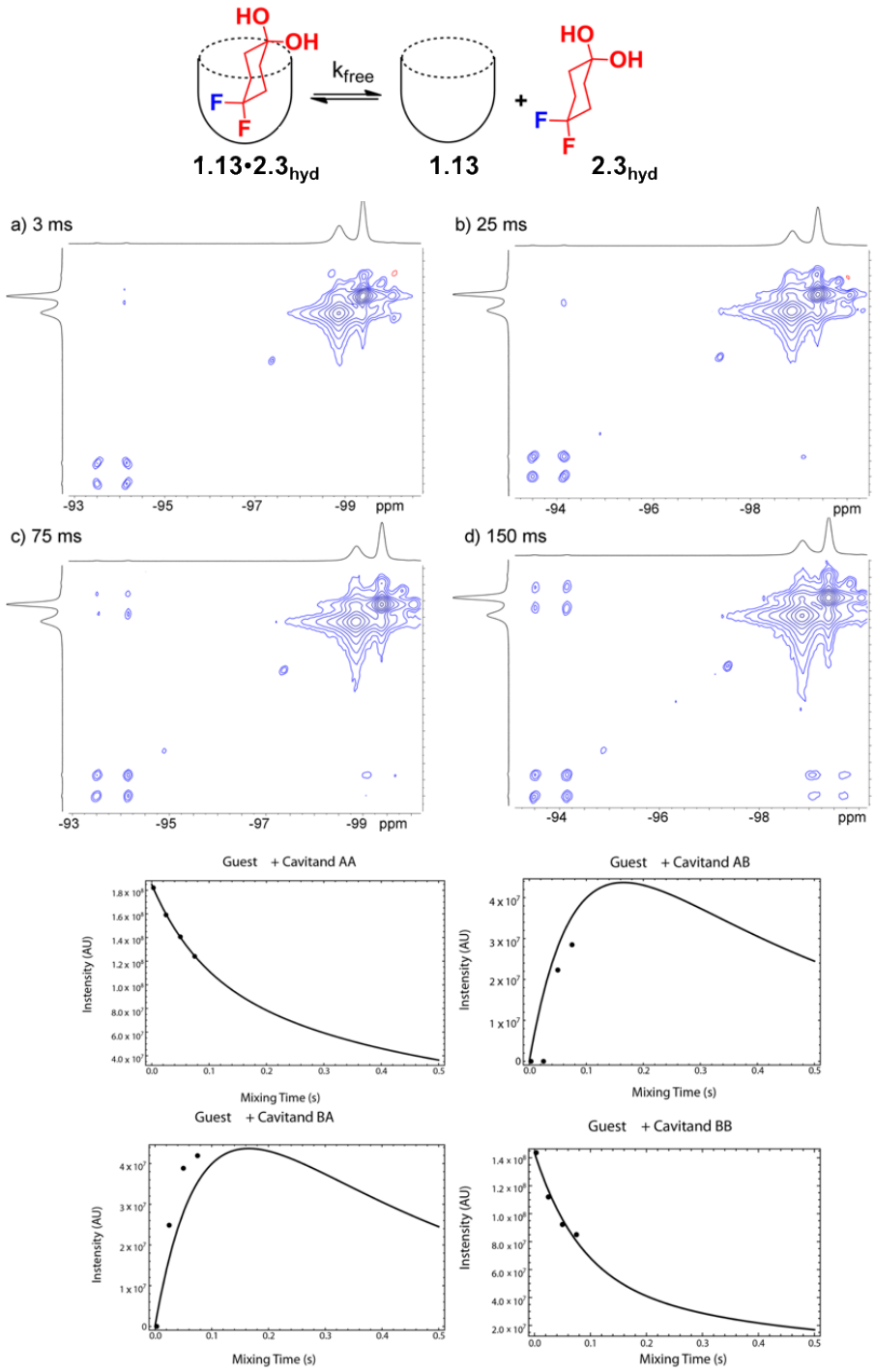

Figure 7.36: Representative ^{19}F EXSY spectra of the cavitand **1.13** • guest **2.3** complex in pure D_2O with varying mixing times (D_2O, 376.50 MHz, 298 K, [**1.13**] = 5.8 mM, [**2.3**] = 39.5 mM) illustrating the exchange peaks of the hydrate; fitted plots of peak intensity correlated with mixing time for each diagonal and crosspeak used to calculate the exchange rate.

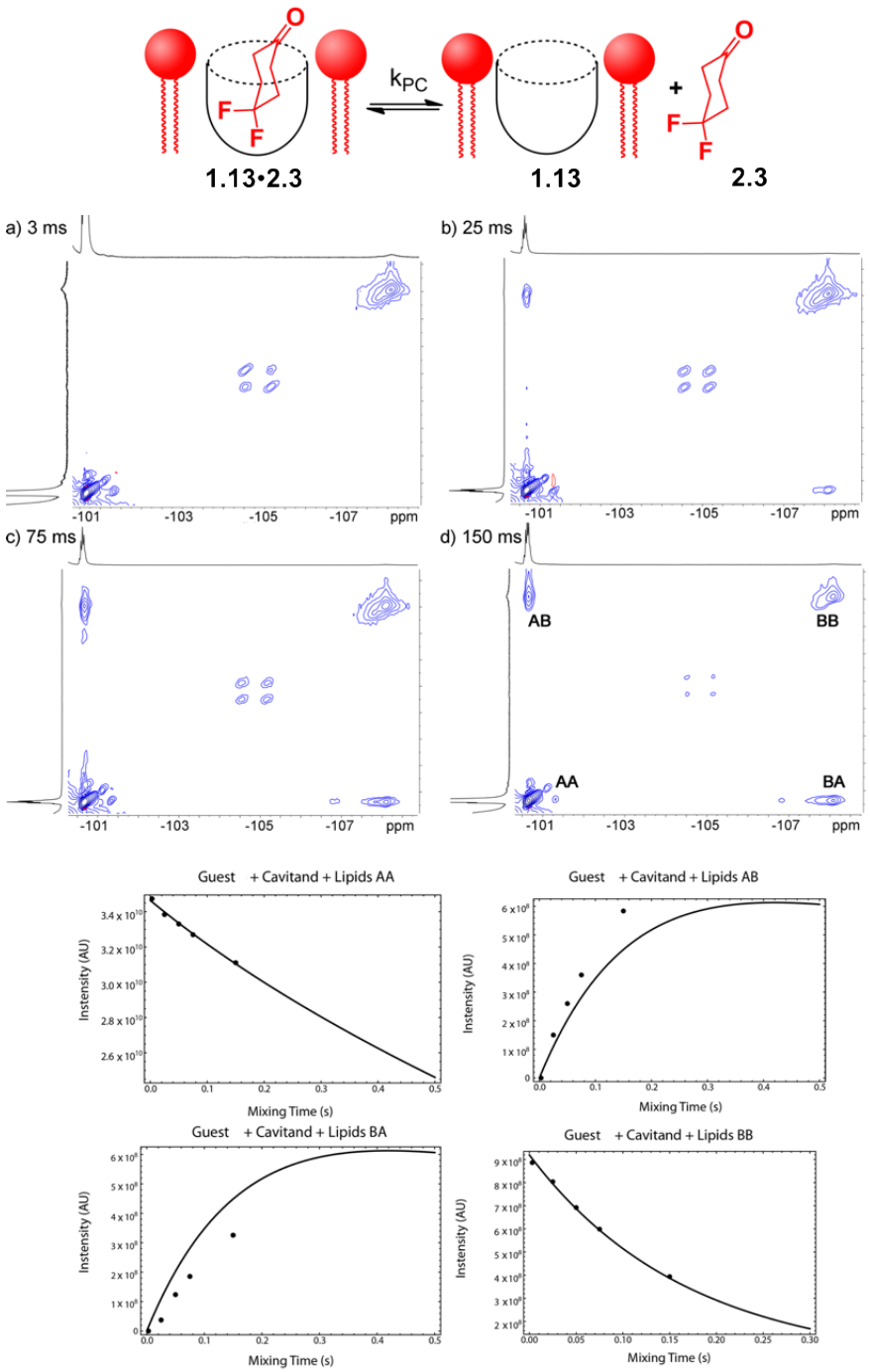

Figure 7.37: Representative ^{19}F EXSY spectra of the cavitand **1.13** • guest **2.3** complex in the PC_m micelles with varying mixing times (1 mM HEPES/D_2O, 376.50 MHz, 298 K, [**1.13**] = 5.8 mM, [**2.3**] = 39.5 mM, ratio DMPC/DHPC = 3.2:1, 60 mg/mL total lipid concentration); fitted plots of peak intensity correlated with mixing time for each diagonal and crosspeak used to calculate the exchange rate.

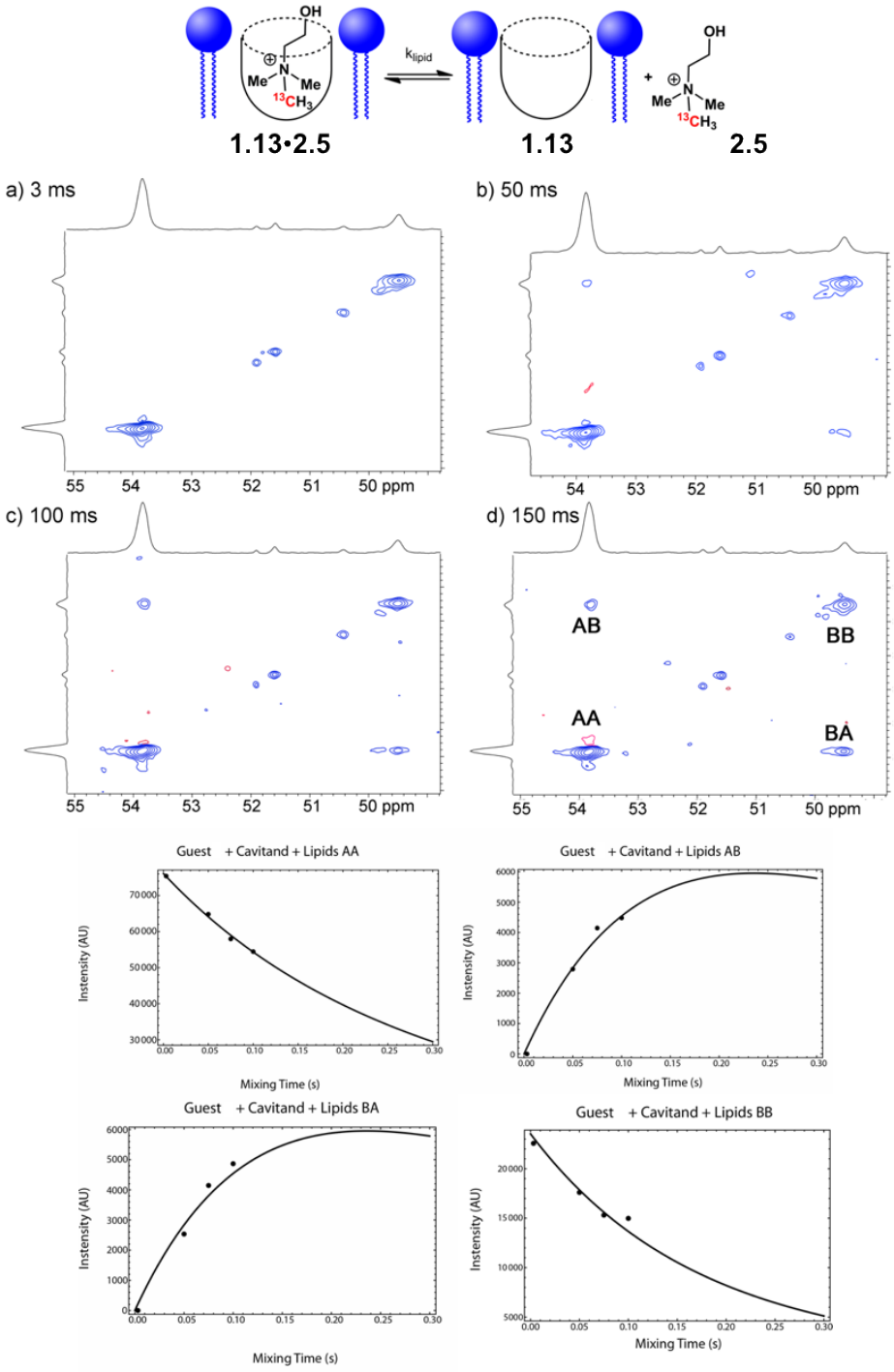

Figure 7.38: Representative ^{13}C EXSY spectra of the cavitand **1.13** •guest **2.5** complex in the PC_m micelles with varying mixing times (1 mM HEPES/D_2O, 150.84 MHz, 298 K, [**1.13**] = 5.8 mM, [**2.5**] = 16 mM, ratio DMPC/DHPC = 3.2:1, 60 mg/mL total lipid concentration); fitted plots of peak intensity correlated with mixing time for each diagonal and crosspeak used to calculate the exchange rate.

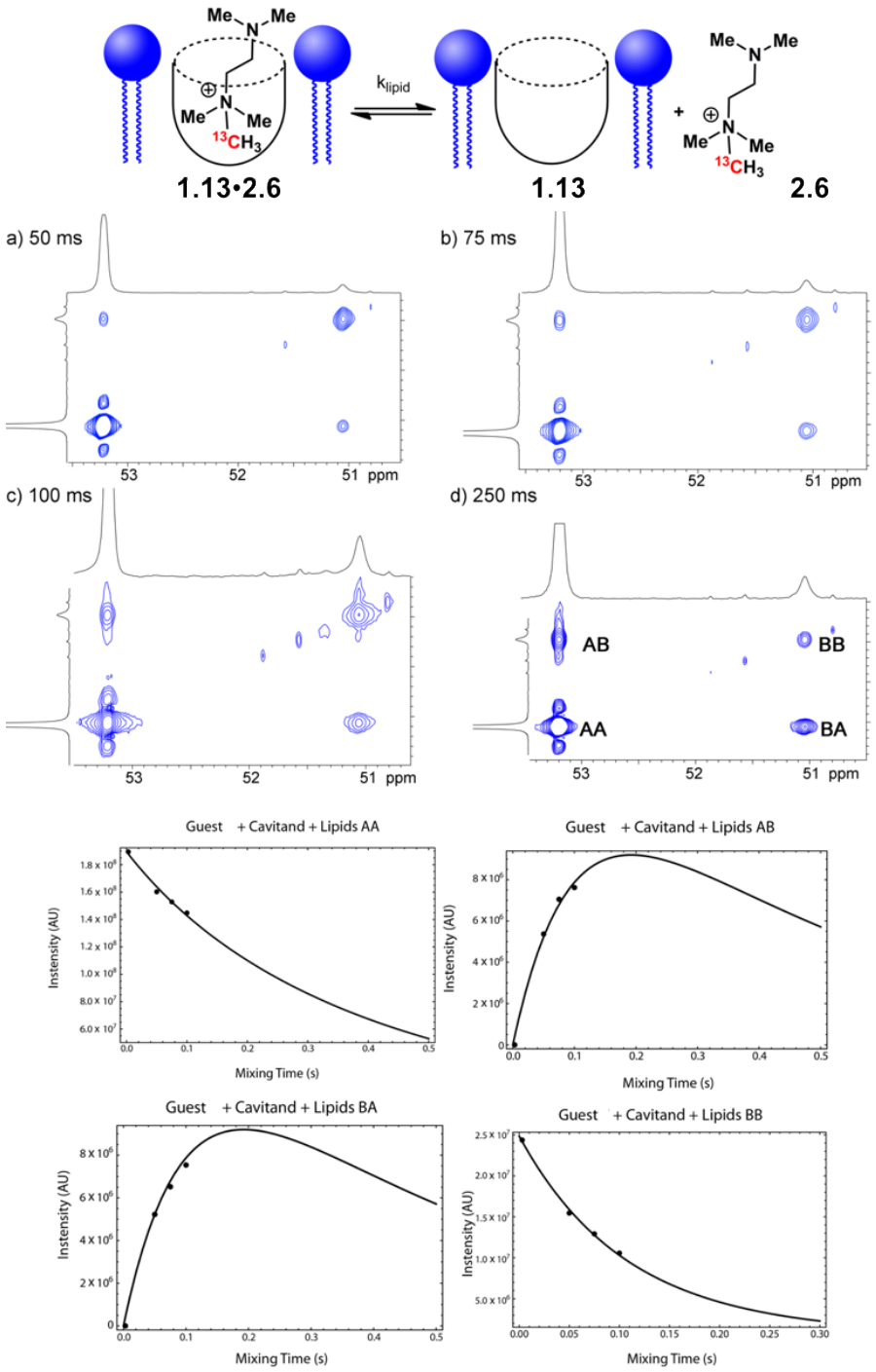

Figure 7.39: Representative ^{13}C EXSY spectra of the cavitand **1.13** • guest **2.6** complex in the PC_m micelles with varying mixing times (1 mM HEPES/D_2O, 150.84 MHz, 298 K, [**1.13**] = 5.8 mM, [**2.6**] = 16 mM, ratio DMPC/DHPC = 3.2:1, 60 mg/mL total lipid concentration); fitted plots of peak intensity correlated with mixing time for each diagonal and crosspeak used to calculate the exchange rate.

NMR Spectra in Magnetically Ordered DMPC/DHPC Bicelles:

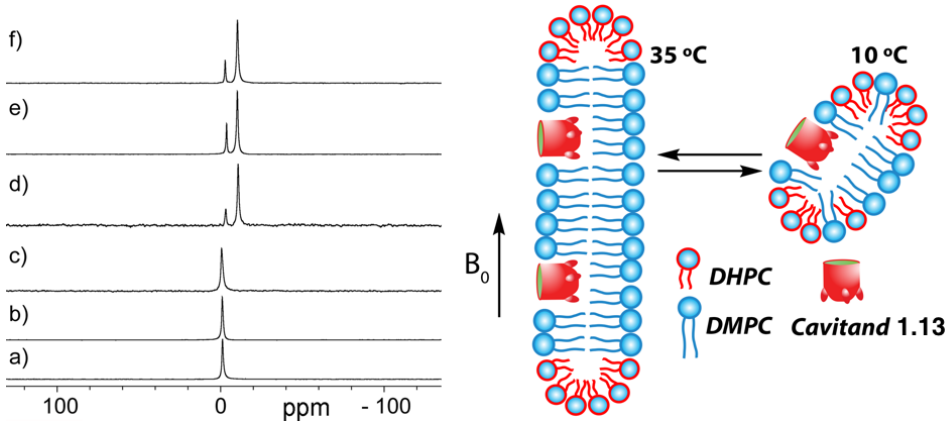

Figure 7.40: Temperature dependence of the lipid aggregate. ^{31}P NMR spectra of the DMPC/DHPC aggregates a) alone, 283 K; b) + 5 mM **1.13**, 283 K; c) + 5 mM **1.13** + 7 mM guest **2.4**, 283 K; d) alone, 303 K; e) + 5 mM **1.13**, 303 K; f) + 5 mM **1.13** + 7 mM guest **2.5**, 303 K. Ratio DMPC/DHPC = 3.2:1, 150 mg/mL total lipid concentration, 162.07 MHz, 2.5 mM HEPES/D_2O.

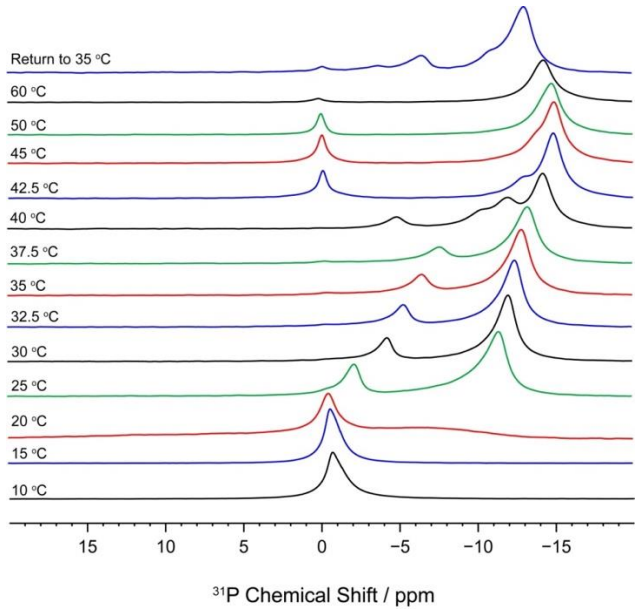

Figure 7.41: Temperature-dependent ^{31}P spectra of DMPC/DHPC bicelles. The two peaks indicative of bicelle formation display maximum splitting at 35 °C, the temperature at which all future experiments were performed, unless otherwise indicated. Low temperatures display a single peak at 0 ppm, indicative of micelle formation. Ratio DMPC/DHPC = 3.2:1, 150 mg/mL total lipid concentration, 162.07 MHz, 2.5 mM HEPES/D_2O.

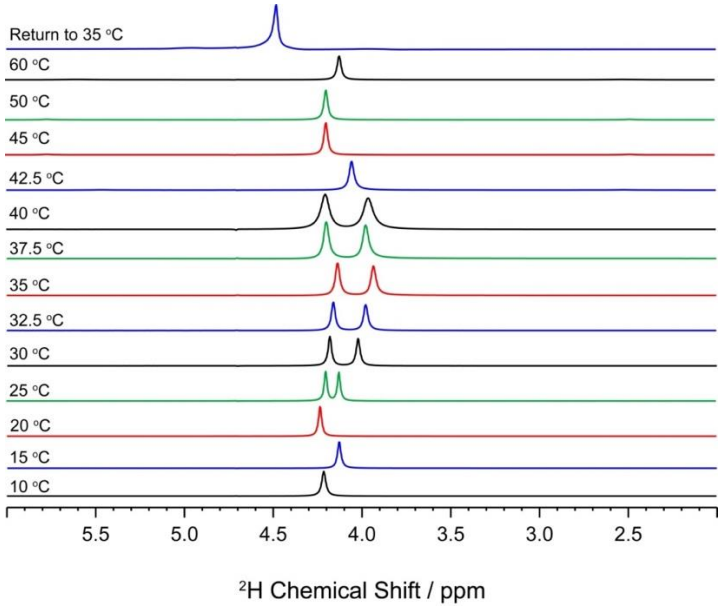

Figure 7.42: Temperature-dependent ^{2}H spectra of DMPC/DHPC bicelles. The two peaks indicative of bicelle formation display maximum splitting at 35 °C, the temperature at which all future experiments were performed, unless otherwise indicated. Low temperatures display a single resonance, indicative of micelle formation. Ratio DMPC/DHPC = 3.2:1, 150 mg/mL total lipid concentration, 92.09 MHz, 2.5 mM HEPES/D_2O.

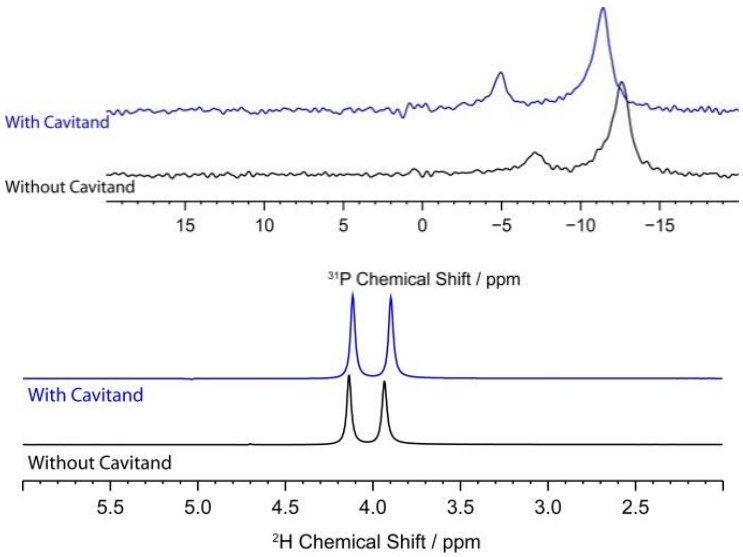

Figure 7.43:. ^{31}P and ^{2}H spectra of bicelles with and without cavitand added. Ratio DMPC/DHPC = 3.2:1, 150 mg/mL total lipid concentration, 162.07/ 92.09 MHz, 2.5 mM HEPES/D_2O.

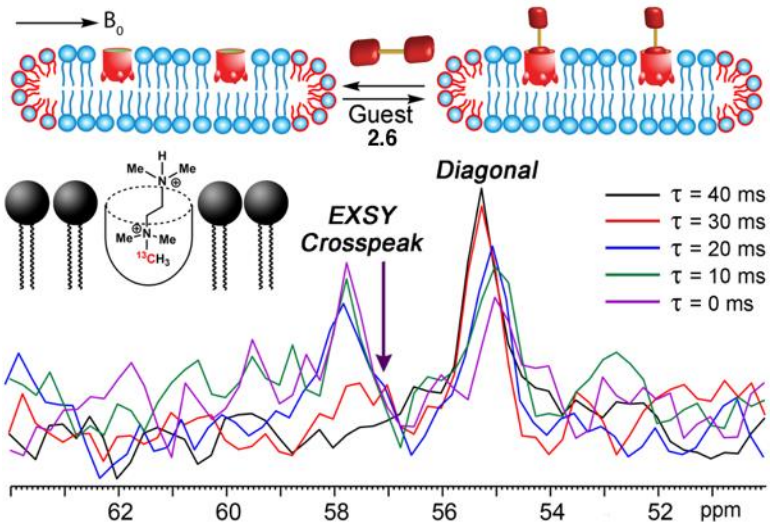

Figure 7.44: In/out exchange of guest **2.6** in the magnetically ordered bicelle system PC_b. Extracted 1D slices of the 2D ^{13}C-^{13}C EXSY NMR spectra at mixing time τ = 0 ms - τ = 40 ms of **1.13 • 2.6 • PC_b**; (2.5 mM HEPES/D_2O, 100.69 MHz, 298 K, [**1.13**] = 20 mM, [**2.6**] = 36 mM, ratio DMPC/DHPC = 3.2:1, 150 mg/mL total lipid concentration). Change in diagonal and crosspeak intensity shown. Slices extracted from F2, δ = 55 ppm.

7.3 Chapter 3 Experimental

Covalent protein modification: 5 mg of Bovine serum albumin (BSA) was dissolved in 100 mM PBS buffer in a glass vial equipped with a stir bar. A 152 mM solution of **3.5**/**3.6** was prepared in 100 mL nanopure water, and 10 mL of this solution was added to the BSA solution and gently stirred at room temperature for 16 h. The reaction mixture was transferred to a 50k centrifugal filter and centrifuged in order to filter any unattached **3.5**/**3.6**. The product was washed and centrifuged three times with 10 mM PBS buffer. The resulting solid was then dissolved in 1 mL 10 mM PBS buffer and a Bradford assay was performed in order to determine the concentration of the solution. The solution was diluted to a concentration of 1 mg/mL 1 using 10 mM PBS buffer and the resulting solution was used in the SPR experiments.

Fabrication of Cavitand Receptor Layer and Protein Binding:

SPR measurement: The calcinated gold substrate was rinsed with ethanol and nanopure water, dried with a gentle stream of N_2 gas, then clamped on an optical stage containing a 30 mL flow cell. The substrate was put in contact with the high-refractive index prism (n = 1.61) using refractive index matching fluid. POPC vesicles (1 mg mL^{-1}) in 10 mM PBS (150 mM NaCl, pH 7.4) were injected through a flow-injection system (5 mL h^{-1}) and incubated for 15–20 min to allow vesicle fusion on the hydrophilic calcinated gold surface, forming a smooth bilayer membrane. After 5–10 min of rinsing to remove excess lipids, 2 mg mL^{-1} cavitand **1.13** in 10% DMSO solution was injected and incubated for 20 min. The surface was extensively rinsed with nanopure water, followed by incubation with 15 mM protein in 10 mM PBS for 20 min. For streptavidin immobilization, 100 mL of a 1 mg mL^{-1} aqueous solution of biotinylated guest (**3.2**–**3.4**) was injected before protein, followed by 20 min incubation. Excess proteins were rinsed with water. Control experiments were performed under identical conditions in the absence of cavitand, or by the injection of POPC vesicles pre-incorporated with cavitand **1.16**. The uncertainties in resonance angle changes were determined by applying the standard deviations of variations over multiple (at least 3) repeated runs.

Saturation binding mode[5] was applied here to determine the equilibrium dissociation constant (K_d) value for the interaction between cavitand **1.13** and guests **3.5**/**3.6** BSA. Increasing concentrations of guests **3.5**/**3.6** BSA (0.01–15 mM) were injected over the cavitand **3.1**:membrane complex, and the minimum angle shift was recorded:

$$AB_{eq} = AB_{max}(1/(1 + K_d/[A]))$$

where AB_{eq} is the average of response signal at equilibrium and AB_{max} is the maximum response that can be obtained for guests **3.5**/**3.6** BSA binding and [A] is the concentration of **3.5**/**3.6** BSA injection. AB_{max}/AB_{eq} was plotted against 1/[A], and the slope is equal to K_d value.

SPR imaging procedure:

Arrayed Chip Preparation: Patterned well SPRi chips were fabricated using BK-7 glass microscope slides. BK-7 substrates were cleaned using boiling piranha solution (3:1 H2SO4/30% H2O2, Caution) for 30 min, followed by rinsing with deionized water and drying under compressed air. A 2 nm thick chromium adhesion layer was attached, followed by the deposition of a 51 nm thick gold layer via e-beam evaporation. Subsequently, photoresist AZ5214E was spin coated on the gold at 4000 rpm, and the surface was patterned into mesas representing the final array spots using standard photolithography methods. After a second electron beam evaporation of 100 nm of gold, the photoresist was lifted off with acetone, leaving an elevated gold grid behind, defining the array elements (800 X 800 mm). The surface was rendered hydrophilic with ca. 4 nm of SiO2 deposited by plasma enhanced chemical vapor deposition (PECVD).

Fabrication of Cavitand Receptor Array and Protein Binding SPRi: POPC SUVs (formed as above) were diluted to a final concentration of 1 mg mL^{-1} in 50 mM trehalose using a trehalose/10 mM PBS mixture. The solution was incubated at 4^{o}C for at least 1 h before use. 200 nL of this solution was deposited in the array wells, and dried overnight in a vacuum desiccator. The arrayed gold chips were mounted on an optical stage containing a 300 mL flow cell. Each array was put in contact with an equilateral SF2 prism (n = 1.616)

using refractive index matching fluid (n = 1.616, Cargille Labora- tories, Cedar Grove, NJ). The optical stage was fixed on a goniometer that allows manual selection of the incident light angle. An incoherent light source (LED, l = 648 nm) was used for SPR excitation, and the reflected images were captured by a cooled 12-bit CCD camera, Retiga 2000R (QImaging, Surrey, BC, Canada) with a resolution of 1600 1200 pixels, and 7.4 mm 7.4 mm pixel size. The dehydrated vesicles were rehydrated under constant flow in the flow cell for 20 min before cavitand injection (either **1.13** or **3.1** depending on the system being formed). The cavitand was incubated for 20 min, then rinsed for 5 to 10 min to remove any unincorporated cavitand. Next, either cyt *c*, biotinylated guest **3.3** followed by streptavidin, or **3.5** BSA were injected and incubated for 20 min before washing away any unincorporated sample for 5 to 10 min. Injections of sample solutions into the flow cell were monitored in real time by recording changes in the reflectance every 300 ms inside the gold array wells and for reference purpose on the surroundings. Sensorgrams were obtained by averaging reflected light intensity over each array element using a home-built LabView program.

Synthesis of New Compounds:

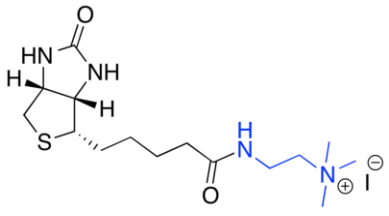

2-Biotinamido-N,N,N-trimethylethanaminium Chlordie 3.2: N-hydroxyssuccinimidyl ester (NHS Biotin, 100 mg, 0.293 mmol) was added to a 10 mL round bottom flask with a stir bar. The system was purged and placed undern nitrogen

followed by addition of dry THF (3 mL). Unsymmetrical N,N-dimethylethylenediamine was added (0.296 mmol) and the reaction was stirred at room temperature overnight. The reaction mixture was concentrated via rotary evaporation and triturated with ether and hexanes before drying under vacuum. The product was then placed in a 10 mL round bottom flask with a stir bar under nitrogen. Dry THF (2 mL) was added followed by iodomethane (41.6 mg, 18.2 µL, 0.293 mmol). The reaction mixture was stirred at room temperature for 4 h then filtered and triturated with dry dichloromethane and hexanes. The product (48 mg, 36 % yield) was collected as a white solid. ^{1}H NMR (400 MHz, D_2O): δ 4.64 (dt, J = 8, 4 Hz, 1H), 4.47 (dd, J = 8, 4 Hz, 1H), 3.72 (t, J = 6 Hz, 2H), 3.52 (t, J = 7, 6, 2H), 3.36 (dd, J = 13, 5 Hz, 1H) 3.31 (dd, J = 13, 5Hz, 1H), 3.21 (s, 9H), 3.03 (dd, J = 13, 5, Hz, 1H), 2.61 (m, 2H), 2.34 (t, J = 7 Hz, 2H), 1.67 (m, 2H), 1.44 (m, 2H) ^{13}C NMR (100 MHz, DMSO): δ 172.8, 162.8, 63.8, 61.1, 59.2, 55.4, 52.6, 44.3, 35.0, 33.0, 30.4, 28.0, 25.0. ESI *m/z* expected: 329.48, found [MH^+] = 329.22.

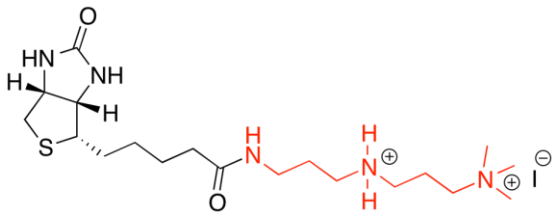

N^1-(3-acetamidopropyl)-N^3,N^3,N^3-trimethylpropane-1,3-diaminium Iodide 3.3: NHS Biotin (100 mg, 0.293 mmol) was added to a 10 mL round bottom flask with a stir bar. The system was purged and placed under nitrogen followed by addition of dry THF (3 mL). N,N-dimethylpropylenediamine was added (0.296 mmol) and the reaction was stirred at room temperature overnight. The reaction mixture was concentrated via rotary

evaporation and triturated with ether and hexanes before drying under vacuum. The product was then placed in a 10 mL round bottom flask with a stir bar under nitrogen. Dry THF (2 mL) were added followed by iodomethane (41.6 mg, 18.2 µL, 0.293 mmol). The reaction mixture was stirred at room temperature for 4 h then filtered and triturated with dry dichloromethane and hexanes. The product (85 mg, 55% yield) was collected as a white solid. ^{1}H NMR (400 MHz, D_2O): δ 4.63 (dt, J = 8, 4 Hz, 1H), 4.46 (dd, J = 8, 4 Hz, 1H), 3.77 (t, J = 6 Hz, 2H) 3.40 (m, 2H), 3.35 (t, J = 7 Hz, 2H), 3.20 (s, 10H), 3.12 (m, 6H), 2.81 (m, 4H), 2.30 (t, J = 7 Hz, 2H), 1.89 (t, J = 7 Hz, 2H), 1.66 (m, 2H), 1.44 (m, 2H). ^{13}C NMR (100 MHz, DMSO-d_6): δ 172.9, 162.7, 63.7, 61.0, 59.2, 55.4, 52.3, 45.9, 45.2, 44.7, 36.2, 35.2, 28.4, 28.2, 27.8, 25.2, 21.6. ESI-MS *m/z* expected: 400.60, found [MH^+] = 400.28.

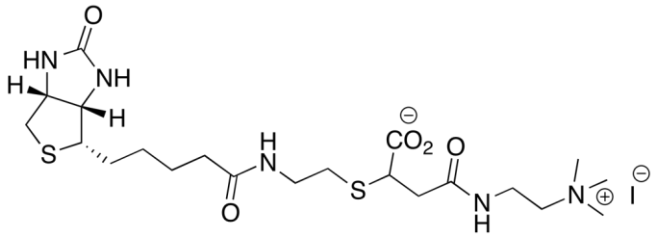

2-((2-biotinamidoethyl)thio)-4-oxo-4-((2-(trimethylammonio)-ethyl)amino)butanoate 3.4: NHS Biotin (100 mg, 0.293 mmol) was added to a 10 mL round bottom flask with a stir bar. The system was purged and placed under nitrogen followed by addition of dry THF (3 mL). Cystamine dihydrochloride was added (0.147 mmol) and the reaction was stirred at room temperature overnight. The reaction mixture was concentrated via rotary evaporation and triturated with ether and hexanes before drying under vacuum to

afford a white solid (60 mg, 68% yield) as product. ^{1}H NMR (400 MHz, D_2O): δ 4.64 (dt, *J* = 8,4 Hz, 2H), 4.47 (dd, *J* = 8,4 Hz, 2H), 3.42 (t, *J* = 6 Hz, 6H), 3.04 (t, *J* = 8 Hz, 6H), 2.79 (m, 6H), 1.82 (m, 4H), 1.66 (m, 4H), 1.55 (m, 4H). ^{13}C NMR (100 MHz, DMSO-d_6): δ 170.2, 162.6, 61.0, 59.2, 55.2, 37.8, 33.9, 30.0, 27.8, 27.6, 25.4, 24.3. ESI-MS *m/z* expected: 604.20, found [MH^+] = 605.21. The disulfide product (1 mg, 1.65 μmol) was then placed in a glass vial equipped with a stir bar under. Nanopure water (500 μL) and excess tris(2-carboxyethyl)phosphine (TCEP) were added (8.3 mg, 33 μmol) and the solution was stirred at room temperature for 1 h. An aliquot of a solution of **7** (1.65 μmol) was added to the solution and stirred at room temperature for 1 h. This solution was then directly used for SPR studies.

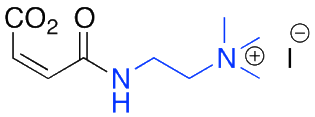

(Z)-4-oxo-4-((2-(trimethylammonio)ethyl)amino)but-2-enoate 3.5: Maleic anhydride (500 mg, 5.10 mmol) was added to a 100 mL round bottomed flask with a stir bar followed by ether (50 mL). N,N-dimethylethylenediamine (5.10 mmol, 450 mg, 511μL) was then added dropwise while stirring and the solution as allowed to stir at room temperature for 10 min (when precipitate was formed). The solid was then filtered, washed with ether and dried. 100 mg (0.540 mmol) of solid was then placed in a round bottom flask followed by DMF (3 mL) and methyl iodide (76.6 mg, 33.6 μL, 0.54 mmol). The reaction mixture was then stirred at room temperature for 4 h. The solid was then filtered and washed with ether and hexanes to afford a yellow-white solid (125 mg, 10 % yield) as product. ^{1}H NMR (400

MHz, D_2O): δ 6.51 (d, *J* = 12 Hz, 1H), 6.36 (t, *J* = 11 Hz, 1H), 3.80 (t, *J* = 7 Hz, 2H), 3.57 (t, *J* = 7 Hz, 2H), 3.22 (s, 9H). ^{13}C NMR (100 MHz, D_2O): δ 221.3, 220.1, 132.5, 129.8, 64.0, 53.5, 33.7. ESI-MS: *m/z* expected: 201.24, found: $[MH^+]$ = 201.14

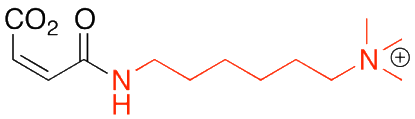

(Z)-4-oxo-4-((2-(trimethylammonio)hexyl)amino)but-2-enoate 3.6: Maleic anhydride (170 mg, 1.73 mmol) was added to a 50 mL round bottomed flask with a stir bar followed by ether (10 mL). 6-(dimethylamino)hexylamine (300 µL, 1.73 mmol) was then added dropwise while stirring and the solution as allowed to stir at room temperature for 10 min (when precipitate was formed). The solid was then filtered, washed with ether and dried. 84 mg (0.347 mmol) of the resulting solid was then placed in a round bottomed flask followed by DMF (1 mL) and methyl iodide (49 mg, 22.0 µL, 0.35 mmol). The reaction mixture was then stirred at room temperature for 4 h. The solid was then filtered and washed with ether and hexanes to afford a thick orange oil (90 mg, 68 % yield) as product. ^1H NMR (400 MHz, D_2O): δ 6.48 (d, *J* = 12.4 Hz, 1H), 6.30 (d, *J* = 12.2 Hz, 1H), 3.32 (m, 4H), 3.12 (s, 9H), 1.82 (q, *J* = 7 Hz, 2H), 1.59 (q, *J* = 7, 2 Hz), 1.42 (m, 2H). ^{13}C NMR (100 MHz, D_2O): δ 169.2, 167.3, 133.5, 130.3, 66.8, 53.1, 39.7, 27.8, 25.7, 25.2, 22.4. ESI-MS: *m/z* expected: 257.35, found: $[MH^+]$ = 257.19.

SPR Data: Native Protein Immobilization

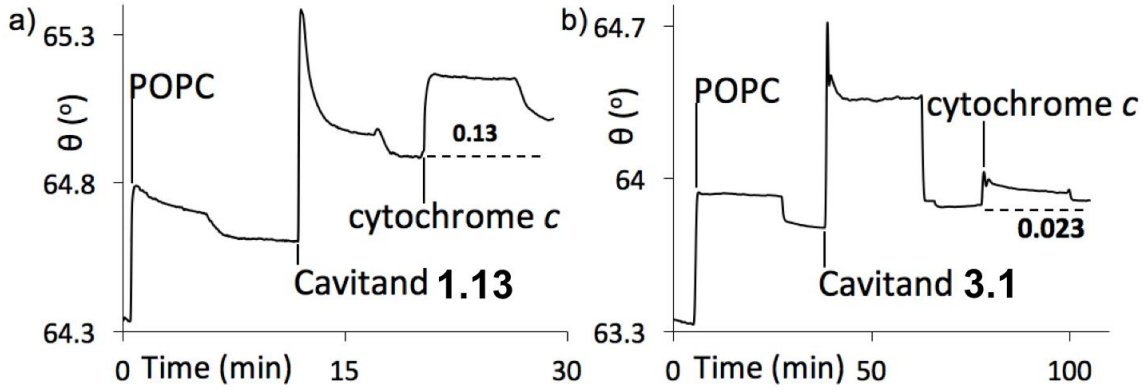

Figure 7.45: SPR sensorgrams showing immobilization of cytochrome *c* at the a) cavitand **1.13**:POPC interface and b) cavitand **3.1**:POPC interface.

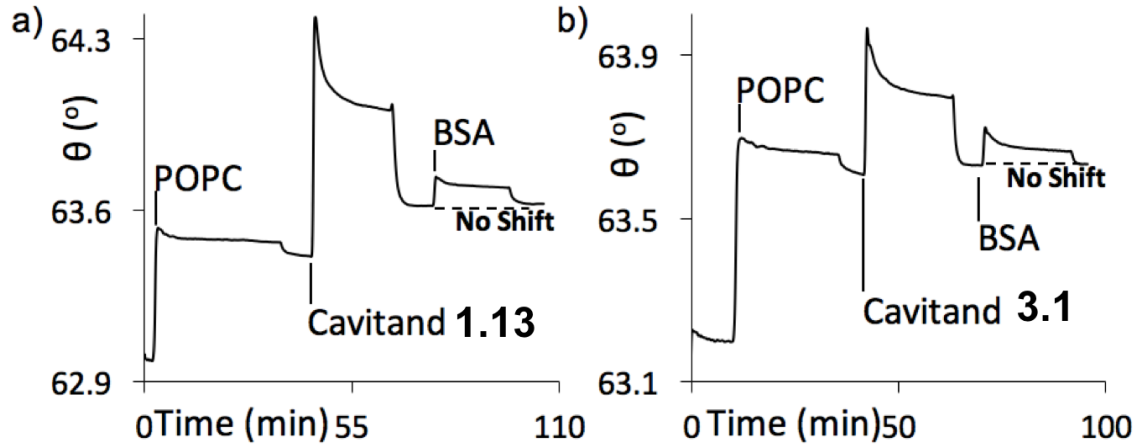

7.46: SPR sensorgrams showing immobilization of BSA at the a) cavitand **1.13**:POPC interface and b) cavitand **3.1**:POPC interface.

Avidin Selectivity for Cavitand 1.13:

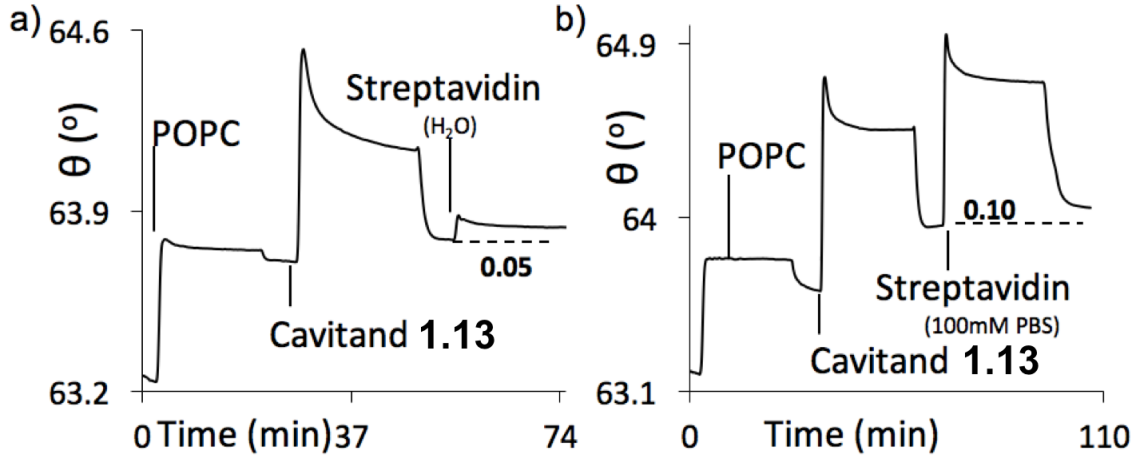

Figure 7.47: SPR sensorgrams showing immobilization of streptavidin by the cavitand **1.13**:POPC interface. Streptavidin injection medium: a) Nanopure H_2O; b) 100 mM PBS.

Dual Mode Binding Guests:

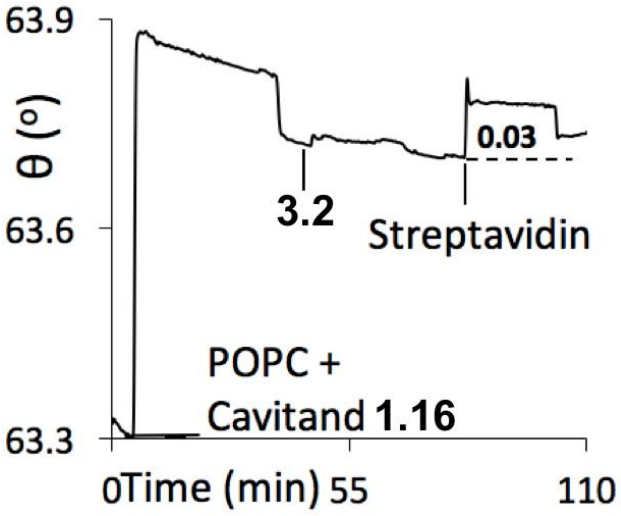

Figure 7.48: SPR sensorgrams showing immobilization of streptavidin in 10 mM PBS by the **3.2**:cavitand **1.16**:POPC interface.

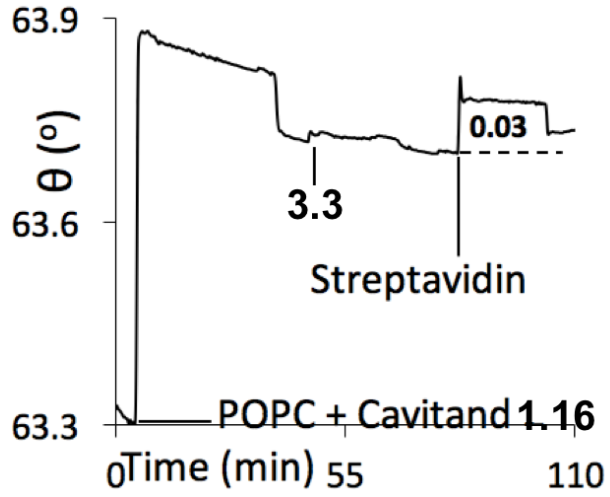

Figure 7.49: SPR sensorgrams showing immobilization of streptavidin in 10 mM PBS by the **3.3**:cavitand **1.16**:POPC interface.

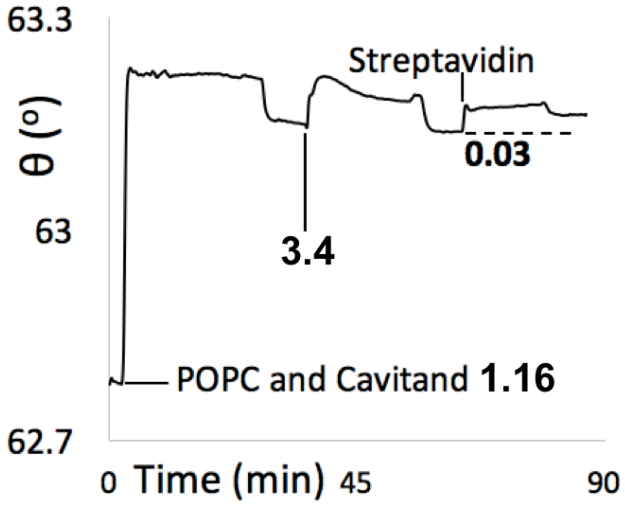

Figure 7.50: SPR sensorgrams showing immobilization of streptavidin in 10 mM PBS by the **3.4**:cavitand **1.16**:POPC interface.

Streptavidin Binding Optimization:

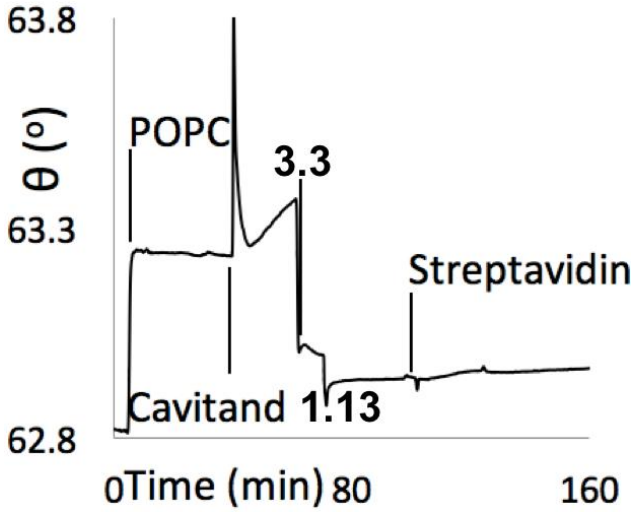

Figure 7.51: SPR sensorgrams showing immobilization of streptavidin in 10 mM PBS by the **3.3**:cavitand **1.13**:POPC interface using 10 mM PBS as running buffer.

SPRi Data:

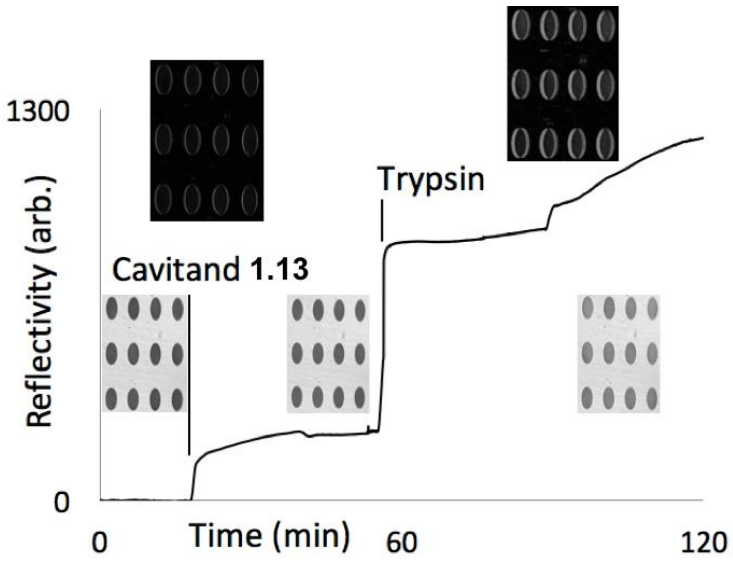

Figure 7.52: Mean SPR sensorgram of the array spots showing immobilization of trypsin in 10 mM PBS at the cavitand **1.13**:POPC interface.

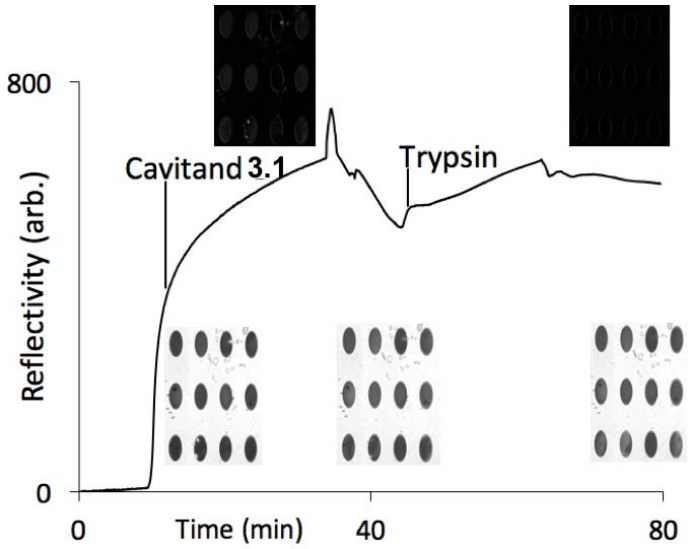

Figure 7.53: Mean SPR sensorgram of the array spots showing immobilization of trypsin in 10 mM PBS at the cavitand **3.1**:POPC interface.

7.4 Chapter 4 Experimental

Trimethylammonium tagged initiator **1.17** was synthesized according to literature procedures.[6]

Fabrication of Cavitand:Supported Lipid Bilayer: The calcinated gold substrate was first rinsed with ethanol and nanopure water and after drying under gentle stream of nitrogen gas was then clamped down by a flow cell on a high-refractive index prism for SPR measurement. POPC vesicles (1 mg mL^{-1} in 10 mM PBS (150 mM NaCl, pH 7.4) were injected through a flow-injection system and incubated for 15 min to allow vesicle fusion on the hydrophilic calcinated gold surface, forming a smooth bilayer membrane. After 5 min of rinsing to remove excess vesicles from the surface, 0.7 mg mL^{-1} cavitand **1.13** in 10% DMSO solution was subsequently injected and incubated for 20 min. The surface was extensively rinsed with water, followed by incubation with 10 mg mL^{-1}

initiator **1.17** in aqueous solution for 5 min. After 5 min of rinsing to remove unbound initiator **1.17** from bilayer lipid membrane, atom transfer radical polymerization (ATRP) reaction was initiated by the injection of monomer **4.1** and HEMA (0.7 M HEMA and 0.7 M AEMA **4.1**) and catalyst (15 mM CuBr/30 mM 2,2′-bipyridine/22 mM L-ascorbic acid or 15 mM FeCl2/ 30 mM 1,10-phenanthroline/22 mM L-ascorbic acid in a 1:2:1.5 molar ratio) mixture solution. After 20 min of incubation for polymer growth, ATRP reaction was terminated by 5 min rinsing with water.

In Situ Reactions of Poly(AEMA): After poly(AEMA) formation on the lipid membrane surface, NHS-biotin was injected into the SPR flow cell (1 mg mL^{-1} in 10% DMSO aqueous solution) and incubated for 20 min followed by 5 min rinsing. Avidin (1 mg mL^{-1} in 10 mM PBS) was then injected, incubated for 20 min, and washed for 5 min. The reaction with NBD-Cl followed the same procedure.

Cell Sample Preparation: Human monocytic THP-1 cells (ATCC TIB-202) were cultured at 37 °C and 5% CO2 in RPMI 1640 media supplemented with 10% FBS, 100 U/ml penicillin, 100 μg/mL streptomycin, and 50 μM 2-mercaptoethanol. Cells were harvested by centrifugation and washed three times with ice cold deionized H_2O. Immediately after washing, cells were resuspended in ice cold deionized H2O to a final concentration of 7.5 $\times 10^6$ cells mL^{-1}.

Cellular Adhesion Studies: After poly(AEMA) formation, human monocytic THP-1 cells were injected into the SPR flow cell and incubated for 20 min, then rinsed for 5 min with nanopure water. The gold chip was then removed from the SPR system and covered with a microscope coverslip and visualized under an optical microscope.

7.5 Chapter 5 Experimental

Measurement of Fluorescence Quenching and Displacement Assays:

In a typical quenching assay, 10 µL of the fluorescent guest (**5.1**, **5.4**, or **5.5**) (30 µM for **5.1** and **5.4** and 15 µM for **5.5**), 10 µL of the cavitand **1.13** (200 µM), and 80 µL of the 1×PBS (10 mM phosphate at pH 7.4 with 150 mM NaCl) were mixed in the 96-well plate, and incubated with mild shaking for 10 minutes. Followed, fluorescence was recorded in a Perkin Elmer Wallac 1420 Victor 2 Microplate Reader (PerkinElmer, Inc., Waltham, MA) with the EX/EM wavelengths at 485/535 nm. To observe the effect of fluorescence recovery induced by analyte molecules, 10 µL of the guest molecule (30 µM) was mixed with 10 µL of cavitand (200 µM) and 70 µL of PBS and incubated for 10 minutes; then 10 µL of the analyte solution was added and fluorescence reading was taken after 20 minutes. LDA Analysis: Linear discriminant analysis (LDA), Jack- knife validation, and hierarchical clustering analysis (HCA) were completed with RStudio (version 1.0.136), an integrated development environment (IDE) for R (version 3.3.2). Fluorescence data was first stored as an Excel file and then read into a matrix in RStudio. The internal function "princomp()" was used to perform PCA; the 'lda()' function was called for Jackknife Validation with the "CV" set as "true". One replicate was left out of the training set, and the LDA classifier was fitted on the input data. The output was recorded in a two-dimensional table. HCA was performed with two steps: the Euclidean distance between any two objects within the data set was first calculated and recorded into a two-dimensional matrix; then the matrix was used as the input for the built-in HCA function "hclust()", and the result was drawn with the "plot()" function. Confidence ellipses were

drawn with the data obtained from PCA using Matlab (version R2016b) and a self-developed script. The full Matlab script is available upon request. The 3D scatter plot was performed with Plotly's R package version 4.

Metal Sensing: The heavy metal ions were produced from their respective chloride salts as following with several exceptions: $MgCl_2$, $CaCl_2$, $MnCl_2$, $FeCl_2$, $CoCl_2$, $NiCl_2$, $CuCl_2$, $ZnCl_2$, $CdCl_2$, $Hg(OAc)_2$, $Pb(NO_3)_2$, $LaCl_3$, $CeCl_3$, $ErCl_3$, $ThCl_4$, and $UO_2(OAc)_2$. In general, the fluorescence assay was carried out by mixing 10 μL of guest **5.4** (30 μM) or guest **5.5** (15 μM), 10 μL of the cavitand (40 μM for **1.13**:**5.4** or 200 μM for **1.13**:**5.5**, 50 μM for **1.16**:**5.4** or **3.1**:**5.4**), 70 μL of the incubation buffer (Tris pH 7.4 or Bis- Tris pH 5.5) in a 96-well plate, adding 10 μL of different metal salt solution to bring the total volume up to 100 μL, and incubating with mild shaking for 15 min at room temperature. The fluorescence signal (F) was recorded in a PerkinElmer Wallac 1420 Victor 2 Microplate Reader (PerkinElmer) with the Ex/Em wavelengths at 530/605 nm for guest **5.4** or 485/605 for guest **5.5**.

Synthesis of New Molecules:

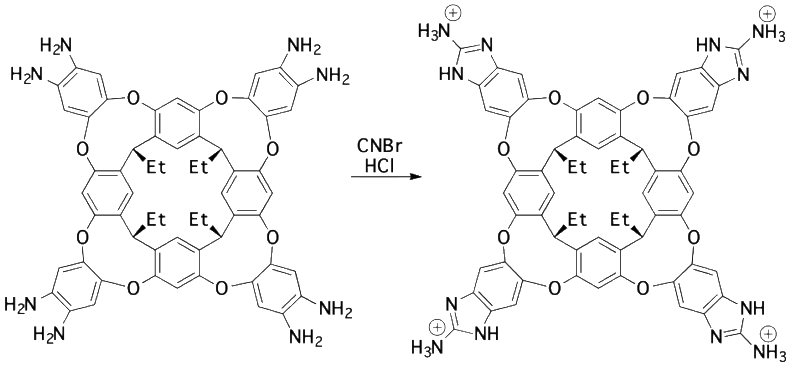

Tetraammonium Cavitand **3.1**: Following a procedure slightly modified from published methods:[4] Octaamine cavitand **1.9** (454 mg, 0.44 mmol) in EtOH was stirred for 15 min at room temperature under N_2 atmosphere. A solution of cyanogen bromide (300 mg, 2.83 mmol) in EtOH was added drop wise over 15 min. reaction mixture was stirred for 24 hr at room temperature. The mixture was then cooled to 0 ^oC and basified to pH ~9. Solvent was removed by rotatory evaporation. The solid was redissolved in MeOH and 2 drop of 1M HCl was added, a white precipitate was formed. The cavitand was obtained as red solid (232 mg, 45% yield). ^1H NMR (300 MHz, DMSO-d_6), δ: 12.1 (s, 8H), 8.7 (s, 8H), 7.79 (s, 4H), 7.7 (s, 8H), 7.65 (s, 4H), 5.33(t, J = 7.8 Hz, 4H), 2.24 (m, 8 H), 0.85 (t, J = 7.2 Hz, 12H); ^{13}C NMR (75 MHz, DMSO-d_6) δ: 155.9, 152.0, 148.7, 135.6, 130.3, 127.1, 125.3, 117.1, 107.4, 35.7, 30.2, 25.2; ESI-HRMS: Calc $C_{64}H_{53}Cl_4N_{12}O_8$: 1117.41; exp. 1117.47 [M+H]+.

Trimethylammonium guest **5.1** was synthesized according to literature procedures.[5]

General Procedure: Fluorescein isothiocyanate (25 mg, 0.64 mmol) was added to a 10 mL round bottom flask with stir bar. The system was purged and placed under nitrogen

followed by addition of dry THF (1 mL). The corresponding amine (either N-methylethylenediamine or *unsym*-N,N-dimethylethylene-diamine was added (0.64 mmol) and the reaction was stirred at room temperature overnight. The reaction mixture was filtered and the product collected as a bright orange solid.

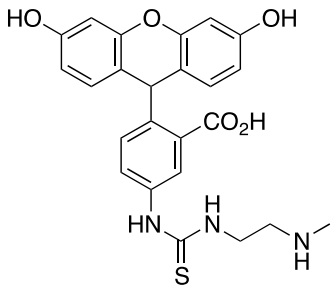

Monomethylated Guest **5.3**: H NMR (500 MHz, D_2O): δ 7.55 (s, 2H), 7.40 (d, *J* = 8.0 Hz, 2H), 7.15 (d, *J* = 8.9 Hz, 2H), 6.93 (d, *J* =8.0 Hz , 1H), 6.62 (dd, *J* = 8.9, 2.6 Hz, 2H), 6.54 (d, *J* = 2.6 Hz, 2H), 4.16 (s, 1H), 3.76 (s, 2H), 3.35 (t, 2H), 3.11 (s, 3H), 3.0 (t, 2H). ^{13}C NMR (125 MHz, D_2O): δ 180.7, 180.4, 173.1, 158.4, 140.4, 131.2, 130.1, 129.4, 122.9, 112.2, 103.6, 67.8, 66.5, 49.6, 37.5, 37.1, 33.2. ESI MH^+ *m/z* expected: 465.14, found: M^+= 464.1296.

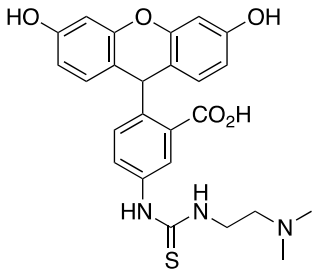

Dimethylated Guest **5.2**: ^1H NMR (700 MHz, DMSO-d_6): δ 8.23 (s, 2H), 7.75 (d, *J* = 8.0 Hz, 2H), 7.09 (d, *J* = 8.0 Hz, 2H), 6.67 (d, *J* = 8.9 Hz, 2H), 6.60 (d, *J* = 2.1 Hz, 2H), 6.44 (dd, *J* = 8.9, 2.1 Hz, 2H), 5.75 (s, 1H), 3.60 (m, 2H), 3.50 (s, 2H), 2.66 (m, 2H), 2.19 (s,

6H). ^{13}C NMR (175 MHz, DMSO-d_6): δ 180.22, 168.78, 166.73, 158.65, 153.88, 152.10, 129.51, 128.86, 125.96, 116.18, 112.38, 110.48, 109.51, 102.34, 66.98, 59.49, 57.12, 45.12. ESI MH^+ *m/z* expected: 479.15, found: M^+= 478.1435.

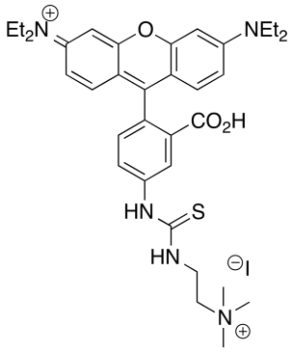

Rhodamine Guest **5.4**: Rhodamine B isothiocyanate (25 mg, 0.03 mmol) along with N,N-dimethylethylenediamine (3.7 µL, 0.03 mmol) was dissolved in MeOH (3 mL), and the resulting mixture was stirred at room temperature for 12 h. The solvent was removed *in vacuo* and the remaining solid was rinsed with ether and filtered. The solid was then placed in a round bottom flask with 3 mL MeOH and iodomethane (2 µL, 0.03 mmol) and stirred at room temperature for four hours. The solvent was removed *in vacuo* and the remaining solid rinsed with ether and filtered to afford a bright purple solid. ^{1}H NMR (500 MHz, DMSO-d_6) δ 12.92 (s, 2H), 8.65 (d, *J* = 2.4 Hz, 1H), 8.01 (s, 1H), 7.81 (d, *J* = 8.5 Hz, 1H), 7.77 (s, 1H), 7.65 (d, *J* = 8.5 Hz, 1H), 7.41 (d, *J* = 8.3 Hz, 1H), 7.00 (d, *J* = 8.1 Hz, 2H), 6.87 (d, *J* = 9.0 Hz, 2H), 6.83 (d, *J* = 8.9 Hz, 2H), 6.71 (d, *J* = 9.0 Hz, 1H), 6.58 (dd, *J* = 8.6, 2.3 Hz, 1H), 6.28 (d, *J* = 2.2 Hz, 1H) 6.10 (m, 4H), 6.00 (m, 3H), 3.87 (t, *J* = 7.0 Hz, 4H), 3.49 (t, *J* = 7.0 Hz, 4H), 3.33 (q, *J* = 7.0 Hz, 16H), 3.10 (s, 18H), 1.12 – 0.97 (t, *J* = 7.0 Hz, 24H). MALDI-TOF/TOF (Rhodamine B Guest • Cl^- • H_2O) *m/z* expected: 656.30, found [MH^+] = 656.10.

Cytotoxicity Test

HeLa cells (4 x 103 cells/well) were cultured in 96-well plate for 24 h at 37°C and cavitand **1.13** was added (final concentration = 20 μM) rhodamine guest **5.4** as well as the corresponding displacing molecule. These cells were incubated at 37 °C for various incubation times and SRB assay was performed.

SRB Assay

SRB assay was performed via literature method.[7] Cell media were removed from each well. Cells were fixed by the adding 100 μL cold 10 wt % trichloroacetic acid and incubated at 4 °C for 1 h. The solution was removed and each well was washed with water five times and air dried. The addition of 50 μL SRB solution (0.4 wt % in 1 wt % acetic acid) was added into each well and the fixed cells were incubated for 10 min at room temperature. After discarding the solution, each well was rinsed with 1 wt % acetic acid five times then air dried. 100 μL of 10 mM Tris buffer (pH 10) were added into each well to solubilize the bound dye. The 96-well plate was shaken on a plate reader and the absorbance at 490 nm was measured.

Cell Counting

HeLa cells (8 x 104 cells/well) were cultured in 6-well plate for 24 h at 37°C and various concentrations of rhodamine guest **5.4** and/or displacer were added. These cells were incubated at 37 °C for 48 h. After incubation, dead HeLa cells were collected from media and adhered live HeLa cells were detached by trypsin. Both dead cells and live cells were combined and collected by centrifugation. Those cells were stained with trypan blue and

counted using a hemocytometer. The % viability of cells was determined by the equation: # live cells / (# live cells + # dead cells)

7.6 Chapter 6 Experimental

Fluorescence Measurements: In general, the fluorescence assay was carried out by mixing 10 µL of the fluorescent guest **5.5** (15 µM) or **5.1** (30 µM), 10 µL of the cavitand **1.13** (200 µM), 10 µL metal salts (500 µM in water), 60 µL of the incubation buffer (Tris buffer HCl, pH 7.4, 20 mM, Bis Tris buffer, pH 5.5, 20 mM, or PBS buffer, 7.4, 10 mM) in the 96-well plate, adding 10 µL of the steroid solution at 1.0 mM in dimethylethylene glycol (DME) to bring the total volume up to 100 µL, and incubating with mild shaking for 15 mins at room temperature. The fluorescence signal (F) was recorded in a Perkin Elmer Wallac 1420 Victor 2 Microplate Reader (PerkinElmer) with the Ex/Em wavelengths at 530/605 nm for guest **5.4** and 485/605 nm for guest **5.5**.

Supporting Figures:

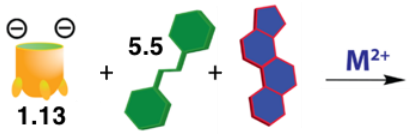

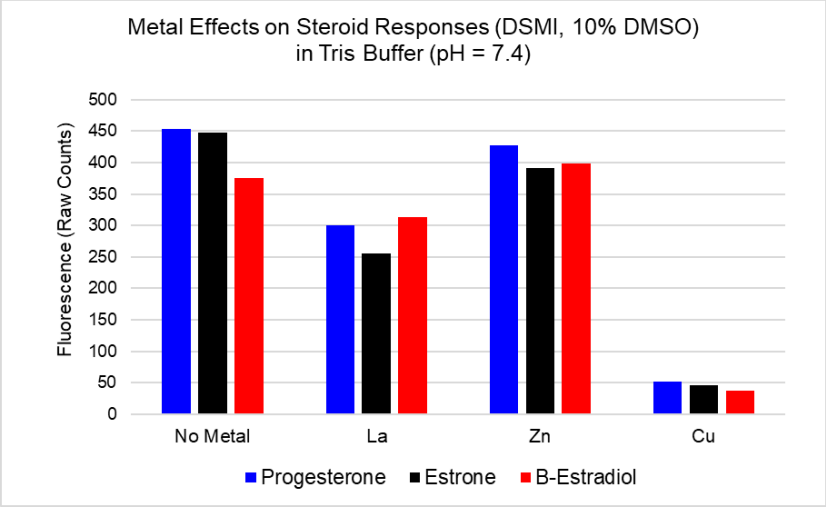

Figure 7.54: Effect of metal addition to the cavitand **1.13**:**5.5**:steroid complex in Tris buffer, pH 7.4, 10% DMSO. [**1.13**] = 20μM, [**5.5**] = 1.5 μM, [Metal] = 50 μM, [Steroid] = 100 μM.

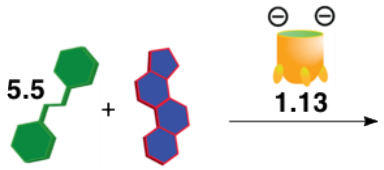

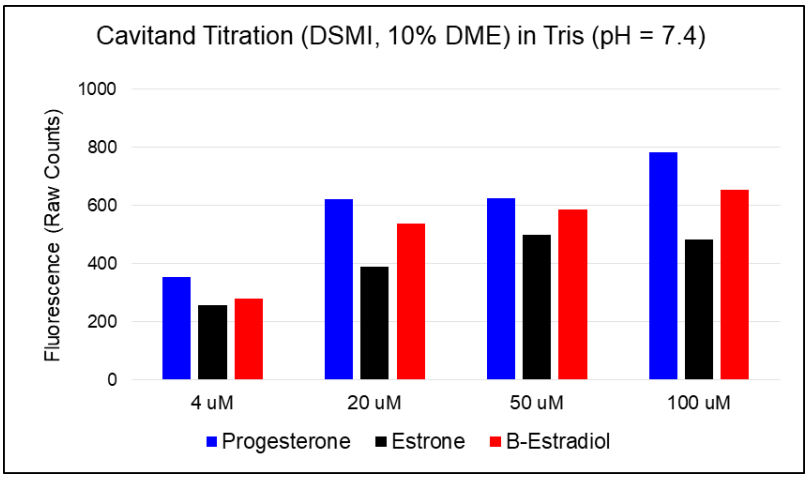

Figure 7.55: Cavitand titration into indicator **5.5**:Steroid mixture in Tris buffer, pH 7.4, 10 % DME. [**5.5**] = 1.5 μM, [Steroid] = 100 μM.

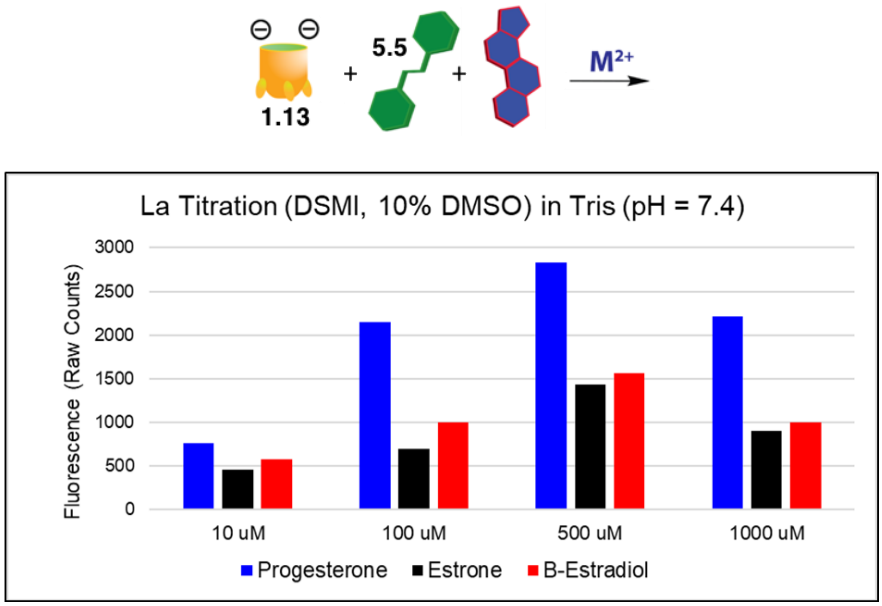

Figure 7.56: Metal (lanthanum) titration into cavitand **1.13**:**5.5**:Steroid complex in Tris buffer, pH 7.4, 10% DMSO. [**1.13**] = 20μM, [**5.5**] = 1.5 μM, [Steroid] = 100 μM.

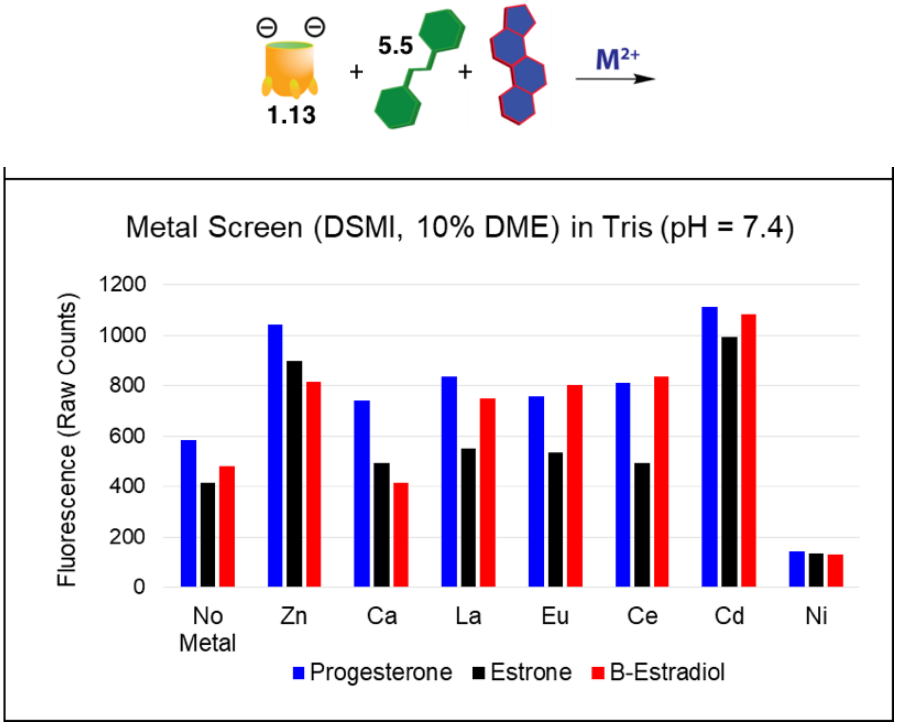

Figure 7.57: Metal screen using **1.13**:**5.5**:Steroid complex with 10% DME. [**1.13**] = 20μM, [**5.5**] = 1.5 μM, [Metal] = 50 μM, [Steroid] = 100 μM.

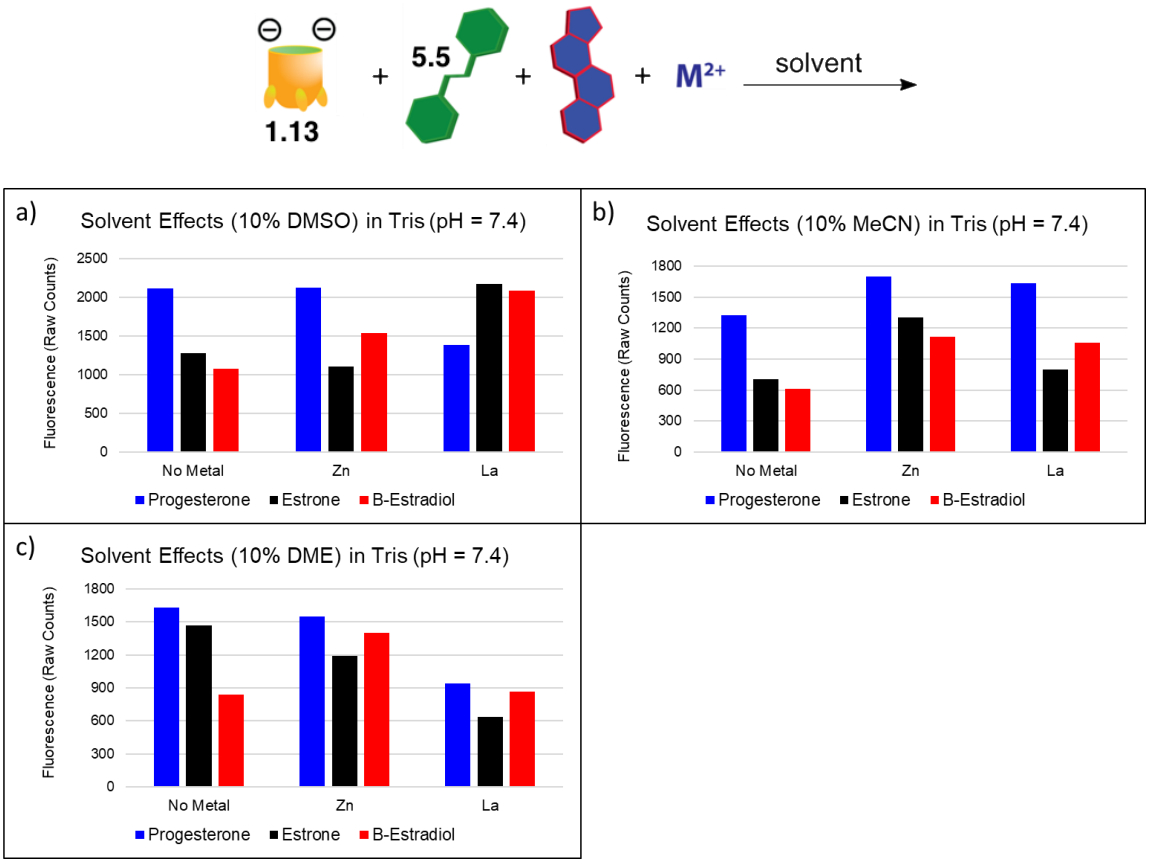

Figure 7.58: Solvent effects on steroid sensor. Sensor response changes due to varying steroid solvents, using (a) 10% DMSO, (b) 10% MeCN, or (c) 10% DME. [**1.13**] = 20μM, [**5.5**] = 1.5 μM, [Metal] = 50 μM, [Steroid] = 100 μM.

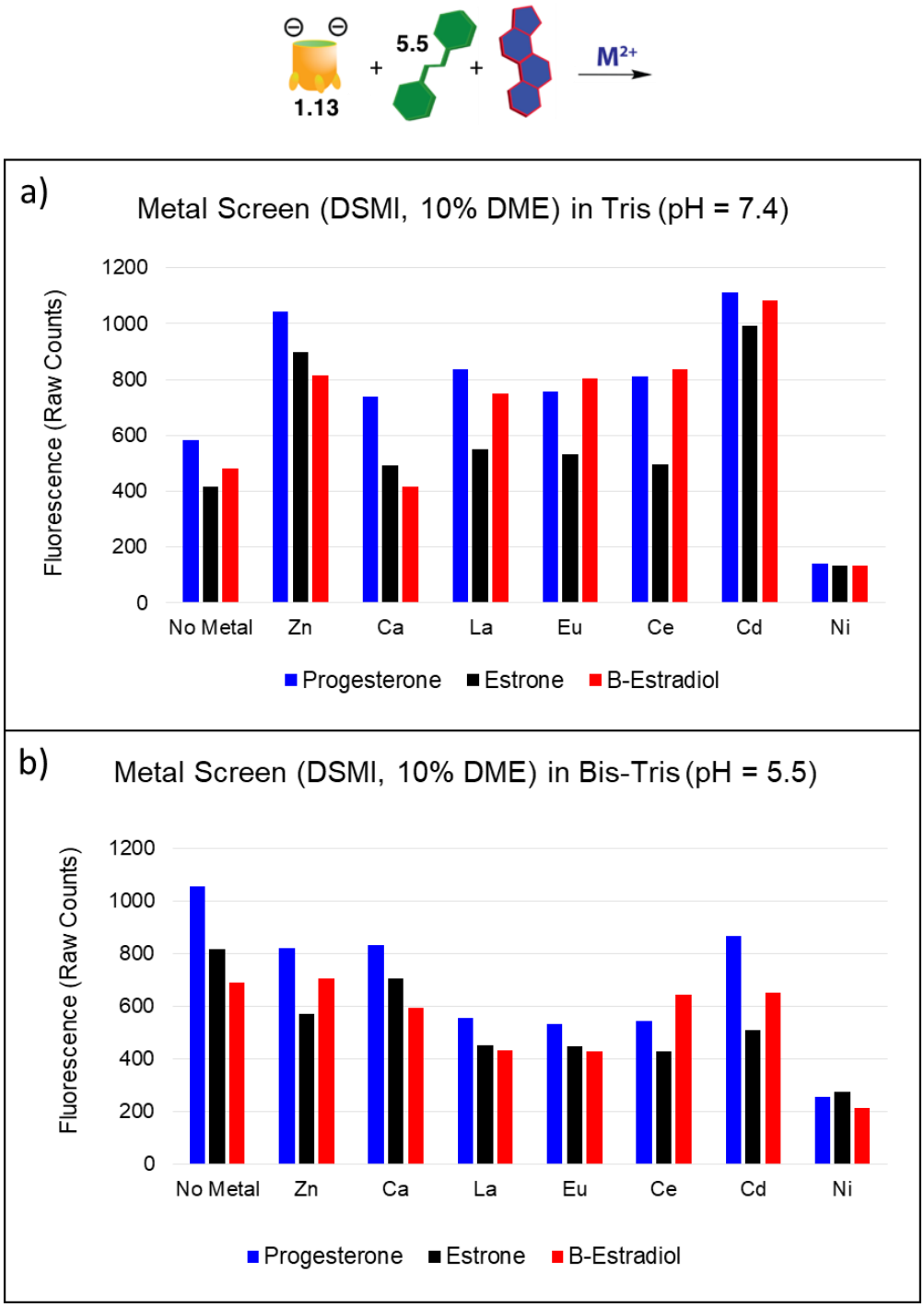

Figure 7.59: Effect of pH on sensor responses. Metal screen using **1.13**:**5.5**:Steroid complex in (a) Tris buffer, pH 7.4 and b) Bis-tris buffer, pH = 5.5 [**1.13**] = 20μM, [**5.5**] = 1.5 μM, [Metal] = 50 μM, [Steroid] = 100 μM.

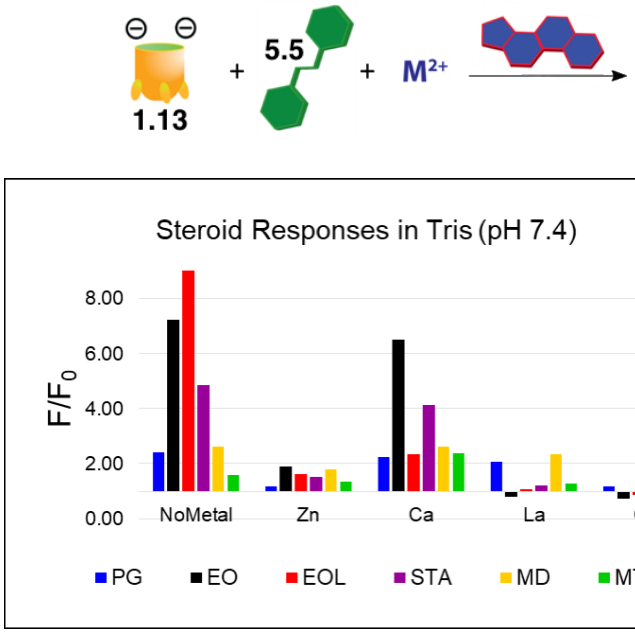

Figure 7.60: Buffer and pH effects on the DSMI sensor. Fluorescence response changes upon addition of steroids to **1.13**:**5.5**:**M** complex in Tris buffer, pH 7.4, 10% DME. [**1.13**] = 20μM, [**5.5**] = 1.5 μM, [Metal] = 50 μM, [Steroid] = 100 μM. F_0 = **1.13**:**5.5**:M complex

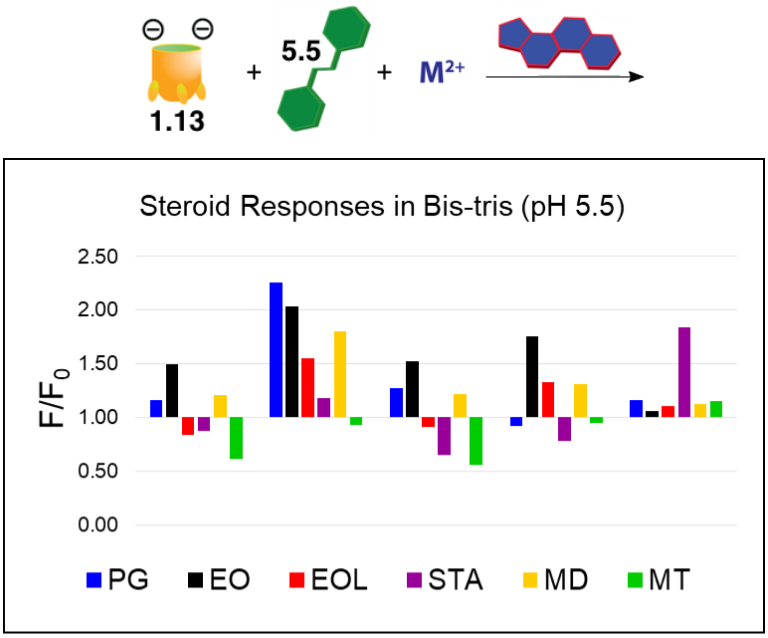

Figure 7.61: Buffer and pH effects on the DSMI sensor. Fluorescence response changes upon addition of steroids to **1.13**:**5.5**:**M** complex in Bis-tris buffer, pH 5.5, 10% DME. [**1.13**] = 20μM, [**5.5**] = 1.5 μM, [Metal] = 50 μM, [Steroid] = 100 μM. F_0 = **1.13**:**5.5**:M complex

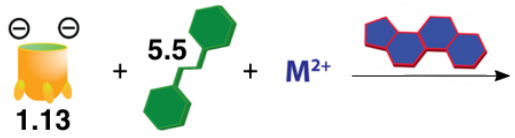

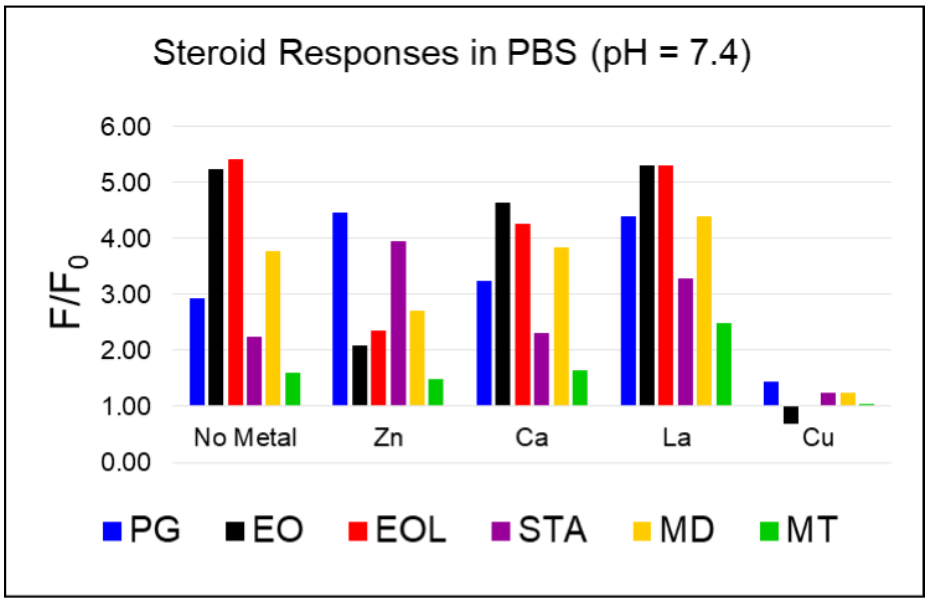

Figure 7.62: Buffer and pH effects on the DSMI sensor. Fluorescence response changes upon addition of steroids to **1.13**:**5.5**:**M** complex in PBS buffer, pH 7.4 and 10% DME. [**1.13**] = 20μM, [**5.5**] = 1.5 μM, [Metal] = 50 μM, [Steroid] = 100 μM. F_0 = **1.13**:**5.5**:M complex

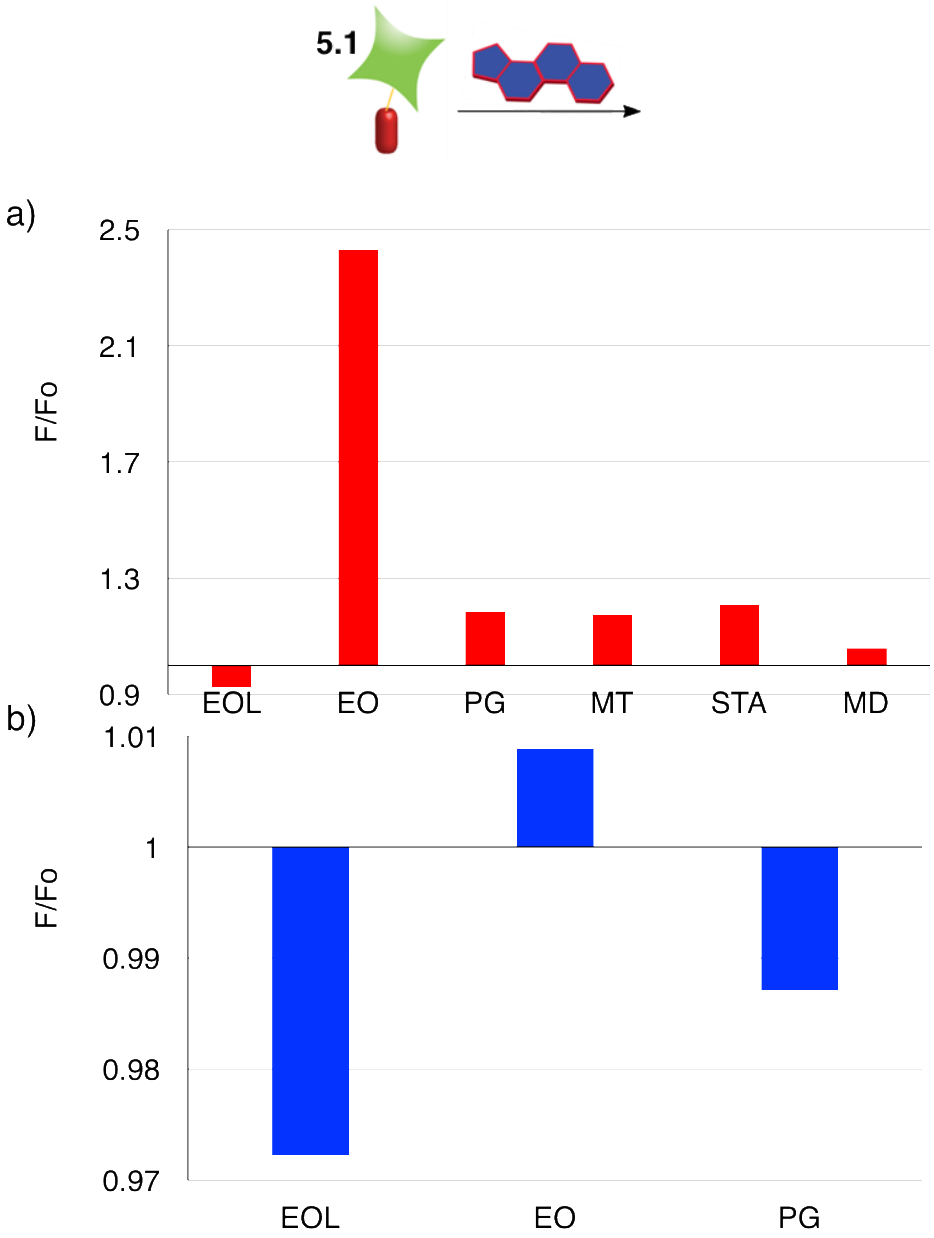

Figure 7.63: Addition of Steroids to fluorophore guest **5.1** in Tris buffer, pH 7.4 in the presence of 10% a) DME and b) DMSO. [**5.1**] = 3 μM, [Steroids] = 100 μM, F_0 = guest **5.1** signal.

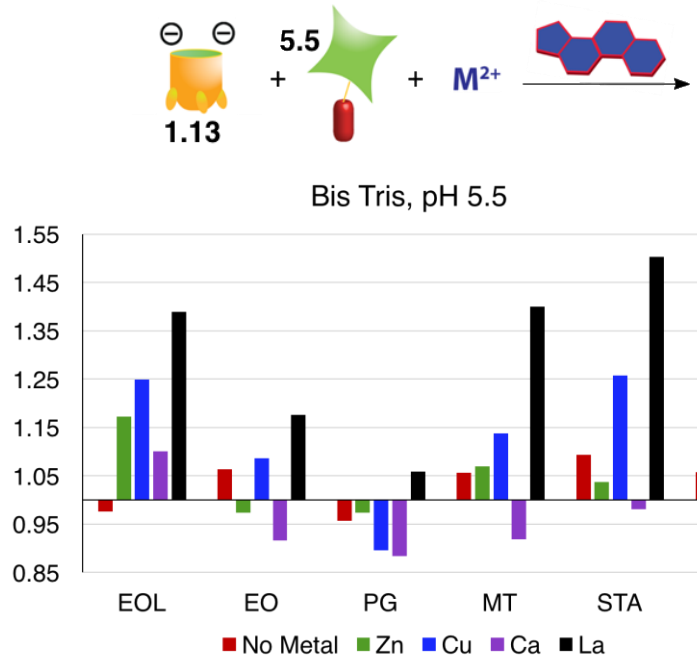

Figure 7.64: Fluorescein steroid sensor in Bis Tris buffer, pH 5.5, 10% DME, [**1.13**] = 20μM, [**5.1**] = 3 μM, [Metal] = 50 μM, [Steroid] = 100 μM. F_0= Cavitand **1.13**:**5.1**:metal complex signal.

LDA Scores Plots

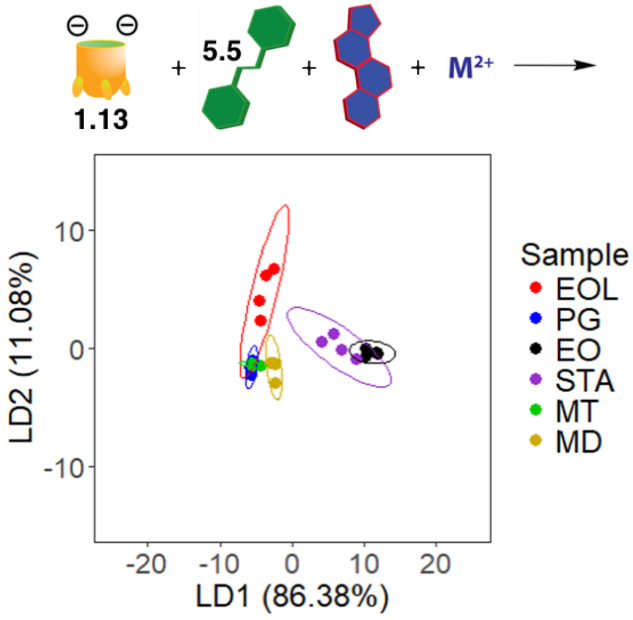

Figure 7.65: LDA plot for fluorescein guest **5.5** steroid sensor in Tris buffer, pH 7.4 (obtained from LDA of data in Figure 7.60). 10% DME, [**1.13**] = 20μM, [**5.5**] = 1.5 μM, [Metal] = 50 μM, [Steroid] = 100 μM.

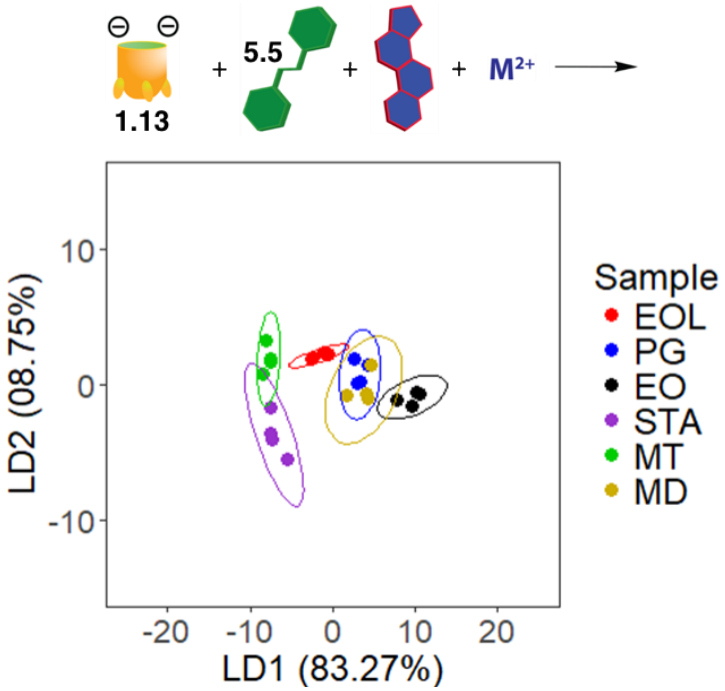

Figure 7.66: LDA plot for DSMI guest **5.5** steroid sensor in Bis Tris buffer, pH 5.5 (obtained from LDA of data in Figure 7.61). 10% DME, [**1.13**] = 20μM, [**5.5**] = 1.5 μM, [Metal] = 50 μM, [Steroid] = 100 μM.

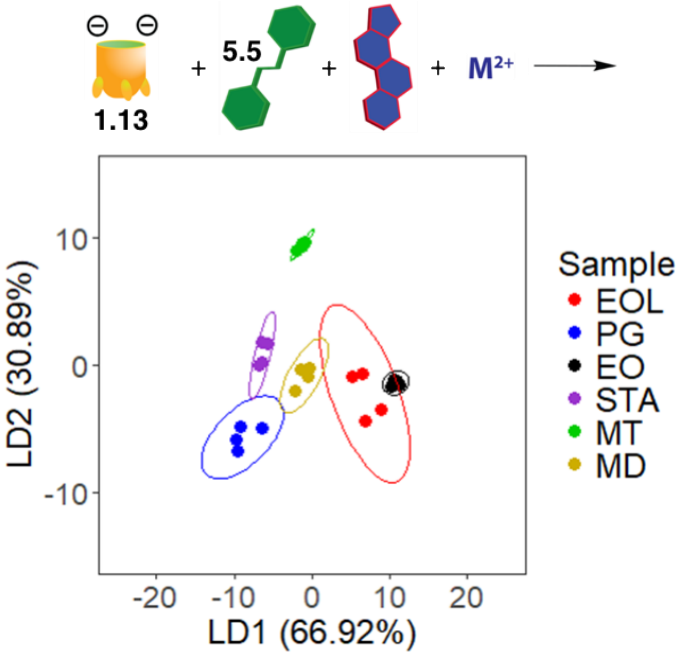

Figure 7.67: LDA plot for fluorescein guest **5.5** steroid sensor in PBS buffer, pH 7.4 (obtained from LDA of data in Figure 7.62). 10% DME, [**1.13**] = 20μM, [**5.5**] = 1.5 μM, [Metal] = 50 μM, [Steroid] = 100 μM.

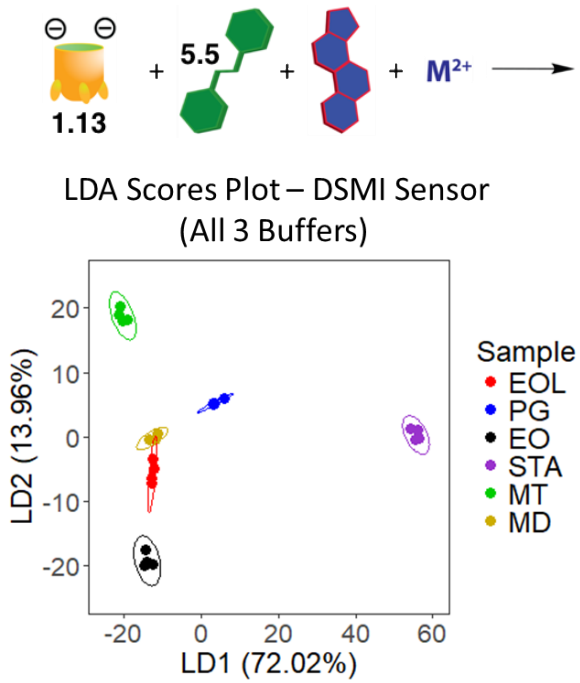

Figure 7.68: LDA scores plot for the full DSMI sensor, combining response data (Fig. 7.60, 7.61, 7.62) from all three buffers (Tris pH = 7.4, Bis-tris pH = 5.5, and PBS pH = 7.4). Ellipses represent 95% confidence intervals. [**1.13**] = 20μM, [**5.5**] = 1.5 μM, [Metal] = 50 μM, [Steroid] = 100 μM.

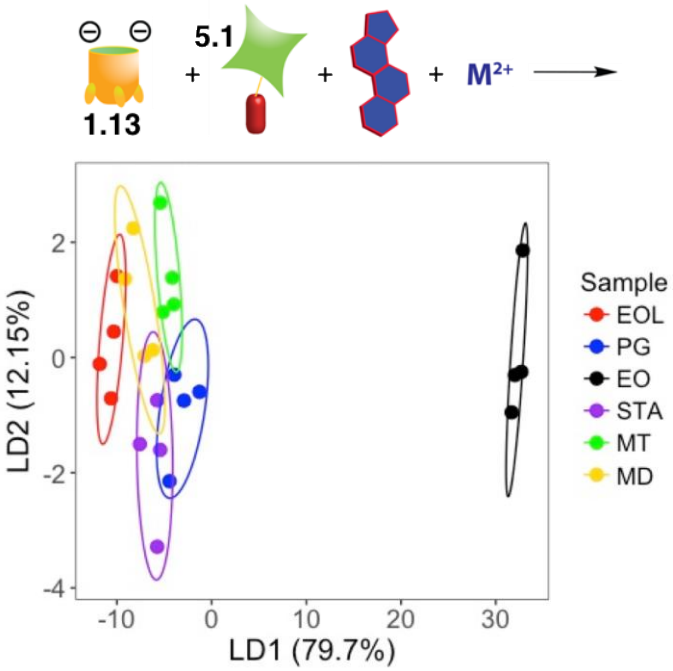

Figure 7.69: LDA plot for fluorescein guest **5.1** steroid sensor in Tris buffer, pH 7.4 (obtained from LDA of data in Figure 6.7d). 10% DME, [**1.13**] = 20μM, [**5.1**] = 3 μM, [Metal] = 50 μM, [Steroid] = 100 μM.

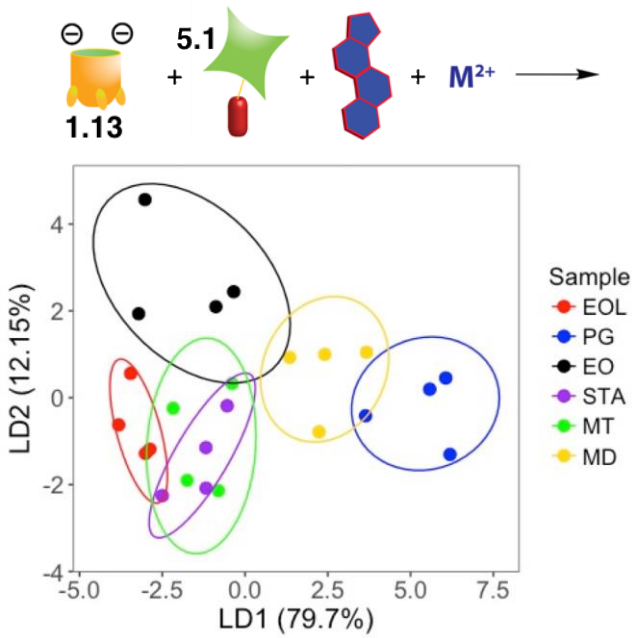

Figure 7.70: LDA plot for fluorescein guest **5.1** steroid sensor in Bis Tris buffer, pH 5.5 (obtained from LDA of data in Figure 7.64). 10% DME, [**1.13**] = 20μM, [**5.1**] = 3 μM, [Metal] = 50 μM, [Steroid] = 100 μM.

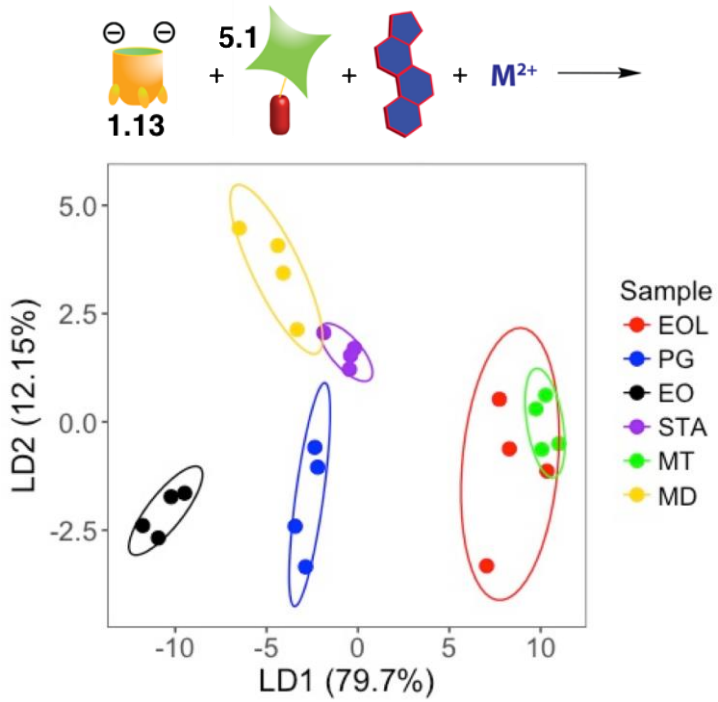

Figure 7.71: LDA plot for fluorescein guest **5.1** steroid sensor in PBS buffer, pH 7.4 (obtained from LDA of data in Figure S-26). 10% DME, [**1.13**] = 20μM, [**5.1**] = 3 μM, [Metal] = 50 μM, [Steroid] = 100 μM.

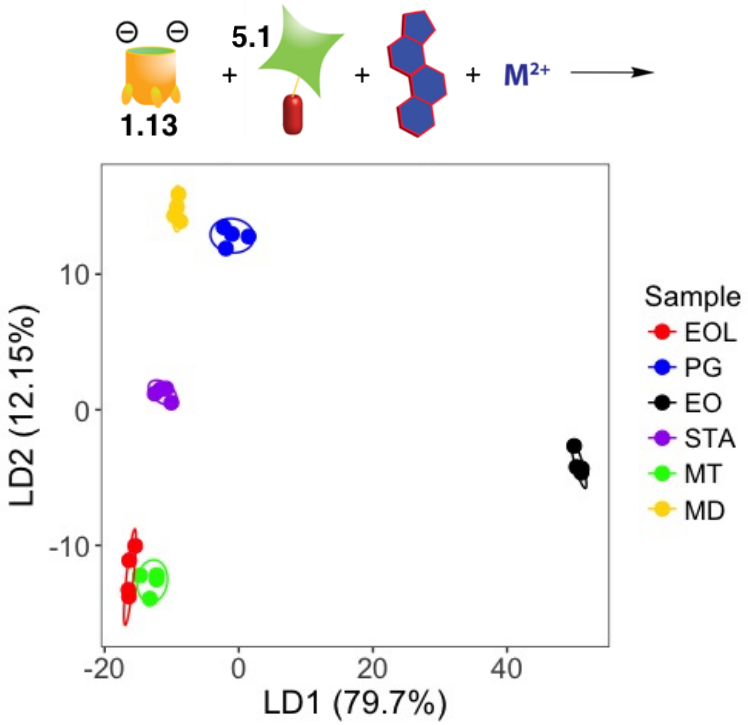

Figure 7.72: LDA plot for combined fluorescein guest **5.1** steroid sensor (obtained from LDA of combined data from Figure S-20, S-21 and S-22). 10% DME, [**1.13**] = 20μM, [**5.1**] = 3 μM, [Metal] = 50 μM, [Steroid] = 100 μM.

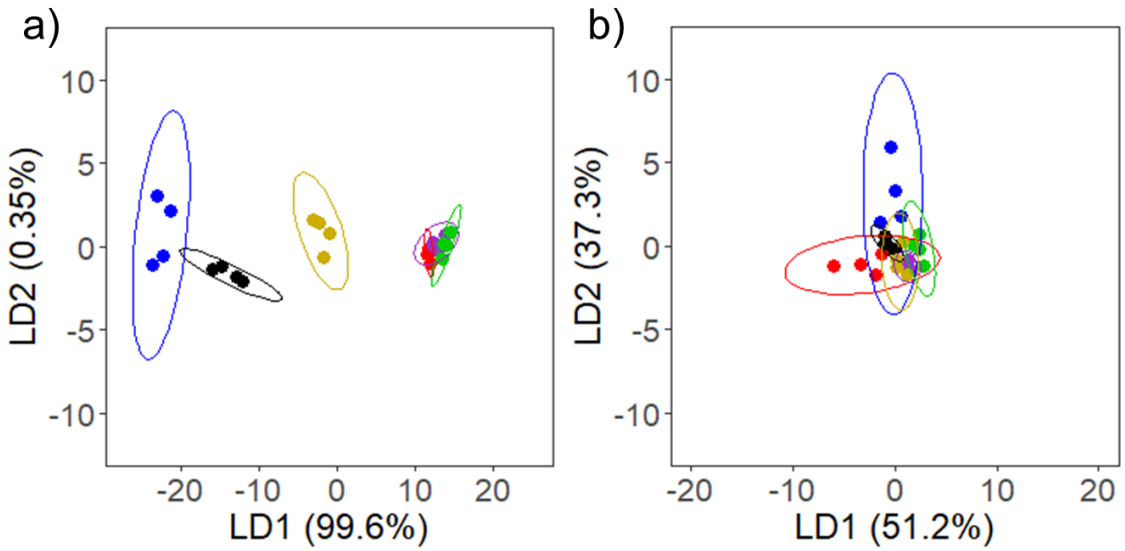

Figure 7.73: a) LDA scores plots with 95% confidence intervals for a) fluorescein steroid sensor in human urine and b) DSMI steroid sensor in human urine.

NMR Titrations

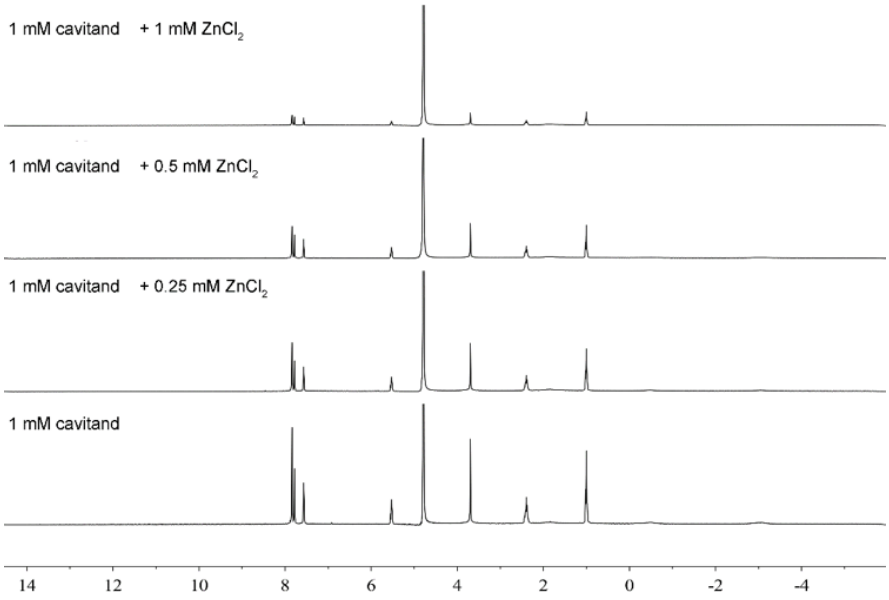

Figure 7.74: ^{1}H NMR spectra of the titration of $ZnCl_2$ into 1 mM cavitand **1.13** (400 MHz, D_2O, 298 K).

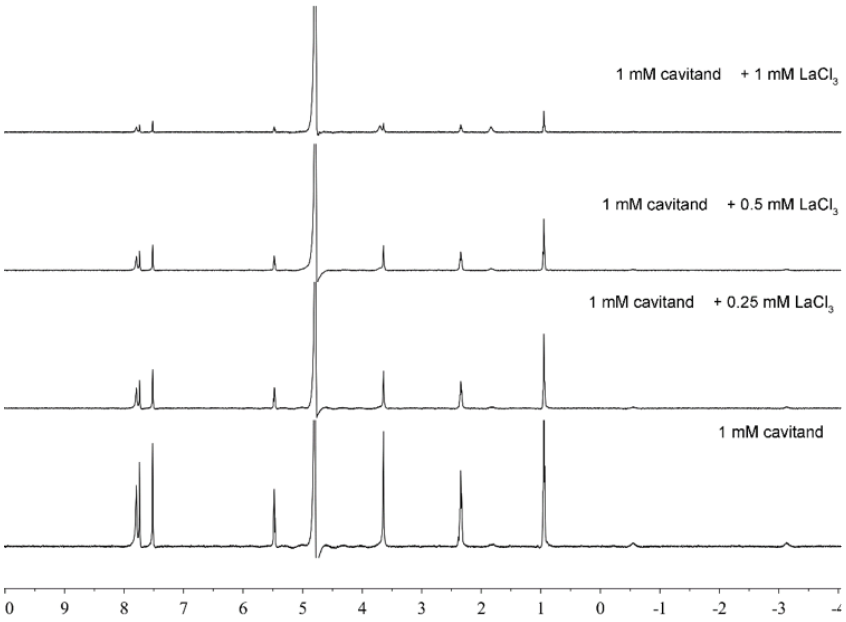

Figure 7.75: ^{1}H NMR spectra of the titration of $LaCl_3$ into 1 mM cavitand **1.13** (400 MHz, D_2O, 298 K).

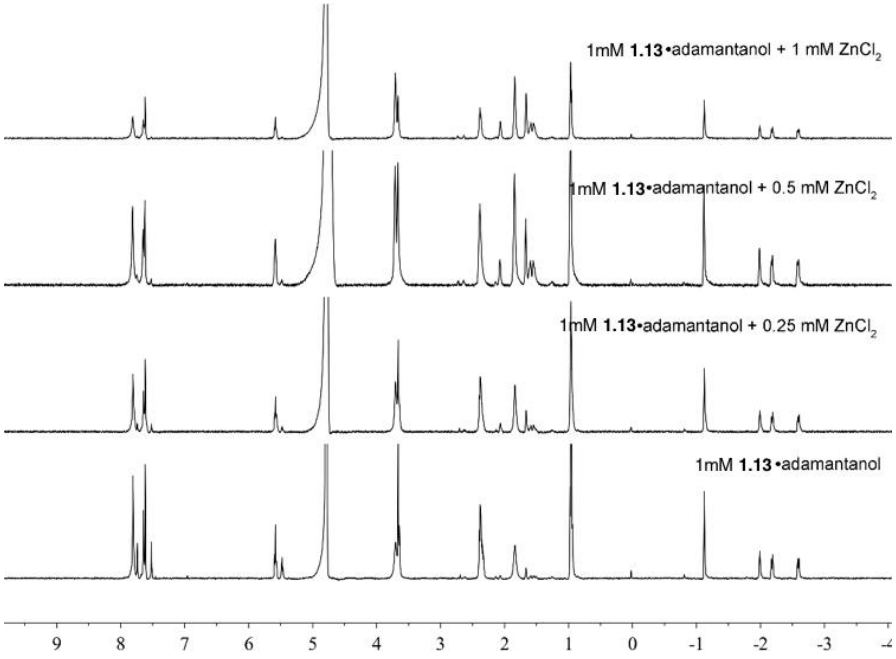

Figure 7.76: ^{1}H NMR spectra of the titration of $ZnCl_2$ into 1 mM cavitand **1.13•**adamantanol (400 MHz, D_2O, 298 K).

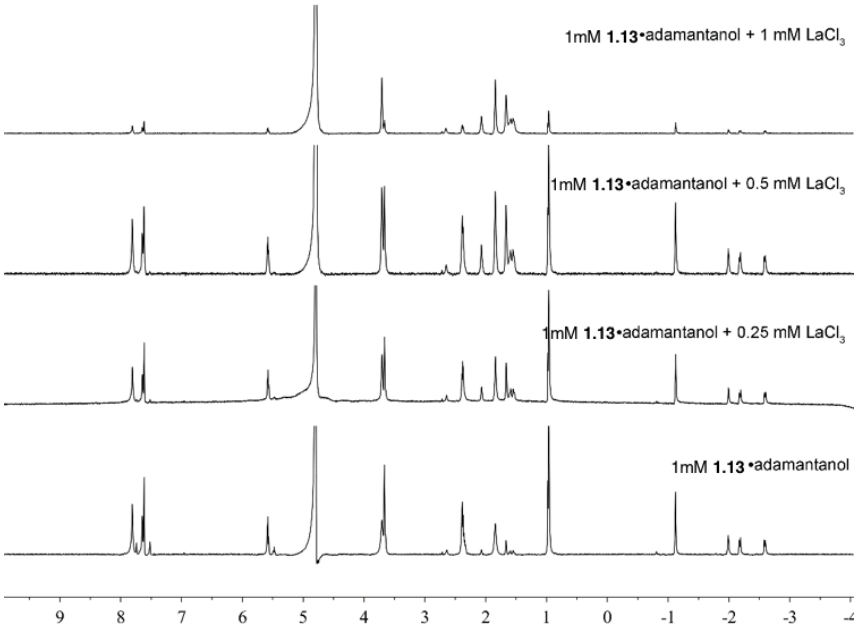

Figure 7.77: ^{1}H NMR spectra of the titration of $LaCl_3$ into 1 mM cavitand **1.10•**adamantanol (400 MHz, D_2O, 298 K).

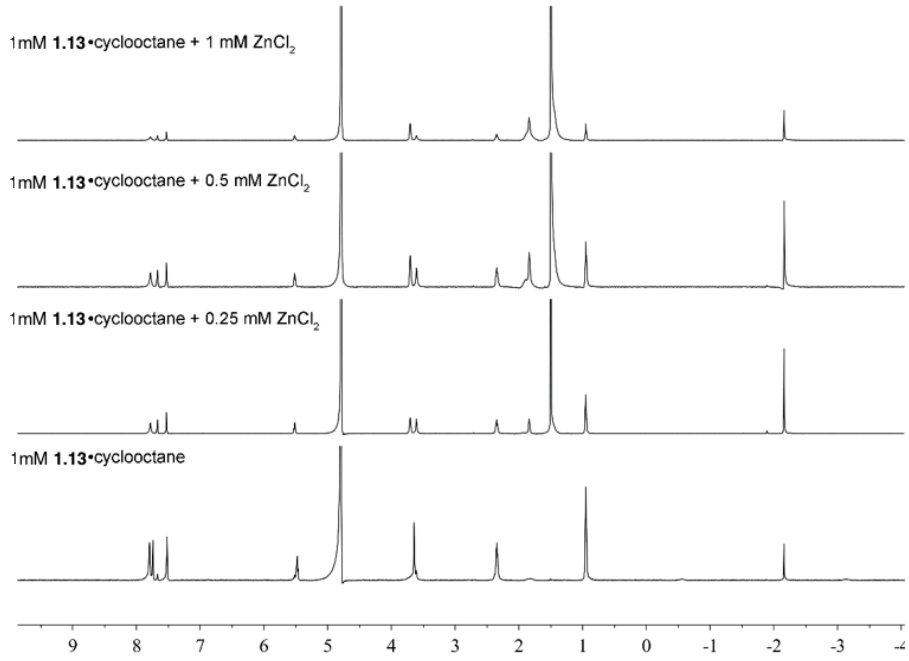

Figure 7.78: ^{1}H NMR spectra of the titration of $ZnCl_2$ into 1 mM cavitand **1.13**•cyclooctane(400 MHz, D_2O, 298 K).

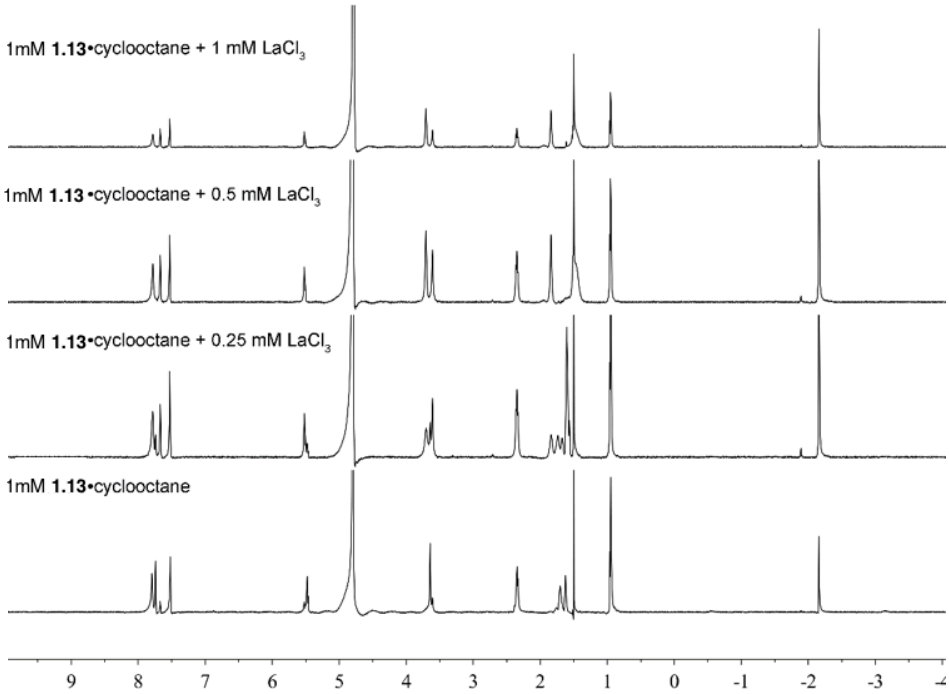

Figure 7.79: ^{1}H NMR spectra of the titration of $LaCl_3$ into 1 mM cavitand **1.13**•cyclooctane(400 MHz, D_2O, 298 K).

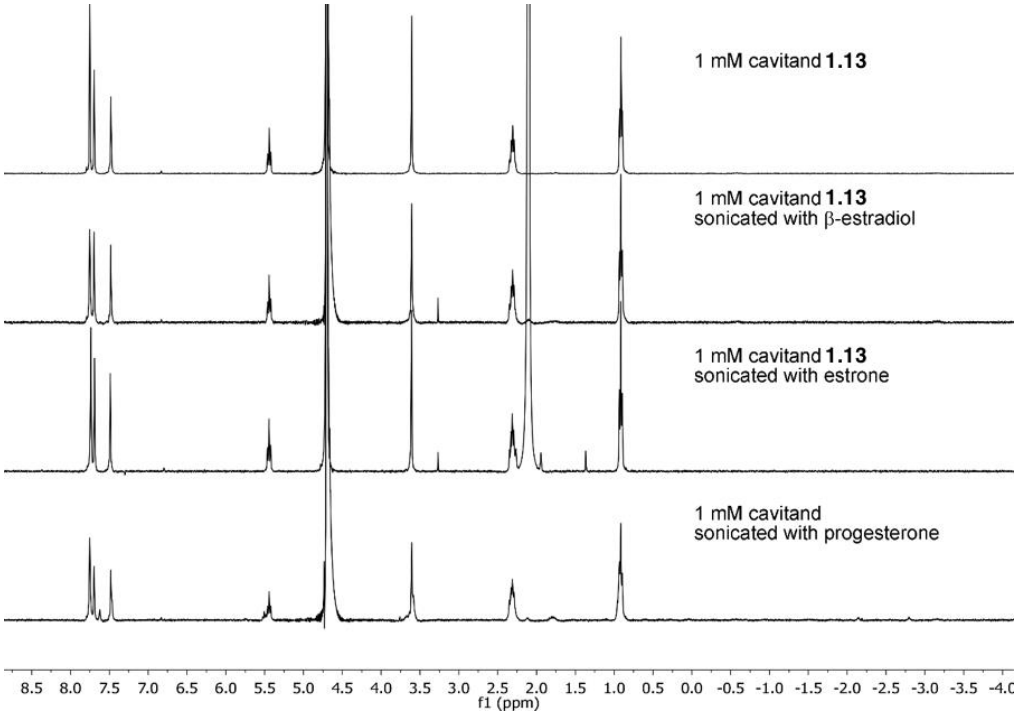

Figure 7.80: ^{1}H NMR spectra resulting from extended sonication of excess steroids with a 1 mM solution of **1.13** in D_2O. No encapsulation of β-estradiol or estrone and <5% extraction of progesterone was observed.

References:

1. Biros, S. M.; Ullrich, E. C.; Hof, F.; Trembleau, L.; Rebek, J. Jr. "Kinetically Stable Complexes in Water: The Role of Hydration and Hydrophobicity" *J. Am. Chem. Soc.* **2004**, *126*, 2870–2876.

2. Rafai Far, A.; Shivanyuk, A.; Rebek, J. Jr. "Water-Stabilized Cavitands" *J. Am. Chem. Soc.* **2002**, *124*, 2854–2855.

3. Liu, Y.; Perez, L.; Mettry, M.; Gill, A. D.; Byers, S. R.; Easley, C. J.; Bardeen, C. J.; Zhong, W.; Hooley, R. J. "Site Selective Reading of Epigenetic Markers by a Dual-Mode Synthetic Receptor Array" *Chem. Sci.* **2017**, *8*, 3960–3970.

4. Soberats, B.; Sanna, E.; Martorell, G.; Rotger, C.; Costa, A. "Programmed Enzyme-Mimic Hydrolysis of a Choline Carbonate by a Metal-Free 2-Aminobenzimidazole-Based Cavitand" *Org. Lett.* **2014**, *16*, 2480-2483.

5. Liu, Y.; Liao, P.; Cheng, Q.; Hooley, R. J. "Protein and Small Molecule Recognition Properties of Deep Cavitands in a Supported Lipid Membrane Determined by Calcination-Enhanced SPR Spectroscopy" *J. Am. Chem. Soc.* **2010**, *132*, 10383–10390.

6. Tang, Y.; Mernaugh, R.; Zeng, X. "Nonregeneration Protocol for Surface Plasmon Resonance: Study of High-Affinity Interaction with High-Density Biosensors" *Anal. Chem.* **2006**, *78*, 1841-1848.

7. Houghton, P.; Fang, R.; Techatanawat, I.; Steventon, G.; Hylands, P.; Lee, C. C. "The Sulphorhodamine (SRB) Assay and Other Approaches to Testing Plant Extracts and Derived Compounds for Activities Related to Reputed Anticancer Activity" *Methods*, **2007**, *42*, 377-387.